Universidade do Minho
Escola de Ciências

Rui Jorge Pinto Dias

Excitation of plasmon-polaritons in Graphene via non-linear mixing of optical waves

setembro de 2023

Excitation of plasmon-polaritons in Graphene via non-linear mixing of optical waves
Rui Jorge Pinto Dias
UMinho | 2023

Universidade do Minho
Escola de Ciências

Rui Jorge Pinto Dias

Excitation of plasmon-polaritons in Graphene via non-linear mixing of optical waves

Dissertação de Mestrado
Mestrado em Física

Trabalho efetuado sob a orientação do

Professor Doutor Mikhail Igorevich Vasilevskiy
Professor Doutor José Carlos Viana Gomes

setembro de 2023

Copyright and Terms of Use for Third Party Work

License granted to users of this work:

Agradecimentos

Eu gostaria de começar por agradecer aos meus orientadores, Professores Mikhail Vasilevskiy e José Carlos Viana Gomes, por me terem orientado nesta dissertação de mestrado e pelas enumeras discussões que tivemos. O trabalho que aqui apresento não existiria sem o seu apoio. Aprendi muito com eles e apesar da enorme dificuldade do projeto, sinto-me feliz por o ter aceitado.

Gostaria de também agradecer ao meu colega Diogo Cunha, pela sua ajuda na aplicação do modelo de eletrões quentes aos dados experimentais e por rever os cálculos numéricos, e ao Professor Michael Belsley e ao Dr. Peter Schellenberg, pela ajuda no laboratório e pelas discussões tivemos. Em especial, quero agradecer ao Dr. Manuel Rodrigues pela enorme ajuda no laboratório. Sempre se mostrou disponível e paciente comigo e salvou-me muitas vezes da minha própria asneira.

Por fim gostaria de agradecer aos meus pais, à minha irmã e aos meus amigos por me sempre aturarem, mesmo nos meus dias mais melancólicos.

Statement of integrity

I hereby declare having conducted this academic work with integrity.

I confirm that I have not used plagiarism or any form of undue use of information or falsification of results along the process leading to its elaboration.

I further declare that I have fully acknowledged the Code of Ethical Conduct of the University of Minho.

University of Minho, Braga, September 2023

Rui Jorge Pinto Dias

Geração ótica não linear de plasmões de superfície em grafeno

Resumo

Em 2015, plasmões de superficie (SPPs) foram pela primeira vez excitados em grafeno por um processo não linear (NL) de diferença de frequências, causado pela interação de dois feixes óticos [1]. Cálculos teóricos, usando teoria de perturbações, preveem uma resposta muito mais fraca do que a necessária para explicar os dados experimentais. Experiências e resultados teóricos recentes revelam a importância dos SPPs na relaxação de portadores de carga em grafeno e apontam para a possibilidade da sua amplificação em condições fora do equilíbrio, por exemplo, quando uma folha de grafeno é incidida por feixes óticos muito intensos. No entanto, o mecanismo por trás da sua geração por diferença de frequências ainda não é totalmente compreendido. Nesta tese, calculamos as condutividades óticas não lineares relevantes ao processo e mostramos que as observações experimentais da Ref. [1] têm a sua origem em processos físicos para além da geração coerente de SPPs por diferença de frequências, descrita pela abordagem da teoria de perturbação da matriz de densidade. Também estudamos a dinâmica dos portadores de carga no grafeno quando estes se encontram fora do equilíbrio e apresentamos o nosso modelo de eletrões quentes para explicar a sua influência na geração de SPPs. Os resultados experimentais podem ser compreendidos se para além do processo de diferença de frequências de segunda ordem, considerarmos também a amplificação do campo SPP devido ao relaxamento interbanda de eletrões quentes. Para descrever esta amplificação na presença da geração por diferença de frequências, escrevemos uma equação de evolução para o número de ocupação de SPPs. Os nossos cálculos mostram que estes dois processos, ocorrendo em simultâneo, podem aumentar fortemente a taxa de geração não-linear de plasmões de superfície.

Finalmente, o trabalho experimental, realizado para gerar SPPs através do mecanismo teoricamente considerado, também é apresentado. O principal desafio foi a contruir um esquema de deteção sensível o suficiente para observar a excitação dos SPPs. Várias técnicas, tais como deteção sensível de fase (lock-in amplifier) e deteção balanceada, foram exploradas. O esquema ótico foi construído, mas a potência do laser precisa ser estabilizada e consequentemente ainda não tivemos sucesso. No entanto, os métodos e resultados apresentados na parte experimental desta tese são uma referência importante para continuação do trabalho no futuro.

Palavras-chave: plasmónica em grafeno; condutividade não linear; eletrões quentes; "laser" de plasmões

Excitation of plasmon-polaritons in graphene via non-linear mixing of optical waves

Abstract

Several years have passed since surface plasmons-polaritons (SPPs) were excited for the first time in graphene by a frequency-difference nonlinear (NL) process caused by the interaction of two optical beams [1, 2]. Theoretical calculations, based on standard perturbation theory predict a much weaker frequency-difference response than it is required to explain the experimental data. Recent experimental results, along with theoretical calculations, demonstrate the importance of SPPs in the relaxation dynamics of non-equilibrium carriers in graphene and point out the possibility of their amplification in non-equilibrium conditions, e.g. under strong optical pumping. Nonetheless, the complete mechanism behind their generation by frequency-difference still remains to be explained. In this thesis, we calculate the relevant NL optical conductivities and show that, indeed, the experimental observations of Ref. [1] must have originated from physical processes beyond the coherent frequency-difference generation of SPPs described by the density-matrix perturbation theory approach. We study the dynamics of non-equilibrium carriers in graphene and present our hot electron model to explain their influence on the SPP generation. This model is used to understand the interplay between the SPPs and non-equilibrium carriers. We suggest that the experimental results of Ref. [1] can be understood by considering, in addition to the second-order frequency-difference process, the amplification of the SPP field via interband relaxation of hot electrons. We propose a master equation to describe this amplification in the presence of the frequency-difference generation. Our calculations show that these two processes, occurring simultaneously, can strongly enhance the rate of *resonant* generation of surface plasmons by two adjusted optical beams.

Finally, experimental work was carried out to generate SPPs via the theoretically considered mechanism. The main challenge appeared to be their detection. Several techniques, such as phase sensitive (lock-in amplifier) and balanced detection, have been explored. The optical setup has been built, but the laser power still needs to be stabilized, so we have not been successful yet. Nevertheless, the methods and results presented in the experimental part of this thesis can be an important benchmark for successes in the future.

Keywords: graphene plasmonics; nonlinear conductivity; hot electrons; plasmon lasing

Contents

List of Figures

Nomenclature

DF	Difference frequency
DFG	Difference Frequency Generation
EM	Electromagnetic
IR	infrared radiation
NL	Nonlinear
OPA	Optical Parametric Amplifier
SF	Sum Frequency
SNR	Signal to Noise Ratio
SPP	Surface Plasmon Polariton
THz	Terahertz
WLC	White Light Continuum

Chapter 1

Introduction

Even though scientists theoretically predicted the potential existence of an atomic-monolayer form of carbon many decades ago [3], graphene was rediscovered, isolated and investigated in the beginning of this century and the seminal paper, co-authored by future Nobel Prize Laureates Andre Geim and Konstantin Novoselov, was published in 2004 [4]. With the Nobel Prize in Physics awarded in 2010, graphene became probably the most popular material in the world and I heard this word many times even before starting my university studies. It took me some time to understand all the excitement around this material and appreciate its really extraordinary properties [5]. I am particularly interested in graphene's capacity to support charge density oscillations coupled to an evanescent electromagnetic field, known as surface plasmon polaritons (SPPs) [6, 7], in the THz-to-IR spectral range. These composite excitations are interesting for a range of potential applications in the field of photonics, optoelectronics and energy [8]. Despite the remarkable progress achieved so far, the field of Graphene Plasmonics still has some serious obstacles to overcome, mainly because SPPs are characterized by large in-plane wavevectors, beyond the light cone, and consequently cannot be excited directly by propagating electromagnetic (EM) waves since the conditions for energy and momentum conservation cannot be fulfilled. Although several methods to excite SPPs do exist, such as the attenuated total internal reflection (ATR) configuration, for many future applications, such as plasmonic circuits and THz sources, an all-optical generation of SPPs in graphene is highly desirable. Theoretical analysis and exploring the experimental feasibility have been the goal of this Master project. A good description of the fundamental electronic properties of graphene can now be found in review article [5] and book [7], so let us dive directly into the subject of this thesis.

A part of this thesis is covered in the papers [9, 10].

1.1 Generation of graphene SPPs by two optical beams

About ten years ago [11] it was theoretically proposed to leverage graphene's NL response and generate SPPs via a difference-frequency (DF) nonlinear (NL) process, using only two optical beams with slightly different frequencies. We shall call these beams b and a, with frequencies ω_b and ω_a,

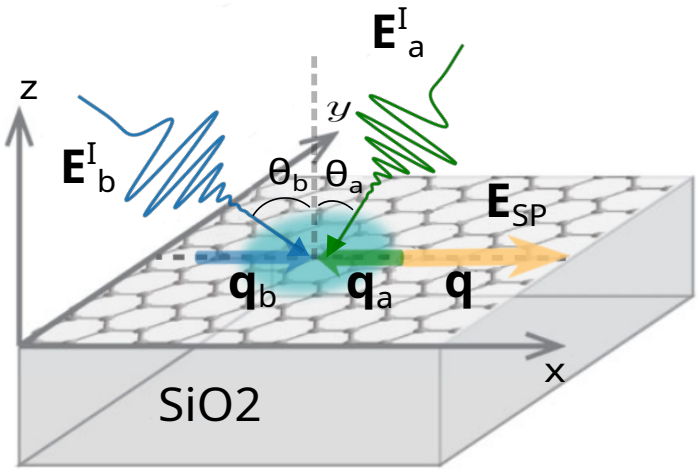

Figure 1.1: Schematics of all-optical generation of surface plasmons via a frequency-difference NL process of interaction of two optical beams, a and b, represented by their electric fields $\mathbf{E}_{a,b}$ and their incident angles $\theta_{a,b}$. $\mathbf{E}_{\rm sp}$ represents the SPP field. $\mathbf{q}_j$ $(j = a, b)$ are the in-plane momentum of the incoming beams and $\mathbf{q} = \mathbf{q}_b - \mathbf{q}_a$ is the SPP momentum.

respectively. The DF process is expected to lead to the generation of SPPs of frequency $\omega = \omega_b - \omega_a$.

In spite of being centrosymmetric, with a second-order optical response that should vanish by symmetry [12], graphene can still display a nonzero second order optical conductivity if one uses oblique optical beams with nonzero and unequal in-plane components of the wavevector, thus effectively breaking graphene's symmetry. This idea was experimentally implemented by Constant et al. [1] and investigated further in a subsequent article [13][1]. These experiments used graphene on top of SiO_2 (quartz) and two 100 fs p-polarized laser pulses, a pump (pulse b), and a probe (pulse a), to excite SPPs, as shown in Fig. 1.1. They fixed the probe wavelength at $\lambda_a = 615$ nm, while the pump wavelength, λ_b, was varied between 615 and 545 nm. By recording the differential reflectivity of the probe, under the condition of energy and in-plane momentum matching for SPPs, they observed a resonance associated with SPP generation (see Figs. 1.2 and 1.3) with the frequency and momentum:

$$\omega = \omega_b - \omega_a \qquad \mathbf{q} = \mathbf{q}_b - \mathbf{q}_a \ , \tag{1.1}$$

where $\omega_j = 2\pi c/\lambda_j$ and $q_j = (\omega_j/c)\sin\theta_j \mathbf{e}_x$ are the in-plane momentum of the pulses.

The differential reflectivity is defined as:

$$\frac{\Delta R}{R\Phi_b} = \frac{R - R_0}{R\Phi_b} \ , \tag{1.2}$$

where R is the reflectance of the probe when the pump is present, R_0 is the reflectance in the absence

[1] All-optical generation of SPPs was also reported in another publication [2]. However, this article does not contain sufficient details and is not clear enough, in my view. Therefore, it will not be discussed further in this thesis.

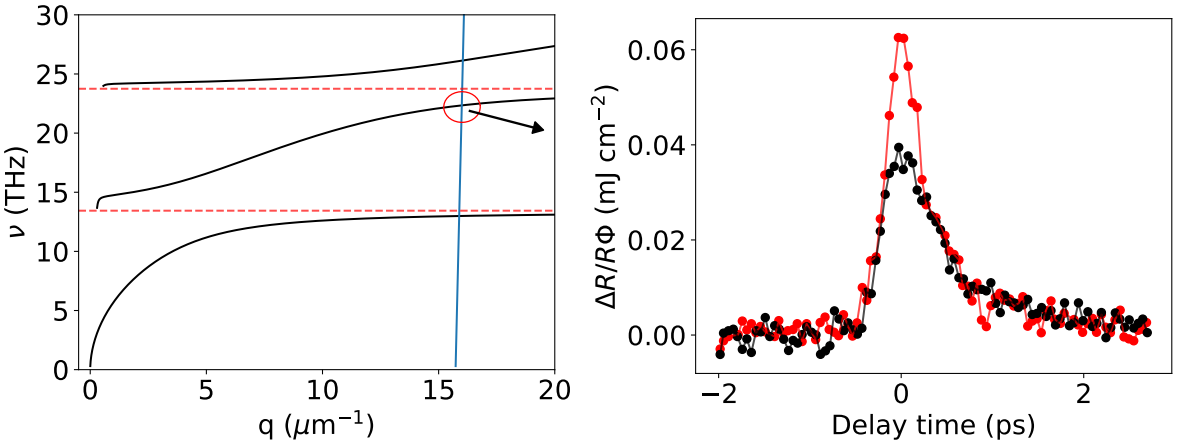

Figure 1.2: Experimental results from Constant et al. [1], taken from figure 2 of the article. For this case, the incident angles were $\theta_b = -35°$ and $\theta_a = 75°$. **Left:** SPP dispersion relation (black lines), for a damping rate $\gamma_p \approx 2\pi \times 1.6$ ps^{-1} and an effective Fermi level of 500 meV, and DF scan $(q_b - q_a, \omega_b - \omega_a)$ as performed in the experiment (blue line). Optical phonons of the substrate are represented by the red dashed lines. **Right:** Measured differential reflectivity as a function of the time delay between probe and pump. The black curve shows a typical non-resonant measurement when the difference frequency between pump and probe (61.2 THz) does not match with a surface plasmon state. The red curve shows an additional symmetric contribution to the recorded reflection signal when the difference frequency matches the frequency of a SPP (23.8 THz), highlighted in the left figure by the red circle.

of the pump and Φ_b is the pump's fluence. The graphene sample used in their experiments was n-doped, with a natural Fermi level of 300 meV. They weakly focused the beams on graphene, with a spot size of approximately 300 μm in radius. The pump pulse fluence used was $\Phi_b \sim 0.1 - 0.2$ mJ cm^{-2} while the probe fluence was two orders of magnitude smaller, $\Phi_a \sim 10^{-2}\Phi_b$. They performed the experiment for three different geometries (different angles of incidence).

The resonance observed in the differential reflectivity was interpreted to be caused by an exchange of energy between pump and probe due to excitation of the SPP field. In other words, pump and probe by DF created SPPs, which in their turn, interacted with the pump, also by a DF process, and generated photons at the frequency of the probe. Consequently, the observed resonance involves an interaction between three fields, therefore it is a third order process, composed of two intermediate second order processes.

To model the SPP dispersion, Constant et al. used an effective Fermi level of 500 meV, which they justified as a consequence of photodoping, expected under illumination by ultrafast pulses [14], and introduced an effective formula for the second order conductivity:

$$\sigma^{(2)}(\omega) = i \left|\sigma^{(2)}\right| \frac{\omega}{\omega_a} , \tag{1.3}$$

where $\left|\sigma^{(2)}\right|$ is a fitting parameter. They accounted for the coupling between graphene SPPs and substrate (quartz) optical phonons according to Ref. [15]. Their main results are summarized in

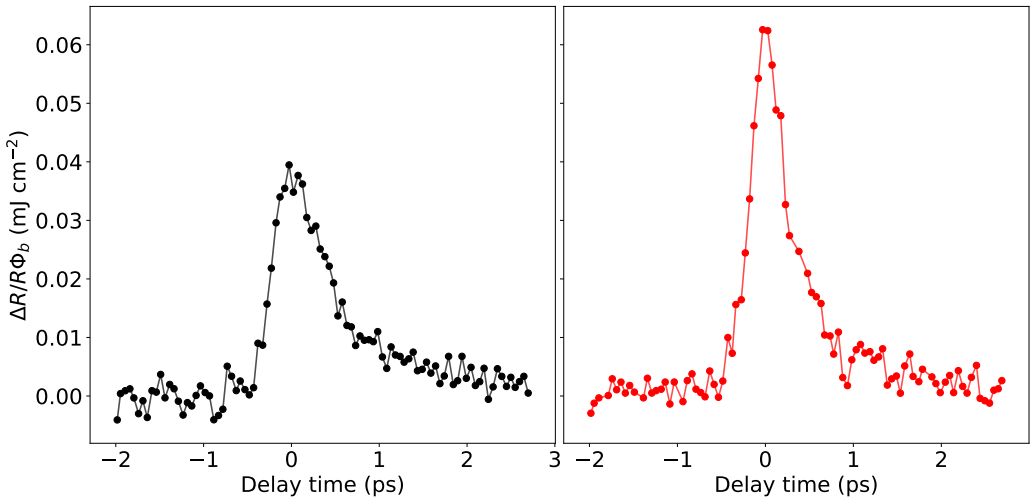

Figure 1.3: Same as in Fig. 1.2, but with non-resonant and resonant signals plotted separately for better visualization.

Geometry	θ_b	θ_a	λ_b (nm)	ν (THz)	$\frac{\Delta R}{R\Phi_b}$ mJ cm^{-2}	$\left\|\sigma^{(2)}\right\|$ (fA m V^{-2})
1)	45°	35°	607	7.0	-0.0097	24
2)	40°	20°	597	12	-0.025	75
3)	-35°	75°	587	23.8	0.062	180

Table 1.1: Main experimental results of Ref. [1] for the three different geometries. ν is the DF frequency at which a SPP resonance was observed. $\left|\sigma^{(2)}\right|$ was extracted using the model of Ref. [1]. For all geometries $\lambda_a = 615$ nm, $\Phi_b \sim 0.1 - 0.2$ mJ cm^{-2} and $\Phi_a \sim 10^{-2}\Phi_b$. To calculate the SPP dispersion curve, they assumed a damping rate of $\gamma_p \approx 2\pi \times 1.6$ ps^{-1} and a effective Fermi level of 500 meV. This table was taken from article [16], where the authors of Ref. [1] further analyzed their results.

Table 1.1.

Even though the relation of the observed resonant peak in the differential reflectance to the generation of graphene surface plasmons looks doubtless, as we will see in the next Sections, the results in Table 1.1 deviate a lot from what had been predicted [9]. First, the resonant signal appears on top of a broader asymmetric band, which is also observed outside of the plasmon resonance. This asymmetric temporal variation of the differential reflectance was tentatively attributed to hot-electron effects [13] and it is not well understood. Secondly, theoretical calculations of the second-order conductivity for the scheme in Fig. 1.1, using perturbation theory [9, 16, 17], predict a response orders of magnitude smaller than estimated by the experiment. Thus, one specific objective of this thesis was to understand the real reason behind the unexpectedly large signal observed by Constant et al.

1.2 Objectives and structure of the thesis

As mentioned above, the main goal of this Master project was to understand the feasibility of generation of useful surface plasmons in graphene by combining two optical beams. The work presented here is divided into two parts. In the first part we study and model theoretically the experimental observations of Refs. [1, 13], namely, the origin of both non-resonant and resonant signals. The second part describes the experimental work done in an attempt to reproduce the results of Refs. [1, 13] and further study the phenomenon.

The thesis consists of seven chapters and eleven appendices. In the next chapter (Chapter 2), fundamental (linear) properties of graphene plasmons and surface plasmon-polaritons are presented. In Chapter 3, the DF nonlinear response of graphene is calculated. The obtained formulae for the nonlinear conductivity are used to model the differential reflectivity. The results are incompatible with the observations in Refs. [1, 13]. In search for an answer, the dynamics of non-equilibrium carriers in graphene is studied and a hot electron model, to describe this carriers, is presented. These are the subjects of Chapter 4. The fifth chapter deals with SPPs in non-equilibrium graphene and proposes a new mechanism, SPP lasing, to explain the experimental observations.

Chapter 6 presents the carried out experimental work. The use of an optical parametric amplifier to control the frequency difference between beams is discussed as well as the best approach to detect the generation of SPPs. The unsolved technical issues are addressed at the end. Finally, Chapter 7 sums up the study.

1.3 Units

The system of units used in this work was the Gaussian one (CGS). However, the nature of the problem is better understood and the calculations are more easily performed in non-system units μm / ps^{-1} / meV. The reason is that in these units the Fermi velocity in graphene is:

$$v_F = 1 \ \mu\text{m ps}^{-1} \ . \tag{1.4}$$

To make things easier for the reader, I present here the necessary fundamental constants in such units. Namely, Plank's constant and the velocity of light are:

$$\hbar = 0.658 \ \text{meV ps} \quad , \quad c = 300 \ \mu\text{m ps}^{-1} \ . \tag{1.5}$$

The fine structure constant is:

$$\alpha_f = \frac{e^2}{\hbar c} = \frac{1}{137} \tag{1.6}$$

and this gives us an easy way of determining the electron's charge e in this units. Finally, as useful conversion relations, we have

$$1 \ \text{W} = 6.24 \cdot 10^9 \ \text{meV ps}^{-1} \tag{1.7}$$

and:

$$\text{W cm}^{-2} = 62.4 \text{ meV ps}^{-1}\mu\text{m}^{-2} \tag{1.8}$$

As a convention, the Greek letter ν is frequency and ω the radial frequency:

$$\omega = 2\pi\nu \ ; \tag{1.9}$$

ν is measured in THz, while ω in ps^{-1}.

Chapter 2

Graphene plasmonics

In this chapter, we introduce basic concepts of the electronic, optical, and plasmonic properties of graphene, which serve as background for the detailed discussions in the following chapters. Details of the calculations can be found in the Appendix.

2.1 Fundamentals

SPPs are evanescent electromagnetic (EM) waves coupled to the free electron plasma oscillations, that propagate along the surface of a conductor [6, 7] and decay exponentially away from it. In our case, the conductor is a graphene sheet placed between two dielectrics, for example air and SiO_2. In graphene, we can distinguish between two types of SPPs [6, 7]: transverse magnetic (TM) SPPs and transverse electric (TE) ones. We are only interested in the TM-SPPs and will not consider TE-SPPs[1].

To introduce the necessary concepts, consider a graphene sheet between two dielectrics, with dielectric constants ε_1 and ε_2, referring respectively to the top and bottom dielectric, as shown in Fig. 2.1. For simplicity, assume monochromatic solutions of Maxwell's equations. For an SPP with

[1]Since, these excitations are composed of electrons coupled to a EM field, the word polariton should be used when addressing them. However, since in this thesis, there is no room for confusion, for simplicity I might call SPPs, surface plasmons or simply plasmons.

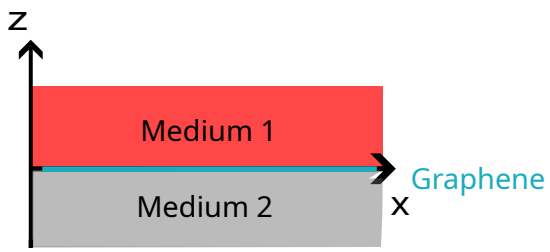

Figure 2.1: Illustration of a single graphene sheet (blue line) between two insulators with dielectric constants ε_1 and ε_2.

a frequency ω and a wavevector $\mathbf{q} = q\mathbf{e}_x$, propagating along the x-direction, its EM field has the form:

$$\mathbf{E}_{\text{sp}} = \begin{cases} (E_{2,x}, 0, E_{2,z})\, e^{iqx} e^{i\kappa_2 z} e^{-i\omega t} & z < 0 \\ (E_{1,x}, 0, E_{1,z})\, e^{iqx} e^{-i\kappa_1 z} e^{-i\omega t} & z > 0 \end{cases} ,$$

$$\mathbf{H}_{\text{sp}} = \begin{cases} H_2 \mathbf{e}_y e^{iqx} e^{i\kappa_2 z} e^{-i\omega t} & z < 0 \\ H_1 \mathbf{e}_y e^{iqx} e^{-i\kappa_1 z} e^{-i\omega t} & z > 0 \end{cases} . \tag{2.1}$$

Inserting the fields (2.1) into Maxwell's equations (see Appendix A for details) we obtain for κ_m and field components:

$$\kappa_m^2 = q^2 - \frac{\omega^2}{c} \varepsilon_m \ , \tag{2.2}$$

$$E_{m,z} = i(-1)^{m+1} \frac{q}{\kappa_m} E_{m,x} \ . \tag{2.3}$$

From the boundary conditions including the continuity of the tangential component of the electric field and discontinuity of the normal component, $E_{j,z}$, when there is a surface charge present, assuming linear optical response of graphene, we find the SPP dispersion equation:

$$D(\omega, q) = \frac{\varepsilon_2}{\kappa_2} + \frac{\varepsilon_1}{\kappa_1} + \frac{4\pi i}{\omega} \sigma^{(1)}(\omega, q) = 0 \ . \tag{2.4}$$

Its solution yields the SPP dispersion relation $\omega(q)$. Here $\sigma^{(1)}(\omega, q)$ is graphene's non-local linear conductivity. The solutions to (2.4) are real or complex, depending on whether the real part of the conductivity vanishes or not. Since we shall include losses in the conductivity, its real part will be non-zero, so the solutions will be complex. We can either look for solutions with a complex wavevector q:

$$q(\omega) = \text{Re}q(\omega) + i\text{Im}q(\omega) \tag{2.5}$$

or with a complex frequency:

$$\omega(q) = \text{Re}\omega(q) + i\text{Im}\omega(q) \tag{2.6}$$

The choice depends on the physical situation. If we have a continuous excitation of SPPs, it is better to consider q complex. On the other hand, if SPPs are excited by pulsed radiation, it is better to take ω complex. We shall use both choices, so it will be specified whenever necessary. An example of the plasmonic dispersion curve is shown in Fig. 2.2.

At the frequencies of interest (low SPP frequencies), $\sigma^{(1)}(\omega, q)$ is well approximated by the local conductivity $\sigma^{(1)}(\omega)$. There are two contributions to $\sigma^{(1)}(\omega)$ coming from intraband and interband optical transitions:

$$\sigma^{(1)}(\omega) = \sigma_{\text{intra}}(\omega) + \sigma_{\text{inter}}(\omega) \ , \tag{2.7}$$

where σ_{intra} is the Drude contribution, describing intraband transitions, and σ_{inter} denotes the con-

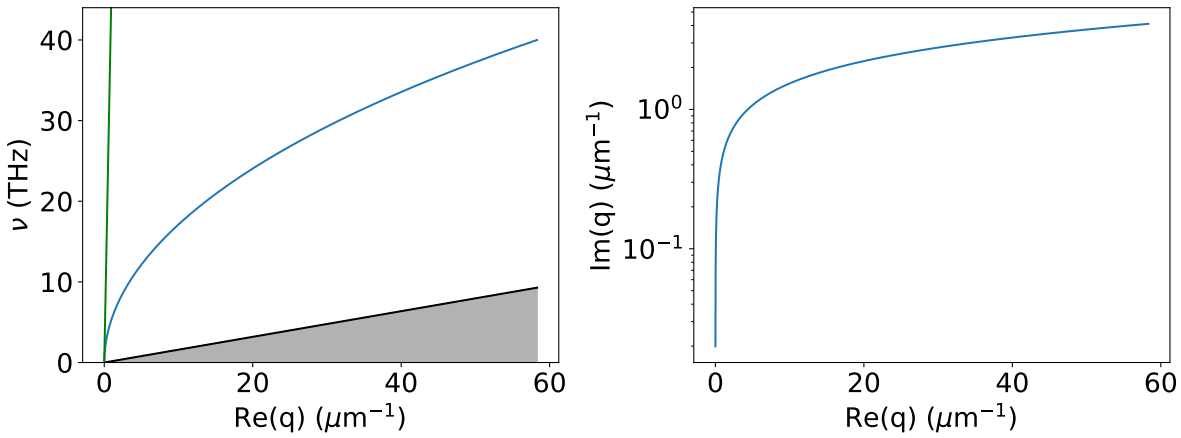

Figure 2.2: **(right)** Plasmon dispersion curve $\omega(q)$ (blue line), calculated using both the Drude and interband conductivities. In this calculation q was chosen to be complex. The light line is shown in green and the black line represents the electronic dispersion, below which we have the Landau Damping region (shaded region). **(left)** Losses. The calculation parameters were: Fermi energy $E_F = 300$ meV, $\varepsilon_1 = 1$ and $\varepsilon_2 = 2.4$, electron momentum relaxation rate $\gamma_p = 2\pi \times 2.6$ ps^{-1}, interband relaxation rate $\gamma_{\text{inter}} = 0.1$ ps^{-1} (added to to avoid bad numerical behavior) and a temperature $T = 300$ k.

tribution of interband transitions. For the Drude term (see Appendix B.2) at equilibrium:

$$\sigma_{\text{intra}}(\omega) = \frac{4\sigma_0 i}{\pi} \frac{k_B T}{\hbar\left(\omega + i\gamma_p\right)} \ln\left\{\left(1 + e^{E_F/k_B T}\right)\left(1 + e^{-E_F/k_B T}\right)\right\} \ , \tag{2.8}$$

while for the interband term we have:

$$\sigma_{\text{inter}}(\omega) = \frac{2\sigma_0}{\pi} \int_0^{+\infty} d\varepsilon \left(f_v(\varepsilon) - f_c(\varepsilon)\right)\left(\frac{1}{\hbar\gamma_{\text{inter}} - i\left(2\varepsilon + \hbar\omega\right)} + \frac{1}{\hbar\gamma_{\text{inter}} + i\left(2\varepsilon - \hbar\omega\right)}\right) \ . \tag{2.9}$$

Here E_F is graphene's Fermi energy with respect to the Dirac point, γ_p is the electron momentum relaxation rate, γ_{inter} is the interband scattering rate and $\sigma_0 = \pi e^2/\left(2h\right)$. For the plasmon frequencies of interest, the Drude term is much bigger than the interband one. Thus unless stated otherwise, only the Drude term will be used to describe SPPs in graphene.

2.1.1 Hybridization of SPPs with substrate excitations

If graphene is placed on top of a polar substrate, such as SiO_2, plasmons will couple to optical phonons of the substrate, leading to new hybrid modes called surface plasmon-phonon polaritons [7] (for simplicity we also refer to them as SPPs). The coupling between optical phonons and SPPs is easily introduced by considering a frequency dependent dielectric function for the substrate of the form [7]:

$$\varepsilon_2(\omega) = \varepsilon_\infty + \sum_j \frac{f_j \omega_{\text{TO},j}^2}{\omega_{\text{TO},j}^2 - \omega^2 - i\omega\gamma_{\text{TO},j}} \ , \tag{2.10}$$

where $\omega_{\mathrm{TO},j}$ are the phonon frequencies, $\gamma_{\mathrm{TO},j}$ the damping rates, f_j the oscillatory weights and ε_∞, high-frequency dielectric constant. This expression works well in THz and the mid-IR regimes.

For SiO_2, from Ref. [15], the high-frequency dielectric constant is $\varepsilon_\infty = 2.4$ while the optical phonon frequencies and oscillatory strengths are:

$$\omega_{\mathrm{TO}} = 2\pi\,(13.44, 23.75, 33.84)\ \ \mathrm{ps}^{-1} \tag{2.11}$$

and

$$f = (0.7514, 0.1503, 0.6011)\ \ , \tag{2.12}$$

respectively. The damping rates are:

$$\gamma_{\mathrm{TO}} = 2\pi\,(0.80, 1.27, 1.27)\ \ \mathrm{ps}^{-1}\ . \tag{2.13}$$

An example of the resulting dispersion relation is plotted in Fig. 1.2.

2.2 Electron-plasmon kinematics

2.2.1 Graphene's electronic dispersion relation

For small energies, most electronic processes in graphene can be described by approximating the electronic dispersion relation as linear near the Dirac point [7]:

$$\varepsilon_{s,\mathbf{k}} = s\hbar v_F k\ , \tag{2.14}$$

with $s = -1(+1)$ for the valence (conduction) band, $v_F = 10^6$ m/s the Fermi velocity and $\mathbf{k}$ is the electron's wavevector. This approximation is known as the Dirac cone approximation. Equation (2.14) is symmetric with respect to zero energy and displays particle-hole symmetry. In this approximation, electrons are well described by an effective Hamiltonian:

$$H_0 = v_F \boldsymbol{\sigma}\cdot\mathbf{p}\ , \tag{2.15}$$

where $\boldsymbol{\sigma} = (\sigma_x, \sigma_y)$ with σ_j denoting the j-th Pauli Matrix and $\mathbf{p}$ the momentum operator. The eigenstates of Hamiltonian (2.15) are:

$$|\mathbf{k}, s\rangle = \chi_s(\mathbf{k})|\mathbf{k}\rangle\ , \tag{2.16}$$

where:

$$|\mathbf{k}\rangle = \frac{e^{i\mathbf{k}\cdot\mathbf{r}}}{\sqrt{\mathcal{S}}}\quad , \quad \chi_s(\mathbf{k}) = \frac{1}{\sqrt{2}}\begin{bmatrix} e^{-i\theta(\vec{k})} \\ s \end{bmatrix}\ . \tag{2.17}$$

Here, $\mathcal{S}$ is the graphene's area and $\theta(\mathbf{k})$ is the angle the electron momentum does with the x-axis.

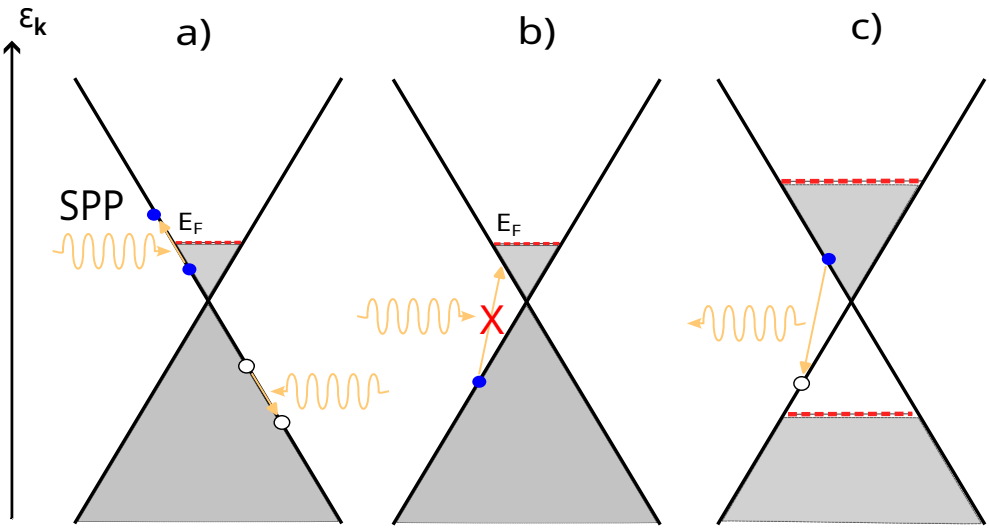

Figure 2.3: Electronic transitions by emission or absorption of a plasmon (SPP), represented by yellow arrows. The electrons are depicted by the blue circles and holes by the white ones. **a)** Intraband transition with absorption of a plasmon, in equilibrium, with Fermi energy E_F. **b)** Interband transition forbidden by Pauli blocking. In equilibrium, plasmons with low energy cannot promote electrons to the conduction band, since the states are already occupied. **c)** Out of equilibrium, with population inversion, these transitions are no longer Pauli blocked.

2.2.2 Electronic transitions via interaction with plasmons

Since SPPs possess a certain dispersion relation and their EM field can be quantified, they can be treated as quasiparticles. In the subsequent Sections, it will be important to understand the role of plasmons in electronic transitions, so here we study the kinematics of electron-plasmon interactions.

An electron can be scattered by a plasmon and either jump to a state in the same band (intraband transition) or to the other band (interband transition), with creation or destruction of an electron-hole pair. Let us consider first the case of intraband transition, shown in Fig. 2.3 **a)**. If the electron is scattered from a state $|\mathbf{k}_i, s\rangle$ to a state $|\mathbf{k}, s\rangle$ by absorption of a plasmon with energy-momentum "coordinates" $(\mathbf{q}, \omega_\mathbf{q})$, energy and momentum conservation conditions read:

$$\begin{cases} \varepsilon_\mathbf{k} - \varepsilon_{\mathbf{k}_i} = \hbar\omega_\mathbf{q} \\ \mathbf{k} - \mathbf{k}_i = \mathbf{q} \end{cases} . \tag{2.18}$$

By choosing a reference frame such that $\mathbf{q} = q\mathbf{e}_x$, we find that the possible electron momenta, which are solutions to system (2.18), lie in the hyperbola:

$$\frac{(k_x - q/2)^2}{a^2} - \frac{k_y^2}{b^2} = k_0^2 \ , \tag{2.19}$$

with the parameters:

$$a = \sqrt{\frac{\omega_{\mathbf{q}}}{v_F\sqrt{q^2 - \omega_{\mathbf{q}}^2/v_F^2}}} \quad , \quad b = \frac{1}{a} \quad , \quad k_0 = \frac{1}{2}\sqrt{\frac{\omega_{\mathbf{q}}}{v_F}\sqrt{q^2 - \omega_{\mathbf{q}}^2/v_F^2}} \; . \tag{2.20}$$

From these relations, we easily conclude that we can only have intraband transitions when $v_F q \geq \omega_{\mathbf{q}}$. This was already expected since it is at $\omega_{\mathbf{q}} = v_F q$ that the SPP dispersion intercepts the Dirac cone. The region $v_F q \geq \omega_{\mathbf{q}}$ of the spectrum is known as the Landau damping region. In this region plasmons are short lived since they can easily be absorbed or emitted by electrons and holes.

For interband transitions, the conservation laws imply that possible $\mathbf{k}$ vector's ending points lie in the ellipse:

$$\frac{(k_x - q/2)^2}{a^2} + \frac{k_y^2}{b^2} = k_0^2 \; , \tag{2.21}$$

with the parameters:

$$a = \sqrt{\frac{\omega_{\mathbf{q}}}{v_F\sqrt{\omega_{\mathbf{q}}^2/v_F^2 - q^2}}} \quad , \quad b = \frac{1}{a} \quad , \quad k_0 = \frac{1}{2}\sqrt{\frac{\omega_{\mathbf{q}}}{v_F}\sqrt{\omega_{\mathbf{q}}^2/v_F^2 - q^2}} \; . \tag{2.22}$$

These transitions are only possible when $\omega_{\mathbf{q}} \leq v_F q$. In doped graphene at equilibrium (for example, with $E_F = 300$ meV), these transitions are usually ignored since they are forbidden by Pauli blocking: only for $\hbar\omega_{\mathbf{q}} \geq 2E_F - \hbar v_F q$ can plasmons promote an electron from the valence to the conduction band (see Fig. 2.3 **b)**). Since in most situations only plasmons with low energy are considered, this kind of interaction is usually discarded. However, in graphene under non-equilibrium conditions (e.g. under strong optical pumping), where inversion of population is possible, this is not necessarily true (see Fig. 2.3 **c)**). In this situation, as we shall see, plasmons play an important role in electron-hole recombination and vice-versa.

Chapter 3

Nonlinear generation of SPPs in graphene

Graphene was predicted and demonstrated to have a strong third-order nonlinearity (the Kerr effect) in the THz-to-IR spectral range [18], with a number of potentially interesting effects following from this, such as the third and also higher-order harmonics generation, saturable absorption, etc. Moreover, as mentioned in the Introduction (Chapter 1), graphene can also have a non-zero second order response if its inversion symmetry is broken, for example by oblique incidence of exciting optical beams (as in Fig. 1.1) or by a deformation of the graphene sheet. Indeed, second-harmonic generation signals were observed for suspended graphene, caused by curvature fluctuations over the graphene sheet [19].

In this chapter, we show how SPPs can be generated by a non-linear DF-process and calculate graphene's second order optical conductivity. Using the derived formula, we will try explaining the results obtained in the experiments by Constant et al. [1].

3.1 DF-field enhancement at the plasmon resonance

We start by showing how SPPs can be generated by the non-linear DF process, at a frequency $\omega = \omega_b - \omega_a$, using two beams, b and a, under oblique incidence, as is shown in Fig. 1.1. For simplicity, we shall consider the optical beams as monochromatic plane waves of the form:

$$\mathbf{E}_j(\mathbf{r},t) = \frac{1}{2}(E_{j,x},0,E_{j,z})\, e^{iq_j x} e^{ik_{j,z}z} e^{-i\omega t} + \text{c.c}\ , \tag{3.1}$$

with q_j denoting the beams in-plane momentum, $\mathbf{q}_j = (\omega_j/c)\sin\theta_j \mathbf{e}_x$, and $k_{j,z}$ the z-component of the wavevector.

The relation between the generated SPP field and the impinging fields is obtained from boundary conditions. For a graphene sheet placed between two dielectrics, ε_1 (medium 1) and ε_2 (medium 2),

as in Fig. 2.1 and for a SPP field of the form (2.1), the boundary conditions (A.5) and (A.7) dictate:

$$\begin{cases} \varepsilon_1 E_{1,z} - \varepsilon_2 E_{2,z} = 4\pi\rho_s \\ E_{1,x} - E_{2,x} = 0 \end{cases} , \tag{3.2}$$

where ρ_s is graphene's charge density. Using relations (2.2) and (2.3), we find that the SPP field component $E_{2,x}$ obeys the equation:

$$\left(\frac{\varepsilon_2}{\kappa_2} + \frac{\varepsilon_1}{\kappa_1}\right) E_{2,x} e^{iqx} e^{-i\omega t} = -\frac{4\pi i}{q}\rho_s \ . \tag{3.3}$$

Since we expect the surface charge density to respond periodically (in time and space) we can expand it in a Fourier series:

$$\rho_s = \sum_j \rho(\omega_j, q_j) e^{i(q_j x - \omega_j t)} \ . \tag{3.4}$$

Also, from the continuity equation we can relate its Fourier components to the Fourier components of the surface current j_x:

$$\rho(\omega_j, q_j) = \frac{q_j}{\omega_j} j_x(\omega_j, q_j) \ . \tag{3.5}$$

Therefore, using Eq. (3.5) and the orthogonality between functions $e^{i(q_j x - \omega_j t)}$, Eq. (3.3) yields:

$$\frac{\varepsilon_2}{\kappa_2} + \frac{\varepsilon_1}{\kappa_1} = -\frac{4\pi i}{\omega E_{2,x}} j_x(\omega, q) \ . \tag{3.6}$$

The surface current can be expanded to the second order:

$$j_x(\omega, q) = \sigma^{(1)}(\omega) E_{2,x} + j_x^{(2)}(\omega, q) \ , \tag{3.7}$$

where $\sigma^{(1)}$ is the graphene's linear conductivity in the local limit. Expression (3.6) yields:

$$E_{2,x} = -\frac{4\pi i}{\omega} \frac{j_x^{(2)}(\omega, q)}{D(\omega, q)} \ , \tag{3.8}$$

with $D(\omega, q)$ representing the SPP dispersion relation (2.4). At the plasmon resonance (with losses included), $\mathrm{Re}D(\omega, q) = 0$ and consequently an enhancement of the field is observed.

The non-linear current, $j_x^{(2)}(\omega, q)$ is due to the DF interaction between the two incoming optical fields, $\mathbf{E}_b$ and $\mathbf{E}_a$ in Eq. (3.1). We express this current as:

$$j_x^{(2)}(\omega, q) = \frac{1}{2}\sigma_{xxx}^{(2)}\left(\mathbf{\Omega}, \mathbf{\Omega}_b, -\mathbf{\Omega}_a\right) E_{b,x} E_{a,x}^* \ , \tag{3.9}$$

with $\sigma_{xxx}^{(2)}\left(\mathbf{\Omega}, \mathbf{\Omega}_b, \mathbf{\Omega}_a\right)$ denoting the second order conductivity for DF mixing. The notation $\mathbf{\Omega}$ means $\mathbf{\Omega} = (\omega = \omega_b - \omega_a, q = q_b - q_a)$, while $\mathbf{\Omega}_j = (\omega_j, q_j)$. When (ω, q) matches a plasmon mode,

$\mathrm{Re}D(\omega, q) = 0$ and SPPs are generated. On the other hand, if ω_b and ω_a and the corresponding in-plane momentum, do not match a plasmon mode, the field is strongly suppressed and no SPP generation takes place.

3.2 Optical response in graphene

As shown by Eqs. (3.8) and (3.9), the SPP field depends on graphene's optical conductivity. The calculation of this response can be quite tricky [20–22]. In the long wavelength limit $q \to 0$, in which the spatial dependence of the radiation electric field is neglected, the calculation using the density-matrix perturbation theory can be done either in the length gauge with the interaction described in the dipole approximation:

$$H(t) = H_0(\mathbf{r}, \mathbf{p}) + e\mathbf{r} \cdot \mathbf{E}(t) \ , \tag{3.10}$$

or in the velocity gauge with the interaction introduced via the so called minimal coupling:

$$H(t) = H_0 \left(\mathbf{r}, \mathbf{p} + e\mathbf{A}(t)\right) \ , \tag{3.11}$$

where H_0 is the unperturbed Hamiltonian of the electronic system, $-e$ is the electron's charge, $\mathbf{A}(t)$ is the vector potential of the EM field and $\mathbf{E}(t)$ the corresponding electric field. These two descriptions, in principle, are equivalent [21, 22], but may have different advantages. The advantage of the velocity gauge is that the perturbation preserves the crystal's translational symmetry**.** However, the calculation using this gauge is plagued by unphysical contributions, diverging at low frequencies**.** On the other side, the length gauge is written in terms of the electric field, which is a gauge invariant entity. Nonetheless, since it contains the position operator $\mathbf{r}$, the perturbation is no longer diagonal in Bloch momentum space and couples different $\mathbf{k}$ values.

There is another big difference between these two gauges. In our case, we do not want to use the full unperturbed Hamiltonian, but rather an effective Hamiltonian that describes the electronic dynamics near the Dirac point, the so called Dirac cone approximation. In this approximation, in which bands are truncated, the two gauges no longer yield the same results [21]. In fact, while in the length gauge, the calculation converges, in the velocity one, it diverges.

Hence, it seems best to calculate the optical response of graphene in the length gauge. This is true for the linear response, as is done Appendix B.2, but for the second order response, other issues appear. In a centrosymmetric material, such as graphene, the second-order nonlinear response in the electric dipole approximation is suppressed. As it is written, the symmetry breaking mechanism is not present in the length gauge. One could circumvent this problem by going beyond the electric dipole approximation [17] and effectively taking into account effects of spatial dispersion. Nevertheless, the choice made in this work was to use Eq. (3.11), i.e. the velocity gauge.

The calculation of the DF second order conductivity, $\sigma^{(2)}$, in graphene, in the velocity gauge

was done in Refs. [9, 11, 16]. In Ref. [11] they obtained an unphysical response that diverged with $q \to 0$:

$$\sigma^{(2)}(\omega, q) \propto \frac{1}{q} \ . \tag{3.12}$$

This cannot be since graphene is centrosymmetric and one expects the second order conductivity to go to zero, $\sigma^{(2)} \to 0$, in the local limit $q \to 0$. In Ref. [16], to avoid the divergence associated with the velocity gauge, they went beyond the Dirac cone approximation and considered higher order terms in the electron momentum to describe the conduction and valence bands. This way, they avoided any divergence, since divergent terms canceled each other out, and obtained a physical expression for the second order conductivity, $\sigma^{(2)} \propto q$, that vanished in the long wavelength limit, as it should. However, as will be shown below, this sophisticated approach is not necessary for the second order response, even in the velocity gauge, and one can perform the calculation in the Dirac cone approximation, as it was done in Ref. [9].

3.3 DF second-order conductivity

In this Section, we present the calculation of the second-order nonlinear conductivity of graphene. This calculation requires taking into account non-local effects, otherwise, the second-order response vanishes. Once again we consider the situation shown Fig. 1.1, with two beams falling onto graphene at different angles.

We shall work within the Dirac cone approximation and use the density matrix formalism to calculate the second-order nonlinear conductivity. In the velocity gauge, the Hamiltonian of the electrons coupled to the electromagnetic field is:

$$\hat{H} = v_F \boldsymbol{\sigma} \cdot \left(\mathbf{p} + \frac{e}{c} \mathbf{A}(t, \mathbf{r}) \right) \ , \tag{3.13}$$

where $\mathbf{A}(\mathbf{r}, t)$ is the vector potential (the electric field is $\mathbf{E} = -\frac{1}{c}(\partial \mathbf{A}/\partial t)$). Using density-matrix perturbation theory [12] with the second term in Eq. (3.13) as perturbation (detailed calculations in Appendix B.1), we find a general expression for the 2nd order conductivity (Appendix B.3 for details):

$$\begin{aligned}
\sigma^{jki}(\boldsymbol{\Omega}, \boldsymbol{\Omega}_p, \boldsymbol{\Omega}_q) = & \frac{e^3}{\hbar^2 \omega_q \omega_p \mathcal{S}} \sum_{nml} \frac{v^k_{mn,-(\mathbf{q}+\mathbf{p})} v^j_{lm,\mathbf{p}} v^i_{nl,\mathbf{q}}}{\omega_{lm} - \omega_p - i\gamma_{lm}} \frac{f(\varepsilon_m) - f(\varepsilon_l)}{\omega_{nm} - (\omega_p + \omega_q) - i\gamma_{nm}} \\
& + \frac{e^3}{\hbar^2 \omega_q \omega_p \mathcal{S}} \sum_{nml} \frac{v^k_{mn,-(\mathbf{q}+\mathbf{p})} v^j_{nl,\mathbf{p}} v^i_{lm,\mathbf{q}}}{\omega_{lm} - \omega_q - i\gamma_{lm}} \frac{f(\varepsilon_m) - f(\varepsilon_l)}{\omega_{nm} - (\omega_p + \omega_q) - i\gamma_{nm}} \\
& - \frac{e^3}{\hbar^2 \omega_q \omega_p \mathcal{S}} \sum_{nml} \frac{v^k_{mn,-(\mathbf{q}+\mathbf{p})} v^j_{nl,\mathbf{p}} v^i_{lm,\mathbf{q}}}{\omega_{nl} - \omega_p - i\gamma_{nl}} \frac{f(\varepsilon_l) - f(\varepsilon_n)}{\omega_{nm} - (\omega_p + \omega_q) - i\gamma_{nm}} \\
& - \frac{e^3}{\hbar^2 \omega_q \omega_p \mathcal{S}} \sum_{nml} \frac{v^k_{mn,-(\mathbf{q}+\mathbf{p})} v^j_{lm,\mathbf{p}} v^i_{nl,\mathbf{q}}}{\omega_{nl} - \omega_q - i\gamma_{nl}} \frac{f(\varepsilon_l) - f(\varepsilon_n)}{\omega_{nm} - (\omega_p + \omega_q) - i\gamma_{nm}} \ ,
\end{aligned} \tag{3.14}$$

where $\boldsymbol{\Omega}_p = (\omega_p, \mathbf{p})$, $\boldsymbol{\Omega}_q = (\omega_q, \mathbf{q})$ and $\boldsymbol{\Omega} = (\omega_p + \omega_q, \mathbf{q} + \mathbf{p})$, with ω_p and ω_q denoting the frequencies of the fields and $\mathbf{p}$ and $\mathbf{q}$ the respective in-plane wavevectors. The sums are over different states near the Dirac point and

$$v^j_{mn,\mathbf{q}} = \langle m | v^j e^{i\mathbf{r}\cdot\mathbf{q}} | n \rangle \tag{3.15}$$

are the matrix elements of the spatially modulated velocity components. Here $\omega_{mn} = (\varepsilon_m - \varepsilon_n)/\hbar$ is the energy difference between states $|m\rangle$ and $|n\rangle$ and $f(\varepsilon_n)$ is the occupation number of state $|n\rangle$, at equilibrium described by the Fermi–Dirac function. Finally, γ_{nm} are phenomenological damping parameters for transitions between $|n\rangle$ and $|m\rangle$.

Equation (3.14) is a general expression for the second-order response and it includes DF generation and other processes such as sum frequency generation. The relevant transitions are shown in Fig. 3.1, forming two channels for DF generation of plasmons [11]: channel 1 with transitions

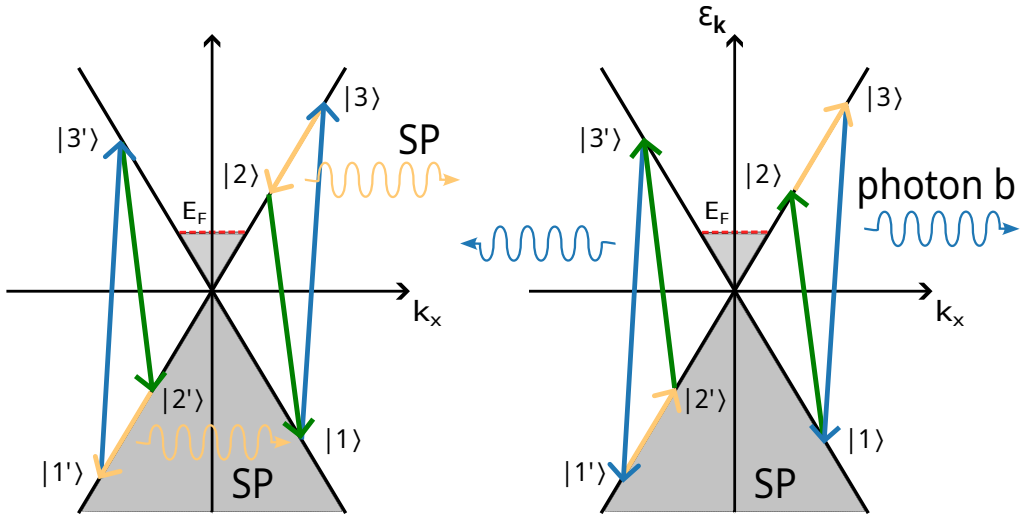

Figure 3.1: **(Left)** Transitions and states considered in the calculation of the conductivity for DF generation at frequency ω and ω_a: Channel 1 (right) and Channel 2 (left). **(Right)** For the process of generation of pump photons (ω_b), the arrows are inverted.

between the states:

$$|1\rangle = |-1, \mathbf{k}_1\rangle \quad , \quad |2\rangle = |1, \mathbf{k}_2\rangle \quad , \quad |3\rangle = |1, \mathbf{k}_3\rangle \ , \tag{3.16}$$

and the intraband transition in the conduction band, and channel 2 involving the states

$$|1'\rangle = |-1, \mathbf{k}_{1'}\rangle \quad , \quad |2'\rangle = |-1, \mathbf{k}_{2'}\rangle \quad , \quad |3'\rangle = |1, \mathbf{k}_{3'}\rangle \ , \tag{3.17}$$

with the intraband transition in the valence band.

For the case of DF generation of the field oscillating with the frequency $\omega = \omega_b - \omega_a$ and momentum $\mathbf{q} = \mathbf{q}_b - \mathbf{q}_a$, we have $\mathbf{\Omega} = (\omega, \mathbf{q})$ and $\mathbf{\Omega}_{a,b} = \left(\omega_{a,b}, \mathbf{q}_{a,b}\right)$. The only relevant component of the conductivity tensor, for the experimental arrangement of Fig. 1.1 is the one with $i = j = k = x$, so the general expression (3.14) takes the form:

$$\begin{aligned}\sigma^{(2)}_{xxx}\left(\mathbf{\Omega}, \mathbf{\Omega}_b, -\mathbf{\Omega}_a\right) = &\frac{e^3}{\hbar^2 \omega_b \omega_a \mathcal{S}} \sum_{123} \frac{v^x_{23,-\mathbf{q}} v^x_{31,\mathbf{q}_b} v^x_{12,-\mathbf{q}_a}}{\omega_{32} - \omega - i\gamma_{32}} \left(\frac{f(\varepsilon_1) - f(\varepsilon_3)}{\omega_{31} - \omega_b - i\gamma_{31}} - \frac{f(\varepsilon_2) - f(\varepsilon_1)}{\omega_{12} + \omega_a - i\gamma_{12}} \right) \\ &+ \frac{e^3}{\hbar^2 \omega_b \omega_a \mathcal{S}} \sum_{1'2'3'} \frac{v^x_{1'2',-\mathbf{q}} v^x_{3'1',\mathbf{q}_b} v^x_{2'3',-\mathbf{q}_a}}{\omega_{2'1'} - \omega - i\gamma_{2'1'}} \left(\frac{f(\varepsilon_{3'}) - f(\varepsilon_{2'})}{\omega_{2'3'} + \omega_a - i\gamma_{2'3'}} - \frac{f(\varepsilon_{1'}) - f(\varepsilon_{3'})}{\omega_{3'1'} - \omega_b - i\gamma_{3'1'}} \right) \ ,\end{aligned} \tag{3.18}$$

where we retained only resonant terms. Evaluation of the matrix elements of the modulated velocity operator (3.15) can be done in different ways, the most straightforward is considering the velocity operator $\mathbf{v} = v_F \boldsymbol{\sigma}$ (see Appendix B.3 for details). In principle, in the velocity gauge one has to calculate them with the full Hamiltonian including the interaction [21, 22]. However, in our case, the interaction operator commutes with $e^{i\mathbf{r}\cdot\mathbf{q}}$ and we can use the unperturbed Hamiltonian (without

A). The matrix elements contain Kronecker δ-s that cancel out two summations in Eq. (3.18) and yield the conservation of momentum $\mathbf{q} = \mathbf{q}_b - \mathbf{q}_a$.

To compute Eq. (3.18), we expand the matrix elements $v^j_{mn,\mathbf{q}}$, the energy differences, ω_{mn}, and the Fermi–Dirac distributions to the first order in the wavevectors $\mathbf{q}_j$ and $\mathbf{q}$. For example, for a state $|n\rangle = |1, \mathbf{k}'\rangle$ with $\mathbf{k}' = \mathbf{k} + \mathbf{q}$,

$$f(\varepsilon_n) = f_c(\varepsilon_{\mathbf{k}'}) \approx f_c(\varepsilon_{\mathbf{k}}) + \partial_{\varepsilon_{\mathbf{k}}} f_c(\varepsilon_{\mathbf{k}})\, \mathbf{q}_j \cdot \nabla_{\mathbf{k}} \varepsilon_{\mathbf{k}} \ . \tag{3.19}$$

We denote by $f_c(\varepsilon)$ the distribution function for the electrons in the conduction band and by $f_v(\varepsilon) = f_c(-\varepsilon)$ the distribution for electrons in the valence band. Additionally, for simplicity, we set equal all phenomenological damping constants, $\gamma_{nm} = \gamma$. With these approximations, considering both channels, the zero-th order terms in momentum cancel out, and the lowest order term in the conductivity is proportional to q, thus yielding a finite result. At zero temperature, the following analytical expression is obtained:

$$\sigma^{(2)}_{xxx}(\mathbf{\Omega}, \mathbf{\Omega}_b, -\mathbf{\Omega}_a) \approx \delta_{\mathbf{q},\mathbf{q}_b-\mathbf{q}_a} \frac{e^3 v_F^2 E_F}{\hbar^3 \omega_b \omega_a \pi^2} \frac{2\omega_F - \omega_a}{(2\omega_F - \omega_a)^2 + \gamma^2} q A(\omega, q, \gamma) \ , \tag{3.20}$$

where $\omega_F = E_F/\hbar$ is the Fermi frequency and

$$A(\omega, q, \gamma) = \frac{\pi(\omega + i\gamma)}{(v_F q)^4} \left\{ (v_F q)^2 + 2(\omega + i\gamma)^2 \left[\sqrt{1 - \left(\frac{v_F q}{\omega + i\gamma} \right)^2} - 1 \right] \right\} \tag{3.21}$$

is an auxiliary function, which is independent of q in the limit $q \to 0$:

$$\lim_{q\to 0} A(\omega, q, \gamma) = -\frac{\pi}{4} \frac{1}{\omega + i\gamma} \ . \tag{3.22}$$

Figure 3.2 shows the behavior of the real and imaginary parts of $\sigma^{(2)}_{xxx}(\mathbf{\Omega}, \mathbf{\Omega}_b, -\mathbf{\Omega}_a)$ as functions of ω and q, for two values of the Fermi energy. The results obtained by the analytical formula (3.20) are confirmed by direct numerical evaluation of Eq. (3.18). In the left panel, for a fixed value of q, the real part of the conductivity peaks at $\omega \approx v_F q$. An important feature of Eq. (3.20) for the second-order conductivity $\sigma^{(2)}_{xxx}(\mathbf{\Omega}, \mathbf{\Omega}_b, -\mathbf{\Omega}_a)$ is that it goes to zero as $q \to 0$, as it should for a centrosymmetric material. This physically meaningful feature was lacking in the results of Ref. [11]. The reason for this probably is the problem with intraband matrix elements for the $\mathbf{r}$ operator, first pointed out by Blount [20]. The analytical formula derived in Ref. [16], although showing the correct limiting behavior for $q \to 0$, is somewhat different from ours and requires more work. It is important to emphasize that the points in Fig. 3.2 represent the results of direct numerical evaluation of Eq. (3.18), performed without approximations such as expansions in terms of wavevectors, so these spectra must be correct within the model and approach used.

According to Eq. (3.8), it is the imaginary part of the conductivity that is important to describe

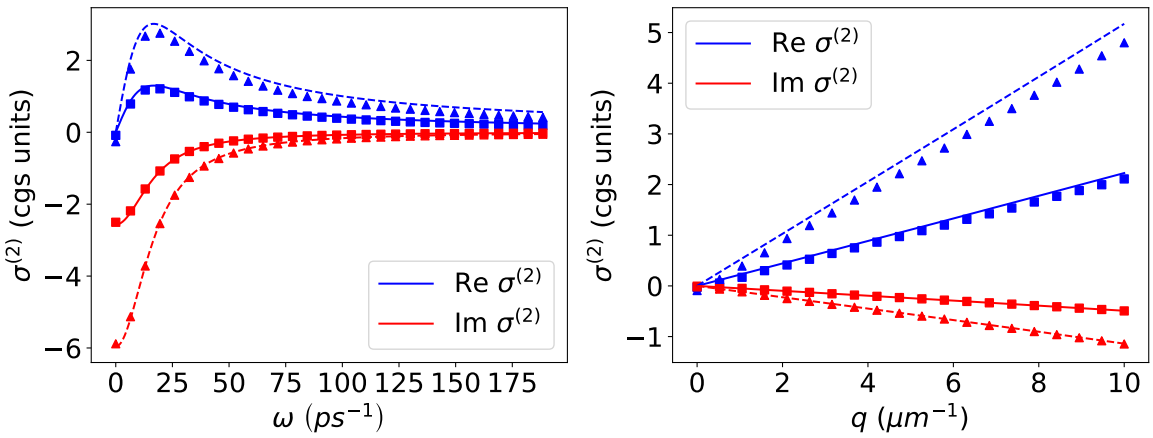

Figure 3.2: Real and imaginary parts of $\sigma^{(2)}_{xxx}(\mathbf{\Omega}, \mathbf{\Omega}_b, -\mathbf{\Omega}_a)$ plotted vs ω **(left)** and q **(right)**. The solid and dashed lines were calculated using expression (3.20) with Fermi levels $E_F = 300$ and 500 meV, respectively. The triangles and squares are numerical calculations of expression (3.18). In the right panel, θ_b^I was fixed at 40°, while in the left plot, ω was fixed at 94ps^{-1}. In both cases $\omega_a = 3065\text{ps}^{-1}$, $\gamma = 10.6$ meV and $\theta_a^I = 20°$.

the SPP generation process, so from Fig. 3.2, $\left|\text{Im}\sigma^{(2)}_{xxx}(\mathbf{\Omega}, \mathbf{\Omega}_b, -\mathbf{\Omega}_a)\right| \approx 3$ esu ≈ 0.1 fA m V^{-2} for $\omega = 50$ ps^{-1}. Even though it is larger than the value calculated in Ref. [16], it is below the experimentally estimated value in Table 1.1 by some 3 orders of magnitude.

Similar calculations can be carried out for the conductivities oscillating with the frequencies ω_a and ω_b, representing the DF generation of photons a and sum frequency generation of photons b, respectively. Diagrammatically, the generation of photons b is the same as for SPP generation, but with the arrows inverted, Fig. 3.1 (**right**). Analytical expressions, obtained with the same approximations as Eq. (3.20), are:

$$\sigma^{(2)}_{xxx}(\mathbf{\Omega}_b, \mathbf{\Omega}_a, \mathbf{\Omega}) \approx -\delta_{\mathbf{q},\mathbf{q}_b-\mathbf{q}_a} \frac{e^3 v_F^2 E_F}{\hbar^3 \omega_a \omega \pi^2} \frac{q}{2\omega_F - \omega_a - i\gamma} A(\omega, q, \gamma) \ , \tag{3.23}$$

$$\sigma_{xxx}(\mathbf{\Omega}_a, \mathbf{\Omega}_b, -\mathbf{\Omega}) \approx \delta_{\mathbf{q},\mathbf{q}_b-\mathbf{q}_a} \frac{e^3 v_F^2 E_F}{\hbar^3 \omega_b \omega \pi^2} \frac{q}{2\omega_F - \omega_a - i\gamma} A(\omega, q, -\gamma) \ . \tag{3.24}$$

We notice that in limit $\gamma \to 0$,

$$\frac{1}{\omega_a}|\sigma_{xxx}(\mathbf{\Omega}_a, \mathbf{\Omega}_b, -\mathbf{\Omega})| = \frac{1}{\omega_b}|\sigma^{(2)}_{xxx}(\mathbf{\Omega}_b, \mathbf{\Omega}_a, \mathbf{\Omega})| = \frac{1}{\omega}|\sigma_{xxx}(\mathbf{\Omega}, \mathbf{\Omega}_b, -\mathbf{\Omega}_a)| \ , \tag{3.25}$$

that is our expressions exhibit the symmetry expected in lossless media.

3.4 Reflection coefficients of the optical beams

The reflection coefficients of the optical beams are affected by the the SPP generation and this is how the latter was detected in Ref. [1]. Here we present the reflection and transmission coefficients and calculate them using the results of the previous Section. The model presented in this Section is similar to the one used by Constant et al. [1]. There are two differences:

1. We will not take into account the coupling between SPPs and optical phonons. This only affects the position of the resonance, not its order of magnitude. So, for the time being, we confine ourselves by this simpler approach;

2. We shall use expressions (3.20), (3.23) and (3.24) for the nonlinear conductivity, not the model (1.3), introduced by Constant et al. [1];

We consider a situation similar to the experiment, with graphene cladded by two dielectrics with dielectric constants $\varepsilon_1 = 1$ and $\varepsilon_2 = 2.4$ and two p-polarized optical waves impinging on it (see Fig. 3.3). The reflection and transmission coefficients, r_j and t_j, respectively, are defined as usual:

$$r_j = E_j^R/E_j^I \quad , \quad t_j = E_j^T/E_j^I \ , \tag{3.26}$$

with $j = a, b$. E_j^I is the incident field and $E_j^{R(T)}$ is the reflected (transmitted) field. The calculation is carried out in a standard way [23]. Graphene's current must include a NL term, such as in Eq. (3.7), so, for fields a and b, the nonlinear currents are:

$$j_x^{(2)}(\omega_a, q_a) = \frac{1}{2}\sigma_{xxx}^{(2)}\left(\mathbf{\Omega}_a, \mathbf{\Omega}_b, -\mathbf{\Omega}\right) E_{b,x}(z=0) E_{\mathrm{SP},x}^*(z=0) \tag{3.27}$$

and:

$$j_x^{(2)}(\omega_b, q_b) = \frac{1}{2}\sigma_{xxx}^{(2)}\left(\mathbf{\Omega}_b, \mathbf{\Omega}_a, \mathbf{\Omega}\right) E_{a,x}(z=0) E_{\mathrm{SP},x}(z=0) \ , \tag{3.28}$$

respectively, with E_{SP} the SPP field generated by DF mixing, as given in Eq. (3.8) and described in Section 3.1. To put it in another way, we are describing the differential reflectivity, recorded in the experiment, as as a measure of exchange of energy between beams b and a, that is mediated by the plasmon field.

From the boundary conditions, the transmission coefficients are (see Appendix C for details):

$$t_a = t_a^{(0)}\left(1 - 2t_a^{(0)}|t_b^{(0)}|^2\pi^2 i \frac{\sigma_{xxx}^{(2)}\left(\mathbf{\Omega}_a, \mathbf{\Omega}_b, -\mathbf{\Omega}\right)\sigma_{xxx}^{(2)*}\left(\mathbf{\Omega}, \mathbf{\Omega}_b, -\mathbf{\Omega}_a\right)|E_b^I|^2\cos^2\theta_b^T}{\sqrt{\varepsilon_1}c\omega D^*(\omega, q)}\cos\theta_a^T\right) \ , \tag{3.29}$$

$$t_b = t_b^{(0)}\left(1 + 2t_b^{(0)}|t_a^{(0)}|^2\pi^2 i \frac{\sigma_{xxx}^{(2)}\left(\mathbf{\Omega}_b, \mathbf{\Omega}_a, \mathbf{\Omega}\right)\sigma_{xxx}^{(2)}\left(\mathbf{\Omega}, \mathbf{\Omega}_b, -\mathbf{\Omega}_a\right)|E_a^I|^2\cos^2\theta_a^T}{\sqrt{\varepsilon_1}c\omega D(\omega, q)}\cos\theta_b^T\right) \ , \tag{3.30}$$

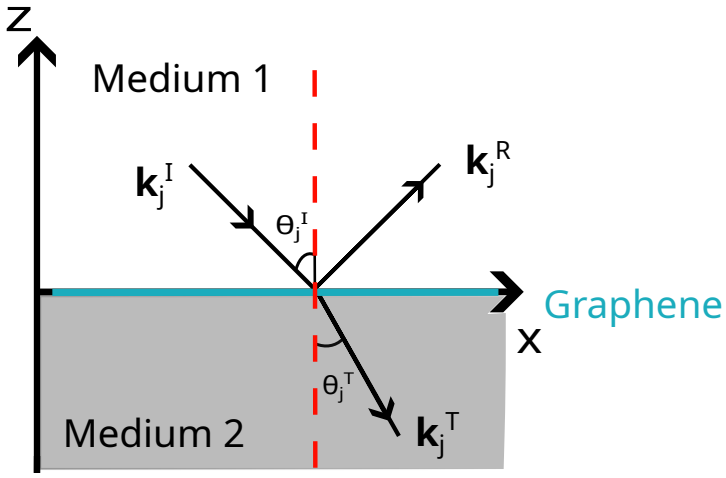

Figure 3.3: Scheme of p-polarized waves propagating from medium 1 to medium 2, with graphene at the interface $z = 0$. The incident angle for wave j is θ_j^I, while the transmitted is θ_j^T. $\mathbf{k}_j^I$ and $\mathbf{k}_j^T$ are the incident and transmitted wavevectors.

where $t_j^{(0)}$ denotes the transmission coefficient in the absence of the second pulse,

$$t_j^{(0)} = \frac{2(\varepsilon_1/k_{jz}^I)\sec\theta_j^T\cos\theta_j^I}{(\varepsilon_1/k_{jz}^I)+(\varepsilon_2/k_{jz}^T)+\dfrac{4\pi i}{\omega_j}\sigma^{(1)}(\omega_j)}\ , \tag{3.31}$$

$k_{jz}^{I(T)}$ is the z-component of the incident (transmitted) wave and $D(\omega, q)$ is the SPP dispersion relation (2.4). The corresponding reflection coefficients are given by:

$$r_j = 1 - \sec\theta_j^I\cos\theta_j^T t_j \qquad (j = a, b)\ , \tag{3.32}$$

with θ_j^I and θ_j^T the incidence and transmission angles.

Notice that at the SPP resonance condition $\mathrm{Re}D(\omega, q) = 0$, and the reflection is enhanced. From Eqs. (3.29) and (3.30), we see that the transfer of energy between the two optical fields is resonant under the condition of DF phase matching between the incident beams and the SPP frequency and momentum. This process, in spite of being due to the second-order response of graphene, is in fact of the third order in optical fields.

Figure 3.4 presents the spectral variation of the differences in the reflectance, $\Delta R = R - R_0$, transmittance, $\Delta T = T - T_0$, and absorbance, $\Delta A = A - A_0$ (the quantities with the subscript 0 correspond to the absence of beam b), for the situation presented in Supplementary Material of Ref. [1] where $\theta_a^I = 20°$ and $\theta_b^I = 40°$. All these spectra show the SPP resonance at $\omega_{\mathrm{SP}} = 80\,\mathrm{ps}^{-1}$. The reflectance of the probe beam in Fig. 3.4 shows a dip at resonance, but it could be a peak if θ_a^I were larger than the Brewster angle (situation corresponding to Fig. 2 of Ref. [1]) because $\Delta R_a \approx (r_a^{(0)}\Delta r_a^* + r_a^{(0)*}\Delta r_a)$, $r_a^{(0)}$ is nearly real and changes its sign at the Brewster angle, while

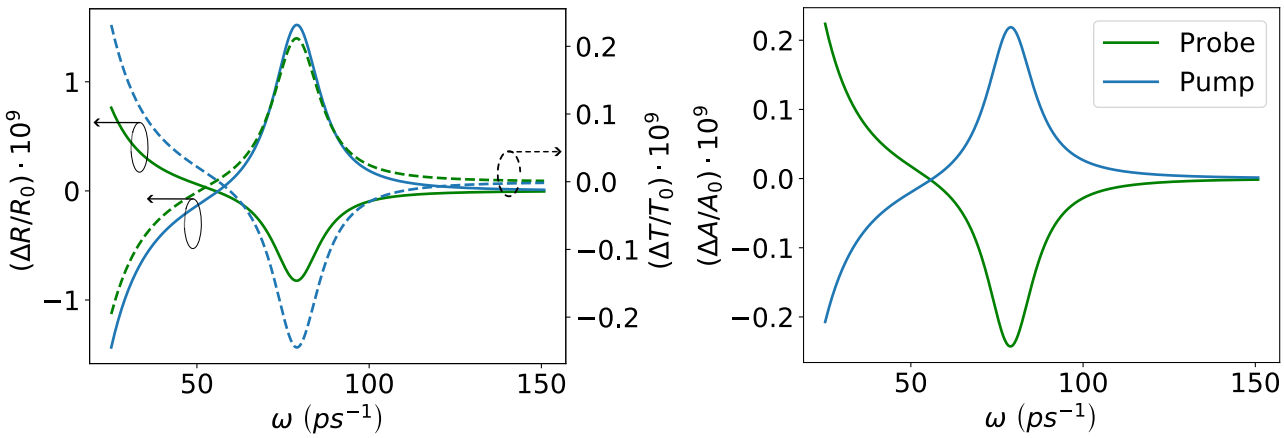

Figure 3.4: Differential reflectance (**left**, solid lines), transmittance (**left**, dashed lines) and absorbance **(right)** of the pump (blue curves) and probe (green curves) beams as functions of ω. Here the Fermi energy $E_F = 500$ meV, $\theta_a^I = 20°$ and $\theta_b^I = 40°$, while other parameters are the same as in Fig. 3.2. The plasmon resonance is observed at approximately $\omega_{\mathrm{SP}} = 80\,\mathrm{ps}^{-1}$. We assumed the same intensities for both optical beams, $I_a = I_b = 10^{16}\,\mathrm{erg\ cm^{-2}s^{-1}}$, in order to facilitate the comparison.

its variation owing to the NL effect, Δr_a, does not. The chosen value of the intensity of the pump, $I_b = 10^{16}\,\mathrm{erg\ cm^{-2}s^{-1}}$, approximately corresponds to the fluence of 0.1 mJ/cm^2 and pulse duration of 0.1 ps, mentioned in Ref. [1]. From figures S1 of Supplementary Material of Ref. [1] we can find the depth of the resonant minimum of $\Delta R/R_0 \approx 1.6\cdot 10^{-3}$, while our calculations predict a value of the order of 10^{-10} at the SP resonance. Since ΔR is quadratic in the second-order conductivity, our calculated result for it is lower than the value extracted from the experiment in Ref. [1] by roughly 3 orders of magnitude, as already mentioned before in Section 3.3.

3.4.1 How to detect the optically generated SPPs?

As pointed out in the previous Section, the differential reflectance method [1, 13] relies on a process that is of the third order with respect to the optical fields. Considering the optical beams as plane waves, it seems that the variation of the reflection coefficients of these beams is small and consequently hard to detect, unless very high intensities of the pump beam are used. Then other (non-electronic) types of nonlinearity can arise, for instance, due to photothermal effects [16], which is less interesting from the point of view of applications. Thus, it might be preferable to try to detect the optically generated surface plasmons using another route. Time-resolved THz spectroscopy is a powerful technique in the spectral range relevant to graphene SPPs [24] and it could help detecting the flux of plasmons escaping from the optical spots where they were generated. Below we shall evaluate this flux.

Let us assume for simplicity that the optical beams are focused by cylindrical lenses, so that the system is uniform along the y-direction. As a first approximation, we neglect the uncertainty of the

in-plane components of the wave vectors $\mathbf{q}_a$ and $\mathbf{q}_b$, as if they were plane waves. In this situation, the energy flux in the x-direction associated with the generated SPPs, per unit length along y, is (see Appendix D for details):

$$J = q\frac{\omega}{16\pi}\sum_{m=1,2}\frac{\varepsilon_m}{\kappa_m^3}|E_{m,x}(\omega,q)|^2 \propto |D(\omega,q)|^{-2} \ . \tag{3.33}$$

At the plasmon resonance, the evanescent field is strongly enhanced and the energy flux increases.

Since SPPs are dissipative because of the Ohmic losses, we can neglect the inverse process of optical photon generation with the propagation of SPPs. Thus, the flux, Eq. (3.33), is responsible for the removal of energy from the optical beams. If the incident energy fluxes are $J_a^{(I)}$, $J_b^{(I)}$ (per unit length along y) and if both reflected and transmitted beams a and b are measured, it should be possible to detect a variation of the total energy of both optical beams since, at the plasmon resonance, it should be diminished by J because of the energy conservation,

$$J_a^{(I)} + J_b^{(I)} = \left(J_a^{(R)} + J_a^{(T)} + J_b^{(R)} + J_b^{(T)} + \mathcal{L}_a + \mathcal{L}_b\right) + J \ , \tag{3.34}$$

where $\mathcal{L}$ stands for losses associated with the transmission and reflection of the optical beams at graphene-covered surface, which are related to $\mathrm{Re}\,\sigma^{(1)}(\omega_{a,b})$ and, therefore, can be evaluated. Detection of a positive difference between the left-hand side and the parenthesis in the right-hand side of Eq. (3.34) will indicate the SPP generation, $J > 0$. Another possibility is to try to detect the SPP flux by converting it into propagating THz light, as it was done in the first demonstrations of graphene surface plasmons [25, 26]. The advantage in this approach, is that the variation is a second-order process with respect to the optical fields, consequently, it should require lower intensities of the optical beams.

3.5 Concluding remarks

It is clear that the calculated value of the second-order conductivity of optically pumped graphene is too low (by approximately 3 orders of magnitude) to explain the experimental results of Ref. [1]. This should be expected since, in the spectral range of interest, the electronic transition for SPP emission, shown in Fig. 3.1, has a very low probability to happen, because intraband transitions via SPP emission/absorption are only phase matched for plasmons with large momenta (see Section 2.2). Thus, there must be an important effect we did not include in the model or the perturbative approach is not valid because of the high intensity of the pump pulse.

The answer seems to lie in the incoherent part of measured differential reflectance, non-resonant curve in Fig. 1.2. This signal is probably due to out-of-equilibrium electrons. In a recent work [27], it was observed that this hot electrons play a crucial role in the efficiency of terahertz high-harmonic generations. Therefore, it may be that the presence of the incoherent part in the measured differential reflectance signal cannot be ignored. In fact, theoretical works [28, 29] suggest that out-of-

equilibrium graphene has the necessary conditions for plasmon amplification and this could account for the huge signal experimentally observed.

So, we have to find out how these hot electrons behave and how they can participate in the generation of SPPs. Unfortunately, in the presence of hot electrons, the use of a perturbative approach to describe the electronic nonlinearities and the nonlinear optical coupling to plasmons is no longer valid in graphene [30]. An alternative could be the use of a hot-electron model to describe the non-equilibrium electrons generated with strong, ultrafast light pulses. In the next two chapters, we explore these ideas.

Chapter 4

Hot carriers in graphene

As discussed in the previous Section, the signal observed by Constant et al. [1] cannot be explained in terms of the standard perturbation theory. Although the idea that the observed signal was due to generation of SPPs by the DF process is not ruled out, the observed resonance is too strong to be attributed to a non-linear process alone. A clue to this enigma, I believe, lies in the asymmetric line shape of the background signal in Fig. 1.2, measured when pump and probe are out of resonance. This signal probably comes from the relaxation dynamics of the out-of-equilibrium electrons [31, 32] excited by pump. At high pump intensity, the shape of the Dirac cone promotes the formation of an inverted population state [33] between holes and electrons. It has been proposed [29, 34] and experimentally shown [35] that graphene SPPs play a role in the dynamics of these hot carriers and *vice-versa*. In particular, theoretical calculations suggest that the SPP field can experience gain via stimulated plasmon emission in photoinverted graphene via electron-hole recombination [29, 36]. In order to understand how plasmons can experience gain, we must first understand the dynamics of hot carriers in graphene. Thus, the subject of this chapter is the study of the dynamics of hot carriers in graphene.

We organize the chapter as follows: in Section 4.1 the dynamics of hot carriers in graphene is discussed, with its several stages and relaxation channels that have been observed. In Section 4.2, we introduce a model based on microscopic rate equations that describes this dynamics. Finally, our calculated results are compared with experiment, in Section 4.3.

4.1 Carrier dynamics in graphene upon ultrafast optical excitation

We start by discussing the ultrafast dynamics of non-equilibrium electrons in graphene [37], when hot carriers are excited optically with an ultrafast laser pulse, usually a femtosecond pulse. We focus on interband excitation, when the incident pump photon energy $\hbar\omega_b$ is high enough to promote electrons to the conduction band, that is, when $\hbar\omega_b > 2E_F$, with E_F being the Fermi level.

When an ultrafast laser pulse impinges on graphene, electrons from the valence band are excited to the conduction band. Two populations of non-thermalized particles are created: the excited

electrons in the conduction band and the respective holes in the valence band. These non-thermalized carriers may block the promotion of new electrons to the conduction band. Also, they evolve to different thermal distributions, with their own temperature. Such electrons and holes, which are in equilibrium between themselves but not with the crystal lattice are called "hot". The true equilibrium of such hot carriers is eventually achieved.

The dynamics of these hot carriers in graphene is nowadays understood to occur via several stages and decay channels [37] (see Fig. 4.1). In the first stage, the promptly excited carriers with a non-Fermi-like distribution primarily undergo carrier-carrier scattering on a 10-fs time scale [38, 39] and two population of hot carriers, one of electrons and another of holes, are formed. These populations can be described as Fermi-like distributions, with different chemical potentials but an equal temperature, different from that of the lattice [30]. For longer timescales, the relaxation of hot carriers towards their equilibrium state is accomplished via several stages and decay channels, such as optical phonon emission [31], Auger recombination and hot plasmon emission [34, 35, 40], on a timescale of hundreds of femtoseconds, as well as direct and disorder-assisted acoustic phonon emission on picoseconds scale. Thermalization with the lattice is achieved before the electrons and holes have reached equilibrium between themselves (i.e, the electrons and holes quasi-Fermi levels become equal, $F_e = F_h = E_F$). Re-establishing the equilibrium concentrations of electrons and holes is the slowest process in graphene.

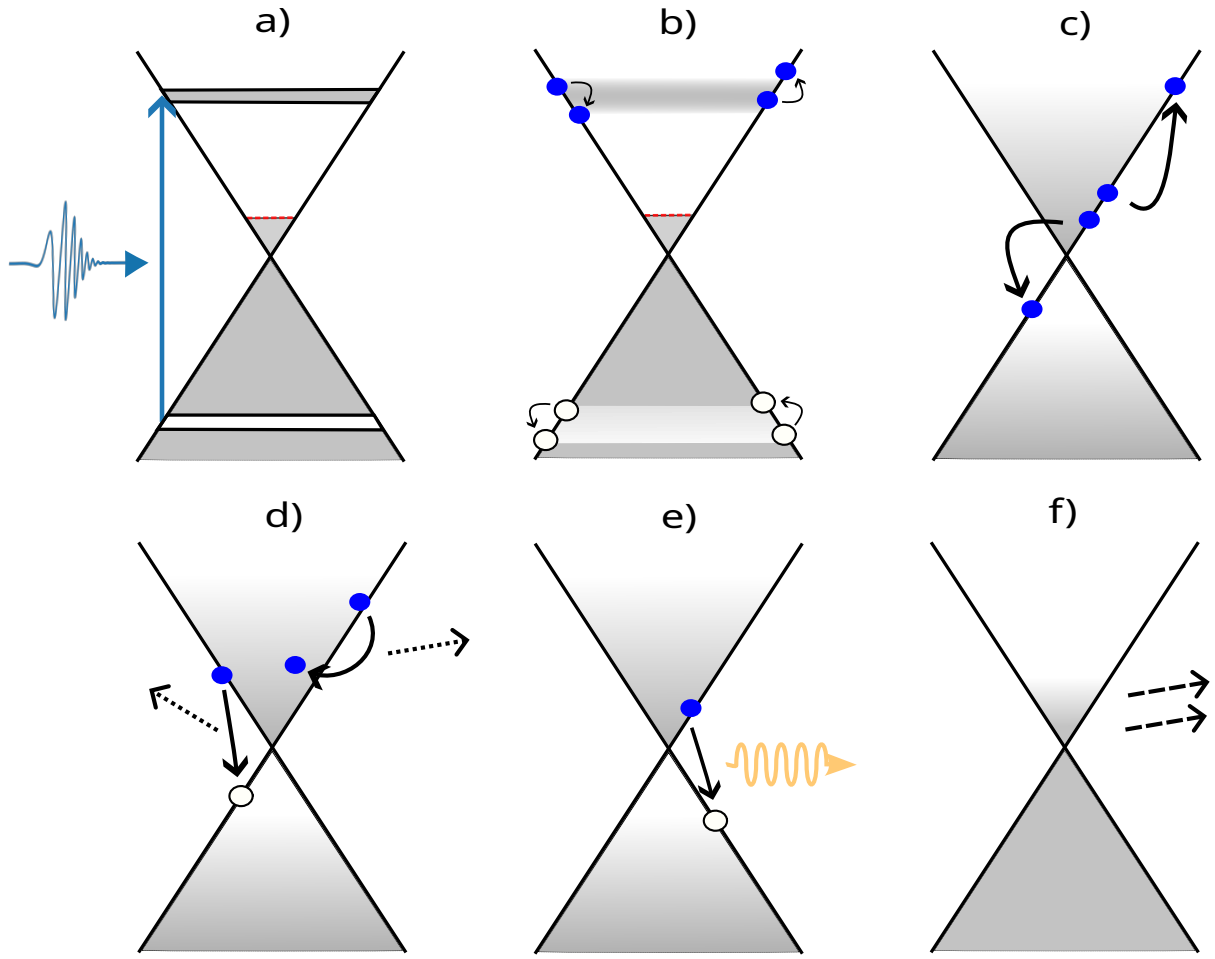

Figure 4.1: Carrier relaxation processes in graphene under ultrafast optical excitation. **a)** Initially graphene is in equilibrium. When the pump arrives (blue arrow) two populations of electrons and holes are created. These electrons and holes have non-Fermi-like distributions. **b)** Electrons and holes undergo carrier-carrier scattering on the 10-fs scale. Through this channel two Fermi-like distributions are formed, one for electrons and another for holes, with different chemical potentials but equal temperatures. **c)**, **d)** and **e)** show the different channels in 100-fs time scale through which electrons and holes recombine and thermalize. **c)** Auger recombination. **d)** Electron-hole recombination and carrier relaxation via optical phonon emission. **e)** Electron-hole recombination via plasmon emission. **f)** Further cooling is assisted by acoustic phonon emission.

4.2 Hot electron model

In this Section, we present our hot carriers model in order to explain the dynamics of the electronic response of optically excited graphene. The goal is, given some parameters to phenomenologically account for the decay channels, to determine the transient temperature and quasi Fermi levels of the hot carriers as well as the time evolution of the distribution functions and graphene's conductivity.

Consider a pump beam, with photons of the energy $\hbar\omega_b$, that creates a non-thermalized population of electrons (holes) in the conduction (valence) band. We divide the dynamics of the hot carriers into two stages. The first one encompasses the first few tens of fs with carrier-carrier collisions, which is faster than the pump duration ($\tau_b \approx 100$ fs) and drives the system towards a quasi-equilibrium distribution, where the charge carriers will have a very high temperature compared to that of the lattice. The second stage is of the 100-fs scale and occurs when the relaxation of carrier energy and electron-hole recombination take place. To model these processes we introduce 4 adjustable parameters:

1. electron-electron (as well as hole-hole and electron-hole) scattering time τ_{ee};
2. energy intraband relaxation time τ_ε due to the electron scattering by lattice imperfections (phonons, impurities, etc.);
3. momentum relaxation rate γ_p, also due to the electron scattering by lattice imperfections;
4. interband recombination time τ_r determined by Auger recombination or by phonon or plasmon emission.

This parameters should satisfy the relation [30]:

$$\tau_{ee} \ll \tau_p \ll \tau_\varepsilon \ll \tau_r \ , \tag{4.1}$$

where $\tau_p = 2\pi\gamma_p^{-1}$.

4.2.1 Non-thermalized carriers

We start by writing down equations that describe the populations of non-thermalized electrons n_{nt} and holes p_{nt}. Upon excitation, given the symmetry of their spectra (within the Dirac cone approximation) and the assumption that $n_{\mathrm{nt}}, p_{\mathrm{nt}} \gg n_0, p_0$ (which are the equilibrium concentrations), both electrons and holes evolve in the same way, so the non-thermalized populations should be equal:

$$p_{\mathrm{nt}}(t) = n_{\mathrm{nt}}(t) \ . \tag{4.2}$$

Due to the carrier-carrier scattering, two populations of *thermalized* (i.e. having reached equilibrium among them but not with the rest of the world) carriers are created. We denote the 2D concentration

of the thermalized electrons by $n_{\rm t}(t)$ and the thermalized holes by $p_{\rm t}(t)$. The total concentrations of electrons and holes are:

$$n(t) = n_{\rm nt}(t) + n_{\rm t}(t) \ , \tag{4.3}$$

$$p(t) = p_{\rm nt}(t) + p_{\rm t}(t) \ . \tag{4.4}$$

The balance equations that govern the depletion of carriers from the non-thermalized to the thermalized population are:

$$\dot{p}_{\rm nt} = \dot{n}_{\rm nt} = \frac{{\rm A}_{\rm abs}(t)}{\hbar\omega_b} I_b(t) - \frac{n_{\rm nt}(t)}{\tau_{ee}} \ , \tag{4.5}$$

where

$$I_b(t) = I_b^{\rm max} \exp\left(-\frac{2t^2}{\tau_b^2}\right) \tag{4.6}$$

is the pump intensity and ${\rm A}_{\rm abs}(t)$ is the absorbance of graphene. The first term in Eq. (4.5) corresponds to the generation of non-thermalized carriers and the second term to their thermalization.

We determine ${\rm A}_{\rm abs}(t)$ using the Fermi's Golden rule. The transition rate is [7]:

$$\Gamma(\mathbf{k}) = \frac{2\pi}{\hbar}\frac{(ev_F)^2}{4}\frac{E_b^2}{\omega_b^2}\sin^2\theta\ \delta\left(2\hbar v_F k - \hbar\omega_b\right)\left\{\left[1-g_h(-\varepsilon_{\mathbf{k}})\right]\left[1-g_e(\varepsilon_{\mathbf{k}})\right] - g_h(-\varepsilon_{\mathbf{k}})g_e(\varepsilon_{\mathbf{k}})\right\} \ , \tag{4.7}$$

where g_e and g_h are the non-thermalized distribution functions for electrons and holes, respectively. Then, the transition rate per unit area is:

$$\Gamma = \frac{e^2E_b^2}{8\hbar^2\omega_b}\left\{\left[1-g_h\left(-\frac{\hbar\omega_b}{2}\right)\right]\left[1-g_e\left(\frac{\hbar\omega_b}{2}\right)\right] - g_h\left(-\frac{\hbar\omega_b}{2}\right)g_e\left(\frac{\hbar\omega_b}{2}\right)\right\} \ . \tag{4.8}$$

Therefore, the power per unit area absorbed by the material reads:

$$W_{\rm abs} = \Gamma\hbar\omega_b = \frac{e^2E_b^2}{8\hbar}\left\{\left[1-g_h\left(-\frac{\hbar\omega_b}{2}\right)\right]\left[1-g_e\left(\frac{\hbar\omega_b}{2}\right)\right] - g_h\left(-\frac{\hbar\omega_b}{2}\right)g_e\left(\frac{\hbar\omega_b}{2}\right)\right\} \ . \tag{4.9}$$

On the other hand, the incident power flux per unit area is given by:

$$W_{\rm inc} = \frac{c}{8\pi}E_b^2 \ . \tag{4.10}$$

The absorbance is given by the ratio between the absorbed and incident fluxes:

$${\rm A}_{\rm abs}(t) = \frac{W_{\rm abs}}{W_{\rm inc}} = \pi\alpha_F\left\{\left[1-g_h\left(-\frac{\hbar\omega_b}{2},t\right)\right]\left[1-g_e\left(\frac{\hbar\omega_b}{2},t\right)\right] - g_h\left(-\frac{\hbar\omega_b}{2},t\right)g_e\left(\frac{\hbar\omega_b}{2},t\right)\right\} \ , \tag{4.11}$$

with α_F denoting the fine structure constant and:

$$\pi\alpha_F = \frac{4\pi}{c}\sigma_0 \ . \tag{4.12}$$

This result only holds for suspended graphene at normal incidence. For graphene on top of a

dielectric with refractive index n, for an arbitrary incident angle α, we can determine $\mathrm{A_{abs}}(t)$ from the expression for the linear reflection and transmission coefficients (see Eq. (C.17)):

$$\hat{r}^{(0)}\left(\hbar\omega_b, t\right) = \frac{n\cos\alpha - \cos\theta + \dfrac{4\pi}{cE_b^2}\mathbf{j}\cdot\mathbf{E}_b\cos\theta\cos\alpha}{n\cos\alpha + \cos\theta + \dfrac{4\pi}{cE_b^2}\mathbf{j}\cdot\mathbf{E}_b\cos\theta\cos\alpha} \ , \tag{4.13}$$

$$\hat{t}^{(0)}\left(\hbar\omega_b, t\right) = \frac{2\cos\alpha}{n\cos\alpha + \cos\theta + \dfrac{4\pi}{cE_b^2}\mathbf{j}\cdot\mathbf{E}_b\cos\theta\cos\alpha} \ . \tag{4.14}$$

The Joule heating term containing $\mathbf{j}\cdot\mathbf{E}_b$ is the power absorbed by graphene ($\mathbf{j}$ is the current and $\mathbf{E}_b$ the pump electric field) and θ is the angle of refraction. The absorbance is related to the reflectivity R and transmittance T by:

$$\mathrm{A_{abs}}(t) = 1 - R(t) - T(t) \ , \tag{4.15}$$

which can be expanded to the first order in $\mathbf{j}\cdot\mathbf{E}_b$:

$$\mathrm{A_{abs}}(t) \approx \frac{4\cos\alpha\cos^2\theta}{\left(n\cos\alpha + \cos\theta\right)^2}\frac{4\pi}{cE_b^2}\mathbf{j}\cdot\mathbf{E}_b \ . \tag{4.16}$$

We consider the situation where absorption by the substrate is negligible. This is a good approximation for the pump energies we are interested in and a substrate such as SiO_2. Then, we have from Eq. (4.11):

$$\frac{4\pi}{cE_b^2}\mathbf{j}\cdot\mathbf{E}_b = \pi\alpha_F\left\{\left[1 - g_h\left(-\frac{\hbar\omega_b}{2}, t\right)\right]\left[1 - g_e\left(\frac{\hbar\omega_b}{2}, t\right)\right] - g_h\left(-\frac{\hbar\omega_b}{2}, t\right)g_e\left(\frac{\hbar\omega_b}{2}, t\right)\right\} \ . \tag{4.17}$$

Finally, the general expression for the absorbance is:

$$\mathrm{A_{abs}}(t) \approx \frac{4\cos\alpha\cos^2\theta}{\left(n\cos\alpha + \cos\theta\right)^2}\pi\alpha_F\left\{\left[1 - g_h\left(-\frac{\hbar\omega_b}{2}, t\right)\right]\left[1 - g_e\left(\frac{\hbar\omega_b}{2}, t\right)\right] - g_h\left(-\frac{\hbar\omega_b}{2}, t\right)g_e\left(\frac{\hbar\omega_b}{2}, t\right)\right\} \ . \tag{4.18}$$

Introducing,

$$\mathrm{A}_0(\alpha, \theta) = \frac{4\pi\alpha_F}{\left(n\cos\alpha + \cos\theta\right)^2}\cos\alpha\cos^2\theta \ , \tag{4.19}$$

we may write:

$$\mathrm{A_{abs}}(t) = \mathrm{A}_0(\alpha, \theta)\left\{1 - g_h\left(-\frac{\hbar\omega_b}{2}, t\right) - g_e\left(\frac{\hbar\omega_b}{2}, t\right)\right\} \ . \tag{4.20}$$

We still need an expression for the non-thermalized distributions g_e and g_h in Eq. (4.20). Since

we have assumed Eq. (4.2) to be valid, by consistency, these distributions should also be the same:

$$g_h(-\varepsilon, t) = g_e(\varepsilon, t) = g(\varepsilon, t) \ . \tag{4.21}$$

Since the pump pulse is well described by a Gaussian wavepacket, we model $g(\varepsilon, t)$ as:

$$g(\varepsilon, t) = \tilde{g}(t)\frac{\Delta_\varepsilon(-\infty)}{\Delta_\varepsilon(t)} \exp\left(-\frac{(\varepsilon - \hbar\omega_b/2)^2}{2\Delta_\varepsilon^2(t)}\right) \ , \tag{4.22}$$

with $\tilde{g}(t)$ denoting a function to be determined. For simplicity, we consider the following points:

1. Since the pulse is much longer in time than τ_{ee}, during pumping a stationary situation is rapidly achieved for g's width $\Delta_\varepsilon(t)$, so we take its asymptotic limit: $\Delta_\varepsilon(t) \approx \Delta_\varepsilon(-\infty)$;

2. For 100 fs pulses, their spectral width (~ 18 meV) should be much smaller than the thermalized distribution energy spread, so we take $\Delta_\varepsilon(-\infty)$ to be the pulse's spectral width:

$$\Delta_\varepsilon(-\infty) \approx 2\pi\hbar\frac{0.44}{\tau_b} \ ; \tag{4.23}$$

3. As the thermalized carriers relax towards lower energies, we assume that the thermalized distributions f_e and f_h at near half of the pump energy ($\varepsilon = \hbar\omega_b/2$) are much smaller than g_e and g_h:

$$f_e\left(\varepsilon, t\right) \ll g_e(\varepsilon, t) \ , \tag{4.24}$$

$$f_h\left(\varepsilon, t\right) \ll g_h(\varepsilon, t) \ , \tag{4.25}$$

   so that we may write the full distribution function for electrons as $f_e\left(\varepsilon, t\right) + g_e(\varepsilon, t)$ and similar for holes, $f_h\left(\varepsilon, t\right) + g_h(\varepsilon, t)$.

To determine $\tilde{g}(t)$, we notice that the transient evolution of the non-thermalized population of charge carriers dictated by Eq. (4.5), may be also calculated using graphene's density of states $\rho(\varepsilon) = 2|\varepsilon|/\left[\pi(\hbar v_F)^2\right]$:

$$\begin{aligned} p_{\mathrm{nt}}(t) = n_{\mathrm{nt}}(t) &= \int_0^\infty d\varepsilon \rho(\varepsilon) g(\varepsilon, t) \\ &= \tilde{g}(t) \int_0^\infty d\varepsilon \rho(\varepsilon) \exp\left(-\frac{(\varepsilon - \hbar\omega_b/2)^2}{2\Delta_\varepsilon^2}\right) \ . \end{aligned} \tag{4.26}$$

The integral can be approximated and yields:

$$p_{\mathrm{nt}}(t) = n_{\mathrm{nt}}(t) = \sqrt{2\pi}\Delta_\varepsilon \tilde{g}(t) \rho\left(\frac{\hbar\omega_b}{2}\right) \tag{4.27}$$

and, consequently, the time dependent amplitude can be written as a function of the non-thermalized

density:

$$\tilde{g}(t) = \frac{n_{\rm nt}(t)}{\sqrt{2\pi}\Delta_\varepsilon \rho\left(\frac{\hbar\omega_b}{2}\right)} \ . \tag{4.28}$$

Using these definitions, the balance Eq. (4.5) is written as:

$$\dot{p}_{\rm nt} = \dot{n}_{\rm nt} = \frac{\mathrm{A}_0(\alpha,\theta)}{\hbar\omega_b} I_b(t) \left\{ 1 - \frac{2n_{\rm nt}(t)}{\sqrt{2\pi}\Delta_\varepsilon \rho\left(\frac{\hbar\omega_b}{2}\right)} \right\} - \frac{n_{\rm nt}(t)}{\tau_{ee}} \ . \tag{4.29}$$

Notice that the maximum possible number of states that can be occupied by the non-thermalized carriers is:

$$p_{\rm nt}^{\rm max} = n_{\rm nt}^{\rm max} = \int_0^{+\infty} d\varepsilon \rho(\varepsilon) \exp\left(-\frac{(\varepsilon - \hbar\omega_b/2)^2}{2\Delta_\varepsilon^2} \right) = \sqrt{2\pi}\Delta_\varepsilon \rho\left(\frac{\hbar\omega_b}{2}\right) \ , \tag{4.30}$$

so we may rewrite Eq. (4.29) as:

$$\dot{n}_{\rm nt} = \frac{\mathrm{A}_0(\alpha,\theta)}{\hbar\omega_b} I_b(t) \left\{ 1 - \frac{2n_{\rm nt}(t)}{n_{\rm nt}^{\rm max}} \right\} - \frac{n_{\rm nt}(t)}{\tau_{ee}} \ . \tag{4.31}$$

Equation (4.31) accounts for Pauli blocking: if $n_{\rm nt}(t) = n_{\rm nt}^{\rm max}/2$, then $\dot{n}_{\rm nt} < 0$, that is, no more electrons can be pumped to the conduction band, thus predicting saturable absorption.

4.2.2 Thermalized carriers

After the non-thermalized population, $n_{\rm nt} + p_{\rm nt}$, has been created, the electrons will go under electron-electron scattering processes leading to a thermalization of the electron gas. We describe this thermalized gas as being in quasi-equilibrium: the electron and hole distributions will be approximated by quasi Fermi-Dirac distributions with chemical potentials F_e and F_h, respectively, but with equal temperature T:

$$f_e(\varepsilon, F_e, T) = f_c(\varepsilon) = \frac{1}{1 + \exp\left(\frac{\varepsilon - F_e}{k_B T}\right)} \quad , \quad \varepsilon > 0 \ , \tag{4.32}$$

$$f_h(\varepsilon, F_h, T) = 1 - f_v(\varepsilon) = \frac{1}{1 + \exp\left(\frac{F_h - \varepsilon}{k_B T}\right)} \quad , \quad \varepsilon < 0 \ . \tag{4.33}$$

This description is justified if the electron-electron, electron-hole, and hole-hole scattering processes (characterized by the typical scattering time τ_{ee}) are more probable than the electron-phonon and electron-impurities ones [30]. Experimental results [33, 38] show that in typical graphene samples this situation usually is the case.

To describe the evolution of thermalized carriers, we write the balance equations for n_t and p_t:

$$\dot{n}_{\rm t} = \frac{n_{\rm nt}}{\tau_{ee}} - \frac{n_t - n_0}{\tau_r} \ , \tag{4.34}$$

$$\dot{p}_{\rm t} = \frac{p_{\rm nt}}{\tau_{ee}} - \frac{p_t - p_0}{\tau_r} \ , \tag{4.35}$$

where n_0 and p_0 are the equilibrium electron and hole concentrations[1]. On the other hand, the instantaneous thermalized electron concentration can be related to a quasi Fermi level $F_e(t)$ and electronic temperature $T(t)$:

$$n_t(t) = \frac{g_s g_v}{\mathcal{S}} \sum_{\mathbf{k}} f_e\left(\varepsilon_{\mathbf{k}}, F_e(t), T(t)\right) = \frac{2}{\pi}\left(\frac{k_B T(t)}{\hbar v_F}\right)^2 \Gamma\left(2\right) \mathrm{F}_1\left(\frac{F_e(t)}{k_B T(t)}\right) \ , \tag{4.36}$$

where g_s and g_v are the spin and valley degeneracies for graphene and $\mathrm{F}_n(z)$ is the Fermi integral:

$$\mathrm{F}_n(z) = \frac{1}{\Gamma(n+1)} \int_0^{+\infty} dx \frac{x^n}{1 + \exp\left(x - z\right)} \ , \tag{4.37}$$

with $\Gamma(n)$ being the Euler gamma function. Equations (4.34) and (4.36) establish a relation between $F_e(t)$ and $T(t)$. To completely determine these two functions we need a second equation. At the smaller timescale $\sim \tau_\varepsilon$, the thermalized electrons, having been scattered by phonons, impurities, and other lattice imperfections, give in their energy, ε_t, to the lattice. We write the energy relaxation for electrons also in the form of a balance equation:

$$\dot{\varepsilon}_t = \frac{\varepsilon_{\rm nt}}{\tau_{ee}} - \frac{\varepsilon_t - \varepsilon_0'}{\tau_\varepsilon} \ , \tag{4.38}$$

where $\varepsilon_{\rm nt}$ is the energy of the non-thermalized electrons. This energy is:

$$\begin{aligned} \varepsilon_{\rm nt} &= \int_0^{+\infty} d\varepsilon \varepsilon \rho(\varepsilon) g(\varepsilon, t) \\ &= \exp\left(-\frac{\hbar^2\omega_b^2}{8\Delta_E^2}\right) \rho\left(\frac{\hbar\omega_b}{2}\right) \Delta_\varepsilon^2 \tilde{g}(t) + \sqrt{2\pi}\Delta_\varepsilon \rho\left(\frac{\hbar\omega_b}{2}\right)\left[\frac{\hbar\omega_b}{2} + \frac{2\Delta_\varepsilon^2}{\hbar\omega_b}\right]\tilde{g}(t) \ . \end{aligned} \tag{4.39}$$

Since $2\Delta_\varepsilon \ll \hbar\omega_b$, using Eq. (4.28), $\varepsilon_{\rm nt}$ approximates to:

$$\varepsilon_{\rm nt} \approx \frac{\hbar\omega_b}{2} n_{\rm nt}(t) \tag{4.40}$$

[1]The second term in Eqs. (4.34) and (4.35) represents e-h recombination. This recombination is a nonlinear two-particle process [30] that is proportional to the product of the electron and hole densities. This recombination rate should be written as $\alpha_{\rm rec}\left(n_t p_t - n_0 p_0\right)$ with $\alpha_{\rm rec}$ called the recombination coefficient. However, at relatively low excitation levels (which may be the case in our situation, at the latest stage of the relaxation process when the interband recombination becomes important) we may introduce a recombination time by writing the recombination coefficient as $\alpha_{\rm rec} = \dfrac{1}{\tau_r\left(n_0 + p_0\right)}$. In this approximation, we can decouple the balance equations for electrons and holes and write them as Eq. (4.34) and (4.35).

and Eq. (4.38) may be simplified:

$$\dot{\varepsilon}_t \approx \frac{\hbar\omega_b}{2}\frac{n_{\rm nt}(t)}{\tau_{ee}} - \frac{\varepsilon_t - \varepsilon_0'(t)}{\tau_\varepsilon} \ , \tag{4.41}$$

where $\varepsilon_0'(t)$ is the energy of the electron distribution when thermalized with the lattice at temperature T_0:

$$\varepsilon_0'(t) = \frac{g_s g_v}{\mathcal{S}}\sum_{\mathbf{k}} \varepsilon_{\mathbf{k}} f_e\left(\varepsilon_{\mathbf{k}}, F_e(t), T_0\right) = \frac{2}{\pi}\frac{\left(k_B T_0\right)^3}{\left(\hbar v_F\right)^2}\Gamma\left(3\right)\mathrm{F}_2\left(\frac{F_e(t)}{k_B T_0}\right) \ . \tag{4.42}$$

Equation (4.41) can be solved using Green's function method:

$$\varepsilon_t = e^{-t/\tau_\varepsilon}\int_{-\infty}^{t} dt' e^{t'/\tau_\varepsilon}\left\{\frac{\hbar\omega_b}{2}\frac{n_{\rm nt}(t')}{\tau_{ee}} + \frac{\varepsilon_0'(t')}{\tau_\varepsilon}\right\} \ . \tag{4.43}$$

We define:

$$\tilde{\varepsilon}(t) = \frac{\hbar\omega_b}{2}\frac{e^{-t/\tau_\varepsilon}}{\tau_{ee}}\int_{-\infty}^{t} dt' e^{t'/\tau_\varepsilon} n_{\rm nt}(t') \tag{4.44}$$

and since $F_e(t)$ is a slowly varying function compared to $1/\tau_\varepsilon$, we approximate:

$$e^{-t/\tau_\varepsilon}\int_{-\infty}^{t} dt' e^{t'/\tau_\varepsilon}\frac{\varepsilon_0'(t')}{\tau_\varepsilon} \approx e^{-t/\tau_\varepsilon}\varepsilon_0'(t)\int_{-\infty}^{t} dt'\frac{e^{t'/\tau_\varepsilon}}{\tau_\varepsilon} = \varepsilon_0'(t) \ . \tag{4.45}$$

Equation (4.43) assumes the form:

$$\varepsilon_t(t) = \tilde{\varepsilon}(t) + \varepsilon_0'(t) \ . \tag{4.46}$$

On the other hand, the energy of the thermalized electrons is:

$$\varepsilon_t = \frac{2}{\pi}\frac{\left(k_B T(t)\right)^3}{\left(\hbar v_F\right)^2}\Gamma\left(3\right)F_2\left(\frac{F_e(t)}{k_B T(t)}\right) \ , \tag{4.47}$$

so equating Eqs. (4.46) and (4.47), the second relation for $F_e(t)$ and $T(t)$ is:

$$\frac{2}{\pi}\frac{\left(k_B T(t)\right)^3}{\left(\hbar v_F\right)^2}\Gamma\left(3\right)F_2\left(\frac{F_e(t)}{k_B T(t)}\right) = \tilde{\varepsilon}(t) + \varepsilon_0'(t) \ . \tag{4.48}$$

It remains to determine the chemical potential for the hole distribution. We could write similar balance equations for holes as we did for electrons. However, since charge must be conserved, we have:

$$p_0 + n(t) = p(t) + n_0 \ . \tag{4.49}$$

This allows us to determine the hole concentration at any given time. Separating contributions from

thermalized and non-thermalized carriers, we have:

$$p_t(t) = p_0 + n_{\rm nt}(t) + n_t(t) - p_{\rm nt}(t) - n_0 \ . \tag{4.50}$$

Remembering that $p_{\rm nt} = n_{\rm nt}$, Eq. (4.50) becomes:

$$p_t(t) = p_0 + n_t(t) - n_0 \ . \tag{4.51}$$

Knowing $p_t(t)$, we can calculate the hole's chemical potential $F_h(t)$ using the relation:

$$p_t(t) = \frac{2}{\pi}\left(\frac{k_B T(t)}{\hbar v_F}\right)^2 \Gamma(2)\,\mathrm{F}_1\left(-\frac{F_h(t)}{k_B T(t)}\right) \ . \tag{4.52}$$

4.2.3 Non-equilibrium conductivity due to hot carriers

Now that we know how the quasi-Fermi levels and the electronic temperature evolve with time, we can study the non-equilibrium transient conductivity. We assume that, to first order, the optical non-equilibrium interband conductivity of graphene can be described by the usual formula (see Eq. (B.33)):

$$\sigma_{\rm neq}(\omega, t) = \frac{4\sigma_0}{\pi}\hbar\left(\gamma_{\rm inter} - i\omega\right)\int_0^{+\infty} d\varepsilon \frac{1 - f^{(e)}(\varepsilon, t) - f^{(h)}(\varepsilon, t)}{\left[\hbar\gamma_{\rm inter} + i\left(2\varepsilon - \hbar\omega\right)\right]\left[\hbar\gamma_{\rm inter} - i\left(2\varepsilon + \hbar\omega\right)\right]} \ , \tag{4.53}$$

with $\gamma_{\rm inter}$ meaning the interband scattering rate. Here $f^{(e)}$ and $f^{(h)}$ are the full distribution functions for the electrons and holes with contributions from thermalized and non-thermalized carriers:

$$f^{(e,h)}(\varepsilon, t) = g_{e,h}(\varepsilon, t) + f_{e,h}\left(\varepsilon, F_{e,h}(t)\right) \ , \tag{4.54}$$

with $g_{e,h}$ given in Eq. (4.21).

The extension of the usual formula for the interband conductivity (B.33) to a time dependent version (4.53) is valid as long as, at the frequency of observation ω, the field oscillates several times before the physical conditions change. In other words, this approach works if the two time scales, $1/\omega$ and the time it takes for chemical potentials and temperature to change, are sufficiently different:

$$\omega\tau_{\rm ee} > 1 \ . \tag{4.55}$$

Here, we take τ_{ee} as the time of change of the system, since it is the smallest characteristic time parameter. Because it is expected that τ_{ee} lies in the time range $10 - 30$ fs [38], at the optical frequencies of interest ($\lambda_a \leq 615$ nm) this condition is satisfied.

As shown in Appendix E, to the first order, the differential reflectivity only depends in the real part of the transient conductivity. Also, it is expected that $\hbar\gamma_{\rm inter} \ll k_B T$ [30] so the real part of

expression (4.53) may be written as:

$$\mathrm{Re}\sigma_{\mathrm{inter}}(\omega,t)=\mathrm{Re}\sigma_{\mathrm{nt}}(\omega,t)+\mathrm{Re}\sigma_{t}(\omega,t)\ , \tag{4.56}$$

with $\sigma_t(\omega,t)$ coming from the thermalized carriers:

$$\mathrm{Re}\sigma_{t}(\omega,t)=\sigma_0\frac{\sinh\left[\dfrac{\hbar\omega-(F_e(t)-F_h(t))}{2k_BT}\right]}{\cosh\left[\dfrac{F_h(t)+F_e(t)}{2k_BT}\right]+\cosh\left[\dfrac{\hbar\omega-(F_e(t)-F_h(t))}{2k_BT}\right]} \tag{4.57}$$

and $\sigma_{\mathrm{nt}}(\omega,t)$ from the non-thermalized carriers[2]:

$$\mathrm{Re}\sigma_{\mathrm{nt}}(\omega,t)=-\sigma_0 g\left(\frac{\hbar\omega}{2},t\right)\ . \tag{4.58}$$

4.2.4 Differential reflectivity

The experimental results we are interested in understanding were obtained by means of pump-probe spectroscopy and measure the changes in the reflectance of graphene. Let us call δ_t the time delay between the pulses b and a. The differential reflectivity is given by (see Appendix E for derivation):

$$\frac{\Delta R_a}{R_a}=-\frac{\cos^2\theta_a}{\cos\alpha_a}\frac{\left(\hat{t}_a^{(0)}\right)^2}{\Phi_a\hat{r}_a^{(0)}}\frac{4\pi}{c}\sigma_0\int_{-\infty}^{\infty}dt'\left|A_i\left(t'\right)\right|^2\left\{f^{(e)}\left(\frac{\hbar\omega_a}{2},t'+\delta_t\right)+f^{(h)}\left(\frac{\hbar\omega_a}{2},t'+\delta_t\right)\right\}\ . \tag{4.59}$$

Here $A_i\left(t'\right)$ is the incident pulse's amplitude:

$$A_i(t)=a_i\exp\left(-\frac{t^2}{\tau_a^2}\right)\ , \tag{4.60}$$

where a_i is a constant and τ_a is the pulse time width. Φ_a is the probe's fluence:

$$\Phi_a=\int dt\left|A_i\left(t\right)\right|^2 \tag{4.61}$$

and $\hat{t}_a^{(0)}$ and $\hat{r}_a^{(0)}$ are the usual linear transmission and reflection coefficients. Finally, α_a and θ_a are the incident and refracted angles, respectively.

[2]We notice that the "slowly varying amplitude" approximation is still valid here because the relevant frequency in Eq. (4.58) is ω_b and also satisfies $\omega\tau_{\mathrm{ee}}>1$.

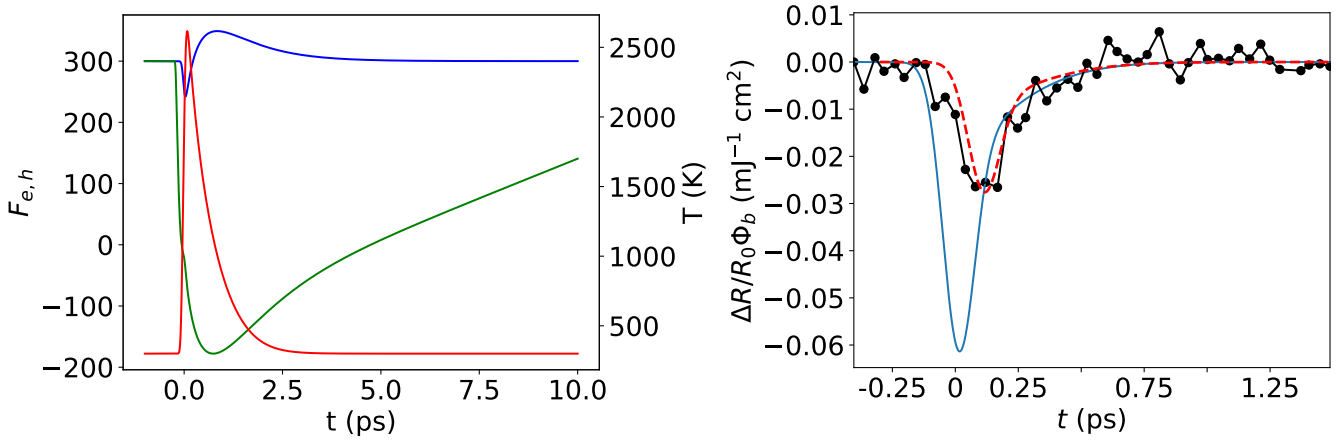

Figure 4.2: **Left:** Quasi-Fermi levels and temperature as functions of the time delay between pump and probe, t, as determined by the model. F_e, F_h and T are represented by the blue, green and red curves, respectively. **Right:** Differential reflectivity normalized to the pump fluence. The black line with dots are the experimental results taken from Ref. [1]. The blue line is the calculated result from our model with $\tau_{ee} = 10$ fs, $\tau_\varepsilon = 0.4$ ps and $\tau_r = 1$ ps. The red dashed line shows the calculation (blue line) but with a correction factor $f = 0.45$ for the amplitude and a shift in time of $t_0 = 0.1$ ps.

4.3 Numerical results and concluding remarks

We can use our model to simulate the non-resonant signal measured by Constant et al. [1], as shown in Figs. 4.2 and 4.3 (see Appendix F for numerical implementation). The time parameters, τ_{ee}, τ_ε and τ_r used were:

$$\tau_{ee} = 10 \text{ fs} \quad , \quad \tau_\varepsilon = 0.4 \text{ ps} \quad , \quad \tau_r = 1 \text{ ps} \, . \tag{4.62}$$

These are not the parameters that best fit our model to the experimental results. Taking $\tau_{ee} = 1$ fs, leads to a better agreement with the experimental results. However, since it is generally accepted that $\tau_{ee} \sim 10 - 30$ fs [38], this value looks unrealistic. The rest of the parameters are the same as in the experiment: the pump and probe incident angles are $\alpha_b = 40°$ and $\alpha_a = 20°$, respectively; pump and probe have equal frequencies, $\omega_b = \omega_a = 3064.97$ ps^{-1} ($\lambda_a = 615$ nm); the substrate is SiO_2 with a refractive index $n_2 = \sqrt{\varepsilon_2} = 1.4601$ at frequency ω_a and the pump fluence is $\Phi_b = 0.26$ mJ cm^{-2}.

The calculated dependence deviates from the observations in two ways: it yields a signal bigger by approximately a factor of two and the peak of the calculation appears approximately 0.1 ps earlier than the measurement. The reasons for these differences could be:

1. Information concerning experimental details that we have from Ref. [1] may be incomplete, for instance, we assume that both pulses are Gaussian and have the same duration. However, if it is not so, the spectral distribution of non-thermalized carriers will be different. We also checked that assuming a non-Gaussian pump would change the temporal distribution of hot

carriers. Both effects would affect the differential reflectance dependence on the probe pulse delay.

2. In the work [1], the beams were focused using a single lens. This technical choice implies that in order to have an angle of incidence different from zero, the beams cannot be centered in the lens, and this introduces spatial and temporal chirp in the pulses [41] that perhaps cannot be ignored.

3. The data of Ref. [1] is noisy, which makes the fit difficult to perform. In fact, the data shows a weird feature: when $\omega_a = \omega_b$, it is expected that the peak of the signal to be positioned at ≈ 0 ps, since it is when most electrons are pumped to the conduction band thus blocking the probe more intensively. This is not the case in the data of Ref. [1] (see black curve in Fig. 4.2). For the peak of the signal to appear later, the non-thermalized electrons must thermalize so that the population of thermalized electrons grows enough to block the probe at frequency $\omega_a = \omega_b$. This is possible if the non-thermalized electrons thermalize over the timescale of 1 fs.

To conclude this chapter, the hot electron model yields a good understanding of the processes taking place in graphene under fast optical pumping. They have to be taken into account when considering all-optical generation of surface plasmons.

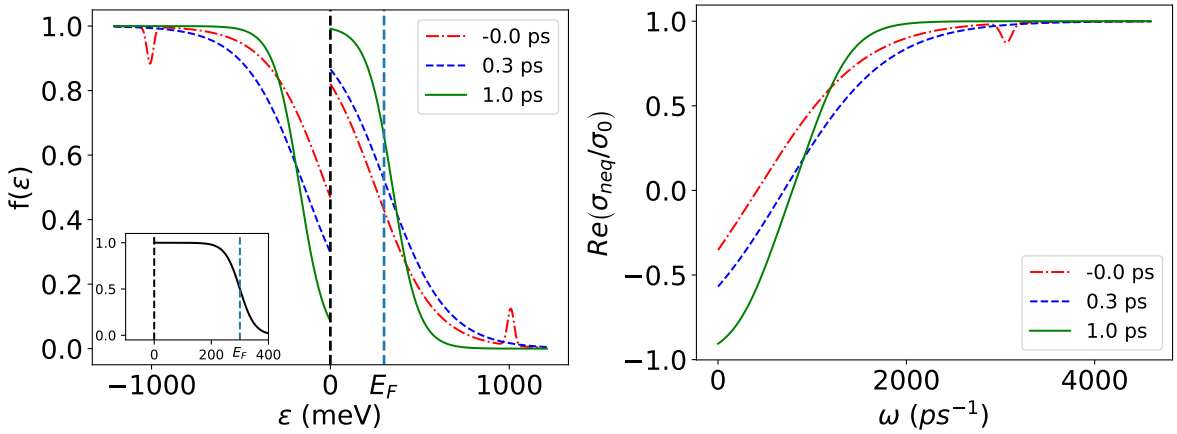

Figure 4.3: **Left:** Hot carrier distribution for different delay times, determined using the the Fermi levels and temperature in Fig. 4.2. The inset shows the equilibrium Fermi-Dirac distribution. **Right:** Transient conductivity (4.56).

Chapter 5

Plasmon lasing

5.1 Plasmon emission as a new electronic relaxation channel

As discussed in Chapter 2, SPPs are collective charge oscillations, mediated by long-range Coulomb interactions. But, in a situation out of equilibrium, is this possible? The answer is yes and experimental evidence for optically generated non-equilibrium plasmons was given by Ni et al. [42]. In their work, using infrared pump–probe nano-spectroscopy, SPPs were activated and detected using femtosecond optical pulses in a specimen of intrinsic graphene that otherwise lacked infrared plasmonic response at equilibrium. To excite SPPs, a focused IR probe beam was used to illuminate a metalized tip of an atomic force microscope and generate a strong evanescent electric field [6]. At equilibrium, no response was observed. However, upon ultrafast optical excitation using a fs pump pulse, Ni et al. observed charge oscillations, consistent with graphene SPPs. The amplitude of this oscillations depended on the delay between pulses: at observation times bigger than 2 ps, when the amount of charge carriers started to be small, the features of the oscillations disappeared. Thus, we may conclude that the out-of equilibrium carriers can hold SPPs or, more correctly, hot SPPs.

Nevertheless, this does not reveal how important are SPPs as a relaxation channel and if they strongly couple to electron-hole pairs. The strong interplay of plasmons and eletron/hole excitations in graphene was revealed by Aaron et al. [43, 44]. Using angle-resolved photoemission spectroscopy, they observed a renormalization of the Dirac cone due to coupling of SPPs with holes. Later, Kim et al. [35, 45] experimentally showed that hot SPPs participate in the relaxation dynamics as a decay channel for the excited carriers. By impinging a graphene device with a 100 fs pulse at 850 nm and collecting the resulting emission spectra using a Fourier-transform infrared microscope, they found that the higher the Fermi level[1] of graphene, the stronger the infrared emission is. This behavior is the opposite of thermal emission, which should reduce for increasing Fermi energy. The observed response is consistent with plasmon emission, as the phase space for plasmonic emission increases with Fermi energy [45]. Some of the plasmons, emitted by the hot electrons, scatter into photons, leading to the observed infrared emission. To enhance conversion of SPPs into thermal radiation,

[1] They controlled the Fermi energy by electrostatic gating.

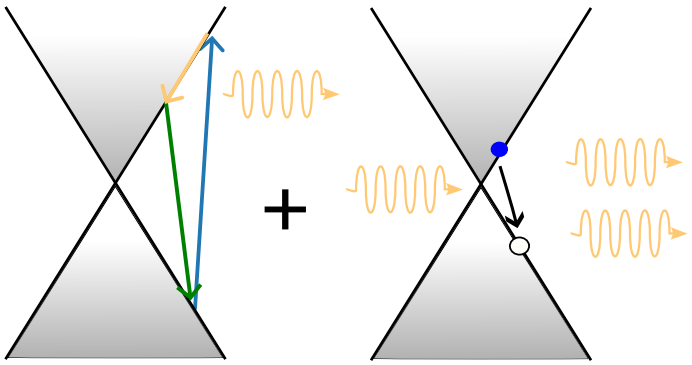

Figure 5.1: Schematics of the plasmon lasing in photoinverted graphene. A particular SPP mode is generated by the DF process (yellow arrow). This mode lives in the SPP reservoir and will stimulate electrons and holes to recombine with emission of a plasmon of the same mode. As a consequence the SPP population grows and the field is amplified.

gold nanodisks were added to the sample. The role of this nanodisks was to scatter the SPP field into photons that could be measured and effectively enhance their presence. Detailed analysis showed a plasmon emission rate of a stunning five orders of magnitude higher than the thermal emission [45].

These results clearly show that we cannot ignore the hot carriers created by the pump. Furthermore, in photoinverted graphene, SPPs may experience gain, through electron-hole recombination [10, 29], thus suggesting that the reason behind the signal observed in Ref. [1] was SPP lasing: a particular SPP mode is selected by the DF process and, due to the non-equilibrium electron-hole population, this mode is amplified, giving rise to a signal several orders of magnitude higher than the predicted by the perturbation theory (see Fig. 5.1).

In this chapter we introduce a model, based on the master equation formalism, to describe this process. In Section 5.2, we explain how the SPP dispersion curve is calculated in non-equilibrium graphene. In Section 5.3, we write the master equation to describe the evolution of the SPP population. Section 5.4 deals with the problem of including DF generation in the master equation. The change in the differential reflectivity, due to the generation of plasmons, is estimated in Section 5.5. Finally, we make some concluding remarks in Section 5.6.

5.2 Non-equilibrium plasmon dispersion relation and gain

Previous theoretical works [29, 36] showed that photoinverted graphene has the right conditions for SPP gain, e.g an increase of their non-equilibrium population. In this Section we explore this effect.

Consider a graphene sheet in a photoinverted state, with electron and hole distributions characterized by the chemical potentials F_e and F_h, respectively, at a temperature T. Interband transitions, with the energies below $\sim (F_e + F_h)$, have low probability of being blocked and, as discussed in Section 2.2, such electron-hole pairs can recombine via plasmon emission. In this regime, the interband

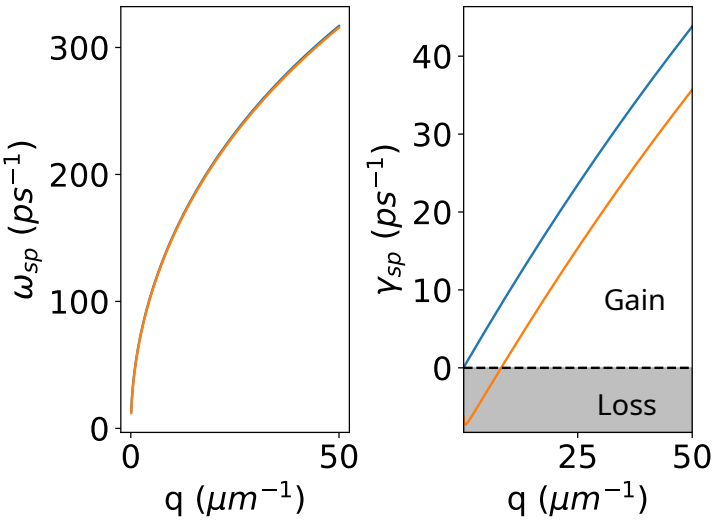

Figure 5.2: Plasmon dispersion, $\omega_{\mathrm{sp}}(q) + i\gamma_{\mathrm{sp}}(q)$, calculated at zero temperature with both intraband and interband conductivities. The parameters of the calculation were $F_e = -F_h = 300$ meV, $\gamma_{\mathrm{inter}} = 0.01$ ps^{-1} to avoid bad numerical behavior, $\varepsilon_1 = 1$ and $\varepsilon_2 = 2.4$ as usual. The blue curve shows the solutions of the Eq. (5.4) for a momentum relaxation rate $\gamma_p = 0.01$ ps^{-1}, while the orange curve shows the dispersion for a much more realistic value of $\gamma_p = 2\pi \times 2.6$ ps^{-1}. The $\gamma_{\mathrm{sp}}(q)$ plot clearly shows that for certain frequencies it is expected plasmonic gain, even for finite γ_p.

conductivity, for a sufficiently low frequency ω, is negative (see Fig. 4.3) and the optical gain is possible. Consequently, the SPP field instead of being damped, is amplified (and off damped).

This idea is easily understood if we consider a particular case of intrinsic photoinverted graphene, $F_e = -F_h > 0$, at zero temperature. In these conditions, expressions (B.26) for the intraband conductivity and (B.33) for the interband conductivity yield the following analytical expressions:

$$\sigma_{\mathrm{intra}}(\omega) = \frac{4\sigma_0}{\pi} \frac{F_e + |F_h|}{\hbar\gamma_p - i\hbar\omega} \tag{5.1}$$

and

$$\begin{aligned}\sigma_{\mathrm{inter}}(\omega) = \sigma_0 \Bigg(1 + \frac{1}{\pi}\arctan\frac{\hbar\omega - 2|F_h|}{\hbar\gamma_{\mathrm{inter}}} + \frac{1}{\pi}\arctan\frac{\hbar\omega - 2F_e}{\hbar\gamma_{\mathrm{inter}}} - \frac{1}{\pi}\arctan\frac{\hbar\omega + 2|F_h|}{\hbar\gamma_{\mathrm{inter}}} - \frac{1}{\pi}\arctan\frac{\hbar\omega + 2F_e}{\hbar\gamma_{\mathrm{inter}}}\Bigg) \\ - \frac{i\sigma_0}{2\pi}\ln\left(\frac{(\hbar\gamma_{\mathrm{inter}})^2 + (2|F_h| + \hbar\omega)^2}{(\hbar\gamma_{\mathrm{inter}})^2 + (2|F_h| - \hbar\omega)^2}\right) - \frac{i\sigma_0}{2\pi}\ln\left(\frac{(\hbar\gamma_{\mathrm{inter}})^2 + (2F_e + \hbar\omega)^2}{(\hbar\gamma_{\mathrm{inter}})^2 + (2F_e - \hbar\omega)^2}\right),\end{aligned} \tag{5.2}$$

respectively. Here γ_p is the momentum relaxation rate introduced in Section 4.2 and γ_{inter} is the interband scattering rate. Notice that the interband conductivity is negative for small ω and γ_{inter}:

$$\lim_{\omega\to 0}\lim_{\gamma_{\mathrm{inter}}\to 0}\sigma_{\mathrm{inter}}(\omega) = -\sigma_0\ . \tag{5.3}$$

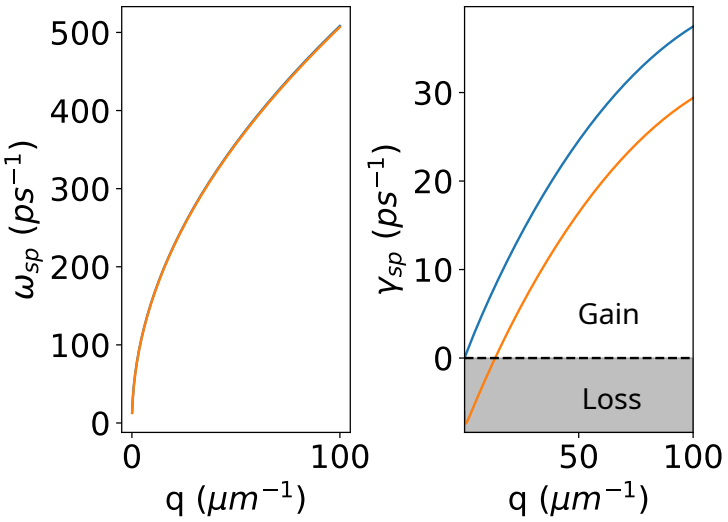

Figure 5.3: Plasmon dispersion, $\omega_{\rm sp}(q) + i\gamma_{\rm sp}(q)$, for the same conditions as in Fig. 5.2, but calculated at finite temperature $T = 2000$ k, also with both intraband and interband conductivities. Even at finite temperatures, plasmon gain is possible.

As before, the plasmon dispersion relation is determined by the poles, $\omega(q)$, of Eq. (2.4):

$$D(\omega, q) = \frac{\varepsilon_1}{\kappa_1} + \frac{\varepsilon_2}{\kappa_2} + \frac{4\pi i}{\omega}\sigma^{(1)}(\omega) = 0 \ . \tag{5.4}$$

However, $\sigma^{(1)}(\omega)$ now is the transient conductivity with both contributions (5.1) and (5.2). For $\gamma_p = \gamma_{\rm inter} = 0$ (no losses) and small ω, in the equilibrium regime, the conductivity is purely imaginary and the solutions of the dispersion equation, $\omega(q)$, are real. However, in photoinverted graphene the real part of the interband conductivity is non-zero for small ω and the solutions to Eq. (5.4) become complex, $\omega_{\rm sp}(q) + i\gamma_{\rm sp}(q)$. For $\mathrm{Re}\sigma_{\rm inter} < 0$, $\gamma_{\rm sp}(q)$ is positive and the SPP field instead of being damped, is amplified with time.

Figure 5.2 shows the plasmon dispersion curve obtained using $\sigma^{(1)}$ modeled with Eqs. (5.1) and (5.2) for different γ_p. Figure 5.3 shows calculated results for temperature $T \neq 0$, obtained using Eqs. (B.28) and (4.57) for the intraband and interband conductivity, respectively. Even at high temperatures, plasmon gain seems possible. These results are in good agreement with what was expected, the plasmon channel of the electronic relaxation is likely in the 100-fs time scale. Figures 5.2 and 5.3 show a damping rate of the order ~ 10 ps^{-1} that corresponds to a time scale of ~ 100 fs.

Using the hot electron model from Section 4.2 we can predict the SPP dispersion for different time delay t. For the same conditions as in Fig. 4.2, we plot the SPP dispersion in Fig. 5.4.

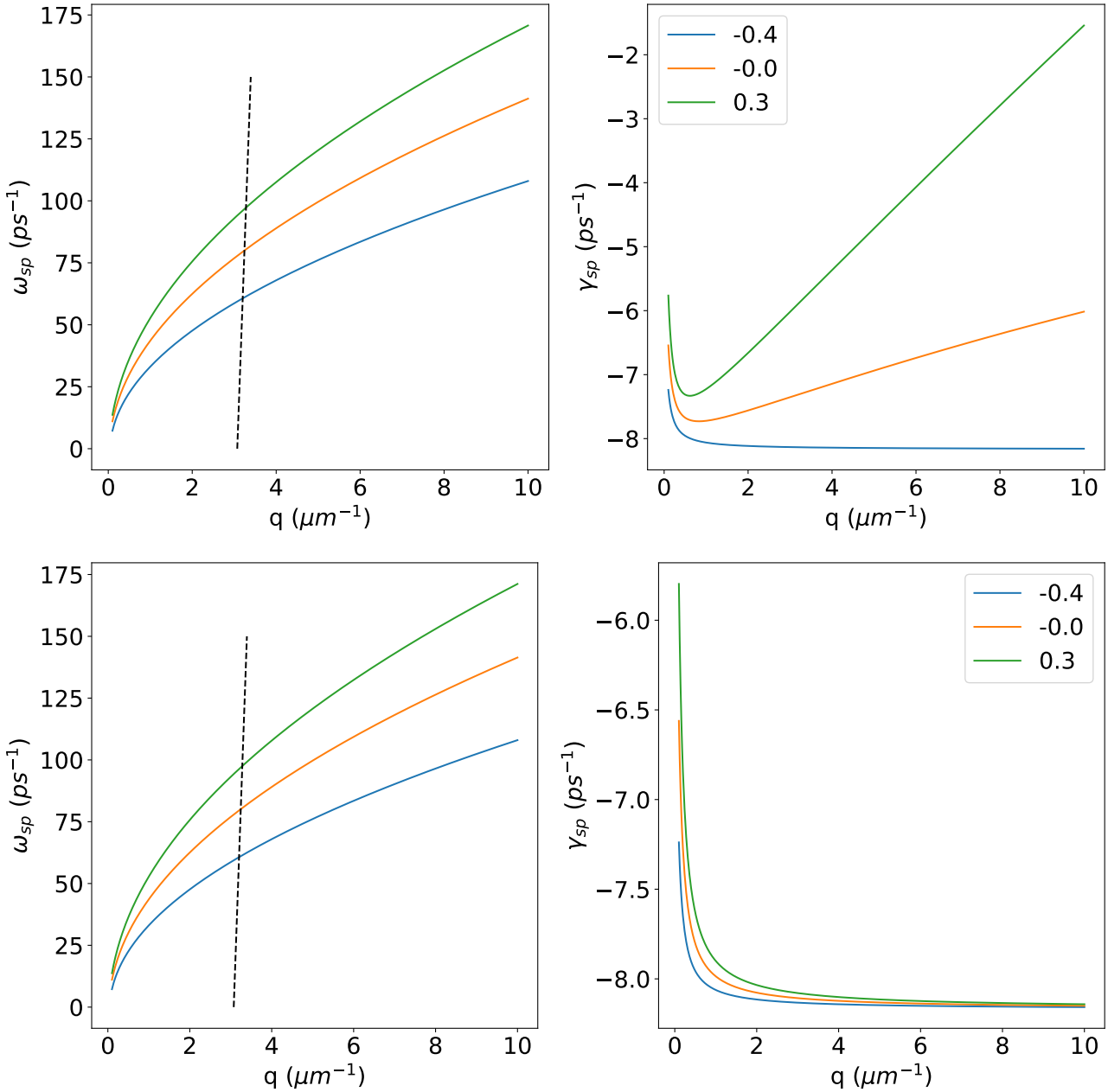

Figure 5.4: Plasmon dispersion, $\omega_{\rm sp}(q)+i\gamma_{\rm sp}(q)$, predicted by the hot electron model, for different time delay t (given in ps on the plot) . Calculation parameters same as in Figs. 4.2 with $\gamma_p = 2\pi \times 2.6$ ps^{-1}. The black dashed line shows the DF scanning as performed by Constant et.al [1]. **(Top)** Calculation of the SPP dispersion with both intraband and interband conductivities taken into account. **(Bottom)** Calculation with the intraband conductivity only.

5.3 Master equation

The question now is, how can the SPP gain coexist with their generation by the DF process? The most straightforward way to incorporate SPP amplification is to treat SPPs as quasiparticles and write a master equation for the SPP population [10], $n_{\mathbf{q}}$, with $n_{\mathbf{q}}$ the population with momentum $\mathbf{q}$. The processes we want to take into account are:

1. plasmon emission via interband recombination and plasmon absorption with creation of an electron-hole pair;

2. generation of plasmons by the DF process;

3. plasmon losses, other than point 1.

We leave out plasmon emission and absorption due to intraband electronic processes, since these are only relevant for plasmons with big momentum q and frequency ω, and we are concerned with low frequency-momentum plasmons. With this in mind, we write the following master equation for the plasmon population $n_{\mathbf{q}}$:

$$\frac{dn_{\mathbf{q}}}{dt} = \left(\frac{dn_{\mathbf{q}}}{dt}\right)_{\text{inter}} + \Gamma_{\text{DF}}(\mathbf{q}) - \gamma_{\text{loss}}(\mathbf{q})\left(n_{\mathbf{q}} - n_{\mathbf{q}}^{\text{eq}}\right) \ . \tag{5.5}$$

The first term in Eq. (5.5) accounts for the interband processes, Γ_{DF} is the SPP rate emission due to the DF interaction between the pump and probe, $\gamma_{\text{loss}}(\mathbf{q})$ is a damping parameter that accounts for losses, and $n_{\mathbf{q}}^{\text{eq}}$ is the Bose-Einstein distribution:

$$n_{\mathbf{q}}^{\text{eq}} = \frac{1}{e^{\hbar\omega_{\mathbf{q}}/k_B T} - 1} \ . \tag{5.6}$$

To determine the interband term we quantify the SPP field (see Appendix G for details) and use the Fermi's Golden rule. Finding $\Gamma_{\text{DF}}(\mathbf{q})$ requires a bit more work, since, as we will see in Section 5.4, the DF emission rate is due to a third order interaction between the pump, probe and SPP fields mediated by the electrons in graphene. Finally, because $\left(\frac{dn_{\mathbf{q}}}{dt}\right)_{\text{inter}}$ accounts for the interband interaction, the SPP dispersion curve is determined by the intraband conductivity only.

5.3.1 Interband interaction

We must know the form of the plasmon-electron interaction to calculate the interband term in Eq. (5.5). In the second quantization formalism the full Hamiltonian (electron+plasmons) is[2]:

$$\hat{H} = \sum_{\mathbf{k},s} \varepsilon_{\mathbf{k},s} c_{\mathbf{k},\text{s}}^{\dagger} c_{\mathbf{k},\text{s}} + \frac{1}{2}\sum_{\mathbf{q}} \hbar\omega_{\mathbf{q}} \left(\hat{a}_{\mathbf{q}}^{\dagger}\hat{a}_{\mathbf{q}} + \hat{a}_{\mathbf{q}}\hat{a}_{\mathbf{q}}^{\dagger}\right) + \hat{H}_{\text{int}} \ , \tag{5.7}$$

[2]See Appendix G for quantization of the SPP field.

with $\hat{H}_{\text{int}}$ representing the interaction between electrons and plasmons. In the Schrödinger representation this term reads:

$$\hat{H}_{\text{int}} = \frac{e}{c} v_F \boldsymbol{\sigma} \cdot \mathbf{A}(t, x, y, z = 0) \ . \tag{5.8}$$

So, in the second quantization form, we have,

$$\begin{aligned}\hat{H}_{\text{int}} = &\frac{e}{c} v_F \sum_{\mathbf{k},\mathbf{q}} \sum_{s,s'} \sqrt{\frac{2\pi c}{L_{\mathbf{q}} \omega_{\mathbf{q}} \mathcal{S}}} \hat{c}^{\dagger}_{\mathbf{k}+\mathbf{q},s'} \hat{c}_{\mathbf{k},s} \hat{a}_{\mathbf{q}} \mathbf{F}_{s',s}(\mathbf{k}+\mathbf{q}, \mathbf{k}) \cdot \mathbf{A}_{\mathbf{q}}(0) e^{-i\omega_{\mathbf{q}} t} \\ &+ \frac{e}{c} v_F \sum_{\mathbf{k},\mathbf{q}} \sum_{s,s'} \sqrt{\frac{2\pi c}{L_{\mathbf{q}} \omega_{\mathbf{q}} \mathcal{S}}} \hat{c}^{\dagger}_{\mathbf{k}-\mathbf{q},s'} \hat{c}_{\mathbf{k},s} \hat{a}^{\dagger}_{\mathbf{q}} \mathbf{F}_{s',s}(\mathbf{k}-\mathbf{q}, \mathbf{k}) \cdot \mathbf{A}^{*}_{\mathbf{q}}(0) e^{i\omega_{\mathbf{q}} t} \ ,\end{aligned} \tag{5.9}$$

where

$$\mathbf{F}_{s',s}(\mathbf{k}+\mathbf{q}, \mathbf{k}) = \left(F^{x}_{s',s}(\mathbf{k}+\mathbf{q}, \mathbf{k}), F^{y}_{s',s}(\mathbf{k}+\mathbf{q}, \mathbf{k}) \right) \tag{5.10}$$

and

$$F^{x}_{s',s}(\mathbf{k}+\mathbf{q}, \mathbf{k}) = \langle \mathbf{k}+\mathbf{q}, s' | e^{i\mathbf{q}\cdot\mathbf{r}} \sigma_x | \mathbf{k}, s \rangle = \frac{s e^{i\theta(\mathbf{k}+\mathbf{q})} + s' e^{-i\theta(\mathbf{k})}}{2} \ , \tag{5.11}$$

$$F^{y}_{s',s}(\mathbf{k}+\mathbf{q}, \mathbf{k}) = \langle \mathbf{k}+\mathbf{q}, s' | e^{i\mathbf{q}\cdot\mathbf{r}} \sigma_y | \mathbf{k}, s \rangle = -i \frac{s e^{i\theta(\mathbf{k}+\mathbf{q})} - s' e^{-i\theta(\mathbf{k})}}{2} \ . \tag{5.12}$$

To determine the transition rate via plasmon emission, we need the probability of decay of an electron in the conduction band to the valence band, with the emission of a plasmon with momentum $\mathbf{q}$. The transition matrix element for this process is:

$$\begin{aligned}M_{-1,1}(\mathbf{k}-\mathbf{q}, \mathbf{k}) &= \langle -1, \mathbf{k}-\mathbf{q} | \langle n_{\mathbf{q}} + 1 | \hat{H}_{\text{int}} | 1, \mathbf{k} \rangle | n_{\mathbf{q}} \rangle \\ &= \frac{e}{c} v_F \sqrt{\frac{2\pi c}{L_{\mathbf{q}} \omega_{\mathbf{q}} \mathcal{S}}} \sqrt{n_{\mathbf{q}} + 1} F^{x}_{-1,1}(\mathbf{k}-\mathbf{q}, \mathbf{k}) \cdot A^{x*}_{\mathbf{q}}(0) e^{i\omega_{\mathbf{q}} t} \ .\end{aligned} \tag{5.13}$$

For the inverse process, with plasmon absorption the transition matrix element is just the hermitian conjugate:

$$M_{1,-1}(\mathbf{k}, \mathbf{k}-\mathbf{q}) = M^{*}_{-1,1}(\mathbf{k}-\mathbf{q}, \mathbf{k}) \ . \tag{5.14}$$

Taking into account all interband transitions, the variation of the plasmon population with a momentum $\mathbf{q}$ is obtained using the Fermi's Golden rule:

$$\begin{aligned}\left(\frac{dn_{\mathbf{q}}}{dt} \right)_{\text{inter}} = &\frac{2\pi}{\hbar} \sum_{\mathbf{k}} |M_{-1,1}(\mathbf{k}-\mathbf{q}, \mathbf{k})|^2 f_c(\varepsilon_{\mathbf{k}}) \left[1 - f_v(\varepsilon_{\mathbf{k}-\mathbf{q}}) \right] \delta\left(\varepsilon_{\mathbf{k}} + \varepsilon_{\mathbf{k}-\mathbf{q}} - \hbar\omega_{\mathbf{q}} \right) (n_{\mathbf{q}} + 1) \\ &- \frac{2\pi}{\hbar} \sum_{\mathbf{k}} |M_{1,-1}(\mathbf{k}, \mathbf{k}-\mathbf{q})|^2 f_v(\varepsilon_{\mathbf{k}-\mathbf{q}}) \left[1 - f_c(\varepsilon_{\mathbf{k}}) \right] \delta\left(\varepsilon_{\mathbf{k}} + \varepsilon_{\mathbf{k}-\mathbf{q}} - \hbar\omega_{\mathbf{q}} \right) n_{\mathbf{q}} \ .\end{aligned} \tag{5.15}$$

Using Eqs. (G.23) to (G.27), the transitions matrix elements are[3]:

$$|M_{-1,1}(\mathbf{k}-\mathbf{q},\mathbf{k})|^2 = |M_{1,-1}(\mathbf{k}-\mathbf{q},\mathbf{k})|^2 = \left(\frac{e}{c}v_F\right)^2 \frac{\pi\hbar c^2}{L_{\mathbf{q}}\omega_{\mathbf{q}}\mathcal{S}}\left[1-\cos\left(\theta(\mathbf{k}-\mathbf{q})+\theta(\mathbf{k})\right)\right]$$

and the interband part of the master equation becomes:

$$\begin{aligned}\left(\frac{dn_{\mathbf{q}}}{dt}\right)_{\text{inter}} &= \frac{2e^2v_F^2}{L_{\mathbf{q}}\omega_{\mathbf{q}}}\int d^2k\left[1-1\cos\left(\theta(\mathbf{k}-\mathbf{q})+\theta(\mathbf{k})\right)\right]f_c(\varepsilon_{\mathbf{k}})\left[1-f_v(\varepsilon_{\mathbf{k}-\mathbf{q}})\right]\delta\left(\varepsilon_{\mathbf{k}}+\varepsilon_{\mathbf{k}-\mathbf{q}}-\hbar\omega_{\mathbf{q}}\right)\\ &+\frac{2e^2v_F^2n_{\mathbf{q}}}{L_{\mathbf{q}}\omega_{\mathbf{q}}}\int d^2k\left[1-1\cos\left(\theta(\mathbf{k}-\mathbf{q})+\theta(\mathbf{k})\right)\right]\left\{f_c(\varepsilon_{\mathbf{k}})-f_v(\varepsilon_{\mathbf{k}-\mathbf{q}})\right\}\delta\left(\varepsilon_{\mathbf{k}}+\varepsilon_{\mathbf{k}-\mathbf{q}}-\hbar\omega_{\mathbf{q}}\right)\ .\end{aligned} \tag{5.16}$$

To solve the integrals, we introduce α as the angle between $\mathbf{k}$ and $\mathbf{q}$ and use the Dirac δ-function to remove the integration over k. The δ-function tells us that the integral is meaningful when energy is conserved,

$$\hbar\omega_{\mathbf{q}}-\varepsilon_{\mathbf{k}}-\varepsilon_{\mathbf{k}-\mathbf{q}}=0 \tag{5.17}$$

and the $\mathbf{k}$ vectors that obey this condition lie in a ellipse (see Section 2.2). Thus, the integral is solved in elliptic coordinates:

$$k_x = ak\cos\alpha+\frac{q}{2}\quad,\quad k_y = bk\sin\alpha\ . \tag{5.18}$$

According to this definition, k is a quantity with the dimensions $[\text{distance}]^{-1}$. The δ-function fixes the radius of the ellipse to:

$$k=\sqrt{\frac{(k_x-q/2)^2}{a^2}+\frac{k_y^2}{b^2}}=k_0\ . \tag{5.19}$$

The volume element is $d^2k = kd\alpha dk$ and the integration over k in Eq. (5.16) yields:

$$\begin{aligned}\left(\frac{dn_{\mathbf{q}}}{dt}\right)_{\text{inter}} &= \frac{2\alpha_f\hbar cv_F^2}{L_{\mathbf{q}}\omega_{\mathbf{q}}}k_0\int_0^{2\pi}d\alpha f_c(\varepsilon_{\mathbf{k}_0})\left[1-f_v(\varepsilon_{\mathbf{k}_0-\mathbf{q}})\right]\frac{1-\cos\left(\theta(\mathbf{k}_0-\mathbf{q})+\theta(\mathbf{k}_0)\right)}{\left|\frac{\partial}{\partial k}\left(\varepsilon_{\mathbf{k}}+\varepsilon_{\mathbf{k}-\mathbf{q}}\right)\right|_{k=k_0}}\\ &+n_{\mathbf{q}}\frac{2\alpha_f\hbar cv_F^2}{L_{\mathbf{q}}\omega_{\mathbf{q}}}k_0\int_0^{2\pi}d\alpha\left\{f_c(\varepsilon_{\mathbf{k}_0})-f_v(\varepsilon_{\mathbf{k}_0-\mathbf{q}})\right\}\frac{1-\cos\left(\theta(\mathbf{k}_0-\mathbf{q})+\theta(\mathbf{k}_0)\right)}{\left|\frac{\partial}{\partial k}\left(\varepsilon_{\mathbf{k}}+\varepsilon_{\mathbf{k}-\mathbf{q}}\right)\right|_{k=k_0}}\ .\end{aligned} \tag{5.20}$$

We introduce the decay rates:

$$\Gamma_1(\mathbf{q}) = \frac{2\alpha_f\hbar cv_F^2}{L_{\mathbf{q}}\omega_{\mathbf{q}}}k_0\int_0^{2\pi}d\alpha f_c(\varepsilon_{\mathbf{k}_0})\left[1-f_v(\varepsilon_{\mathbf{k}_0-\mathbf{q}})\right]\frac{1-\cos\left(\theta(\mathbf{k}_0-\mathbf{q})+\theta(\mathbf{k}_0)\right)}{\left|\frac{\partial}{\partial k}\left(\varepsilon_{\mathbf{k}}+\varepsilon_{\mathbf{k}-\mathbf{q}}\right)\right|_{k=k_0}}\ , \tag{5.21}$$

[3]We fix the reference frame such that $\mathbf{q}$ is parallel to the x-axis.

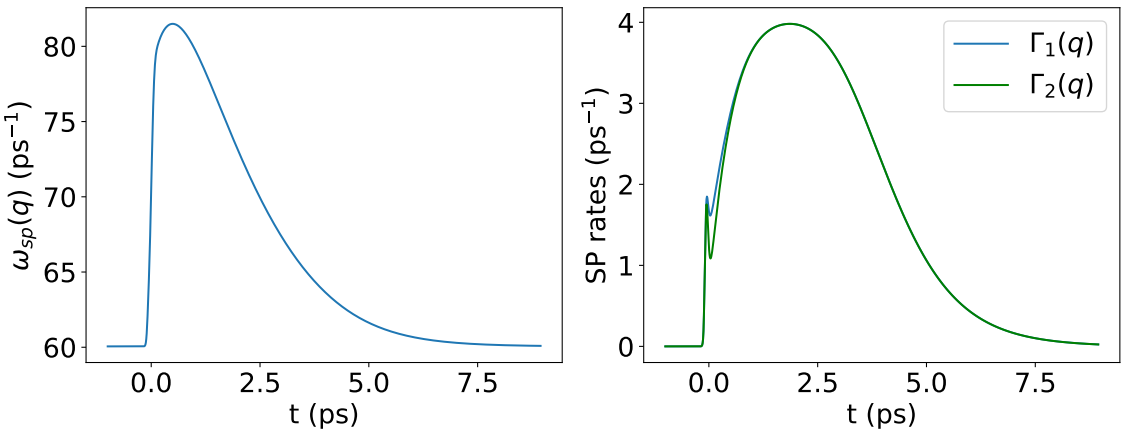

Figure 5.5: **(left)** Evolution of the SPP frequency, $\omega_{\rm sp}(q)$, as a function of the time delay t, for the particular mode $q = q_b - q_a = 3.1\ \mu\text{m}^{-1}$. **(right)** Evolution of the SPP interband recombination rates (5.21) and (5.22), also for $q = q_b - q_a = 3.1\ \mu\text{m}^{-1}$. The dynamical evolution of the hot carriers is described using the hot electron model from Section 4.2. The calculation was performed for the same conditions and parameters as in Fig. 4.2. The SPP frequencies $\omega_{\rm sp}$ are determined by the poles, $\omega_{\rm sp} + i\gamma_{\rm sp}$, of Eq. (5.4), with $\varepsilon_1 = 1$ and $\varepsilon_2 = 2.4$. The conductivity $\sigma^{(1)}(\omega)$ is modeled by the Drude term (B.28) only, with a momentum relaxation rate $\gamma_p = 2\pi \times 2.6\ \text{ps}^{-1}$.

$$\Gamma_2(\mathbf{q}) = \frac{2\alpha_f \hbar c v_F^2}{L_{\mathbf{q}}\omega_{\mathbf{q}}} k_0 \int_0^{2\pi} d\alpha \left\{ f_c(\varepsilon_{\mathbf{k}_0}) - f_v(\varepsilon_{\mathbf{k}_0-\mathbf{q}}) \right\} \frac{1 - \cos\left(\theta(\mathbf{k}_0 - \mathbf{q}) + \theta(\mathbf{k}_0)\right)}{\left| \frac{\partial}{\partial k} \left(\varepsilon_{\mathbf{k}} + \varepsilon_{\mathbf{k}-\mathbf{q}}\right) \right|_{k=k_0}} , \tag{5.22}$$

and write the dynamical Eq. (5.20) for interband processes as:

$$\left(\frac{dn_{\mathbf{q}}}{dt}\right)_{\text{inter}} = \Gamma_1(\mathbf{q}) + \Gamma_2(\mathbf{q}) n_{\mathbf{q}} \ . \tag{5.23}$$

In Fig. 5.5, for fixed DF momentum $q = q_b - q_a = 3.1\ \mu\text{m}^{-1}$, the decay rates (5.21) and (5.22) are plotted as functions of the time delay t between pump and probe. The dynamics of the hot carriers is simulated according to the model in Section 4.2.

5.4 DF-generation of plasmons

Two processes schematically shown in Fig. 3.1 (left), are analogous to the well-known phenomenon of inelastic (Raman) scattering of light in solids [46]. Typically, an incident photon loses a part of its energy by emitting an optical phonon, while here we have emission of a surface plasmon. Also, in our case, the interaction between the incident (pump) photon and the plasmon is stimulated by the presence of the probe beam (if the resonance conditions are satisfied), which does not take place in typical Raman scattering experiments.

The third-order processes, so far designated as Channels I and II, can be represented by Feynman diagrams shown in Fig. 5.6 [47]. In these, a photon $(\omega_b, \mathbf{k}_b)$ with p-polarization is absorbed by

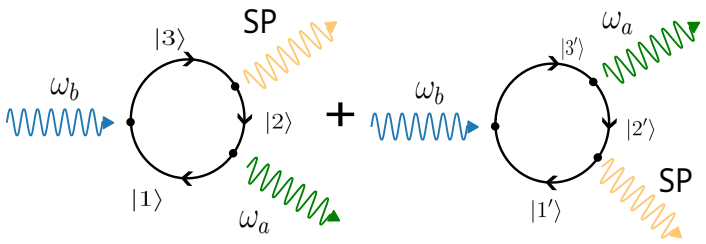

Figure 5.6: Two Feynman diagrams for absorption of a photon b and creation of a photon a and a SPP in graphene. The process is mediated by the electrons. The left diagram corresponds to Channel I, while the right is Channel II. The states $|n\rangle$ are the same as in Fig. 3.1. There are four more diagrams that represent the remaining terms in Eq. (5.45).

graphene and a photon $(\omega_a, \mathbf{k}_a)$, also with p-polarization, is created. The process is accompanied by the creation of a SPP $(\omega_\mathbf{q}, \mathbf{q})$, such that the in-plane momentum and energy are conserved. The inverse can also occur: a SPP and a photon a are absorbed and a photon b is emitted. These interactions are described by an effective Hamiltonian [47]:

$$\hat{H}_{\text{int}} = \sum_{\mathbf{q}} \sum_{\mathbf{k}_1} \sum_{\mathbf{k}_2} M\left(\mathbf{q}, \mathbf{q}_1, \mathbf{q}_2\right) \left(\hat{a}^\dagger_\mathbf{q} + \hat{a}_{-\mathbf{q}}\right) \hat{b}^\dagger_{\mathbf{k}_1} \hat{b}_{\mathbf{k}_2} \ , \tag{5.24}$$

where $\hat{b}_{\mathbf{k}_j}$ are the destruction operators for the EM radiation field $(\omega_j, \mathbf{k}_j)$ and $\hat{a}_\mathbf{q}$ is the destruction operator for the plasmon $(\omega_\mathbf{q}, \mathbf{q})$. As usual, those with dagger are the corresponding creation operators. $\mathbf{q}_j$ is the in-plane wavevector of $\mathbf{k}_j$ and $M\left(\mathbf{q}, \mathbf{q}_1, \mathbf{q}_2\right)$ is the interaction matrix element. The initial and final states of the system, that belong to the Fock space for photons + SPP + graphene, are denoted by $|I\rangle$ and $|F\rangle$:

$$|I\rangle = |n_b\rangle|n_a\rangle|n_\mathbf{q}\rangle|i\rangle \quad , \quad |F\rangle = |n_b \mp 1\rangle|n_a \pm 1\rangle|n_\mathbf{q} \pm 1\rangle|i\rangle \ , \tag{5.25}$$

where $|n_j\rangle$ are the photon states, with n_j denoting the occupation number for a photon $(\omega_j, \mathbf{k}_j)$, $|n_\mathbf{q}\rangle$ are the SPP states and $|i\rangle$ is an electronic state of graphene. The initial and final electronic states should be the same. The minus or plus sign depends on whether we have plasmon emission or absorption.

The probability per unit time (the transition rate) for scattering from the initial state to the final state is given by the Fermi's Golden Rule:

$$\Gamma\left(I \to F\right) = \frac{2\pi}{\hbar} \left|\langle F|\hat{H}_{\text{int}}|I\rangle\right|^2 \delta\left(E_F - E_I\right) \ , \tag{5.26}$$

where E_F and E_I are the energies of the initial and final states:

$$E_F - E_i = \mp\left(\hbar\omega_b - \hbar\omega_a - \hbar\omega_\mathbf{q}\right) \ . \tag{5.27}$$

The matrix element in (5.26) for the process in Fig. 5.6 is:

$$\langle F|\hat{H}_{\rm int}|I\rangle = \sqrt{n_b}\sqrt{n_a+1}\sqrt{n_{\mathbf{q}}+1}M\left(\mathbf{q},\mathbf{q}_a,\mathbf{q}_b\right) \tag{5.28}$$

and the emission rate of plasmons is:

$$\Gamma_{\rm sp} = \frac{2\pi}{\hbar}\left(n_{\mathbf{q}}+1\right)\left(n_a+1\right)n_b\left|M\left(\mathbf{q},\mathbf{q}_a,\mathbf{q}_b\right)\right|^2\delta\left(\hbar\omega_b-\hbar\omega_a-\hbar\omega_{\mathbf{q}}\right)\ , \tag{5.29}$$

where $M\left(\mathbf{q},\mathbf{q}_a,\mathbf{q}_b\right)$ will be specified below.

The photon modes in Eq. (5.29) are not specified. At the surface, for a particular frequency, three type of modes are present, corresponding to incident, reflected and transmitted photons. These modes have equal in-plane momentum $\mathbf{q}_j$ but the z-component of the wavevector and the polarization vector are different. One could say that the optical field at the interface $z=0$ is in a superposition of incident, reflected and transmitted states. The interaction, which causes reflection/refraction of photons on the surface and leads to the three kind of photons, is not included in the Hamiltonian (5.24) and diagrams of Fig. 5.6. We include this interaction phenomenologically. For example, in the emission rate of plasmons (5.29) both reflected and transmitted photons contribute. In fact, the full field at the interface contributes and stimulates the emission of plasmons. Thus, ignoring absorption in graphene, the photon occupation numbers n_a and n_b in Eq. (5.29) should be equal to the number of incident photons. For the emission rate of photons a the situation is different. Here, one has to distinguish between emission in reflection or emission in transmission, since the emission in a particular direction will be stimulated differently by the presence of the beam. The same will be true for the inverse process, where a plasmon and a photon a are absorbed and a photon b is emitted.

5.4.1 Electron-photon and electron-plasmon interaction

The SPP generation is mediated by electrons that are hidden in the matrix element $M\left(\mathbf{q},\mathbf{q}_a,\mathbf{q}_b\right)$ in Hamiltonian (5.24). The full Hamiltonian describes graphene's electrons, the radiation fields a and b, and the plasmon field:

$$\hat{H} = \hat{H}_0 + \hat{H}_{\text{e-ph}} + \hat{H}_{e-\rm pl}\ , \tag{5.30}$$

where $\hat{H}_0$ is graphene's + fields's + plasmons's bare Hamiltonian that is diagonal, in the appropriate basis. $\hat{H}_{e-\rm pl}$ is the interaction between electron and plasmon as determined in Eq. (5.9) and $\hat{H}_{\text{e-ph}}$ is the electron-photon interaction. We write this term as in Section (3.3):

$$H_{\text{e-ph}} = \frac{e}{c}v_F\sum_j \sigma_x A_j^x(t,\mathbf{x},z=0)\ , \tag{5.31}$$

so in the second quantization[4]:

$$\hat{H}_{\text{e-ph}} = \frac{e}{c} v_F \sum_j \sum_{\mathbf{k}_j} \sum_{s',s} \sum_{\mathbf{k}} A^x_{\mathbf{k}_j} c^\dagger_{s',\mathbf{k}+\mathbf{q}_j} c_{s,\mathbf{k}} \hat{b}_{\mathbf{k}_j} F^x_{s',s}(\mathbf{k}+\mathbf{q}_j, \mathbf{k}) e^{-i\omega_{\mathbf{k}_j} t} + \frac{e}{c} v_F \sum_j \sum_{\mathbf{k}_j} \sum_{s',s} \sum_{\mathbf{k}} A^x_{\mathbf{k}_j} c^\dagger_{s',\mathbf{k}-\mathbf{q}_j} c_{s,\mathbf{k}} \hat{b}_{\mathbf{k}_j} F^x_{s',s}(\mathbf{k}-\mathbf{q}_j, \mathbf{k}) e^{i\omega_{\mathbf{k}_j} t} \ , \tag{5.32}$$

where:

$$A^x_{\mathbf{k}_j} = \sqrt{\frac{2\pi\hbar c^2}{\eta^2 V \omega_{\mathbf{k}_j}}} \mathbf{e}_{\mathbf{k}_j} \cdot \mathbf{e}_x \ . \tag{5.33}$$

Here, η is the index of refraction. For the incident and reflected fields $\eta = 1$, while for the transmitted field η is the index of refraction of the substrate. For future calculations it is better to distinguish between a and b fields, so we rewrite this term as:

$$\hat{H}_{e-\text{ph}} = \hat{V}_a + \hat{V}_b \ , \tag{5.34}$$

with:

$$\hat{V}_j = \frac{e}{c} v_F \sum_{\mathbf{k}_j} \sum_{s',s} \sum_{\mathbf{k}} A^x_{\mathbf{k}_j} c^\dagger_{s',\mathbf{k}+\mathbf{q}_j} c_{s,\mathbf{k}} \hat{b}_{\mathbf{k}_j} F^x_{s',s}(\mathbf{k}+\mathbf{q}_j, \mathbf{k}) e^{-i\omega_{\mathbf{k}_j} t} + \frac{e}{c} v_F \sum_{\mathbf{k}_j} \sum_{s',s} \sum_{\mathbf{k}} A^x_{\mathbf{k}_j} c^\dagger_{s',\mathbf{k}-\mathbf{q}_j} c_{s,\mathbf{k}} \hat{b}_{\mathbf{k}_j} F^x_{s',s}(\mathbf{k}-\mathbf{q}_j, \mathbf{k}) e^{i\omega_{\mathbf{k}_j} t} \ . \tag{5.35}$$

The sum over $\mathbf{k}_j$ runs over incident, reflected and transmitted fields.

The process of interest involves the annihilation of a photon, the creation of another photon and the creation of a plasmon. This is a third-order process in which $\hat{H}_{e-\text{ph}}$ acts twice and $\hat{H}_{\text{e-pl}}$ acts once. The Hamiltonian needs to be transformed into a form that contains an effective photon–plasmon interaction [47]. As given above, the Hamiltonian is written in terms of a basis set that spans the Hilbert space of the system (electrons, plasmons, and photons), that diagonalizes $\hat{H}_0$. The basis consists of states:

$$|m\rangle = |n_b\rangle |n_a\rangle |n_{\mathbf{q}}\rangle |..., N_{\mathbf{k},s}, ...\rangle \ , \tag{5.36}$$

where $N_{\mathbf{k},s}$ is the occupation number for the electron state $|\mathbf{k}, s\rangle$. We can change to a new basis set of states $|\tilde{m}\rangle = U|m\rangle$ via unitary transformation U. In this new basis, the Hamiltonian matrix elements are:

$$\langle \tilde{n}|\hat{H}|\tilde{m}\rangle = \langle n|\tilde{H}|m\rangle \ , \tag{5.37}$$

where $\tilde{H} = U^\dagger \hat{H} U$. Hence, consider the canonical transformation $U = e^{-S}$ where S is an operator such that $S^\dagger = -S$. $\tilde{H}$ has the same eigenvalues as $\hat{H}$ and its eigenstates are obtained by the

[4]See Appendix (G.1) for quantization of the optical field.

operator e^S acting on the corresponding eigenstates of $\hat{H}$. Expanding $e^{\pm S}$, $\tilde{H}$ reads:

$$\begin{aligned}\tilde{H} = \hat{H}_0 + \hat{H}_{\text{int}} + \left[S, \hat{H}_0\right] + \left[S, \hat{H}_{\text{int}}\right] + \frac{1}{2!}\left[S, \left[S, \hat{H}_0\right]\right] + \frac{1}{2!}\left[S, \left[S, \hat{H}_{\text{int}}\right]\right] \\ + \frac{1}{3!}\left[S, \left[S, \left[S, \hat{H}_0\right]\right]\right] + \frac{1}{3!}\left[S, \left[S, \left[S, \hat{H}_{\text{int}}\right]\right]\right] + ... \ ,\end{aligned} \tag{5.38}$$

where $\hat{H}_{\text{int}} = \hat{V}_a + \hat{V}_b + \hat{H}_{e-\text{pl}}$. The operator S is chosen such that:

$$\left[S, \hat{H}_0\right] = -\hat{H}_{\text{int}} \ . \tag{5.39}$$

This choice simplifies Eq. (5.38) to:

$$\begin{aligned}\tilde{H} &= \hat{H}_0 + \frac{1}{2}\left[S, \hat{H}_{\text{int}}\right] + \frac{1}{3}\left[S, \left[S, \hat{H}_{\text{int}}\right]\right] + ... \\ &= \hat{H}_0 + \hat{H}_2 + \hat{H}_3 + ...\end{aligned} \tag{5.40}$$

Consider two eigenstates $|I\rangle$ and $|F\rangle$ of $\hat{H}_0$. The choice given by Eq. (5.39) establishes:

$$\langle F| \left[S, \hat{H}_0\right] |I\rangle = -\langle F|\hat{H}_{\text{int}}|I\rangle \equiv \langle F|S|I\rangle = \frac{\langle F|\hat{H}_{\text{int}}|I\rangle}{E_F - E_I} \ . \tag{5.41}$$

This shows that S is proportional to $\hat{H}_{\text{int}}$. Since our interest is in third-order interaction, we consider the third term $\hat{H}_3$ in Eq. (5.40):

$$\hat{H}_3 = \frac{1}{3}\left[S, \left[S, \hat{H}_{\text{int}}\right]\right] = \frac{1}{3}\left(S^2\hat{H}_{\text{int}} - 2S\hat{H}_{\text{int}}S + \hat{H}_{\text{int}}S^2\right) \ , \tag{5.42}$$

that using identity (5.41) gives the transition element M_{FI}:

$$\begin{aligned}M_{FI} &= \frac{1}{3}\langle F|\hat{H}_3|I\rangle \\ &= \frac{1}{3}\sum_{m,n}\frac{\langle F|\hat{H}_{\text{int}}|m\rangle\langle m|\hat{H}_{\text{int}}|n\rangle\langle n|\hat{H}_{\text{int}}|I\rangle}{(E_F - E_m)(E_n - E_I)(E_m - E_n)}\left\{3E_n - 3E_m + E_F - E_I\right\} \ .\end{aligned} \tag{5.43}$$

In the Fermi's golden rule, energy is conserved, so the initial and final states have the same energy, $E_F = E_I$, and we obtain:

$$M_{FI} = \sum_{m,n}\frac{\langle F|\hat{H}_{\text{int}}|m\rangle\langle m|\hat{H}_{\text{int}}|n\rangle\langle n|\hat{H}_{\text{int}}|I\rangle}{(E_F - E_m)(E_n - E_I)} \ . \tag{5.44}$$

We now substitute the expression for $\hat{H}_{\text{int}}$ while keeping only the terms that correspond to ph $\rightarrow$ pl

→ ph processes with different photons:

$$M_{FI} = \sum_{m,n} \frac{\langle F|\hat{V}_a|m\rangle\langle m|\hat{V}_b|n\rangle\langle n|\hat{H}_{e-\mathrm{pl}}|I\rangle}{(E_F - E_m)(E_n - E_I)} + \sum_{m,n} \frac{\langle F|\hat{V}_a|m\rangle\langle m|\hat{H}_{e-\mathrm{pl}}|n\rangle\langle n|\hat{V}_b|I\rangle}{(E_F - E_m)(E_n - E_I)}$$
$$+ \sum_{m,n} \frac{\langle F|\hat{V}_b|m\rangle\langle m|\hat{V}_a|n\rangle\langle n|\hat{H}_{e-\mathrm{pl}}|I\rangle}{(E_F - E_m)(E_n - E_I)} + \sum_{m,n} \frac{\langle F|\hat{V}_b|m\rangle\langle m|\hat{H}_{e-\mathrm{pl}}|n\rangle\langle n|\hat{V}_a|I\rangle}{(E_F - E_m)(E_n - E_I)}$$
$$+ \sum_{m,n} \frac{\langle F|\hat{H}_{e-\mathrm{pl}}|m\rangle\langle m|\hat{V}_a|n\rangle\langle n|\hat{V}_b|I\rangle}{(E_F - E_m)(E_n - E_I)} + \sum_{m,n} \frac{\langle F|\hat{H}_{e-\mathrm{pl}}|m\rangle\langle m|\hat{V}_b|n\rangle\langle n|\hat{V}_a|I\rangle}{(E_F - E_m)(E_n - E_I)} \ . \tag{5.45}$$

We can look at the terms in Eq. (5.45) as diagrams of the form shown in Fig. 5.6 and use Feynman rules to calculate the matrix element[5]. The rules are:

1. With each internal fermion line, associate a wavevector $\mathbf{k}$;

2. Conserve wavevector at each vertex;

3. Assign at each vertex the respective interaction matrix element:

   (a) plasmon vertex

   $$\frac{e}{c} v_F A^{x*}_{\mathbf{q}}(0) \sqrt{n_{\mathbf{q}} + 1} \sqrt{\frac{2\pi c}{L_{\mathbf{q}} \omega_{\mathbf{q}} \mathcal{S}}} \ , \tag{5.46}$$

   for plasmon emission and

   $$\frac{e}{c} v_F A^{x}_{\mathbf{q}}(0) \sqrt{n_{\mathbf{q}}} \sqrt{\frac{2\pi c}{L_{\mathbf{q}} \omega_{\mathbf{q}} \mathcal{S}}} \ , \tag{5.47}$$

   for plasmon absorption;

   (b) photon vertex

   $$\frac{e}{c} v_F \sqrt{n_j + 1} \sum_{\mathbf{k}_j} \sum_{\mathbf{k}} \sum_{s,s'} A^{x*}_{\mathbf{k}_j} F^{x}_{s',s}(\mathbf{k} - \mathbf{q}_j, \mathbf{k}) \ , \tag{5.48}$$

   for photon emission and

   $$\frac{e}{c} v_F \sqrt{n_j} \sum_{\mathbf{k}_j} \sum_{\mathbf{k}} \sum_{s,s'} A^{x}_{\mathbf{k}_j} F^{x}_{s',s}(\mathbf{k} + \mathbf{q}_j, \mathbf{k}) \ , \tag{5.49}$$

   for photon absorption;

4. Multiply by the factor $(-1)^{F+n}$, where F is the number of closed fermion loops and n the number of vertices[6];

5. To each vertex assign the respective fermion occupation number;

[5] Only the first two are shown, the others are obtained by permutations of the vertices.

[6] This can be seen explicitly if we say that the initial state is:

$$|..., N_1, ..., N_{2'}, ..., N_2, ..., N_3\rangle = (-1)^p |N_1, N_{2'}, N_2, N_3, ...\rangle \tag{5.50}$$

6. Choose an initial state. Assign the propagator to the first fermion line:

$$\frac{1}{E_n - E_I} \ , \tag{5.55}$$

where E_n is the energy of the intermediate state and E_I the energy of the initial state;

7. Choose an initial state. Assign the propagator to the second fermion line:

$$\frac{1}{E_F - E_m} \ , \tag{5.56}$$

where E_m is the energy of the intermediate state and E_F is the energy of the final state.

5.4.2 Plasmon emission/absorption

In a non-equilibrium situation, we have electrons in the conduction band and holes in the valence band, so the initial state for the process can be any state filled with an electron. For example, in the diagram in Fig. 5.6 we could have:

$$1 \to 3 \to 2 \to 1 \quad \text{or} \quad 2 \to 1 \to 3 \to 2 \quad \text{or} \quad 3 \to 1 \to 2 \to 3 \ . \tag{5.57}$$

All these permutations and different channels are encoded in the sums in Eq. (5.45).

Consider Channel I from Fig. 5.6, with plasmon emission by the electronic transition in the conduction band. This process is composed of interactions with permutation:

$$\xrightarrow{1} b(\text{absorption}) \xrightarrow{3} \text{pl}(\text{emission}) \xrightarrow{2} a(\text{emission}) \xrightarrow{1} \ . \tag{5.58}$$

We discard terms that do not respect this permutation. The initial electronic state is:

$$|i\rangle = |N_1, N_{2'}, N_2, N_3, ...\rangle \ . \tag{5.59}$$

As discussed above, the photon a can be emitted in reflection or in transmission. For SPP emission, both cases contribute, so one should consider the total field. If absorption by graphene is ignored, the photon modes relevant for the emission of SPPs are the incident modes. Using the Feynman

Thus, the matrix elements introduce for example:

$$\langle 3|\hat{V}_b|I,1\rangle \to (-1)^{2p}\langle N_1-1, N_{2'}, N_2, N_3+1|c_3^\dagger c_1|N_1, N_{2'}, N_2, N_3\rangle = (-1)^{2p}\,(1-N_3)\,N_1\,(-1)^{N_1-1+N_{2'}+N_2} \tag{5.51}$$

$$\langle 2|\hat{H}_{e-\text{pl}}|3\rangle \to (-1)^{2p}\,\langle N_1{-}1, N_{2'}, N_2{+}2, N_3|c_2^\dagger c_3|N_1{-}1, N_{2'}, N_2, N_3{+}1\rangle = (-1)^{2p}\,(1-N_2)\,(-1)^{N_1-1+N_{2'}+N_2}\,(-1)^{N_1-1+N_{2'}} \tag{5.52}$$

$$\langle F,1|\hat{V}_a|2\rangle \to (-1)^{2p}\,\langle N_1, N_{2'}, N_2, N_3|c_1^\dagger c_2|N_1-1, N_{2'}, N_2+2, N_3\rangle = (-1)^{2p}\,(-1)^{N_1-1+N_{2'}} \tag{5.53}$$

so when multiplied the sign is positive:

$$\langle F,1|\hat{V}_a|2\rangle\langle 2|\hat{H}_{e-\text{pl}}|3\rangle\langle 3|\hat{V}_b|I,1\rangle \to (1-N_2)\,(1-N_3)\,N_1 \tag{5.54}$$

rules, the contributions from Channel I to the matrix element M_{FI} are:

$$\begin{aligned} C_1 = & \left(\frac{e}{c}v_F\right)^3 A^x_{\mathbf{k}_b} A^{x*}_{\mathbf{q}}(0) A^{x*}_{\mathbf{k}_a} \sqrt{n_{\mathbf{k}_b}}\sqrt{n_{\mathbf{q}}+1}\sqrt{n_{\mathbf{k}_a}+1}\sqrt{\frac{2\pi c}{L_{\mathbf{q}}\omega_{\mathbf{q}}\mathcal{S}}}\delta_{\mathbf{q},\mathbf{q}_b-\mathbf{q}_a} \\ & \times \sum_{\mathbf{k}_3}\sum_{\mathbf{k}_2} \delta_{\mathbf{k}_3,\mathbf{k}_1+\mathbf{q}_b}\delta_{\mathbf{k}_1+\mathbf{q}_a,\mathbf{k}_2} F_{-1,1}\left(\mathbf{k}_1,\mathbf{k}_2\right) F_{1,1}\left(\mathbf{k}_2,\mathbf{k}_3\right) F_{1,-1}\left(\mathbf{k}_3,\mathbf{k}_1\right) \\ & \times \left(\frac{N_1\left(1-N_3\right)\left(1-N_2\right)}{\left(\hbar\omega_a-\varepsilon_{\mathbf{k}_1}-\varepsilon_{\mathbf{k}_2}\right)\left(\varepsilon_{\mathbf{k}_3}+\varepsilon_{\mathbf{k}_1}-\hbar\omega_b\right)} + \frac{N_3\left(1-N_2\right)\left(1-N_1\right)}{\left(\varepsilon_{\mathbf{k}_3}+\varepsilon_{\mathbf{k}_1}-\hbar\omega_b\right)\left(\hbar\omega_{\mathbf{q}}+\varepsilon_{\mathbf{k}_2}-\varepsilon_{\mathbf{k}_3}\right)} \right. \\ & \left. + \frac{N_2\left(1-N_1\right)\left(1-N_3\right)}{\left(\hbar\omega_{\mathbf{q}}+\varepsilon_{\mathbf{k}_2}-\varepsilon_{\mathbf{k}_3}\right)\left(\hbar\omega_a-\varepsilon_{\mathbf{k}_1}-\varepsilon_{\mathbf{k}_2}\right)} \right) . \end{aligned} \tag{5.60}$$

The sums over $\mathbf{k}_j$ are dropped because only the incident fields contribute to generation of SPPs. For Channel II, the process is of the form:

$$\xrightarrow{1} b(\text{absorption}) \xrightarrow{3} a(\text{emission}) \xrightarrow{2'} \text{pl (emission)} \xrightarrow{1} \ , \tag{5.61}$$

so the contribution from this channel is:

$$\begin{aligned} C_2 = & \left(\frac{e}{c}v_F\right)^3 A^x_{\mathbf{k}_b} A^{x*}_{\mathbf{q}}(0) A^{x*}_{\mathbf{k}_a} \sqrt{n_{\mathbf{k}_b}}\sqrt{n_{\mathbf{q}}+1}\sqrt{n_{\mathbf{k}_a}+1}\sqrt{\frac{2\pi c}{L_{\mathbf{q}}\omega_{\mathbf{q}}\mathcal{S}}}\delta_{\mathbf{q},\mathbf{q}_b-\mathbf{q}_a} \\ & \times \sum_{\mathbf{k}_{2'}}\sum_{\mathbf{k}_{1'}} \delta_{\mathbf{k}_3-\mathbf{q}_b,\mathbf{k}_1}\delta_{\mathbf{k}_{2'},\mathbf{k}_3-\mathbf{q}_a} F_{-1,-1}\left(\mathbf{k}_1,\mathbf{k}_{2'}\right) F_{-1,1}\left(\mathbf{k}_{2'},\mathbf{k}_3\right) F_{1,-1}\left(\mathbf{k}_3,\mathbf{k}_1\right) \\ & \times \left(\frac{N_1\left(1-N_3\right)\left(1-N_{2'}\right)}{\left(\hbar\omega_{\mathbf{q}}+\varepsilon_{\mathbf{k}'_2}-\varepsilon_{\mathbf{k}_1}\right)\left(\varepsilon_{\mathbf{k}_3}+\varepsilon_{\mathbf{k}_1}-\hbar\omega_b\right)} + \frac{N_3\left(1-N_{2'}\right)\left(1-N_1\right)}{\left(\varepsilon_{\mathbf{k}_3}+\varepsilon_{\mathbf{k}_1}-\hbar\omega_b\right)\left(\hbar\omega_a-\varepsilon_{\mathbf{k}'_2}-\varepsilon_{\mathbf{k}_3}\right)} \right. \\ & \left. + \frac{N_{2'}\left(1-N_1\right)\left(1-N_3\right)}{\left(\hbar\omega_a-\varepsilon_{\mathbf{k}'_2}-\varepsilon_{\mathbf{k}_3}\right)\left(\hbar\omega_{\mathbf{q}}+\varepsilon_{\mathbf{k}_{2'}}-\varepsilon_{\mathbf{k}_1}\right)} \right) . \end{aligned} \tag{5.62}$$

Finally, we average over quasi-equilibrium electrons to yield the quasi-FD functions. For example:

$$N_1\left(1-N_3\right)\left(1-N_2\right) \rightarrow f_v\left(\mathbf{k}_1\right)\left(1-f_c\left(\mathbf{k}_3\right)\right)\left(1-f_c\left(\mathbf{k}_2\right)\right) \ , \tag{5.63}$$

The elements $A^x_{\mathbf{k}_j}$ in Eqs. (5.60) and (5.62) are given in Eq. (5.33). As explained in the Appendix (G.1), the normalization factor:

$$\left(\frac{2\pi\hbar c^2}{\omega_j \eta^2 V}\right)^{1/2} \tag{5.64}$$

corresponds to one photon in a volume V. If we have a beam of cross section $\mathcal{S}$ and the laser is placed at a distance R from the sample, then V is the volume of the beam:

$$V = \mathcal{S} \times R \ . \tag{5.65}$$

If the laser power is P and it generates photons with wavevector $\mathbf{k} \approx \mathbf{k}_j$, the number of photons in this volume is:

$$n_{\mathbf{k}_j} = \frac{P}{\hbar\omega_{\mathbf{k}_j}}\Delta t \ , \tag{5.66}$$

where:

$$\Delta t = \frac{R}{c}n \tag{5.67}$$

is the time that it takes a photon to reach the surface where it is removed from the beam (either reflected or absorbed). Using expressions (G.35) and (G.37), for the electric and magnetic fields, the space average of the Poynting vector operator,

$$\hat{\mathbf{P}}\left(\mathbf{r},t\right) = \frac{c}{4\pi}\left(\hat{\mathbf{E}}\times\hat{\mathbf{H}}\right) \ , \tag{5.68}$$

is:

$$\hat{\mathbf{P}} = \frac{c}{4\pi}\sum_{\mathbf{k}}\left(\frac{2\pi\hbar\omega_{\mathbf{k}}}{V\eta}\right)\left\{\hat{b}^{\dagger}_{\mathbf{k}}\hat{b}_{\mathbf{k}} + \hat{b}^{\dagger}_{\mathbf{k}}\hat{b}_{\mathbf{k}}\right\}\hat{\mathbf{k}} \ .$$

The expectation value for the state $|n_{\mathbf{k}_j}\rangle$ is:

$$\left\langle\hat{\mathbf{P}}\right\rangle = \frac{\hbar c\omega_j}{2V\eta}\left\{2n_{\mathbf{k}_j}+1\right\}\hat{\mathbf{k}}_j \ . \tag{5.69}$$

As $n_{\mathbf{k}_j} \gg 1$:

$$\left\langle\hat{\mathbf{P}}\right\rangle \approx \frac{\hbar c\omega_j}{V\eta}n_{\mathbf{k}_j}\hat{\mathbf{k}}_j = I_j\hat{\mathbf{k}}_j \ . \tag{5.70}$$

Here I_j is the intensity:

$$I_j = \frac{\hbar c\omega_j}{V\eta}n_{\mathbf{k}_j} \ . \tag{5.71}$$

Therefore, the final expression for the matrix element M_{FI} in the case of emission is:

$$\begin{aligned}
M^{(+)}_{FI} &= C_1 + C_2 \\
&= \sqrt{\frac{2\pi\hbar c^2}{V\omega_b}}\sqrt{\frac{2\pi\hbar c^2}{V\omega_a}}\cos\alpha_b\cos\alpha_a\sqrt{n_{\mathbf{k}_b}}\sqrt{n_{\mathbf{q}}+1}\sqrt{n_{\mathbf{k}_a}+1}\sqrt{\frac{\hbar c}{\mathcal{S}}}\delta_{\mathbf{q},\mathbf{q}_b-\mathbf{q}_a}M_{\mathbf{k}} \\
&\approx \frac{2\pi c}{\eta\omega_b\omega_a}\sqrt{\frac{\hbar c\omega_b n_{\mathbf{k}_b}}{V}}\sqrt{\frac{\hbar c\omega_a n_{\mathbf{k}_a}}{V}}\sqrt{n_{\mathbf{q}}+1}\cos\alpha_b\cos\alpha_a\sqrt{\frac{\hbar c}{\mathcal{S}}}\delta_{\mathbf{q},\mathbf{q}_b-\mathbf{q}_a}M_{\mathbf{k}} \\
&= \frac{2\pi c}{\omega_b\omega_a}\sqrt{I_bI_a}\sqrt{n_{\mathbf{q}}+1}\cos\alpha_b\cos\alpha_a\sqrt{\frac{\hbar c}{\mathcal{S}}}\delta_{\mathbf{q},\mathbf{q}_b-\mathbf{q}_a}M_{\mathbf{k}} \ ,
\end{aligned} \tag{5.72}$$

where α_j is the angle of incidence of field j, I_a and I_b are the intensities of the incident optical fields

a and b and:

$$
\begin{aligned}
M_{\mathbf{k}} = \left(\frac{e}{c}v_F\right)^3 \sqrt{\frac{2\pi c}{L_{\mathbf{q}}\omega_{\mathbf{q}}}} \Bigg\{ & \sum_{\mathbf{k}_3}\sum_{\mathbf{k}_2} \delta_{\mathbf{k}_3,\mathbf{k}+\mathbf{q}_b}\delta_{\mathbf{k}+\mathbf{q}_a,\mathbf{k}_2} F_{-1,1}\left(\mathbf{k},\mathbf{k}_2\right) F_{1,1}\left(\mathbf{k}_2,\mathbf{k}_3\right) F_{1,-1}\left(\mathbf{k}_3,\mathbf{k}\right) \\
& \left(\frac{f_v(\varepsilon_{\mathbf{k}})\left(1-f_c(\varepsilon_{\mathbf{k}_3})\right)\left(1-f_c(\varepsilon_{\mathbf{k}_2})\right)}{\left(\hbar\omega_a-\varepsilon_{\mathbf{k}}-\varepsilon_{\mathbf{k}_2}\right)\left(\varepsilon_{\mathbf{k}_3}+\varepsilon_{\mathbf{k}}-\hbar\omega_b\right)} + \frac{f_c(\varepsilon_{\mathbf{k}_3})\left(1-f_c(\varepsilon_{\mathbf{k}_2})\right)\left(1-f_v(\varepsilon_{\mathbf{k}})\right)}{\left(\varepsilon_{\mathbf{k}_3}+\varepsilon_{\mathbf{k}}-\hbar\omega_b\right)\left(\hbar\omega_{\mathbf{q}}+\varepsilon_{\mathbf{k}_2}-\varepsilon_{\mathbf{k}_3}\right)} \right. \\
& \left. + \frac{f_c(\varepsilon_{\mathbf{k}_2})\left(1-f_v(\varepsilon_{\mathbf{k}})\right)\left(1-f_c(\varepsilon_{\mathbf{k}_3})\right)}{\left(\varepsilon_{\mathbf{k}_2}-\varepsilon_{\mathbf{k}_3}+\hbar\omega_{\mathbf{q}}\right)\left(\hbar\omega_a-\varepsilon_{\mathbf{k}}-\varepsilon_{\mathbf{k}_2}\right)} \right) \\
& + \sum_{\mathbf{k}_{2'}}\sum_{\mathbf{k}_{1'}} \delta_{\mathbf{k}-\mathbf{q}_b,\mathbf{k}_{1'}}\delta_{\mathbf{k}_{2'},\mathbf{k}-\mathbf{q}_a} F_{-1,-1}\left(\mathbf{k}_{1'},\mathbf{k}_{2'}\right) F_{-1,1}\left(\mathbf{k}_{2'},\mathbf{k}\right) F_{1,-1}\left(\mathbf{k},\mathbf{k}_{1'}\right) \\
& \left(\frac{f_v(\varepsilon_{\mathbf{k}_{1'}})\left(1-f_c(\varepsilon_{\mathbf{k}})\right)\left(1-f_v(\varepsilon_{\mathbf{k}_{2'}})\right)}{\left(\hbar\omega_{\mathbf{q}}+\varepsilon_{\mathbf{k}_2'}-\varepsilon_{\mathbf{k}_{1'}}\right)\left(\varepsilon_{\mathbf{k}}+\varepsilon_{\mathbf{k}_{1'}}-\hbar\omega_b\right)} + \frac{f_c(\varepsilon_{\mathbf{k}})\left(1-f_v(\varepsilon_{\mathbf{k}_{2'}})\right)\left(1-f_v(\varepsilon_{\mathbf{k}_{1'}})\right)}{\left(\varepsilon_{\mathbf{k}}+\varepsilon_{\mathbf{k}_{1'}}-\hbar\omega_b\right)\left(\hbar\omega_a-\varepsilon_{\mathbf{k}_2'}-\varepsilon_{\mathbf{k}}\right)} \right. \\
& \left. + \frac{f_v(\varepsilon_{\mathbf{k}_{2'}})\left(1-f_v(\varepsilon_{\mathbf{k}_{1'}})\right)\left(1-f_c(\varepsilon_{\mathbf{k}})\right)}{\left(\hbar\omega_a-\varepsilon_{\mathbf{k}_2'}-\varepsilon_{\mathbf{k}}\right)\left(\hbar\omega_{\mathbf{q}}+\varepsilon_{\mathbf{k}_{2'}}-\varepsilon_{\mathbf{k}_{1'}}\right)} \right) \Bigg\} \ .
\end{aligned}
\tag{5.73}
$$

For the situation where a plasmon and a photon a are absorbed and a photon b is emitted, the result is similar to Eq. (5.72) as expected, since the electronic transitions are the same (only the direction of the arrows is different, but since this is third order process, the minus sign cancels out). The only true difference is the occupation number for the fields a and b and the plasmon field: in this case, plasmons are absorbed and photons of frequency ω_b are emitted to the reflected field and transmitted fields, so the final occupation number of plasmons is $n_{\mathbf{q}}$ instead of $n_{\mathbf{q}}+1$. For the photons, if absorption is ignored the total field at the interface should, again, be equal to the incident field so the the occupation numbers to be consider are again n_a and n_b and the matrix M_{FI} in the case of absorption is

$$
M_{FI}^{(-)} = \frac{2\pi c}{\omega_b\omega_a}\sqrt{I_bI_a}\sqrt{n_{\mathbf{q}}}\cos\alpha_b\cos\alpha_a\sqrt{\frac{\hbar c}{\mathcal{S}}}\delta_{\mathbf{q},\mathbf{q}_b-\mathbf{q}_a}M_{\mathbf{k}} \ . \tag{5.74}
$$

If the reader is not convinced that indeed this is the case, consider the sum of both reflected and transmitted photons of frequency ω_b:

$$
\left| A_{\mathbf{k}_b}^{(T),x}\sqrt{n_{\mathbf{k}_b^{(T)}}+1} + A_{\mathbf{k}_b}^{(R),x}\sqrt{n_{\mathbf{k}_b^{(R)}}+1} \right|^2 \ , \tag{5.75}
$$

where $A_{\mathbf{k}_b}^{(j),x}$ is the field amplitude in Eq. (5.33) with $j=R,\ T$ and $n_{\mathbf{k}_b^{(T)}}$ and $n_{\mathbf{k}_b^{(R)}}$ are the occupation

numbers for transmitted and reflected photons. Using Eq. (5.71), this sum can be written:

$$\begin{aligned} A^{(T),x}_{\mathbf{k}_b}\sqrt{n_{\mathbf{k}_b^{(T)}}+1}+A^{(R),x}_{\mathbf{k}_b}\sqrt{n_{\mathbf{k}_b^{(R)}}+1} &= \sqrt{\frac{2\pi\hbar c^2}{\eta^2 V\omega_b}}\sqrt{n_{\mathbf{k}_b^{(T)}}+1}\cos\theta_b+\sqrt{\frac{2\pi\hbar c^2}{V\omega_b}}\cos\alpha_b\sqrt{n_{\mathbf{k}_b^{(R)}}+1} \\ &\approx \sqrt{\frac{2\pi c}{\omega_b^2}}\left(\sqrt{\frac{I_j^{(T)}}{\eta}}\cos\theta_b+\sqrt{I_j^{(T)}}\cos\alpha_b\right) \\ &= \sqrt{\frac{2\pi c}{\omega_b^2}I_b}\cos\alpha_b\left(\sqrt{\frac{T}{\eta}}\frac{\cos\theta_b}{\cos\alpha_b}+\sqrt{R}\right) \ . \end{aligned}$$

Ignoring absorption in graphene, the reflection and transmission coefficients satisfy Eq.(C.15):

$$r_j = 1-\sec\alpha_b\cos\theta_b t_j \ , \tag{5.76}$$

so that the sum becomes:

$$A^{(T),x}_{\mathbf{k}_b}\sqrt{n_{\mathbf{k}_b^{(T)}}+1}+A^{(R),x}_{\mathbf{k}_b}\sqrt{n_{\mathbf{k}_b^{(R)}}+1} = \sqrt{\frac{2\pi c}{\omega_b^2}I_b}\cos\alpha_b \ , \tag{5.77}$$

that is the sum of transmitted and reflected photons, in zero-th order, equals the incident photons.

5.4.3 DF plasmon emission rate

We now have all the necessary tools to calculate the frequency difference emission rate of a SPP with energy-momentum coordinates $(\omega_{\mathbf{q}},\mathbf{q})$. Using Eq. (5.72), the emission rate of plasmons, $\Gamma^{(+)}_{\rm sp}$, becomes:

$$\Gamma^{(+)}_{\rm sp} = \frac{(2\pi c)^3}{\omega_b^2\omega_a^2}I_bI_a\left(n_{\mathbf{q}}+1\right)\cos^2\alpha_b\cos^2\alpha_a M_{\rm DF}\left(\mathbf{q},\mathbf{q}_a,\mathbf{q}_b\right)\delta\left(\hbar\omega_b-\hbar\omega_a-\hbar\omega_{\mathbf{q}}\right) \ , \tag{5.78}$$

where:

$$M_{\rm DF}\left(\mathbf{q},\mathbf{q}_a,\mathbf{q}_b\right) = \delta_{\mathbf{q},\mathbf{q}_b-\mathbf{q}_a}\frac{1}{\mathcal{S}}\sum_{\mathbf{k}}\left|M_{\mathbf{k}}\right|^2 \ . \tag{5.79}$$

In Eq. (5.79), the summation is over the electronic sates. The rate for plasmon absorption is obtained using Eq. (5.74):

$$\Gamma^{(-)}_{\rm sp} = \frac{(2\pi c)^3}{\omega_b^2\omega_a^2}I_bI_a n_{\mathbf{q}}\cos^2\alpha_b\cos^2\alpha_a M_{\rm DF}\left(\mathbf{q},\mathbf{q}_a,\mathbf{q}_b\right)\delta\left(\hbar\omega_b-\hbar\omega_a-\hbar\omega_{\mathbf{q}}\right) \ . \tag{5.80}$$

The DF-generation rate in the master equation is:

$$\Gamma_{\rm DF}\left(\mathbf{q}\right) = \Gamma^{(+)}_{\rm sp}-\Gamma^{(-)}_{\rm sp} = \frac{(2\pi c)^3}{\omega_b^2\omega_a^2}I_bI_a\cos^2\alpha_b\cos^2\alpha_a M_{\rm DF}\left(\mathbf{q},\mathbf{q}_a,\mathbf{q}_b\right)\delta\left(\hbar\omega_b-\hbar\omega_a-\hbar\omega_{\mathbf{q}}\right) \ . \tag{5.81}$$

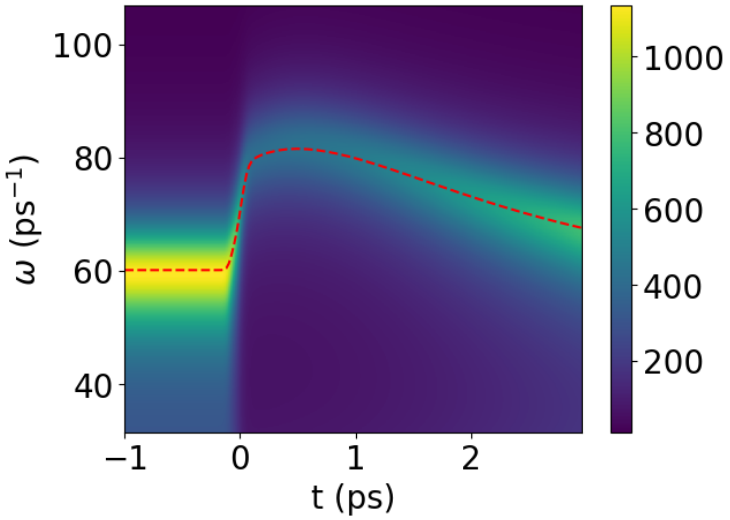

Figure 5.7: Γ_{DF} (ps^{-1}) as a function of time delay t between the pump and probe and the frequency difference ω. The dynamical evolution of hot carriers is described using the hot electron model from Section 4.2. The calculation was performed for the same conditions and parameters as in Figs. 4.2 and 5.5. The red dashed line is the time-dependent SPP dispersion curve calculated using only the intraband conductivity (B.28).

To introduce losses and the corresponding broadening we replace the Dirac δ-function by a Lorentzian:

$$\delta\left(\hbar\omega_b - \hbar\omega_a - \hbar\omega_{\mathbf{q}}\right) \to \frac{1}{\pi\hbar}\frac{\gamma_{\mathrm{loss}}(\mathbf{q})}{\left(\omega_b - \omega_a - \omega_{\mathbf{q}}\right)^2 + \gamma_{\mathrm{loss}}^2(\mathbf{q})} \ , \tag{5.82}$$

where $\gamma_{\mathrm{loss}} = -\gamma_{\mathrm{sp}}(\mathbf{q})$, and write:

$$\Gamma_{\mathrm{DF}}\left(\mathbf{q}\right) = \frac{(2\pi c)^3}{\pi\hbar\omega_b^2\omega_a^2} I_b I_a \cos^2\alpha_b \cos^2\alpha_a M_{\mathrm{DF}}\left(\mathbf{q}, \mathbf{q}_a, \mathbf{q}_b\right) \frac{\gamma_{\mathrm{loss}}(\mathbf{q})}{\left(\omega - \omega_{\mathbf{q}}\right)^2 + \gamma_{\mathrm{loss}}^2(\mathbf{q})} \ . \tag{5.83}$$

$\gamma_{\mathrm{sp}}(\mathbf{q})$ is obtained by considering complex solutions, $\omega_{\mathrm{sp}} = \omega_{\mathbf{q}} + i\gamma_{\mathrm{sp}}$, for the dispersion equation and $\omega = \omega_b - \omega_a$. In Fig. 5.7 we plot Γ_{DF} as a function of ω and time. To obtain Fig. 5.7, the integral in Eq. (5.79) was calculated numerically. The calculation is quite time-consuming and was performed in the following way: the electron dynamics was determined using the hot electron model for $\omega = 0$ and it was used to calculate Γ_{DF} for all other frequencies. To put it in another way, the situation simulated was the one with a pre-pump at $\omega = 0$ and then the frequency of field b was varied, $\omega_b = \omega_a + \omega$. This is a somewhat different from the Constant et al. experiment, where the field b and the pump are the same. The latter would require the simulation of the electron dynamics for each ω.

The final form of the Eq. (5.5) for the SPP population is:

$$\frac{dn_{\mathbf{q}}}{dt} = \Gamma_1(\mathbf{q}) + \Gamma_2(\mathbf{q})n_{\mathbf{q}} + \Gamma_{\mathrm{DF}}(\mathbf{q}) - \gamma_{\mathrm{loss}}(\mathbf{q})\left(n_{\mathbf{q}} - n_{\mathbf{q}}^{\mathrm{eq}}\right) \ . \tag{5.84}$$

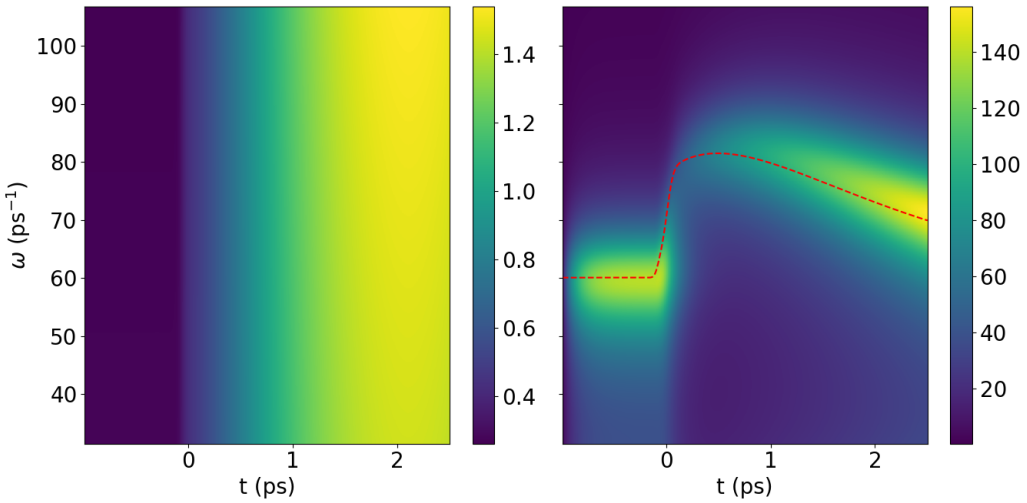

Figure 5.8: Evolution of $n_{\mathbf{q}}$. **Left:** solution of the master equation (5.84) without the DF generation term. **Right**: evolution with DF term. The calculation was performed for the same conditions and parameters as in Figs. 4.2, 5.5 and 5.7. The red dashed line is the time-dependent SPP dispersion curve.

Its numerical solution was performed as above: the electron dynamics was determined using the hot electron model for $\omega = 0$ and was used to solve the master equation (5.84) for other frequencies. Only the intraband conductivity is used to model the SPPs since the interband contributions are contained in Γ_1 and Γ_2. Figure 5.8 shows how the SPP population evolves with and without the DF generation term. Clearly, the presence of the beams b and a with the right frequency difference contributes to the steeper growth of the resonant SPP mode.

5.5 SPP assisted light scattering

The emission of photons a into the reflected beam is stimulated by the presence of the reflected beam. Thus, in the calculation of the emission rate of photons a for reflection, we consider the field at $z = 0^+$ and the relevant mode is the reflected mode, $\left(\omega_a, \mathbf{k}_a^{(R)}\right)$. Obviously, the full electric field b contributes, so the incident mode for field b is considered. Hence, for this case, the matrix element M_{FI} is:

$$M_{FI} = \frac{2\pi c}{\omega_b \omega_a} \sqrt{I_b I_a^{(R)}} \sqrt{n_{\mathbf{q}} + 1} \cos\alpha_b \cos\alpha_a \sqrt{\frac{\hbar c}{\mathcal{S}}} \delta_{\mathbf{q},\mathbf{q}_b - \mathbf{q}_a} M_{\mathbf{k}} \tag{5.85}$$

and the rate of emission of reflected photons a is given by:

$$\Gamma_a^{(R)} = \frac{(2\pi c)^3}{\pi \hbar \omega_b^2 \omega_a^2} I_b I_a^{(R)} \left(n_{\mathbf{q}} + 1\right) \cos^2\alpha_b \cos^2\alpha_a M_{\mathrm{DF}}\left(\mathbf{q}, \mathbf{q}_a, \mathbf{q}_b\right) \frac{\gamma_{\mathrm{loss}}(\mathbf{q})}{\left(\omega - \omega_{\mathbf{q}}\right)^2 + \gamma_{\mathrm{loss}}^2(\mathbf{q})} \ . \tag{5.86}$$

Here, $I_a^{(R)}$ is the reflected intensity, related to the incident intensity by:

$$I_a^{(R)} = R_a^{(0)} I_a \ , \tag{5.87}$$

where $R_a^{(0)} = \left| r_a^{(0)} \right|^2$, with $r_a^{(0)}$ denoting the linear reflection coefficient defined in Eq. (E.31).

To estimate the change in differential reflectivity due to this generated photons, we shall assume coherence of the generated and reflected photons (having the same frequency and 3D wavevector), i.e. the absence of any phase shift between the electric fields associated with them. In this approximation, the correction to the reflected field due to the generation of SPPs is approximately:

$$E_a^{(3)} \approx \sqrt{\frac{\Gamma_a^{(R)} \hbar \omega_a}{\mathcal{S}}}, \tag{5.88}$$

that according to our assumption, is in phase with the reflected field (photons that only interact with the substrate):

$$E_a^{(R)} = \hat{r}_a^{(0)} \sqrt{\frac{P_a^I}{\mathcal{S}}} \ , \tag{5.89}$$

where P_a^I is the incident power. Consequently, the reflectance is:

$$\begin{aligned} R = \frac{\left| E_a^{(R)} + E_a^{(3)} \right|^2}{\left| E_a^{(I)} \right|^2} &\approx \left| \hat{r}_a^{(0)} \right|^2 + \frac{2}{\left| E_a^{(I)} \right|^2} \mathrm{Re} \left\{ E_a^{(R)} E_a^{(3)} \right\} \\ &= R_a^{(0)} + 2 \frac{\hat{r}_a^{(0)}}{\left| E_a^{(I)} \right|} \sqrt{\frac{\Gamma_a^{(R)} \hbar \omega_a}{\mathcal{S}}} \ , \end{aligned}$$

where $\left| E_a^{(I)} \right|$ is the incident field amplitude:

$$\left| E_a^{(I)} \right| = \sqrt{\frac{P_a^I}{\mathcal{S}}} \ . \tag{5.90}$$

The contribution to the differential reflectivity is then:

$$\frac{\Delta R_a}{R_a} \approx \frac{2}{\hat{r}_a^{(0)}} \sqrt{\frac{\Gamma_a^{(R)} \hbar \omega_a}{P_a^I}} \ . \tag{5.91}$$

According to this expression, using the results from Figs. (5.7) and (5.8), the generation of plasmons should give a contribution of the order of:

$$\frac{\Delta R_a}{R_a \Phi_b} \sim 10^{-2} \ \mathrm{mJ}^{-1} \mathrm{cm}^2 \ , \tag{5.92}$$

as measured by Constant et al. In calculating (5.92) we used $P_a^I = I_a A_{\text{spot}}$, where A_{spot} is the effective spot size area of the beam in the sample (see Section 1.1).

5.6 Concluding remarks

With our model combining two mechanisms of generation of graphene plasmons, we have been able to explain, for the first time the high values of differential reflectance observed in Ref. [1]. The key point is that plasmons of different momenta and energies, which are generated by hot carriers' relaxation, facilitate the resonant difference-frequency process that leads to the enhanced generation of a particular type of SPPs and also affects the probe beam. The former is the goal of this work, while the latter is just the means of its registration. As discussed in Chapter 3, there can be other possibilities for (more direct) detection of the generated plasmons. However, the understanding of the high differential reflectance of the probe beam validates the idea of simultaneous action of two mechanisms of the SPP generation.

The theory presented in this chapter can be developed further by using a density matrix formalism instead of the master equation with the DF rate calculated by Fermi's Golden Rule. Such an approach was proposed in the past to describe the dynamic absorption spectra in femtosecond pump-probe experiments [48] and stimulated Raman scattering [49].

Chapter 6

Experimental generation of SPPs

Generation of SPPs using an all-optical setup proved to be a much bigger challenge than we had anticipated. The major difficulty was setting a detection scheme sensitive enough to reveal the presence of the excited SPPs. The best approach to study the DF-generation of SPPs in graphene is to record the changes in reflectivity, as was done in Refs. [1, 13]. Why measure the changes in the reflectivity and not in the transmission? The reason is that the probe may suffer changes as it propagates through the substrate, thus contaminating the transmission signal with substrate effects. On the other hand, the reflection travels through air and no extra effects are introduced in the probe.

In this chapter, we present the experimental work done and discuss the techniques used. Two approaches to generate the SPPs via frequency difference process were explored: DF-generation using chirped pulses and tuning of the pump frequency using optical parametric amplification. Also, two detection methods were tested: a lock-in amplifier and a boxcar averager with balanced photodetection. Unfortunately, because of several unexpected problems that appeared along the way, we have not yet successfully generated SPPs in graphene.

6.1 DF using chirped pulses

The initial proposal to generate SPPs in graphene involved the use of chirped pulses. A chirped pulse's electric field, $E(t)$, has a phase term ϕ_2 quadratic in time [50]:

$$E(t) = E_0 g(t) e^{-i\omega_0 t} e^{-i\phi_2 t^2} \ , \tag{6.1}$$

where $g(t)$ is a wavepacket function, E_0 is the field's amplitude and ω_0 the pulse's central frequency. For a Ti:sapphire LASER, this quadratic phase term represents a time delay between the frequencies of the pulse, in other words, different frequencies arrive at different times. The pulse instantaneous frequency as a function of time t is:

$$\nu(t) = \nu_0 - \frac{\phi_2}{\pi} t \ , \tag{6.2}$$

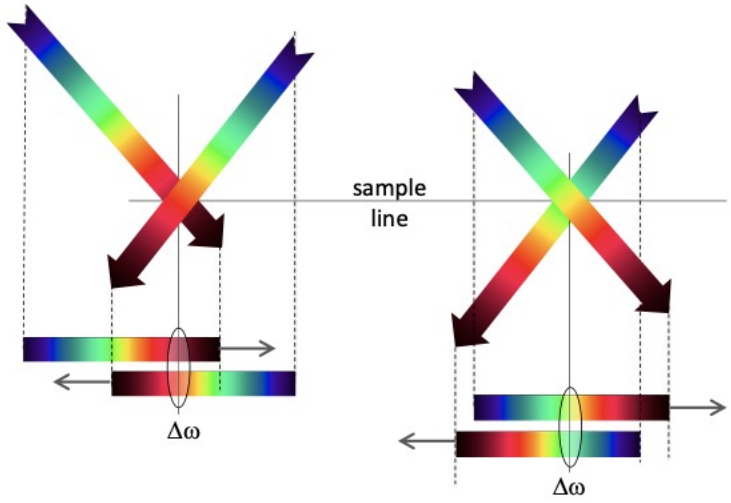

Figure 6.1: DF-generation using two chirped pulses, with equal quadratic phase term ϕ_2. By changing the delay time between them, the instantaneous DF ($\Delta\omega = 2\pi\nu_{\mathrm{DF}}$) changes.

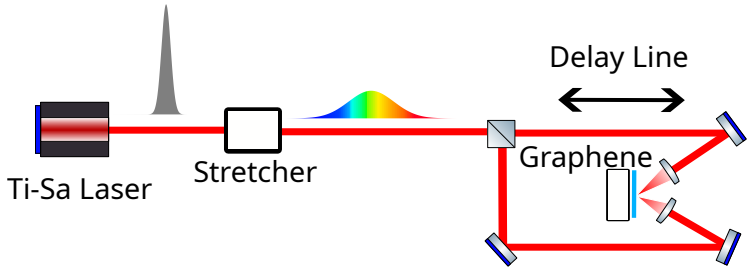

Figure 6.2: Optical setup for generation of SPPs in Graphene using chirped pulses. The Ti:sapphire LASER emits a pulse with a zero quadratic phase term $\phi_2 = 0$. A stretcher is used to introduce a nonzero ϕ_2, chirping the pulse.

where $\nu_o = \omega_0/(2\pi)$. Two chirped pulses, b and a, with equal phase term ϕ_2, can interact at a fixed frequency difference,

$$\nu_{\mathrm{DF}}(\Delta) = \nu_b(t+\Delta) - \nu_a(\Delta) = -\frac{\phi_2}{\pi}\Delta \ , \tag{6.3}$$

by changing the time delay Δ between them, as shown in Fig. 6.1. With this approach, SPPs could be excited at controlled frequency ν_{DF}.

The thought optical setup to implement this idea is shown in Fig. 6.2. The pulse is emitted by a Ti:sapphire laser with negligible chirp,

$$E(t) = E_0 g(t) e^{-i\omega_0 t} \ . \tag{6.4}$$

Using a stretcher [51, 52], a phase term ϕ_2 is introduced, stretching the pulse in time, as represented

in Fig. 6.2. The stretched pulse is then split into two that impinge on the graphene sample at fixed angles. By changing the delay line and the phase term ϕ_2, one can leverage the instantaneous difference frequency (6.3) to match the SPP resonance. This is a compact and simple method to excite SPPs in graphene that does not require tunable pulsed lasers, which are expensive, large and rather hard to operate, with the SPP frequency tuning done just by changing a delay line.

Nonetheless, this approach has one drawback: for a Ti:sapphire LASER, the pulse spectral width is approximately 5 THz, giving a 10 THz narrow window for SPP excitation. Besides, for such small frequencies, the SPP momentum is also small, which requires small incident angles. Measuring the reflectivity in an optical system with small angles is a challenge. Moreover, at the time, it was unclear if we could detect the presence of SPPs. As a consequence, this idea to use chirped pulses was abandoned and we decided to follow a similar approach to Ref. [1].

6.2 DF using an optical parametric amplifier

As discussed in Section 5.2, the SPP dispersion will change over time and, as a consequence, it is not easy to correctly predict at which DF is the SPP resonance. To find a resonance, it is important to have a tunable way of scanning the frequency space. This can be done with an optical parametric amplifier (OPA), that can change the output frequency of an otherwise fixed femtosecond laser system. The OPA we used in the lab was the TOPAS-C (see Appendix J).

The setup in mind to reproduce the experiment is shown in Fig. 6.3. A Ti:sapphire LASER, at wavelength $\lambda_0 = 794$ nm and 80 MHz repetition rate, seeds the amplifier, which outputs 100 fs pulses at wavelength $\lambda_a = 800$ nm, at a one KHz rate. This output is split into two beams b and a. Beam a goes directly into the sample while b is used for TOPAS-C. The latter changes the output frequency to λ_b and is used to scan the DF and find the SPP resonance. The presence of SPPs is found by detecting changes in the reflectivity.

The open question is, can we set up a detection scheme sensitive enough to detect the optically excited SPPs, through changes in the reflectivity? From Constant et al. results [1], this seems a difficult task, so it is important to understand if we can do it, before proceeding any further.

6.3 Testing sensitivity

Since the reflectivity of graphene on glass, R_0, is of the order of 0.03, from Fig. 1.2 we may estimate the variation of the reflectivity, ΔR, to be of the order of:

$$\Delta R = \left(\frac{\Delta R}{R_0 \Phi}\right) R_0 \Phi \sim 0.06 \times 0.03 \times 0.1 \sim 10^{-4} \ . \tag{6.5}$$

Thus, to detect the generation of SPPs, through changes in the differential reflectivity, we must at least have the ability to detect signal variations of 10^{-5} in magnitude, relative to the background. This requires a sensitive experimental apparatus. Therefore, it was decided to perform an interme-

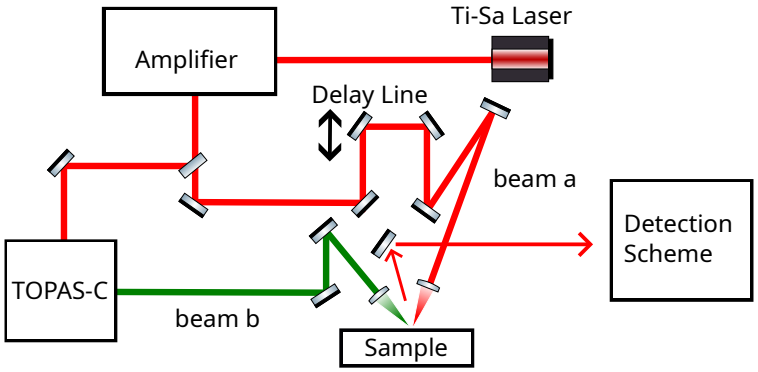

Figure 6.3: Optical setup for generation of SPPs in Graphene using the amplifier and TOPAS-C. The Ti:sapphire laser seeds the amplifier and the output pulse is used to excite SPPs and seed the TOPAS-C.

diate experiment to determine how sensitive the set up mounted in the Femtosecond Laboratory of the CF-UM-UP could be.

The designed experiment is a simple sum frequency (SF) experiment [12] (see Fig. 6.4). Two 84 fs Ti:sapphire laser pulses, a and b, at wavelength $\lambda_0 = 794$ nm are focused on a BBO crystal, using a spherical lens with 2.5 cm of focal length. The beams are focused at equal angles $\theta_a = \theta_b = 20°$. A SF-signal is generated at wavelength, $\lambda_s = 397$ nm, and propagates at angle $\theta = 0°$. To control the phase matching between fields, the BBO crystal was mounted on a rotating stage to allow control of the angle Ψ. The crystal used was bought from Eksma Optics [53]. The goal of the experiment was to measure the power depletion of beam a. This measurement was carried out using a fast photodetector and a lock-in amplifier, whose principle is explained in Appendix I.

Although BBO is a very efficient medium for SF-generation, the power depletion, ΔP_a, should be small compared to the incident power, P_a^I. For the geometry shown in Fig. 6.4, we may estimate this power depletion. For $P_a^I \approx P_b^I \approx 10$ mW, the measured power of the SF-signal was $P_s \approx 60\ \mu$W. From the Manley–Rowe relations (see Appendix H for details), the power depletion should then be of the order:

$$\Delta P_a \sim \frac{P_s}{2} = 30\mu W\ . \tag{6.6}$$

This corresponds to a power variation $\Delta P_a / P_a^I \sim 10^{-3}$. This experiment has two main advantages:

1. The SF-signal is visible by eye, making the alignment of the setup easy.

2. The SF-signal is proportional to the product of the powers of the incident pulses (see Appendix H):

$$P_s \propto P_a P_b\ . \tag{6.7}$$

This means that if both P_a and P_b are lowered by a factor of 10, the SF-power and the power depletion will drop by 100, thus allowing us to easily test the sensitivity of the fast photodetector + lock-in amplifier system.

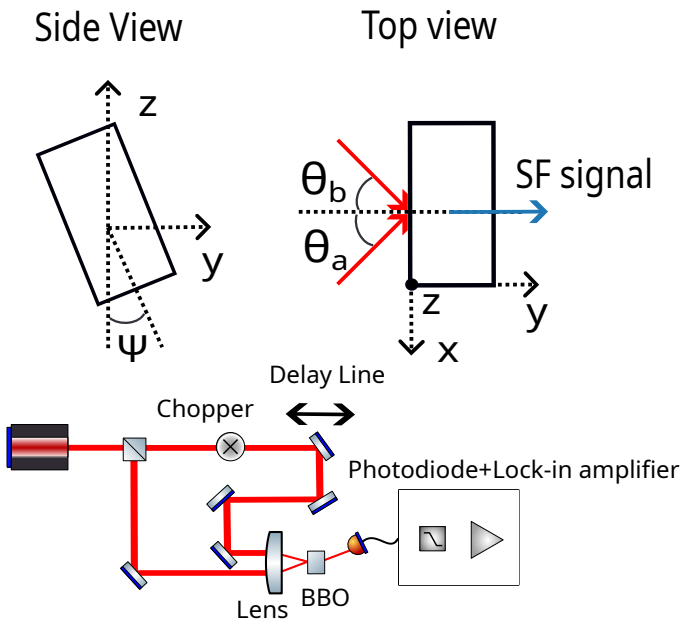

Figure 6.4: Sum frequency generation in BBO crystal. The Ti:sapphire laser pulses are the red arrows and the SF signal is the blue arrow. θ_b and θ_a are the incident angles and Ψ is the crystal's rotation angle. **(Top)** Geometry of the problem, side and top view of the crystal. **(Bot)** Experimental setup.

A detailed description of the BBO as well as a semi-qualitative calculation of the SF-generation rate in the context of this experiment are given in Appendix (H).

The photodetector used has a fast response, with a rise time of 1 ns [54]. To estimate the intrinsic noise of the photodiode, we used a tektronix oscilloscope with a 500 MHz bandwidth to acquire the data fastly. Since the pulses had a time width of approximately 100 fs, what we saw in the oscilloscope was the photodiode's RC response convoluted with that of the oscilloscope. We acquired in total 32967 pulses, at sampling rate of 20 GHz, and integrated the signal of each pulse. The obtained average value was:

$$A = 1.49 \pm 0.02 \text{ mV} \ . \tag{6.8}$$

Using this value, we estimate the noise of the measurement using the photodetector to be around 1%. For a small signal with a magnitude of 10^{-5}, this corresponds to a signal to noise ratio (SNR) of [1]:

$$\text{SNR} = 20 \log_{10} \frac{10^{-5}}{10^{-2}} = -60 \text{ dB} \ . \tag{6.9}$$

Hence, in order to measure such small signals, the lock-in must be of capable of removing at least 60 dB of noise. This is possible, if in the lock-in amplifier we set a time constant of 1 second and a 60 dB/decade filter.

[1] The definition of the dB unit is given in Appendix (I.1).

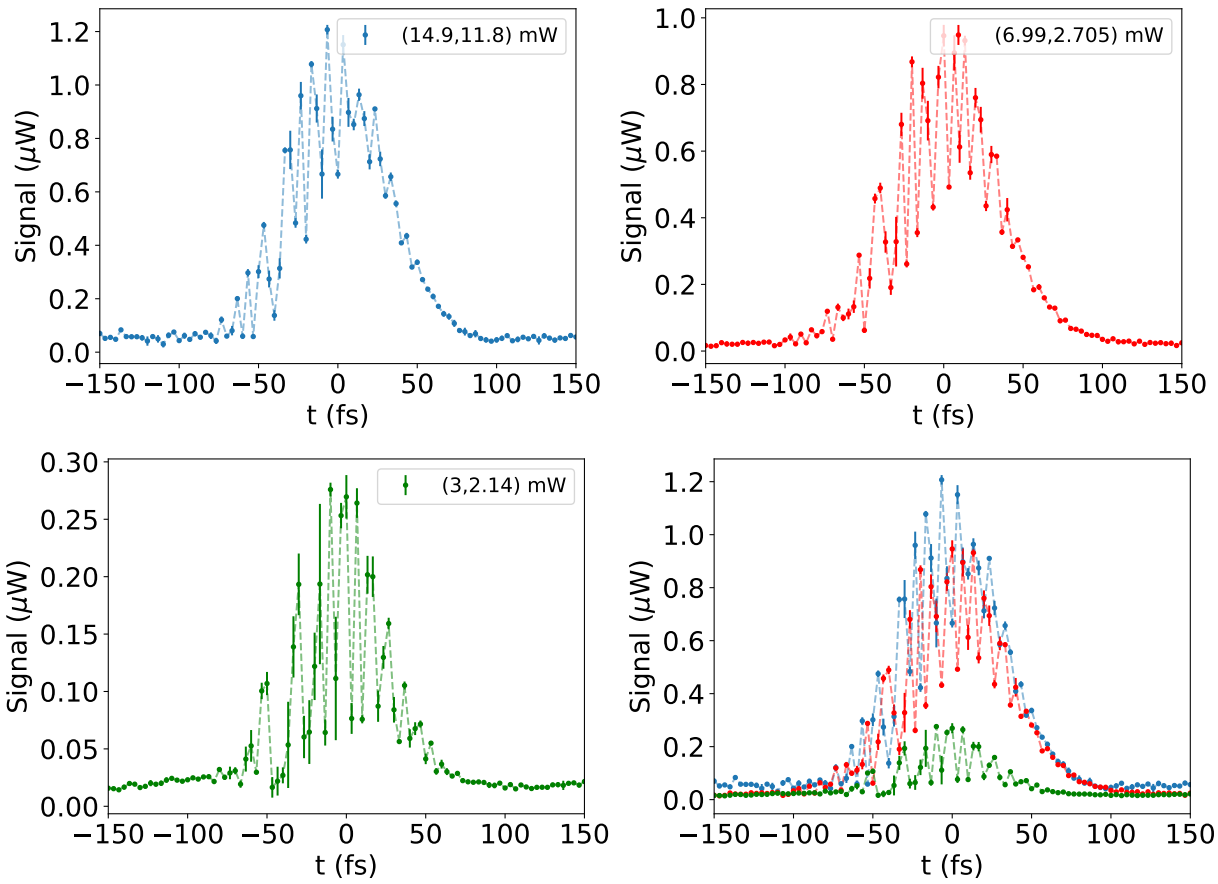

Figure 6.5: Measured pump depletion signal. These results were obtained in the early runs. At each run, the power is cut down. The legends in the images are the incident power of beams a and b, (P_a^I, P_b^I). The last image is a combination of the 3 runs, for comparison. As it can be seen, the oscillations appear on top of the pump depletion and seem to be random. Furthermore, they do not go down with $P_a^I P_b^I$.

6.3.1 Results

The first results obtained are shown in Fig. 6.5. On top of the pump depletion signal, we observe oscillations that do not decrease with the incident power, $P_a^I P_b^I$, contrary to what was expected. These oscillations seem to be linear and to some degree random in nature since they do not match for different runs. Although we do not know exactly the cause, these oscillations might be modulated scattered light that somehow finds its way to the photodetector and interferes with the main beam. The scattering mechanism must have its origin in an interaction between the beams, because if the beam a is blocked, these oscillations disappear, so it cannot just be the light scattered from the surface (see Fig. 6.6).

To make sure that the oscillations were not caused by bad alignment, the optical setup was realigned. The oscillations disappeared and the results obtained are shown in Fig. 6.7. The observed

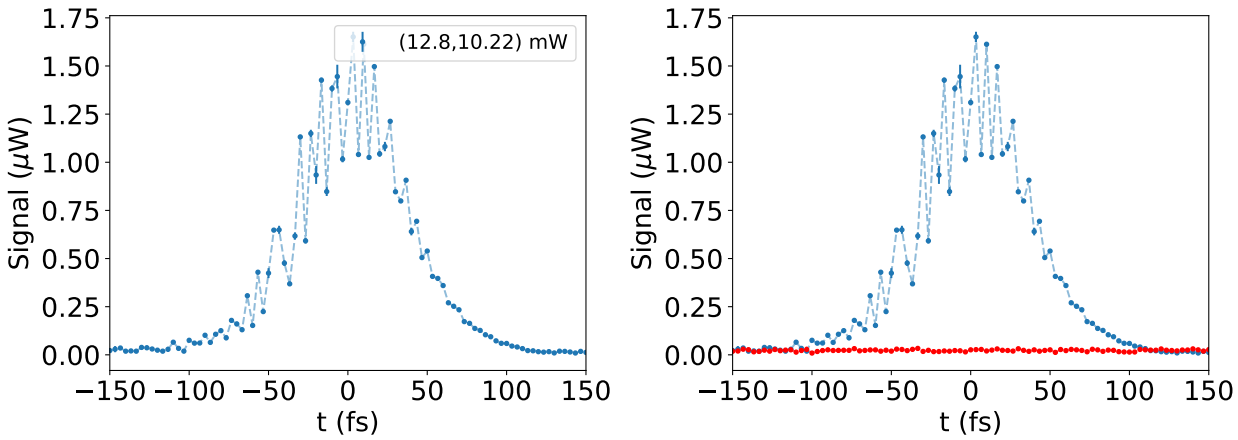

Figure 6.6: **(Left)** Pump depletion. **(Right)** Pump depletion (same as in the left) (blue) plus the result when beam a is blocked (red). This result shows that the oscillations cannot be attributed only to simple scatter of light from beam b.

behavior is as expected. The results were taken during the same day. For the second situation, the total power was reduced approximately by a factor of 10. We were able to detect signal variations down to:

$$\frac{\Delta P_a}{P_a^I} \approx \frac{0.08 \cdot 10^{-3}}{1.85} \sim 10^{-5} \ , \tag{6.10}$$

as desired. Nonetheless, it is clear that there are considerable fluctuations. In principle, the results can be improved by a more careful alignment and by increasing the time constant and filter roll-off in the lock-in, so the sensitivity of the measurement can be improved if needed.

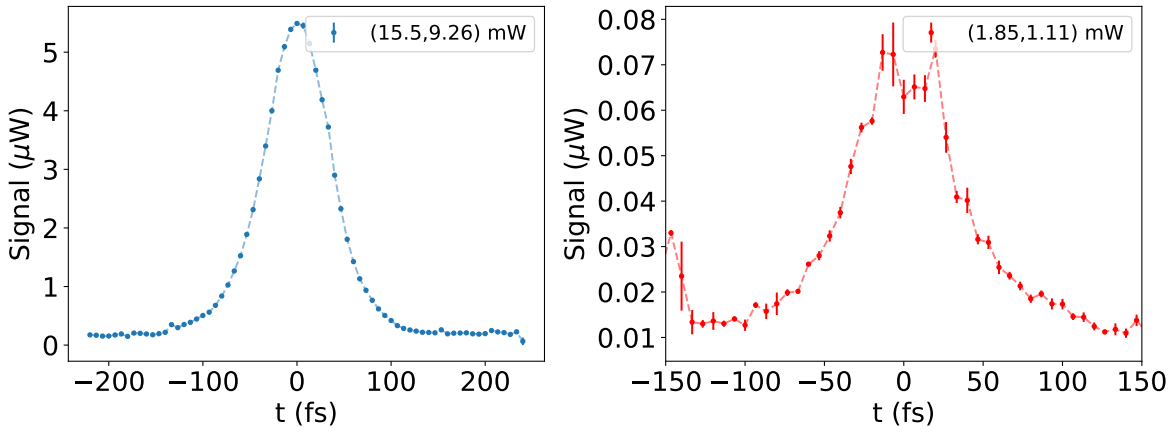

Figure 6.7: Measured pump depletion signal. The legend shows the incident power of each beam (P_a^I, P_b^I). The situation on the right has the total power reduced by a factor of 8.369 relatively to the situation on the left.

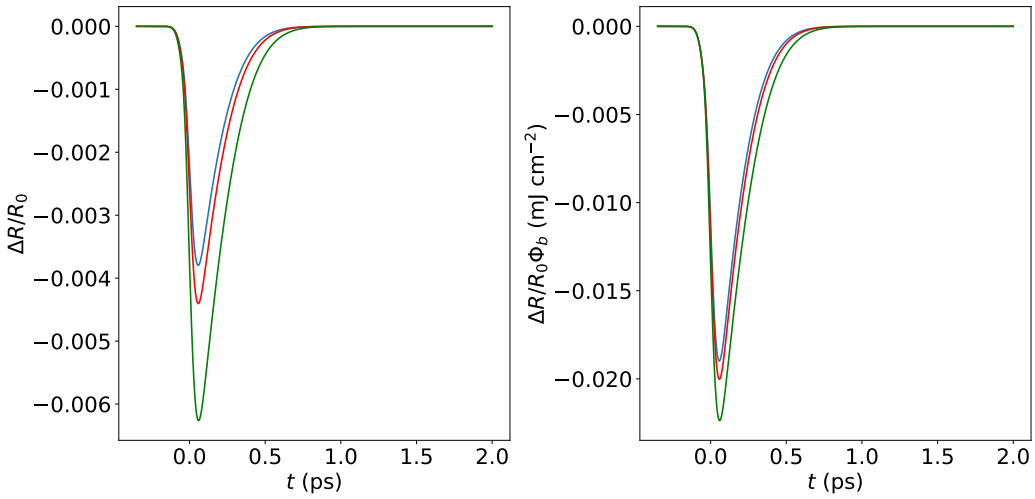

Figure 6.8: Expected signal fluctuations in the differential reflectivity. **(Left)** Differential reflectivities calculated using the hot electron model of Sec. 4.2. The parameters are the same as in Fig. 4.2. The curves were calculated for different fluence $f\Phi_b$. The blue line was calculated with a correction factor $f = 1$, while the red and green lines for $f = 1.1$ and $f = 1.4$, corresponding to fluctuations of 10 and 40%, respectively. **(Right)** Same as in the left plot but the differential reflectivity is normalized by the pump fluence.

6.4 Aligning TOPAS-C

After concluding that the lock-in amplifier could be used to detect small changes in the reflectivity due to the presence of SPPs, we went on to aligning the setup in Fig. 6.3, including the TOPAS-C[2]. The main difficulties encountered in setting the TOPAS-C were finding the correct position of the lenses to focus on the nonlinear crystals as well as the right crystal and beam angles for phase matching. Since TOPAS-C is built in a very compact way, these tasks are challenging. The easiest way to perform the alignment is to remove most optical components and then reinstall them, one by one to ensure that the beam goes in a straight line and is centered in the lenses. Even with this approach, problems appear because the lenses are not normal ones: depending on the lens rotational angle, the focal point changes. Moreover, the input pump must have a good spatial and temporal profile to ensure maximum efficiency and stability. Therefore, the optics before the TOPAS-C, especially the amplifier, must also be correctly aligned.

In the end, the TOPAS-C was not properly working. The output pulses had a nice spectral shape, but the output power was very unstable; power fluctuations up to 40% in the course of one second were observed. We looked for the problem but have not found it. Additional alignment of the TOPAS-C did not lead to any considerable improvement. The problem must come from the amplifier.

The power fluctuations of the pump are a serious problem because the hot electron signal is nonlinear and consequently it also fluctuates. This fluctuations are not removed by the lock-in, since they are intrinsic to the signal. The solution is monitoring the output power of TOPAS-C,

[2]Aligning the TOPAS-C alone took us a month.

pulse by pulse, and normalize the signal to the pump fluence, pulse by pulse (see Fig. 6.8). This is not possible with the lock-in. Moreover, the lock-in was tested in an experiment using a laser at 80 MHz rate. Will it work as well at a 1 KHz rate? In principle, the lock-in should still be capable of removing the same amount of noise as determined before, but it will take more time to stabilize since the sampling rate is much lower. Consequently, the detection scheme needs to be changed.

6.5 Balanced detection

In spite of knowing that the problem was in the amplifier, it was unclear where it came from and fixing it could take months. As a consequence, we decided that normalizing the signal to the pump (TOPAS-C) fluence was the best approach. For this, we needed a way of both measuring the probe and monitor the pump power, pulse by pulse. This can be done using two photodetectors, one for the probe and another for the pump. The signals from the photodetectors are integrated separately using two boxcars and are divided, pulse by pulse, posteriorly in the computer. The used setup is shown in Fig. 6.9. The operation principle and functioning of the boxcar is explained in Appendix K.

Since the experiment required increased SNR, the probe was measured using a balanced photodetector, which has the ability to cancel common noise and detect small signal fluctuations in a large DC signal. This detector uses a reference and a beam with the signal to be measured, in our case the reflection from the graphene sample. The two photodiodes in the balanced photodetector are identical and connected in such a way that their photocurrents cancel. The output of the balanced pair is zero until there is some difference in the intensity of one of the beams, causing the pair to become unbalanced and a net signal to appear in the output. Consequently, common-mode noise that is present in both the reference and signal beams is cancelled out and does not appear as part of the signal. On the other hand, any imbalance between the photocurrents generated by the reference and signal detectors is amplified and is seen as the received signal.

6.5.1 Use of the boxcar SR250

To integrate the pulses, the boxcar used was the SR250 [55], which is an analog model, with associated limitations [56]. This model does not have graphical user interface, so the SR245 is used to communicate via PC. The SR245 can communicate simultaneously with two SR250, and can store in its memory 3711 integrals (1855 from each boxcar). If one wants to acquire more data, the information in the SR245 needs to be exported to the computer and its memory emptied.

To communicate with the SR245, a communication interface with computer is needed. The easiest to use is the GPIB, but for an unknown reason, when data is scanned, the return values between channels (fast photodiode and balanced photodetector) are not synchronized. In other words, the two boxcars are not interrogated at the same time, so while one boxcar sends a value only after a pulse was integrated, the other would answer earlier or later, and return a value for

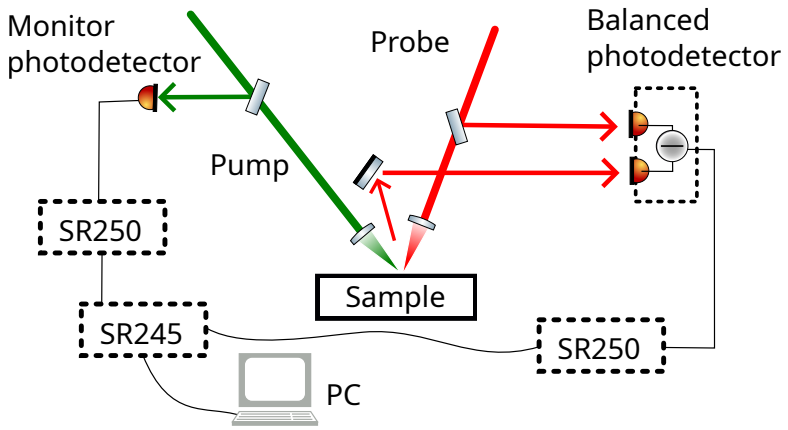

Figure 6.9: Second approach to detect generation of SPPs. The changes in the probe are measured using a balanced photodetector. The pump power is monitored by a fast photodetector. Two boxcar averagers SR250 integrate the signals and send them to the SR245 computer interface module. This module sends the data to the computed where the integrated signals are divided.

the moment when no pulse was present. As a consequence, the channels are not correlated and the signal cannot be normalized.

In the end, we had to use the RS232 interface, which is older and less friendly than the GPIB. For a baud rate of 9600, this interface worked fine when the data was downloaded value by value. This takes a long time; for example, for a scan of 1800 pulses in each boxcar, which corresponds to 1.8 seconds, it takes approximately 1 min to fully download the data to the computer. A much faster option is to download the full data from the SR245 in a 2 byte binary format. However, a timeout error appeared and the download always failed. We do not know the origin of this error, but it is something to be fixed to optimize data acquisition.

6.5.2 Testing the balanced photodetector

We used the Nirvana auto-balanced photoreceivers, Model 2007 [57]. According to the detector's data sheet, this model is capable of reducing common noise in 50 dB at frequencies from DC to 125 kHz. The device measures the difference in power between the reference and signal photodiodes:

$$\mathrm{Sig} = P_{\mathrm{sig}} - P_{\mathrm{ref}} \ , \tag{6.11}$$

where P_{sig} and P_{ref} are the incident powers on the signal and reference photodiodes, respectively.

The device has shown some problems in the past and we were not confident if it would perform well. To test the device, we set up the experiment in Fig. 6.10. The goal was to verify Malus's law, using the unstable TOPAS-C, and measure the balanced photodiode output, $\mathrm{Sig}(\theta)$, where θ is the polarizer's angle. At each θ, 500 pulses were integrated. The polarizer was mounted in the signal beam's path.

Figure 6.11 **a)** shows how the measured voltage fluctuates with each pulse, for a fast photodiode

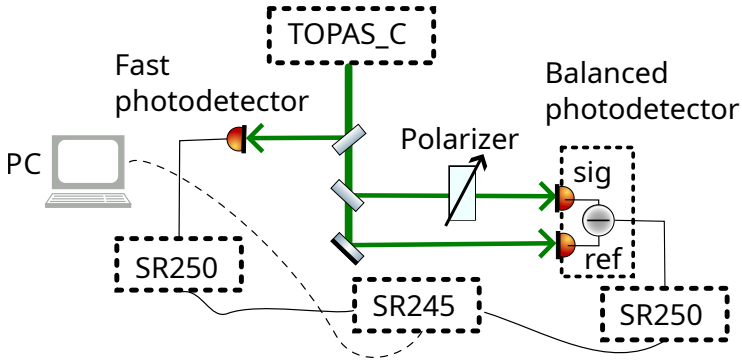

Figure 6.10: Balanced Photodetection Setup.

and for the balanced photodetector. At a first look, it seams that the balanced photodetection yields a much more stable measurement, effectively removing common noise. The noise in the fast photodetector is given by the standard deviation of the measurement. With this detector, the measured mean, μ_1, and the standard deviation, σ_1, were:

$$\begin{aligned} \mu_1 &\approx 390\ \mu\text{W}\ , \\ \sigma_1 &\approx 40\ \mu\text{W}\ . \end{aligned} \tag{6.12}$$

The ratio between the signal and full background is:

$$\frac{\sigma_1}{\mu_1} \approx 0.1 = 10\%\ . \tag{6.13}$$

This means that the fast photodiode can detect signal variations down to 10% in the TOPAS-C. Smaller changes are completely washed out by the noise.

To estimate the rejection in common noise by the balanced photodetector, we used the results in Fig. 6.11 **b).** The plot shows Sig(θ) (blue dots with error bars) and the fit function (black line):

$$\text{Sig}(\theta) = P_{\text{ref}} \left\{ r \cos^2 \theta - 1 \right\}\ , \tag{6.14}$$

where P_{ref} and r are fitting parameters. r is the ratio between the incident powers,

$$r = \frac{P_{\text{sig}}\,(\theta = 0)}{P_{\text{ref}}}\ . \tag{6.15}$$

The fitted values are:

$$r = 1.04 \quad , \quad P_{\text{ref}} = 187.4\ \mu\text{W}\ ,$$

with negligible uncertainty. Close to the balanced state ($\theta = 10.5°$), the standard deviation of the

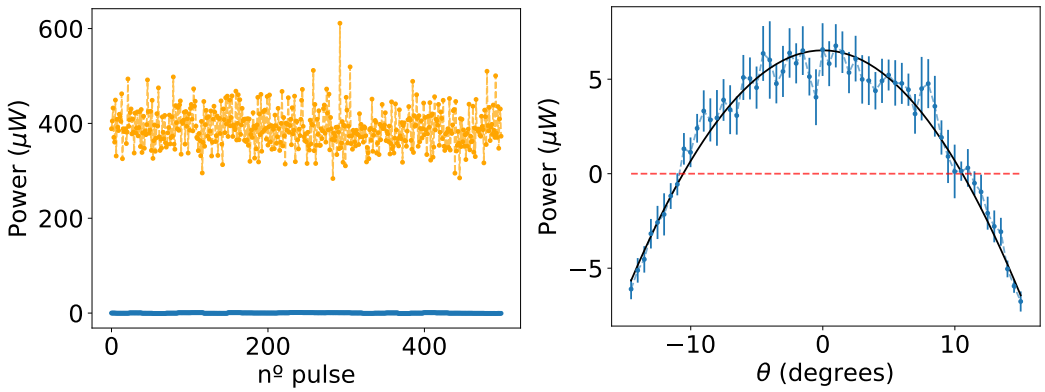

Figure 6.11: **(Left)** Measured pulse power from TOPAS-C. In total, 500 pulses were acquired. The orange dots are the power measured with the fast photodiode and the blue dots, with the balanced photoreceivers. **(Right)** Signal measured using the balanced photodetector for different angles θ of the polarizer. At each θ, 500 pulses were acquired. The blue dots with error bars are experimental data while the black line is resulting fit. The horizontal dashed red line shows the perfect balanced region.

measurement is $\sigma_2 = 0.5\ \mu$W. Thus, the ratio between the signal and full background is:

$$\frac{\sigma_2}{V_0} \approx 3 \cdot 10^{-3} = 0.3\% \ . \tag{6.16}$$

The balanced photodetectors improved the noise-background ratio from 10% of the full scale down to 0.3%. We estimate the rejected common noise (RCN) to be:

$$\mathrm{RCN} = 20 \log_{10}\left(\frac{\sigma_2}{P_{\mathrm{ref}}}\right) - 20 \log_{10}\left(\frac{\sigma_1}{\mu_1}\right) \approx 32\ \mathrm{dB} \ . \tag{6.17}$$

This is lower than what is expected to be the full capacity of the Nirvana auto-balanced photoreceiver. In principle, the rejection of noise could be improved by injecting the beams using optical fibers, instead of free space incidence. There is a chance that the detector is broken. In fact, the device shows a weird behavior: when more light goes to the signal photodiode than to the reference photodiode, the signal blows up and goes to a DC value. To get it working again, the power ratio needs to be readjusted and the beams have to be blocked, so that the detector has time to completely discharge. Only then it responds again. This behavior is unexpected and its origin is unknown to us.

Is the balanced detector + boxcar averager system sensitive enough to detect SPPs? It is difficult to answer this question, but it is possible to estimate the sensitivity of the measurement in a best case scenario. To detect SPPs with a SNR = 10, the detection must be sensitive to changes of the order of:

$$\frac{P_{\mathrm{sig}} - P_{\mathrm{ref}}}{P_{\mathrm{ref}}} \sim 10^{-5} \tag{6.18}$$

in magnitude. For this to be possible, noise must be lowered to:

$$20\log_{10}\left(10^{-5}\right) - 20\log_{10}\left(\frac{\sigma_2}{P_{\text{ref}}}\right) \approx -50 \text{ dB} . \tag{6.19}$$

Considering laser noise only and assuming that it behaves as a white noise, to remove 50 dB of noise, the number of acquired pulses N must be at least (see Appendix K):

$$N = \left(\frac{\sigma_2/P_{\text{ref}}}{10^{-5}}\right)^2 = 10^4 . \tag{6.20}$$

6.6 Problems to be solved

A lot of work still needs to be done in order to be capable of generating and detecting SPPs. According to the estimates from the previous section, to detect changes of the order of 10^{-5}, we need to acquire about 10^4 pulses. We have performed performed the experiment in these conditions, but never saw a signal that corresponded to either SPP generation or hot electrons. Clearly, more pulses need to be integrated to improve the statistics. The problem is that it takes approximately 6 minutes to acquire 10^4 pulses, so, if for example we want to increase the acquisition number by a factor of 5, the acquisition time would increase to 30 minutes and the experiment would take too much time. Thus, data acquisition must be improved and to do this, the timeout error mentioned in Subsection 6.5.1 must be fixed.

Moreover, the amplifier needs to be fixed: the origin of the instability must be found and corrected. This will change the conditions and will require a fine tune of TOPAS-C, which will have to be calibrated again. Finally, we must find an easy way of knowing if the pulses arrive at the sample at the same time. Using a NL crystal, such as BBO, this is easily done by finding the SF-signal, generated when the pulses are superimposed in time. However, this approach only works for small incident angles. For larger angles, the phase match condition is never satisfied.

Chapter 7

Conclusions and outlook

This master thesis focused on understanding the nonlinear generation of SPPs in graphene, using high intensity 100 fs pulses. A theoretical model was proposed to explain the observations in Ref. [1] and experimental work was also carried out in an attempt to study the process in more detail.

In the first part, we attempted to understand the second-order NL response of graphene and how one could leverage this response to excite SPPs. In particular, the DF conductivity was calculated using perturbation theory. The obtained formulae, derived in Chapter 3, predict a response three orders of magnitude weaker than the experimentally estimated value, thus suggesting that a perturbative treatment of the problem is not quite correct. In search for an answer, we studied the dynamics of non-equilibrium carriers in graphene and employed a hot electron model to describe this dynamics using few adjustable parameters, presented in Chapter 4. The model correctly predicts the change in reflectivity of the probe beam in agreement with experiment. The best fitted value of the carrier-carrier scattering time is somewhat shorter than usually reported in the literature, however, our fitting could be affected by deviations of the experimental pulse shape from the assumed Gaussian one.

The transient conductivity with a negative real part, resulting from the population inversion described by the hot electron model, opens the possibility for optical gain and plasmonic amplification. With this in mind, in Chapter 5, we studied the dynamical dispersion relation of the SPPs and proposed plasmon lasing to explain experimental results [1]. The evolution of the SPP population was described by a master equation which included stimulated emission, decay of plasmons and their generation by the difference-frequency process. The latter was described as an effective third-order interaction between fields, mediated by the electrons in graphene, similar to Raman scattering, with the rate calculated using the Fermi's Golden Rule. This process, beyond plasmons, produces photons of frequency ω_a and is stimulated by those of the probe beam, reflected by the substrate. Assuming coherence of the generated and reflected photons, we have been able to explain, for the first time, the strong differential reflectance signal observed in Ref. [1]. The key point is that plasmons of different momenta and energies, which are generated by hot carriers' relaxation, facilitate the resonant difference-frequency process that leads to the enhanced generation of a particular type of SPPs [10]

and also results in the strongly altered variation of the intensity of the probe beam.

In the second part, we explored several methods for SPP generation and detection, using 100 fs pulses. Given the characteristics of our lab, the best approach to generate SPPs by the DF process was to use the TOPAS-C device to control the frequency difference between pump and probe. We determined that the lock-in amplifier was sensitive enough to detect the changes in the order of 10^{-5}, but it is not the best method to detect SPPs if the TOPAS-C is unstable, since the lock-in can not remove the TOPAS-C signal fluctuations. We then proceeded to use a balanced photodetection scheme in combination with a fast photodiode and two boxcar avargers to normalize the measurement. This approach has not fully succeeded yet, but the performed tests yielded positive results. If we are capable of stabilizing TOPAS-C output and improving the speed of data acquisition, we should be able to see changes in the reflectivity of magnitude 10^{-5}, enough to see SPPs. Another possibility of detection of the generated surface plasmons is converting them into propagating far-IR photons using e.g. an Atomic Force Microscope tip placed outside of the generation spot, as it was done in the first works where graphene SPPs were observed [25, 26]. Unfortunately, this is beyond our experimental capacities, but we suggested it to other experimental groups in our publication [9].

Appendix A

SPP basics

A.1 Maxwell's equations and boundary conditions

In Gaussian units, Maxwell's equations are:

$$\nabla \cdot \mathbf{D} = 4\pi\rho_s \ , \tag{A.1}$$

$$\nabla \cdot \mathbf{B} = 0 \ , \tag{A.2}$$

$$\nabla \times \mathbf{H} = \frac{1}{c}\partial_t \mathbf{D} + \frac{4\pi}{c}\mathbf{J}_s \ , \tag{A.3}$$

$$\nabla \times \mathbf{E} = -\frac{1}{c}\partial_t \mathbf{B} \ , \tag{A.4}$$

where $\mathbf{E}$ and $\mathbf{H}$ are the electric and magnetic fields, respectively, while $\mathbf{D}$ is the electric displacement field and $\mathbf{B}$ is the magnetic induction. Furthermore, ρ_s and $\mathbf{J}_s$ are the free charge and current densities, in our case the surface charge and current from graphene. Boundary conditions at an interface between two media are:

$$\mathbf{n} \times (\mathbf{E}_2 - \mathbf{E}_1) = 0 \ , \tag{A.5}$$

$$\mathbf{n} \times (\mathbf{H}_2 - \mathbf{H}_1) = \frac{4\pi}{c}\mathbf{J}_s \ , \tag{A.6}$$

$$\mathbf{n} \cdot (\mathbf{D}_2 - \mathbf{D}_1) = 4\pi\rho_s \ , \tag{A.7}$$

$$\mathbf{n} \cdot (\mathbf{B}_2 - \mathbf{B}_1) = 0 \ , \tag{A.8}$$

with $\mathbf{n}$ denoting the normal to the interface.

The relations between the fields, polarization $\mathbf{P}$ and magnetization $\mathbf{M}$ are given by the constitutive relations,

$$\mathbf{D} = \mathbf{E} + 4\pi\mathbf{P} \ , \tag{A.9}$$

$$\mathbf{H} = \mathbf{B} - 4\pi\mathbf{M} \ . \tag{A.10}$$

A.2 SPP field relations

In this Section, using Maxwell's equations, we derive the relation between field components for the SPP field in Eq. (2.1). Consider a graphene sheet between two dielectric, medium 2 ($z < 0$) and medium 1 ($z > 0$). From Maxwell's Eq. (A.3) we find:

$$iqE_{m,z} + (-1)^{m+1}\kappa_m E_{m,x} = -i\frac{\omega}{c}H_{m,y} \ , \tag{A.11}$$

while from (A.4), setting $J_f = 0$,

$$(-1)^{m+1}\kappa_m H_{m,y} = -i\frac{\omega\varepsilon_m}{c}E_{m,x} \ , \tag{A.12}$$

$$iqH_{m,y} = -i\frac{\omega\varepsilon_m}{c}E_{m,z} \ . \tag{A.13}$$

Combining (A.11), (A.12) and (A.13), the relations between field components are:

$$H_{m,y} = -(-1)^{m+1}i\frac{\omega\varepsilon_m}{c\kappa_m}E_{m,x} \ , \tag{A.14}$$

$$E_{m,z} = -\frac{qc}{\omega\varepsilon_m}H_{m,y} = i(-1)^{m+1}\frac{q}{\kappa_m}E_{m,x} \ , \tag{A.15}$$

and the wave number is,

$$\kappa_m^2 = q^2 - \frac{\omega^2}{c}\varepsilon_m \ . \tag{A.16}$$

The SPP dispersion equation can be determined from the boundary conditions (A.5) and (A.7). In terms of the electric field, these conditions are:

$$\begin{cases} \varepsilon_1 E_{1,z}e^{iqx}e^{-i\omega t} - \varepsilon_2 E_{2,z}e^{iqx}e^{-i\omega t} = 4\pi\rho_s \\ E_{1,x} - E_{2,x} = 0 \end{cases} \ , \tag{A.17}$$

or using the relation (A.15) between field components:

$$\left(\frac{\varepsilon_2}{\kappa_2} + \frac{\varepsilon_1}{\kappa_1}\right)E_{2,x}e^{iqx}e^{-i\omega t} = -\frac{4\pi i}{q}\rho_s \ . \tag{A.18}$$

Since it is expected that the surface charge density responds periodically, one can expand it in a Fourier series:

$$\rho_s = \sum_j \rho(\omega_j, q_j)e^{i(q_j x - \omega_j t)} \ . \tag{A.19}$$

From the continuity equation, its Fourier components are related to the Fourier components of the surface current:

$$\rho(\omega_j, q_j) = \frac{q_j}{\omega_j}j_x(\omega_j, q_j) \ . \tag{A.20}$$

Therefore, as a consequence of the orthogonality between $e^{i(q_j x - \omega_j t)}$, Eq. (A.18) yields:

$$\frac{\varepsilon_2}{\kappa_2} + \frac{\varepsilon_1}{\kappa_1} = -\frac{4\pi i}{\omega E_{2,x}} j_x(\omega, q) \ . \tag{A.21}$$

For a linear response, the current relates to the electric field according to:

$$j_x(\omega, q) = \sigma^{(1)}(\omega, q) E_{2,x} \ , \tag{A.22}$$

so the above equation gives the SPP dispersion equation:

$$D(\omega, q) = \frac{\varepsilon_2}{\kappa_2} + \frac{\varepsilon_1}{\kappa_1} + \frac{4\pi i}{\omega} \sigma^{(1)}(\omega, q) = 0 \ . \tag{A.23}$$

Appendix B

Optical response of graphene

B.1 Density matrix perturbation theory formalism

Consider the system's Hamiltonian (electron+light) to be of the form:

$$\hat{H} = \hat{H}_0 + \hat{V}_{\text{int}} \ , \tag{B.1}$$

where $\hat{H}_0 = v_F \boldsymbol{\sigma} \cdot \mathbf{p}$ is the single electron Hamiltonian and $\hat{V}_{\text{int}}$ is the interaction term between the electromagnetic field and the electrons in graphene. If $\hat{\rho}$ is the density matrix of the system, its time evolution is given by:

$$\partial_t \rho_{nm} = -\frac{i}{\hbar}[\hat{H}, \hat{\rho}]_{nm} - \gamma_{nm}\left(\rho_{nm} - \rho_{nm}^{(\text{eq})}\right) \ , \tag{B.2}$$

where $\rho_{nm}^{(\text{eq})}$ is the density matrix at equilibrium. Here γ_{nm} are phenomenological decay rates and we assume $\gamma_{nm} = \gamma_{mn}$. In addition, we make the physical assumption:

$$\rho_{nm}^{(\text{eq})} = \delta_{nm} f(\varepsilon_n) \ , \tag{B.3}$$

where $f(\varepsilon)$ is the Fermi-Dirac distribution or possibly a quasi-equilibrium distribution that is a slowly varying function of time.

We now follow a perturbative approach and write the full Hamiltonian as:

$$\hat{H} = \hat{H}_0 + \lambda \hat{V}_{\text{int}} \ , \tag{B.4}$$

where the second term is treated as a perturbation with λ appearing as a perturbation parameter that is set equal to one at the end. We expand the density matrix in powers of λ:

$$\rho_{nm} = \rho_{nm}^{(0)} + \lambda \rho_{nm}^{(1)} + \lambda^2 \rho_{nm}^{(2)} + ... \tag{B.5}$$

Substituting expansion (B.5) and the expression (B.4) for the Hamiltonian into Eq. (B.2) and

grouping terms of the same order in λ, we find for zeroth order:

$$\partial_t \rho_{nm}^{(0)} = -\frac{i}{\hbar}[\hat{H}_0, \hat{\rho}^{(0)}]_{nm} - \gamma_{nm}\left(\rho_{nm}^{(0)} - \rho_{nm}^{(\mathrm{eq})}\right) \tag{B.6}$$

and for N-th order:

$$\partial_t \rho_{nm}^{(N)} = -\frac{i}{\hbar}[\hat{H}_0, \hat{\rho}^{(N)}]_{nm} - \frac{i}{\hbar}[\hat{V}_{\mathrm{int}}, \hat{\rho}^{(N-1)}]_{nm} - \gamma_{nm}\rho_{nm}^{(N)} \qquad , N > 0 \ . \tag{B.7}$$

The commutator $[\hat{H}_0, \hat{\rho}^{(N)}]_{nm}$ is easy to calculate since we know unperturbed eigenfunction and eigenvalues:

$$[\hat{H}_0, \hat{\rho}^{(N)}]_{nm} = (\varepsilon_n - \varepsilon_m)\, \rho_{nm}^{(N)} \ .$$

Equation (B.6) becomes:

$$\partial_t \rho_{nm}^{(0)} = -\frac{i}{\hbar}(\varepsilon_n - \varepsilon_m)\, \rho_{nm}^{(0)} - \gamma_{nm}\left(\rho_{nm}^{(0)} - \rho_{nm}^{(\mathrm{eq})}\right) \ . \tag{B.8}$$

This equation describes the time evolution of the system in the absence of any external field, so it has as solution the system in equilibrium:

$$\rho_{nm}^{(0)} = \rho_{nm}^{(\mathrm{eq})} = \delta_{nm} f(\varepsilon_n) \ . \tag{B.9}$$

Equation (B.7) becomes:

$$\partial_t \rho_{nm}^{(N)} = -(i\omega_{nm} + \gamma_{nm})\, \rho_{nm}^{(N)} - \frac{i}{\hbar}[\hat{V}_{\mathrm{int}}, \hat{\rho}^{(N-1)}]_{nm} \ , \tag{B.10}$$

with $\omega_{nm} = (\varepsilon_n - \varepsilon_m)/\hbar$ and has the solution:

$$\rho_{nm}^{(N)}(t) = \rho_{nm}^{(N)}(-\infty) - \frac{i}{\hbar}\int_{-\infty}^{t} dt' [\hat{V}_{\mathrm{int}}, \hat{\rho}^{(N-1)}]_{nm} e^{(i\omega_{nm}+\gamma_{nm})(t'-t)} \ . \tag{B.11}$$

B.2 Linear optical response of graphene

Here we shall derive graphene's linear optical conductivity in the long-wavelength limit. To avoid any divergence, the calculation is done in the length gauge[1] [21, 22]. Consider a graphene sheet that is being impinged by an electric field of the form:

$$E_x(t) = \frac{E_0}{2} e^{-i\omega t} + \mathrm{c.c} \ . \tag{B.12}$$

[1] Actually, the calculation can also be done in the velocity gauge, but it requires considering electronic states that depend on the effective momentum $(\hbar\mathbf{k} + e\mathbf{A}/c)$ and is less straightforward.

In the length gauge, the interaction term is written:

$$\hat{V}_{\text{int}} = exE_x(t) \ . \tag{B.13}$$

To determine the linear response, Eq. (B.11) must be solved for $N = 1$:

$$\rho^{(1)}_{nm}(t) = -\frac{i}{\hbar}\left(f(\varepsilon_m) - f(\varepsilon_n)\right)\int_{-\infty}^{t} dt' V_{nm}(t') e^{(i\omega_{nm}+\gamma_{nm})(t'-t)} \ . \tag{B.14}$$

The evaluation of V_{nm} is a bit tricky because the operator x is not well defined in momentum space. From Refs. [7, 20, 21]:

$$\begin{aligned}\langle \mathbf{k}_1, s_1|x|\mathbf{k}_2, s_2\rangle &= \frac{(2\pi)^2}{iA}\delta_{s_1,s_2}\frac{\partial}{\partial k_{2,x}}\delta\left(\mathbf{k}_1 - \mathbf{k}_2\right) - \frac{(2\pi)^2}{A}\frac{\sin\theta_1}{2k_1}\left(1-\delta_{s_1,s_2}\right)\delta\left(\mathbf{k}_1 - \mathbf{k}_2\right) \\ &= F_{s_1,s_2}(\mathbf{k}_1, \mathbf{k}_2) \ .\end{aligned} \tag{B.15}$$

Consequently, the matrix elements V_{nm} are:

$$V_{nm}(t) = eF_{s_n,s_m}(\mathbf{k}_n, \mathbf{k}_m)\frac{E_0}{2}e^{-i\omega t} + eF_{s_n,s_m}(\mathbf{k}_n, \mathbf{k}_m)\frac{E_0^*}{2}e^{i\omega t} \tag{B.16}$$

and Eq. (B.14) gives:

$$\rho^{(1)}_{nm}(t) = -\frac{ie}{\hbar}\left(f(\varepsilon_m) - f(\varepsilon_n)\right)F_{s_n,s_m}(\mathbf{k}_n, \mathbf{k}_m)\left(\frac{E_0}{2}\frac{e^{-i\omega t}}{\gamma_{nm} + i\left(\omega_{nm} - \omega\right)} + \frac{E_0^*}{2}\frac{e^{i\omega t}}{\gamma_{nm} + i\left(\omega_{nm} + \omega\right)}\right) \ . \tag{B.17}$$

The x-component of the current operator is:

$$\hat{j}_x = -ev_F\sigma_x \ , \tag{B.18}$$

so the averaging yields:

$$\begin{aligned} j_x &= \text{Tr}\left(\hat{j}_x\hat{\rho}^{(1)}\right) \\ &= \frac{ie^2v_F}{\hbar}\sum_{s_\nu\mathbf{k}_\nu}\sum_{s_n,\mathbf{k}_n}\left(f(\varepsilon_\nu) - f(\varepsilon_n)\right)F_{s_n,s_\nu}(\mathbf{k}_n, \mathbf{k}_\nu)\left(\frac{E_0}{2}\frac{e^{-i\omega t}}{\gamma_{n\nu} + i\left(\omega_{n\nu} - \omega\right)} + \frac{E_0^*}{2}\frac{e^{i\omega t}}{\gamma_{n\nu} + i\left(\omega_{n\nu} + \omega\right)}\right)\sigma^x_{\nu n} \\ &= \frac{1}{2}j(\omega)e^{-i\omega t} + \frac{1}{2}j^*(\omega)e^{i\omega t} \ . \end{aligned} \tag{B.19}$$

By definition the conductivity is:

$$j_x(\omega) = \sigma(\omega)E_0(\omega) \tag{B.20}$$

so:

$$\sigma(\omega) = \frac{ie^2 v_F}{\hbar} \sum_{s_\nu \mathbf{k}_\nu} \sum_{s_n, \mathbf{k}_n} \left(f(\varepsilon_\nu) - f(\varepsilon_n)\right) F_{s_n,s_\nu}(\mathbf{k}_n, \mathbf{k}_\nu) \frac{\sigma^x_{\nu n}}{\gamma_{n\nu} + i\left(\omega_{n\nu} - \omega\right)} \ . \tag{B.21}$$

We now consider separately, interband and intraband contributions.

B.2.1 Intraband conductivity

The intraband contributions correspond to terms with $s_\nu = s_n = \pm 1$. Equation (B.21) yields:

$$\sigma_{\text{intra}}(\omega) = \frac{ie^2 v_F}{\hbar} \sum_{s_n} \sum_{\mathbf{k}_\nu \mathbf{k}_n} \left(f(\varepsilon_{s_n}(\mathbf{k}_\nu)) - f(\varepsilon_{s_n}(\mathbf{k}_n))\right) F_{s_n,s_n}(\mathbf{k}_n, \mathbf{k}_\nu) \frac{\sigma^x_{s_n s_n}(\mathbf{k}_\nu, \mathbf{k}_n)}{\gamma_{n\nu} + i\left(\omega_{s_n,s_n}(\mathbf{k}_n, \mathbf{k}_\nu) - \omega\right)} \ . \tag{B.22}$$

We simplify the problem and write the same damping parameter γ_p (electron momentum relaxation rate) for all states. Furthermore, the matrix element $F_{s_n,s_n}(\mathbf{k}_n, \mathbf{k}_\nu)$ for intraband transitions is simply:

$$F_{s_n,s_n}(\mathbf{k}_n, \mathbf{k}_\nu) = -\frac{(2\pi)^2}{iA} \delta_{s_n,s_n} \delta\left(\mathbf{k}_n - \mathbf{k}_\nu\right) \frac{\partial}{\partial k_{n,x}} \ , \tag{B.23}$$

so Eq. (B.22) becomes:

$$\sigma_{\text{intra}}(\omega) = -\frac{e^2 v_F}{\hbar A} \sum_{\mathbf{k}} \left(\frac{\partial}{\partial k_x} f_c(\varepsilon(\mathbf{k})) \frac{\sigma^x_{1,1}(\mathbf{k}, \mathbf{k})}{\gamma - i\omega} + \frac{\partial}{\partial k_x} f_v(\varepsilon(\mathbf{k})) \frac{\sigma^x_{-1,-1}(\mathbf{k}, \mathbf{k})}{\gamma - i\omega} \right) \ . \tag{B.24}$$

Replacing the sum by integration, Eq. (B.24) simplifies to :

$$\sigma_{\text{intra}}(\omega) = -\frac{e^2}{2\pi h} \frac{4\pi}{\hbar\gamma - i\hbar\omega} \int_0^\infty d\varepsilon \varepsilon \left(\frac{\partial}{\partial \varepsilon} f_c(\varepsilon) - \frac{\partial}{\partial \varepsilon} f_v(\varepsilon) \right) \ .$$

Introducing:

$$\sigma_0 = \frac{\pi e^2}{2h} \ , \tag{B.25}$$

allows us to write $\sigma_{\text{intra}}(\omega)$ as:

$$\sigma_{\text{intra}}(\omega) = -\frac{4\sigma_0}{\pi} \frac{1}{\hbar\gamma - i\hbar\omega} \int_0^\infty d\varepsilon \varepsilon \left(\frac{\partial}{\partial \varepsilon} f_c(\varepsilon) - \frac{\partial}{\partial \varepsilon} f_v(\varepsilon) \right) \ . \tag{B.26}$$

The integral has analytical solution, if f_c and f_v are Fermi like distributions. Consider the more general situation of quasi-equilibrium:

$$f_c = \frac{1}{1 + \exp\left(\dfrac{\varepsilon - F_e}{k_B T}\right)} \quad , \quad f_v = \frac{1}{1 + \exp\left(-\dfrac{\varepsilon + F_h}{k_B T}\right)} \ , \tag{B.27}$$

where F_e and F_h the electron and hole chemical potentials, respectively and T the temperature. In this regime the integral in (B.26) yields the analytical expression:

$$\sigma_{\text{intra}}(\omega) = \frac{4\sigma_0 i}{\pi} \frac{k_B T}{\hbar\left(\omega + i\gamma_p\right)} \ln\left\{\left(1 + e^{F_e/k_B T}\right)\left(1 + e^{-F_h/k_B T}\right)\right\} \ . \tag{B.28}$$

The equilibrium regime is easily obtained by setting $F_e = F_h = E_F$.

B.2.2 Interband conductivity

The interband contributions correspond to the terms with $s_\nu = -s_n = \pm 1$. For this case we set $\gamma_{nm} = \gamma_{\text{inter}}$. Equation (B.21) yields:

$$\begin{aligned}\sigma_{\text{inter}}(\omega) = &\frac{ie^2 v_F}{\hbar} \sum_{\mathbf{k}_\nu, \mathbf{k}_n} \left(f_c(\varepsilon_{\mathbf{k}_\nu}) - f_v(\varepsilon_{\mathbf{k}_n})\right) F_{-1,1}(\mathbf{k}_n, \mathbf{k}_\nu) \frac{\sigma^x_{1,-1}(\mathbf{k}_\nu, \mathbf{k}_n)}{\gamma_{\text{inter}} + i\left(\omega_{-1,1}(\mathbf{k}_n, \mathbf{k}_\nu) - \omega\right)} \\ &+ \frac{ie^2 v_F}{\hbar} \sum_{\mathbf{k}_\nu, \mathbf{k}_n} \left(f_v(\varepsilon_{\mathbf{k}_\nu}) - f_c(\varepsilon_{\mathbf{k}_n})\right) F_{1,-1}(\mathbf{k}_n, \mathbf{k}_\nu) \frac{\sigma^x_{-1,1}(\mathbf{k}_\nu, \mathbf{k}_n)}{\gamma_{\text{inter}} + i\left(\omega_{1,-1}(\mathbf{k}_n, \mathbf{k}_\nu) - \omega\right)} \ .\end{aligned} \tag{B.29}$$

Since:

$$F_{-1,1}(\mathbf{k}_n, \mathbf{k}_\nu) = F_{1,-1}(\mathbf{k}_n, \mathbf{k}_\nu) = -\frac{(2\pi)^2}{A} \frac{\sin\theta_n}{2k_n} \delta\left(\mathbf{k}_n - \mathbf{k}_\nu\right) \tag{B.30}$$

and:

$$\omega_{1,-1}(\mathbf{k}_n, \mathbf{k}_\nu) = -\omega_{-1,1}(\mathbf{k}_n, \mathbf{k}_\nu) = v_F(k_n + k_\nu) \ , \tag{B.31}$$

Eq. (B.29) simplifies to:

$$\sigma_{\text{inter}}(\omega) = \frac{e^2 v_F}{\hbar} \sum_{\mathbf{k}} \frac{\sin^2\theta}{2k} \left(\frac{f_v(\varepsilon_{\mathbf{k}}) - f_c(\varepsilon_{\mathbf{k}})}{\gamma_{\text{inter}} - i\left(2v_F k + \omega\right)} + \frac{f_v(\varepsilon_{\mathbf{k}}) - f_c(\varepsilon_{\mathbf{k}})}{\gamma_{\text{inter}} + i\left(2v_F k - \omega\right)}\right) \ . \tag{B.32}$$

Replacing the sum by integration:

$$\sigma_{\text{inter}}(\omega) = \frac{2\sigma_0}{\pi} \int_0^\infty d\varepsilon \left(f_v(\varepsilon) - f_c(\varepsilon)\right) \left(\frac{1}{\hbar\gamma_{\text{inter}} - i\left(2\varepsilon + \hbar\omega\right)} + \frac{1}{\hbar\gamma_{\text{inter}} + i\left(2\varepsilon - \hbar\omega\right)}\right) \ . \tag{B.33}$$

In equilibrium, at zero temperature Eq. (B.33) yields:

$$\sigma_{\text{inter}}(\omega) = \sigma_0 \left(1 + \frac{1}{\pi}\arctan\frac{\hbar\omega - 2E_F}{\hbar\gamma_{\text{inter}}} - \frac{1}{\pi}\arctan\frac{\hbar\omega + 2E_F}{\hbar\gamma_{\text{inter}}}\right) - \frac{i\sigma_0}{2\pi} \ln\left(\frac{\left(\hbar\gamma_{\text{inter}}\right)^2 + \left(2E_F + \hbar\omega\right)^2}{\left(\hbar\gamma_{\text{inter}}\right)^2 + \left(2E_F - \hbar\omega\right)^2}\right) \ .$$

In quasi-equilibrium, taking the zero-temperature limit, a simple expression is also obtained:

$$\begin{aligned}\sigma_{\text{inter}}(\omega) = \sigma_0 &\left(1 + \frac{1}{\pi}\arctan\frac{\hbar\omega - 2F_e}{\hbar\gamma_{\text{inter}}} - \frac{1}{\pi}\arctan\frac{\hbar\omega + 2F_e}{\hbar\gamma_{\text{inter}}}\right) \\ &+ \sigma_0\left(\frac{1}{\pi}\arctan\frac{\hbar\omega - 2|F_h|}{\hbar\gamma_{\text{inter}}} - \frac{1}{\pi}\arctan\frac{\hbar\omega + 2|F_h|}{\hbar\gamma_{\text{inter}}}\right) \\ &- \frac{i\sigma_0}{2\pi}\ln\left(\frac{(\hbar\gamma_{\text{inter}})^2 + (2|F_h| + \hbar\omega)^2}{(\hbar\gamma_{\text{inter}})^2 + (2|F_h| - \hbar\omega)^2}\right) - \frac{i\sigma_0}{2\pi}\ln\left(\frac{(\hbar\gamma_{\text{inter}})^2 + (2F_e + \hbar\omega)^2}{(\hbar\gamma_{\text{inter}})^2 + (2F_e - \hbar\omega)^2}\right) \ . \end{aligned} \tag{B.34}$$

This is similar to the equilibrium result, but with the additional contribution from the holes. Nonetheless, there is a crucial difference. In the limit $\gamma_{\text{inter}} \to 0$ (no interband losses) and $\omega \to 0$, $\sigma_{\text{inter}}(\omega)$ yields a negative value:

$$\lim_{\gamma_{\text{inter}},\omega\to 0} \sigma_{\text{inter}}(\omega) = -\sigma_0 \ .$$

This is different from the equilibrium situation, where the conductivity should yield zero. The fact that the real part of the interband conductivity is negative implies that the solution for ω and q from the SPP dispersion equation are complex. Physically, it represents gain, i.e. generation of photons.

In real situations $\hbar\gamma_{\text{inter}} \ll k_B T$ so, in the limit $\gamma_{\text{inter}} \to 0$, Eq. (B.33) has the analytical form:

$$\sigma_{\text{inter}}(\omega) = \sigma_0 \frac{\sinh\left[\dfrac{\hbar\omega - (F_e - F_h)}{2k_B T}\right]}{\cosh\left[\dfrac{F_h + F_e}{2k_B T}\right] + \cosh\left[\dfrac{\hbar\omega - (F_e - F_h)}{2k_B T}\right]} \ . \tag{B.35}$$

B.3 Second order conductivity

In this section we derive the expressions (3.20), (3.23) and (3.24) for DF conductivity. We start by determining the general expression (3.14) for second order conductivity. The calculation is performed in the velocity gauge to account for effects of spatial dispersion:

$$\hat{H} = v_F \boldsymbol{\sigma} \cdot \left(\mathbf{p} + \frac{e}{c}\mathbf{A}(t, \mathbf{r})\right) \ , \tag{B.36}$$

where $\mathbf{A}(t, \mathbf{r})$ is the vector potential. The interaction term is:

$$\hat{V}_{\text{int}} = \frac{e v_F}{c} \boldsymbol{\sigma} \cdot \mathbf{A}(t, \mathbf{r}) \ . \tag{B.37}$$

We expand $\mathbf{A}(t, \mathbf{r})$ in plane waves:

$$\mathbf{A}(t, \mathbf{r}) = \frac{1}{2}\sum_{\mathbf{q}} \left(\mathbf{A}\left(\omega_q, \mathbf{q}\right) e^{i(\mathbf{q}\cdot\mathbf{r} - \omega_q t)} + \text{c.c}\right) \ . \tag{B.38}$$

For each frequency ω_q, there is a wave-vector $\mathbf{q}$ associated to it. Since the field is real, its Fourier components satisfy the relation $\mathbf{A}(\omega_q, \mathbf{q}) = \mathbf{A}^*(-\omega_q, -\mathbf{q})$. We work in the gauge where the electrostatic potential is zero and $\nabla \cdot \mathbf{A} = 0$. Then, by definition, the electric field is $\mathbf{E}(t) = -(1/c)\,\partial_t \mathbf{A}(t)$ and the relation between the Fourier components is:

$$\mathbf{E}(\omega_q, \mathbf{q}) = \frac{i\omega_q}{c}\mathbf{A}(\omega_q, \mathbf{q}) \ . \tag{B.39}$$

The calculation of the second-order response in graphene is performed using the density matrix formalism. To determine the second order conductivity, Eq. (B.11) needs to be solved for $N = 2$. Using Eq. (B.17) we find:

$$\begin{aligned}\rho^{(2)}_{nm}(t) = &\left(\frac{e}{2\hbar}\right)^2 \sum_l \sum_{\mathbf{q}} \sum_{\mathbf{p}} \frac{f(\varepsilon_l) - f(\varepsilon_n)}{\omega_q \omega_p} \frac{v^j_{nl\mathbf{p}} v^i_{lm\mathbf{q}}}{\omega_{nl} - \omega_p - i\gamma_{nl}} \frac{E_j(\omega_p, \mathbf{p}) E_i(\omega_q, \mathbf{q})}{\omega_{nm} - (\omega_p + \omega_q) - i\gamma_{nm}} e^{-i(\omega_p + \omega_q)t} \\ &- \left(\frac{e}{2\hbar}\right)^2 \sum_l \sum_{\mathbf{q}} \sum_{\mathbf{p}} \frac{f(\varepsilon_m) - f(\varepsilon_l)}{\omega_q \omega_p} \frac{v^i_{nl\mathbf{q}} v^j_{lm\mathbf{p}}}{\omega_{lm} - \omega_p - i\gamma_{lm}} \frac{E_j(\omega_p, \mathbf{p}) E_i(\omega_q, \mathbf{q})}{\omega_{nm} - (\omega_p + \omega_q) - i\gamma_{nm}} e^{-i(\omega_p + \omega_q)t} \ ,\end{aligned} \tag{B.40}$$

where $v^j_{mn\mathbf{q}} = v_F \langle m | \sigma^j e^{i\mathbf{r}\cdot\mathbf{q}} | n \rangle$ are the matrix elements of the spatially modulated velocity operator. In Eq. (B.40) the Einstein summation convention is used.

The single particle current operator is:

$$\mathbf{J}(\mathbf{r}_0, t) = -e\mathbf{v}\delta(\mathbf{r} - \mathbf{r}_0) = -\frac{e}{\mathcal{S}}\mathbf{v} \sum_{\mathbf{u}} e^{i\mathbf{u}(\mathbf{r} - \mathbf{r}_0)} \ , \tag{B.41}$$

with $\mathcal{S}$ being the area of the graphene sheet and $\mathbf{r}_0$ the particle's position. The second order contribution to the expectation value of the this operator is:

$$\begin{aligned}\langle J^k \rangle &= \mathrm{Tr}\left(\rho^{(2)} J^k(\mathbf{r}_0, t)\right) \\ &= \frac{e^3}{(2\hbar)^2 \mathcal{S}} \sum_{nml} \sum_{\mathbf{q}} \sum_{\mathbf{p}} \sum_{\mathbf{u}} \frac{f(\varepsilon_m) - f(\varepsilon_l)}{\omega_p \omega_q} \frac{v^i_{nl\mathbf{q}} v^j_{lm\mathbf{p}} v^k_{mn\mathbf{u}}}{\omega_{lm} - \omega_p - i\gamma_{lm}} \frac{E_j(\omega_p, \mathbf{p}) E_i(\omega_q, \mathbf{q})}{\omega_{nm} - (\omega_p + \omega_q) - i\gamma_{nm}} e^{-i(\omega_p + \omega_q)t} e^{-i\mathbf{u}\cdot\mathbf{r}_0} \\ &- \frac{e^3}{(2\hbar)^2 \mathcal{S}} \sum_{nml} \sum_{\mathbf{q}} \sum_{\mathbf{p}} \sum_{\mathbf{u}} \frac{f(\varepsilon_l) - f(\varepsilon_n)}{\omega_p \omega_q} \frac{v^j_{nl\mathbf{p}} v^i_{lm\mathbf{q}} v^k_{mn\mathbf{u}}}{\omega_{nl} - \omega_p - i\gamma_{nl}} \frac{E_j(\omega_p, \mathbf{p}) E_i(\omega_q, \mathbf{q})}{\omega_{nm} - (\omega_p + \omega_q) - i\gamma_{nm}} e^{-i(\omega_p + \omega_q)t} e^{-i\mathbf{u}\cdot\mathbf{r}_0} \ .\end{aligned} \tag{B.42}$$

The matrix elements $v^i_{nl\mathbf{q}}v^j_{lm\mathbf{p}}v^k_{mn\mathbf{u}}$ impose momentum conservation relations that cancel out the summation over $\mathbf{u}$, that is $\mathbf{u} = -(\mathbf{q}+\mathbf{p})$. Therefore, expression (B.42) is rewritten as:

$$\begin{aligned}\langle J^k\rangle = &\frac{(ev_F)^3}{4\hbar^2\mathcal{S}}\sum_{nml}\sum_{\mathbf{q}}\sum_{\mathbf{p}}\frac{f(\varepsilon_m)-f(\varepsilon_l)}{\omega_q\omega_p}\frac{\sigma^i_{nl\mathbf{q}}\sigma^j_{lm\mathbf{p}}\sigma^k_{mn-(\mathbf{q}+\mathbf{p})}}{\omega_{lm}-\omega_p-i\gamma_{lm}}\frac{E_j(\omega_p,\mathbf{p})E_i(\omega_q,\mathbf{q})}{\omega_{nm}-(\omega_p+\omega_q)-i\gamma_{nm}}e^{-i(\omega_p+\omega_q)t}e^{i(\mathbf{q}+\mathbf{p})\cdot\mathbf{r}_0}\\ &-\frac{(ev_F)^3}{4\hbar^2\mathcal{S}}\sum_{nml}\sum_{\mathbf{q}}\sum_{\mathbf{p}}\frac{f(\varepsilon_l)-f(\varepsilon_n)}{\omega_q\omega_p}\frac{\sigma^j_{nl\mathbf{p}}\sigma^i_{lm\mathbf{q}}\sigma^k_{mn-(\mathbf{q}+\mathbf{p})}}{\omega_{nl}-\omega_p-i\gamma_{nl}}\frac{E_j(\omega_p,\mathbf{p})E_i(\omega_q,\mathbf{q})}{\omega_{nm}-(\omega_p+\omega_q)-i\gamma_{nm}}e^{-i(\omega_p+\omega_q)t}e^{i(\mathbf{q}+\mathbf{p})\cdot\mathbf{r}_0}\ .\end{aligned} \tag{B.43}$$

Notice that $E_j(\omega_p,\mathbf{p})$ is the total field. It is more convenient to write the incoming fields a and b explicitly:

$$E_j(\omega_p,\mathbf{p}) = E_{b,j}(\omega_p,\mathbf{p}) + E_{a,j}(\omega_p,\mathbf{p})\ . \tag{B.44}$$

Making this substitution in (B.43), terms corresponding to interaction of the field with itself will appear. We are not interested in these, so we truncate them and rewrite (B.43) as:

$$\begin{aligned}\langle J^k\rangle = &\frac{e^3}{4\hbar^2\mathcal{S}}\sum_{nml}\sum_{\mathbf{q}}\sum_{\mathbf{p}}\frac{f(\varepsilon_m)-f(\varepsilon_l)}{\omega_q\omega_p}\frac{v^i_{nl\mathbf{q}}v^j_{lm\mathbf{p}}v^k_{mn-(\mathbf{q}+\mathbf{p})}}{\omega_{lm}-\omega_p-i\gamma_{lm}}\frac{E_{a,j}(\omega_p,\mathbf{p})E_{b,i}(\omega_q,\mathbf{q})}{\omega_{nm}-(\omega_p+\omega_q)-i\gamma_{nm}}e^{-i(\omega_p+\omega_q)t}e^{i(\mathbf{q}+\mathbf{p})\cdot\mathbf{r}_0}\\ &+\frac{e^3}{4\hbar^2\mathcal{S}}\sum_{nml}\sum_{\mathbf{q}}\sum_{\mathbf{p}}\frac{f(\varepsilon_m)-f(\varepsilon_l)}{\omega_q\omega_p}\frac{v^i_{nl\mathbf{q}}v^j_{lm\mathbf{p}}v^k_{mn-(\mathbf{q}+\mathbf{p})}}{\omega_{lm}-\omega_p-i\gamma_{lm}}\frac{E_{b,j}(\omega_p,\mathbf{p})E_{a,i}(\omega_q,\mathbf{q})}{\omega_{nm}-(\omega_p+\omega_q)-i\gamma_{nm}}e^{-i(\omega_p+\omega_q)t}e^{i(\mathbf{q}+\mathbf{p})\cdot\mathbf{r}_0}\\ &-\frac{e^3}{4\hbar^2\mathcal{S}}\sum_{nml}\sum_{\mathbf{q}}\sum_{\mathbf{p}}\frac{f(\varepsilon_l)-f(\varepsilon_n)}{\omega_q\omega_p}\frac{v^j_{nl\mathbf{p}}v^i_{lm\mathbf{q}}v^k_{mn-(\mathbf{q}+\mathbf{p})}}{\omega_{nl}-\omega_p-i\gamma_{nl}}\frac{E_{a,j}(\omega_p,\mathbf{p})E_{b,i}(\omega_q,\mathbf{q})}{\omega_{nm}-(\omega_p+\omega_q)-i\gamma_{nm}}e^{-i(\omega_p+\omega_q)t}e^{i(\mathbf{q}+\mathbf{p})\cdot\mathbf{r}_0}\\ &-\frac{e^3}{4\hbar^2\mathcal{S}}\sum_{nml}\sum_{\mathbf{q}}\sum_{\mathbf{p}}\frac{f(\varepsilon_l)-f(\varepsilon_n)}{\omega_q\omega_p}\frac{v^j_{nl\mathbf{p}}v^i_{lm\mathbf{q}}v^k_{mn-(\mathbf{q}+\mathbf{p})}}{\omega_{nl}-\omega_p-i\gamma_{nl}}\frac{E_{b,j}(\omega_p,\mathbf{p})E_{a,i}(\omega_q,\mathbf{q})}{\omega_{nm}-(\omega_p+\omega_q)-i\gamma_{nm}}e^{-i(\omega_p+\omega_q)t}e^{i(\mathbf{q}+\mathbf{p})\cdot\mathbf{r}_0}\ .\end{aligned} \tag{B.45}$$

The second order conductivity is defined as:

$$J^k(\omega_p+\omega_q,\mathbf{p}+\mathbf{q}) = \frac{1}{2}\sigma^{(2)}_{kji}(\mathbf{\Omega},\mathbf{\Omega}_p,\mathbf{\Omega}_q)E_{b,j}(\omega_p,\mathbf{p})E_{a,i}(\omega_q,\mathbf{q})\ , \tag{B.46}$$

where the vectors $\mathbf{\Omega}_p = (\omega_p,\mathbf{p})$ and $\mathbf{\Omega} = (\omega_p+\omega_q,\mathbf{p}+\mathbf{q})$ are used to simplify the notation. From comparison with (B.45), we conclude that the second order conductivity is:

$$\sigma^{(2)}_{jki}\left(\mathbf{\Omega},\mathbf{\Omega}_p,\mathbf{\Omega}_q\right) = \frac{e^3}{\hbar^2\omega_q\omega_p\mathcal{S}}\sum_{nml}\frac{v^k_{mn-(\mathbf{q}+\mathbf{p})}v^j_{lm\mathbf{p}}v^i_{nl\mathbf{q}}}{\omega_{lm}-\omega_p-i\gamma_{lm}}\frac{f(\varepsilon_m)-f(\varepsilon_l)}{\omega_{nm}-(\omega_p+\omega_q)-i\gamma_{nm}}$$
$$+\frac{e^3}{\hbar^2\omega_q\omega_p\mathcal{S}}\sum_{nml}\frac{v^k_{mn-(\mathbf{q}+\mathbf{p})}v^j_{nl\mathbf{p}}v^i_{lm\mathbf{q}}}{\omega_{lm}-\omega_q-i\gamma_{lm}}\frac{f(\varepsilon_m)-f(\varepsilon_l)}{\omega_{nm}-(\omega_p+\omega_q)-i\gamma_{nm}}$$
$$-\frac{e^3}{\hbar^2\omega_q\omega_p\mathcal{S}}\sum_{nml}\frac{v^k_{mn-(\mathbf{q}+\mathbf{p})}v^j_{nl\mathbf{p}}v^i_{lm\mathbf{q}}}{\omega_{nl}-\omega_p-i\gamma_{nl}}\frac{f(\varepsilon_l)-f(\varepsilon_n)}{\omega_{nm}-(\omega_p+\omega_q)-i\gamma_{nm}}$$
$$-\frac{e^3}{\hbar^2\omega_q\omega_p\mathcal{S}}\sum_{nml}\frac{v^k_{mn-(\mathbf{q}+\mathbf{p})}v^j_{lm\mathbf{p}}v^i_{nl\mathbf{q}}}{\omega_{nl}-\omega_q-i\gamma_{nl}}\frac{f(\varepsilon_l)-f(\varepsilon_n)}{\omega_{nm}-(\omega_p+\omega_q)-i\gamma_{nm}}\ . \tag{B.47}$$

In general, $\sigma^{jki}\left(\mathbf{\Omega},\mathbf{\Omega}_p,\mathbf{\Omega}_q\right)$ is a function of ω_p, ω_q, $\mathbf{q}$ and $\mathbf{p}$ as well as $\omega_p+\omega_q$ and $\mathbf{q}+\mathbf{p}$.

B.3.1 Derivation of the second-order conductivities

Beginning with the general expression (B.47) for the 2-nd order conductivity, we derive explicit formulae for the processes of generation of a frequency difference excitation out of two incident photons, $\omega=\omega_a-\omega_b$, and for the inverse processes contributing to the reflected optical beams. We use the notation $\mathbf{\Omega}=(\omega,\mathbf{q})$, $\mathbf{\Omega}_a=(\omega_a,\mathbf{q}_a)$ and $\mathbf{\Omega}_b=(\omega_b,\mathbf{q}_b)$.

The recipe of the calculation of all three different cases is the same : in the summation, only the two channels in Fig. 3.1 are considered and the elements ω_{nm}, $v^j_{nm\mathbf{p}}$ and the Fermi-Dirac distributions are expanded to the first order in the momenta, $\mathbf{q}_j$ and $\mathbf{q}$. With these approximations, a cancellation of the zeroth order contribution, between the channels, is observed, and only the first order contributes to the conductivity.

We start with the calculation of $\sigma^{(2)}_{xxx}\left(\mathbf{\Omega},\mathbf{\Omega}_b,-\mathbf{\Omega}_a\right)$. Inserting in expression (B.47) the states in Fig. 3.1 we obtain:

$$\sigma^{(2)}_{xxx}\left(\mathbf{\Omega},\mathbf{\Omega}_b,-\mathbf{\Omega}_a\right) = \frac{e^3}{\hbar^2\omega_b\omega_a\mathcal{S}}\sum_{123}\frac{v^x_{23,-\mathbf{q}}v^x_{31,\mathbf{q}_b}v^x_{12,-\mathbf{q}_a}}{\omega_{32}-\omega-i\gamma_{32}}\left(\frac{f(\varepsilon_1)-f(\varepsilon_3)}{\omega_{31}-\omega_b-i\gamma_{31}}-\frac{f(\varepsilon_2)-f(\varepsilon_1)}{\omega_{12}+\omega_a-i\gamma_{12}}\right)$$
$$+\frac{e^3}{\hbar^2\omega_b\omega_a\mathcal{S}}\sum_{1'2'3'}\frac{v^x_{1'2',-\mathbf{q}}v^x_{3'1',\mathbf{q}_b}v^x_{2'3',-\mathbf{q}_a}}{\omega_{2'1'}-\omega-i\gamma_{2'1'}}\left(\frac{f(\varepsilon_{3'})-f(\varepsilon_{2'})}{\omega_{2'3'}+\omega_a-i\gamma_{2'3'}}-\frac{f(\varepsilon_{1'})-f(\varepsilon_{3'})}{\omega_{3'1'}-\omega_b-i\gamma_{3'1'}}\right)\ . \tag{B.48}$$

We call the first line in (B.48), channel 1, and the second line, channel 2. Let us focus on channel 1. Expansion of the spatially modulated velocity matrix elements and of the elements ω_{nm} yields, respectively:

$$v^x_{23,-\mathbf{q}}v^x_{31,\mathbf{q}_b}v^x_{12,-\mathbf{q}_a}\approx\delta_{\mathbf{q},\mathbf{q}_b-\mathbf{q}_a}\delta_{\mathbf{k}_3,\mathbf{k}_1+\mathbf{q}_b}\delta_{\mathbf{k}_1+\mathbf{q}_a,\mathbf{k}_2}v_F^3\cos\theta_1\sin^2\theta_1 \tag{B.49}$$

and $\omega_{31}\approx 2v_Fk_1+v_Fq_b\cos\theta_1$, $\omega_{12}\approx -2v_Fk_1-v_Fq_a\cos\theta_1$ and $\omega_{32}\approx v_Fq\cos\theta_1$. The expansion of

the Fermi-Dirac distribution gives:

$$f_c(\varepsilon_{\mathbf{k}+\mathbf{p}}) \approx f_c(\varepsilon_{\mathbf{k}}) + \partial_{\varepsilon_{\mathbf{k}}} f_c(\varepsilon_{\mathbf{k}}) \hbar v_F p \cos\theta \ . \tag{B.50}$$

$f_c(\varepsilon)$ is the occupation function of conduction states and $f_v(\varepsilon) = f_c(-\varepsilon)$ of the valence states. With these approximations, setting $\mathbf{k}_1 = \mathbf{k}$ and $\theta_1 = \theta$, we can write for Channel 1:

$$\begin{aligned} C_1 \approx\ & \delta_{\mathbf{q},\mathbf{q}_b-\mathbf{q}_a} \frac{(ev_F)^3}{\hbar^2 \omega_b \omega_a \mathcal{S}} \sum_{\mathbf{k}} \frac{\cos\theta \sin^2\theta}{\omega_{32} - \omega - i\gamma} \left(\frac{f_v(\varepsilon_{\mathbf{k}}) - f_c(\varepsilon_{\mathbf{k}})}{\omega_{31} - \omega_b - i\gamma} - \frac{f_c(\varepsilon_{\mathbf{k}}) - f_v(\varepsilon_{\mathbf{k}})}{\omega_{12} + \omega_a - i\gamma} \right) \\ & + \delta_{\mathbf{q},\mathbf{q}_b-\mathbf{q}_a} \frac{(ev_F)^3 \hbar v_F}{\hbar^2 \omega_b \omega_a \mathcal{S}} \sum_{\mathbf{k}} \frac{\cos\theta \sin^2\theta}{\omega_{32} - \omega - i\gamma} \partial_{\varepsilon_{\mathbf{k}}} f_c(\varepsilon_{\mathbf{k}}) \left(\frac{-q_b \cos\theta}{\omega_{31} - \omega_b - i\gamma} - \frac{q_a \cos\theta}{\omega_{12} + \omega_a - i\gamma} \right) \ . \end{aligned}$$

Changing the summation to integration and then performing a change of variable, $\varepsilon = \hbar v_F k$,

$$\sum_{\mathbf{k}} \to \frac{g\mathcal{S}}{(2\pi)^2} \int_0^{k_C} dk k \int_0^{2\pi} d\theta \to \frac{g\mathcal{S}}{(\hbar v_F)^2 (2\pi)^2} \int_0^{\varepsilon_C} d\varepsilon \varepsilon \int_0^{2\pi} d\theta \ . \tag{B.51}$$

Channel 1 contribution is written:

$$\begin{aligned} C_1 = & \delta_{\mathbf{q},\mathbf{q}_b-\mathbf{q}_a} \frac{e^3 v_F}{\hbar^4 \omega_b \omega_a \pi^2} \int_0^{\varepsilon_C} d\varepsilon \varepsilon \int_0^{2\pi} d\theta \frac{\cos\theta \sin^2\theta}{v_F q \cos\theta - \omega - i\gamma} \frac{f_v(\varepsilon) - f_c(\varepsilon)}{2\varepsilon/\hbar + v_F q_b \cos\theta - \omega_b - i\gamma} \\ & - \delta_{\mathbf{q},\mathbf{q}_b-\mathbf{q}_a} \frac{e^3 v_F}{\hbar^4 \omega_b \omega_a \pi^2} \int_0^{\varepsilon_C} d\varepsilon \varepsilon \int_0^{2\pi} d\theta \frac{\cos\theta \sin^2\theta}{v_F q \cos\theta - \omega - i\gamma} \frac{f_v(\varepsilon) - f_c(\varepsilon)}{2\varepsilon/\hbar + v_F q_a \cos\theta - \omega_a + i\gamma} \\ & - \delta_{\mathbf{q},\mathbf{q}_b-\mathbf{q}_a} \frac{e^3 v_F^2}{\hbar^3 \omega_b \omega_a \pi^2} \int_0^{\varepsilon_C} d\varepsilon \varepsilon \int_0^{2\pi} d\theta \frac{\cos\theta \sin^2\theta}{v_F q \cos\theta - \omega - i\gamma} \partial_\varepsilon f_c(\varepsilon) \frac{q_b \cos\theta}{2\varepsilon/\hbar + v_F q_b \cos\theta - \omega_b - i\gamma} \\ & + \delta_{\mathbf{q},\mathbf{q}_b-\mathbf{q}_a} \frac{e^3 v_F^2}{\hbar^3 \omega_b \omega_a \pi^2} \int_0^{\varepsilon_C} d\varepsilon \varepsilon \int_0^{2\pi} d\theta \frac{\cos\theta \sin^2\theta}{v_F q \cos\theta - \omega - i\gamma} \partial_\varepsilon f_c(\varepsilon) \frac{q_a \cos\theta}{2\varepsilon/\hbar + v_F q_a \cos\theta - \omega_a + i\gamma} \ . \end{aligned} \tag{B.52}$$

Here g is the degeneracy factor equal to 4 and k_c is an upper limit that has to be specified. If we require that the circle in k-space has the same area as the hexagon (the first BZ), then:

$$k_c = \sqrt{\frac{8\pi}{3\sqrt{3}}} \frac{1}{a} \tag{B.53}$$

and for $a = 1.42$ Å [7], $\varepsilon_c \approx 10^4$ meV. At zero temperature, Eq. (B.52) simplifies to:

$$\begin{aligned}
C_1 = {} & \delta_{\mathbf{q},\mathbf{q}_b-\mathbf{q}_a} \frac{e^3 v_F}{\hbar^4 \omega_b \omega_a \pi^2} \int_{E_F}^{\varepsilon_C} d\varepsilon\varepsilon \int_0^{2\pi} d\theta \frac{\cos\theta \sin^2\theta}{v_F q \cos\theta - \omega - i\gamma} \frac{1}{2\varepsilon/\hbar + v_F q_b \cos\theta_1 - \omega_b - i\gamma} \\
& - \delta_{\mathbf{q},\mathbf{q}_b-\mathbf{q}_a} \frac{e^3 v_F}{\hbar^4 \omega_b \omega_a \pi^2} \int_{E_F}^{\varepsilon_C} d\varepsilon\varepsilon \int_0^{2\pi} d\theta \frac{\cos\theta \sin^2\theta}{v_F q \cos\theta - \omega - i\gamma} \frac{1}{2\varepsilon/\hbar + v_F q_a \cos\theta_1 - \omega_a + i\gamma} \\
& + \delta_{\mathbf{q},\mathbf{q}_b-\mathbf{q}_a} \frac{e^3 v_F^2 E_F}{\hbar^3 \omega_b \omega_a \pi^2} \int_0^{2\pi} d\theta \frac{\cos^2\theta \sin^2\theta}{v_F q \cos\theta - \omega - i\gamma} \frac{q_b}{2\omega_F + v_F q_b \cos\theta - \omega_b - i\gamma} \\
& - \delta_{\mathbf{q},\mathbf{q}_b-\mathbf{q}_a} \frac{e^3 v_F^2 E_F}{\hbar^3 \omega_b \omega_a \pi^2} \int_0^{2\pi} d\theta \frac{\cos^2\theta \sin^2\theta}{v_F q \cos\theta - \omega - i\gamma} \frac{q_a}{2\omega_F + v_F q_a \cos\theta - \omega_a + i\gamma} \ . \qquad \text{(B.54)}
\end{aligned}$$

Now let us turn to Channel 2. For this channel:

$$v^x_{1'2',-\mathbf{q}} v^x_{3'1',\mathbf{q}_b} v^x_{2'3',-\mathbf{q}_a} \approx -\delta_{\mathbf{q},\mathbf{q}_b-\mathbf{q}_a} \delta_{\mathbf{k}_{2'},\mathbf{k}_3-\mathbf{q}_a} \delta_{\mathbf{k}_3-\mathbf{q}_b,\mathbf{k}_1} v_F^3 \cos\theta_3 \sin^2\theta_3 \qquad \text{(B.55)}$$

and $\omega_{2'3} \approx -2v_F k_3 + v_F q_a \cos\theta_3$, $\omega_{31} \approx 2v_F k_3 - v_F q_b \cos\theta_3$ and $\omega_{2'1} = \omega_{2'3} + \omega_{31} \approx -v_F q \cos\theta_3$. As before, the Fermi-Dirac function is also expanded, in this case, $f_v(\varepsilon)$. However, the first order contribution vanishes at equilibrium. Setting $\mathbf{k}_3 = \mathbf{k}, \theta_3 = \theta$ and going to integration, assuming zero temperature situation, C_2 is written:

$$\begin{aligned}
C_2 \approx {} & -\delta_{\mathbf{q},\mathbf{q}_b-\mathbf{q}_a} \frac{e^3 v_F}{\hbar^4 \omega_b \omega_a \pi^2} \int_{E_F}^{E_C} d\varepsilon\varepsilon \int_0^{2\pi} d\theta \frac{\cos\theta \sin^2\theta}{-v_F q \cos\theta - \omega - i\gamma} \frac{1}{2\varepsilon/\hbar - v_F q_a \cos\theta - \omega_a + i\gamma} \\
& + \delta_{\mathbf{q},\mathbf{q}_b-\mathbf{q}_a} \frac{e^3 v_F}{\hbar^4 \omega_b \omega_a \pi^2} \int_{E_F}^{E_C} d\varepsilon\varepsilon \int_0^{2\pi} d\theta \frac{\cos\theta \sin^2\theta}{-v_F q \cos\theta - \omega - i\gamma} \frac{1}{2\varepsilon/\hbar - v_F q_b \cos\theta - \omega_b - i\gamma} \ . \qquad \text{(B.56)}
\end{aligned}$$

Notice that the two lines in expression (B.56) for channel 2 cancel out the first two lines in for channel (B.54), when we sum the channels, thus avoiding any divergent behavior. This observation is made clear if we perform the change of variable $\theta \to \theta + \pi$ in (B.56) and use the periodicity of the integrand to rewrite the limits of integration in θ to be 0 and 2π, again. With this modification, the final expression for the conductivity is:

$$\begin{aligned}
\sigma^{(2)}_{xxx}(\mathbf{\Omega}, \mathbf{\Omega}_b, -\mathbf{\Omega}_a) \approx {} & \delta_{\mathbf{q},\mathbf{q}_b-\mathbf{q}_a} \frac{e^3 v_F^2 E_F}{\hbar^3 \omega_b \omega_a \pi^2} \int_0^{2\pi} d\theta \frac{\cos^2\theta \sin^2\theta}{v_F q \cos\theta - \omega - i\gamma} \frac{q_b}{2\omega_F + v_F q_b \cos\theta - \omega_b - i\gamma} \\
& - \delta_{\mathbf{q},\mathbf{q}_b-\mathbf{q}_a} \frac{e^3 v_F^2 E_F}{\hbar^3 \omega_b \omega_a \pi^2} \int_0^{2\pi} d\theta \frac{\cos^2\theta \sin^2\theta}{v_F q \cos\theta - \omega - i\gamma} \frac{q_a}{2\omega_F + v_F q_a \cos\theta - \omega_a + i\gamma} \\
\approx {} & \delta_{\mathbf{q},\mathbf{q}_b-\mathbf{q}_a} \frac{e^3 v_F^2 E_F}{\hbar^3 \omega_b \omega_a \pi^2} \frac{2\omega_F - \omega_a}{(2\omega_F - \omega_a)^2 + \gamma^2} q A(\omega, q, \gamma) \ , \qquad \text{(B.57)}
\end{aligned}$$

where

$$A(\omega,q,\gamma)=\int_0^{2\pi}d\theta\frac{\cos^2\theta\sin^2\theta}{v_Fq\cos\theta-\omega-i\gamma}$$
$$=\frac{\pi(\omega+i\gamma)}{(v_Fq)^4}\left\{(v_Fq)^2+2(\omega+i\gamma)^2\left[\sqrt{1-\left(\frac{v_Fq}{\omega+i\gamma}\right)^2}-1\right]\right\}\ .$$

We now focus on the calculation of the conductivity $\sigma^{(2)}_{xxx}(\mathbf{\Omega}_a,\mathbf{\Omega}_b,-\mathbf{\Omega})$, for the inverse process of DF generation at frequency ω_a. The procedure here is the same used for the case of $\sigma^{(2)}_{xxx}(\mathbf{\Omega},\mathbf{\Omega}_b,-\mathbf{\Omega}_a)$. Inserting the channels 1 and 2 in the general expression (B.47), we write for this case:

$$\sigma^{(2)}_{xxx}(\mathbf{\Omega}_a,\mathbf{\Omega}_b,-\mathbf{\Omega})=\frac{e^3}{\hbar^2\omega\omega_b\mathcal{S}}\sum_{123}\frac{v^x_{12-\mathbf{q}_a}v^x_{31\mathbf{q}_b}v^x_{23-\mathbf{q}}}{\omega_{21}-\omega_a-i\gamma_{21}}\left(\frac{f(\varepsilon_3)-f(\varepsilon_2)}{\omega_{23}+\omega-i\gamma_{23}}-\frac{f(\varepsilon_1)-f(\varepsilon_3)}{\omega_{31}-\omega_b-i\gamma_{31}}\right)$$
$$+\frac{(ev_F)^3}{\hbar^2\omega\omega_b\mathcal{S}}\sum_{1'2'3'}\frac{\sigma^x_{2'3'-\mathbf{q}_a}\sigma^x_{3'1'\mathbf{q}_b}\sigma^x_{1'2'-\mathbf{q}}}{\omega_{3'2'}-\omega_a-i\gamma_{3'2'}}\left(\frac{f(\varepsilon_{1'})-f(\varepsilon_{3'})}{\omega_{3'1'}-\omega_b-i\gamma_{3'1'}}-\frac{f(\varepsilon_{2'})-f(\varepsilon_{1'})}{\omega_{1'2'}+\omega-i\gamma_{1'2'}}\right)\ . \tag{B.58}$$

As before, expansion of the matrix elements and the Fermi-Dirac functions to the first order in momentum, and setting the temperature to zero, yields for channels 1 (first line in (B.58)) and 2 (second line in (B.58)), respectively:

$$C_1\approx-\delta_{\mathbf{q},\mathbf{q}_b-\mathbf{q}_a}\frac{e^3v_F}{\hbar^4\omega_b\omega\pi^2}\int_{E_F}^{\varepsilon_C}d\varepsilon\varepsilon\int_0^{2\pi}d\theta\frac{\cos\theta\sin^2\theta}{2\varepsilon/\hbar+v_Fq_a\cos\theta-\omega_a-i\gamma}\frac{1}{2\varepsilon/\hbar+v_Fq_b\cos\theta-\omega_b-i\gamma}$$
$$-\delta_{\mathbf{q},\mathbf{q}_b-\mathbf{q}_a}\frac{e^3v_F^2E_F}{\hbar^3\omega_b\omega\pi^2}\int_0^{2\pi}d\theta\frac{\cos^2\theta\sin^2\theta}{2\omega_F+v_Fq_a\cos\theta-\omega_a-i\gamma}\frac{q}{-v_Fq\cos\theta+\omega-i\gamma}$$
$$-\delta_{\mathbf{q},\mathbf{q}_b-\mathbf{q}_a}\frac{e^3v_F^2E_F}{\hbar^3\omega_b\omega\pi^2}\int_0^{2\pi}d\theta\frac{\cos^2\theta\sin^2\theta}{2\omega_F+v_Fq_a\cos\theta-\omega_a-i\gamma}\frac{q_b}{2\omega_F+v_Fq_b\cos\theta-\omega_b-i\gamma}\ , \tag{B.59}$$

$$C_2\approx-\delta_{\mathbf{q},\mathbf{q}_b-\mathbf{q}_a}\frac{e^3v_F}{\hbar^4\omega_b\omega\pi^2}\int_{E_F}^{\varepsilon_C}d\varepsilon\varepsilon\int_0^{2\pi}d\theta\frac{\cos\theta\sin^2\theta}{2\varepsilon/\hbar-v_Fq_a\cos\theta-\omega_a-i\gamma}\frac{1}{2\varepsilon/\hbar-v_Fq_b\cos\theta-\omega_b-i\gamma}\ . \tag{B.60}$$

Once again, making the change of variable $\theta\to\theta+\pi$ and using the periodicity of the function under integration, makes it clear that Eq. (B.60) for channel 2 cancels out the first line in Eq. (B.59) for channel 1. Thus, summing both channels yields a second-order response:

$$\sigma^{(2)}_{xxx}(\mathbf{\Omega}_a,\mathbf{\Omega}_b,-\mathbf{\Omega})\approx\delta_{\mathbf{q},\mathbf{q}_b-\mathbf{q}_a}\frac{e^3v_F^2E_F}{\hbar^3\omega_b\omega\pi^2}\frac{q}{2\omega_F-\omega_a-i\gamma}A(\omega,q,-\gamma)\ . \tag{B.61}$$

For the inverse process, $\sigma^{(2)}_{xxx}(\mathbf{\Omega}_b,\mathbf{\Omega}_a,\mathbf{\Omega})$, the calculation follows the same procedure as the two cases before. Considering the channels 1 and 2 in the general expression (B.47), yields:

$$\sigma^{(2)}_{xxx}(\mathbf{\Omega}_b,\mathbf{\Omega}_a,\mathbf{\Omega}) = \frac{(ev_F)^3}{\hbar^2\omega_a\omega\mathcal{S}}\sum_{123}\frac{\sigma^x_{32\mathbf{q}}\sigma^x_{21\mathbf{q}_a}\sigma^x_{13-\mathbf{q}_b}}{\omega_{31}-\omega_b-i\gamma_{31}}\left(\frac{f(\varepsilon_1)-f(\varepsilon_2)}{\omega_{21}-\omega_a-i\gamma_{21}}-\frac{f(\varepsilon_2)-f(\varepsilon_3)}{\omega_{32}-\omega-i\gamma_{32}}\right)$$
$$+\frac{(ev_F)^3}{\hbar^2\omega_a\omega\mathcal{S}}\sum_{1'2'3'}\frac{\sigma^x_{3'2'\mathbf{q}_a}\sigma^x_{2'1'\mathbf{q}}\sigma^x_{1'3'-\mathbf{q}_b}}{\omega_{3'1'}-\omega_b-i\gamma_{3'1'}}\left(\frac{f(\varepsilon_{1'})-f(\varepsilon_{2'})}{\omega_{2'1'}-\omega-i\gamma_{2'1'}}-\frac{f(\varepsilon_{2'})-f(\varepsilon_{3'})}{\omega_{3'2'}-\omega_a-i\gamma_{3'2'}}\right)\ . \tag{B.62}$$

As before, expansion of the matrix elements and the Fermi-Dirac functions to the first order in momentum, and setting the temperature to zero, yields for channels 1 and 2, respectively:

$$C_1 \approx \delta_{\vec{q},\vec{q}_b-\vec{q}_a}\frac{e^3v_F}{\hbar^4\omega_a\omega\pi^2}\int_{E_F}^{\varepsilon_C}d\varepsilon\varepsilon\int_0^{2\pi}d\theta\frac{\cos\theta\sin^2\theta}{2\varepsilon/\hbar+v_Fq_b\cos\theta-\omega_b-i\gamma}\frac{1}{2\varepsilon/\hbar+v_Fq_a\cos\theta-\omega_a-i\gamma}$$
$$-\delta_{\vec{q},\vec{q}_b-\vec{q}_a}\frac{e^3v_F^2E_F}{\hbar^3\omega_a\omega\pi^2}\int_0^{2\pi}d\theta\frac{\cos^2\theta\sin^2\theta}{2\omega_F+v_Fq_b\cos\theta-\omega_b-i\gamma}\left(\frac{q}{v_Fq\cos\theta-\omega-i\gamma}-\frac{q_a}{2\omega_F+v_Fq_a\cos\theta-\omega_a-i\gamma}\right)\ , \tag{B.63}$$

$$C_2 \approx \delta_{\vec{q},\vec{q}_b-\vec{q}_a}\frac{e^3v_F}{\hbar^4\omega_a\omega\pi^2}\int_{E_F}^{\varepsilon_C}d\varepsilon\varepsilon\int_0^{2\pi}d\theta\frac{\cos\theta\sin^2\theta}{2\varepsilon/\hbar-v_Fq_b\cos\theta-\omega_b-i\gamma}\frac{1}{2\varepsilon/\hbar-v_Fq_a\cos\theta-\omega_a-i\gamma}\ . \tag{B.64}$$

Summing both channels yields the expression (3.23) for $\sigma^{(2)}_{xxx}(\mathbf{\Omega}_b,\mathbf{\Omega}_a,\mathbf{\Omega})$.

Appendix C

Transmission and reflection coefficients

In this section, the reflection and transmission coefficients for the situation in Fig. 3.3 are derived. Let us consider two monochromatic plane waves, with frequencies ω_b (pump) and ω_a (probe) ($\omega_b > \omega_a$), that interact with graphene via a difference frequency generation process (DFG). The graphene sheet is placed between two dielectrics with dielectric constants ε_1 and ε_2, see Fig. 3.3. The incident and reflected electric fields are:

$$\mathbf{E}_j^{I/R}(\mathbf{r},t) = \frac{1}{2}(E_{j,x}^{I/R}, 0, E_{j,z}^{I/R}) e^{i(\mathbf{k}_j^{I/R}\cdot\mathbf{r}-\omega_j t)} + \text{c.c} \qquad (j=a,b)\ , \tag{C.1}$$

where

$$k_j^{I/R} = \frac{\omega_j}{c}\sqrt{\varepsilon_1} \tag{C.2}$$

and the transmitted fields are:

$$\mathbf{E}_j^{T}(\mathbf{r},t) = \frac{1}{2}(E_{j,x}^{T}, 0, E_{j,z}^{T}) e^{i(\mathbf{k}_j^{T}\cdot\mathbf{r}-\omega_j t)} + \text{c.c} \qquad (j=a,b)\ , \tag{C.3}$$

with

$$k_j^{T} = \frac{\omega_j}{c}\sqrt{\varepsilon_2}\ . \tag{C.4}$$

We use the boundary conditions of Appendix A to relate the incident field with the reflected and transmitted electric fields:

$$\begin{cases} \varepsilon_1 E_{1,z} - \varepsilon_2 E_{2,z} = 4\pi\rho_s \\ E_{1,x} - E_{2,x} = 0 \end{cases}\ . \tag{C.5}$$

The total electric field in medium 1 is:

$$\mathbf{E}_1 = \mathbf{E}_a^I + \mathbf{E}_b^I + \mathbf{E}_a^R + \mathbf{E}_b^R\ , \tag{C.6}$$

while in medium 2:

$$\mathbf{E}_2 = \mathbf{E}_a^T + \mathbf{E}_b^T\ , \tag{C.7}$$

so Eqs. (C.5) yield:

$$\begin{cases} \varepsilon_1 \sum_j \left(E^I_{j,z} e^{i(\mathbf{k}^I_j \cdot \mathbf{r} - \omega_j t)} + E^R_{j,z} e^{i(\mathbf{k}^R_j \cdot \mathbf{r} - \omega_j t)} \right) - \varepsilon_2 \sum_j E^T_{j,z} e^{i(\mathbf{k}^T_j \cdot \mathbf{r} - \omega_j t)} = 8\pi\rho_s \\ \sum_j \left[E^I_{j,x} e^{i(\mathbf{k}^I_j \cdot \mathbf{r} - \omega_j t)} + E^R_{j,x} e^{i(\mathbf{k}^R_j \cdot \mathbf{r} - \omega_j t)} - E^T_{j,x} e^{i(\mathbf{k}^T_j \cdot \mathbf{r} - \omega_j t)} \right] = 0 \,. \end{cases} \quad . \tag{C.8}$$

The position vector $\mathbf{r}$ is to be taken at $z = 0$ (interface between dielectrics). We expect graphene to have a periodic response along it. This means that the surface charge density can be expanded in a Fourier series. Using the orthogonality between $e^{i(k_{j,x}x - \omega_j t)}$ functions, (C.8) simplifies to:

$$\begin{cases} \varepsilon_1 \left(E^I_{j,z} + E^R_{j,z} \right) - \varepsilon_2 E^T_{j,z} = 4\pi\rho(\omega_j, q_j) \\ E^T_{j,x} = E^I_{j,x} + E^R_{j,x} \end{cases} \tag{C.9}$$

and the conservation of momentum is obtained:

$$k^I_{j,x} = k^R_{j,x} = k^T_{j,x} = q_j \ . \tag{C.10}$$

Using basic trigonometry, the field components can be related to the field itself and the angle with respect to the normal to the plane $z = 0$. Introducing the reflection and transmission coefficients:

$$r_j = \frac{E^R_j}{E^I_j} \quad , \quad t_j = \frac{E^T_j}{E^I_j} \ , \tag{C.11}$$

simplifies eq.C.9 to:

$$\begin{cases} -\varepsilon_1 \sin\theta^I_j \left(1 + r_j\right) + \sin\theta^T_j \varepsilon_2 t_j = 4\pi \dfrac{\rho(\omega_j, q_j)}{E^I_j} \\ \cos\theta^T_j t_j - \cos\theta^I_j \left(1 - r_j\right) = 0 \end{cases} \quad . \tag{C.12}$$

The surface charge density, $\rho(\omega_j, q_j)$, is related to the surface current density, $j(\omega_j, q_j)$, by the continuity equation. On the other hand, $j_x(\omega_j, q_j)$ can be expanded to the second order in response:

$$j_x(\omega_j, q_j) = \sigma^{(1)}(\omega_j) E_{j,x} + j^{(2)}_x(\omega_j, q_j) \ , \tag{C.13}$$

where $j^{(2)}_x(\omega_j, q_j)$ is the second order current. These considerations allow us to rewrite Eq. (C.12) in the form:

$$\begin{aligned} t_j = & \frac{2\varepsilon_1}{k^I_j \cos\theta^T_j \left(\varepsilon_1 / k^I_{j,z} + \varepsilon_2 / k^T_{j,z} + \dfrac{4\pi}{\omega_j} \sigma^{(1)}(\omega_j) \right)} \\ & + 4\pi \frac{j^{(2)}_x(\omega_j, q_j)}{\omega_j E^I_j \cos\theta^T_j \left(\varepsilon_1 / k^I_{j,z} + \varepsilon_2 / k^T_{j,z} + \dfrac{4\pi}{\omega_j} \sigma^{(1)}(\omega_j) \right)} \ , \end{aligned} \tag{C.14}$$

$$r_j = 1 - \sec\theta_j^I \cos\theta_j^T t_j \ . \tag{C.15}$$

If $j_x^{(2)}(\omega_j, q_j) = 0$, then:

$$t_j = \frac{2\varepsilon_1}{k_j^I \cos\theta_j^T \left(\varepsilon_1/k_{j,z}^I + \varepsilon_2/k_{j,z}^T + \dfrac{4\pi}{\omega_j}\sigma^{(1)}(\omega_j)\right)} = t_j^{(0)} \ . \tag{C.16}$$

Here $t_j^{(0)}$ is the usual linear transmission coefficient. Thus we rewrite (C.14):

$$t_j = t_j^{(0)} + 4\pi \frac{j_x^{(2)}(\omega_j, q_j)}{\omega_j E_j^I \cos\theta_j^T \left(\varepsilon_1/k_{j,z}^I + \varepsilon_2/k_{j,z}^T + \dfrac{4\pi}{\omega_j}\sigma^{(1)}(\omega_j)\right)} \ . \tag{C.17}$$

Now we shall calculate the transmission coefficient for each field. We use a truncated scheme, where only the DFG process is considered. For the field a, we get:

$$j_x^{(2)}(\omega_a, q_a) = \frac{1}{2}\sigma_{xxx}^{(2)}\left(\mathbf{\Omega}_a, \mathbf{\Omega}_b, -\mathbf{\Omega}\right) E_{b,x}(z=0) E_{\mathrm{SP},x}^*(z=0) \ , \tag{C.18}$$

with E_{SP} being the SPP field. Using Eq. (3.8) for the SP-field, we conclude that (C.18) yields:

$$j_x^{(2)}(\omega_a, q_a) = -\pi i \frac{\sigma_{xxx}^{(2)}\left(\mathbf{\Omega}_a, \mathbf{\Omega}_b, -\mathbf{\Omega}\right) \sigma_{xxx}^{(2)*}\left(\mathbf{\Omega}, \mathbf{\Omega}_b, -\mathbf{\Omega}_a\right)}{\omega D^*(\omega, q)} |t_b|^2 |E_b^I|^2 t_a E_a^I \cos^2\theta_b^T \cos\theta_a^T \ . \tag{C.19}$$

For the field b, a similar expression is obtained:

$$j_x^{(2)}(\omega_b, q_b) = \pi i \frac{\sigma_{xxx}^{(2)}\left(\mathbf{\Omega}_b, \mathbf{\Omega}_a, \mathbf{\Omega}\right) \sigma_{xxx}^{(2)}\left(\mathbf{\Omega}, \mathbf{\Omega}_b, -\mathbf{\Omega}_a\right) t_b E_b^I}{\omega D(\omega, q)} |t_a|^2 |E_a^I|^2 \cos\theta_b^T \cos^2\theta_a^T \ . \tag{C.20}$$

Thus the final expressions for the transmission coefficients are:

$$t_a = t_a^{(0)} \left(1 + 2\pi^2 i \frac{\sigma_{xxx}^{(2)}\left(\mathbf{\Omega}_a, \mathbf{\Omega}_b, -\mathbf{\Omega}\right) \sigma_{xxx}^{(2)*}\left(\mathbf{\Omega}, \mathbf{\Omega}_b, -\mathbf{\Omega}_a\right) |E_b^I|^2 \cos^2\theta_b^T}{\sqrt{\varepsilon_1} c\omega D^*(\omega, q)} \cos\theta_a^T t_a^{(0)} |t_b|^2\right)^{-1} \ , \tag{C.21}$$

$$t_b = t_b^{(0)} \left(1 - 2\pi^2 i \frac{\sigma_{xxx}^{(2)}\left(\mathbf{\Omega}_b, \mathbf{\Omega}_a, \mathbf{\Omega}\right) \sigma_{xxx}^{(2)}\left(\mathbf{\Omega}, \mathbf{\Omega}_b, -\mathbf{\Omega}_a\right) |E_a^I|^2 \cos^2\theta_a^T}{\sqrt{\varepsilon_1} c\omega D(\omega, q)} \cos\theta_b^T t_b^{(0)} |t_a|^2\right)^{-1} \ . \tag{C.22}$$

To linearize Eqs. (C.21) and (C.22), we apply a perturbation treatment with the second order conductivity as a perturbation. We call the perturbation parameter λ and expand the transmission coefficients:

$$t_j = t_j^{(0)} + \lambda t_j^{(1)} + \lambda^2 t_j^{(2)} + ... \tag{C.23}$$

Formal expansion of the coefficients t_a and t_b yields a null first order contribution:

$$t_a^{(1)} = t_b^{(1)} = 0 \tag{C.24}$$

and the second-order contribution is:

$$t_a^{(2)} = -2\pi^2 t_a^{(0)} |t_b^{(0)}|^2 i \frac{\sigma_{xxx}^{(2)}\left(\mathbf{\Omega}_a, \mathbf{\Omega}_b, -\mathbf{\Omega}\right) \sigma_{xxx}^{(2)*}\left(\mathbf{\Omega}, \mathbf{\Omega}_b, -\mathbf{\Omega}_a\right) |E_b^I|^2 \cos^2\theta_b^T}{\sqrt{\varepsilon_1} c\omega D^*(\omega, q)} \cos\theta_a^T t_a^{(0)} \ , \tag{C.25}$$

$$t_b^{(2)} = 2\pi^2 t_b^{(0)} |t_a^{(0)}|^2 i \frac{\sigma_{xxx}^{(2)}\left(\mathbf{\Omega}_b, \mathbf{\Omega}_a, \mathbf{\Omega}\right) \sigma_{xxx}^{(2)}\left(\mathbf{\Omega}, \mathbf{\Omega}_b, -\mathbf{\Omega}_a\right) |E_a^I|^2 \cos^2\theta_a^T}{\sqrt{\varepsilon_1} c\omega D(\omega, q)} \cos\theta_b^T t_b^{(0)} \ . \tag{C.26}$$

Therefore,

$$t_a \approx t_a^{(0)} \left(1 - 2t_a^{(0)} |t_b^{(0)}|^2 \pi^2 i \frac{\sigma_{xxx}^{(2)}\left(\mathbf{\Omega}_a, \mathbf{\Omega}_b, -\mathbf{\Omega}\right) \sigma_{xxx}^{(2)*}\left(\mathbf{\Omega}, \mathbf{\Omega}_b, -\mathbf{\Omega}_a\right) |E_b^I|^2 \cos^2\theta_b^T}{\sqrt{\varepsilon_1} c\omega D^*(\omega, q)} \cos\theta_a^T \right) \ , \tag{C.27}$$

$$t_b \approx t_b^{(0)} \left(1 + 2t_b^{(0)} |t_a^{(0)}|^2 \pi^2 i \frac{\sigma_{xxx}^{(2)}\left(\mathbf{\Omega}_b, \mathbf{\Omega}_a, \mathbf{\Omega}\right) \sigma_{xxx}^{(2)}\left(\mathbf{\Omega}, \mathbf{\Omega}_b, -\mathbf{\Omega}_a\right) |E_a^I|^2 \cos^2\theta_a^T}{\sqrt{\varepsilon_1} c\omega D(\omega, q)} \cos\theta_b^T \right) \ . \tag{C.28}$$

Appendix D

Energy flux of SPPs

Here we calculate the energy flux, associated with the generated graphene plasmons, that propagates along the surface, in the direction of the wavevector of the plasmons.

The energy flux density is given by the Stokes vector:

$$\mathbf{S} = \mathrm{Re}\left(\frac{c}{8\pi}\mathbf{E}\times\mathbf{H}^{*}\right) \ , \tag{D.1}$$

with $\mathbf{H}$ being the magnetic field. For SPPs, this vector has the form:

$$\mathbf{S}_{\mathrm{SP}} = \begin{cases} (S_{2,x}, 0, S_{2,z})\, e^{2\kappa_2 z} & z<0 \\ (S_{1,x}, 0, S_{1,z})\, e^{-2\kappa_1 z} & z>0 \end{cases} . \tag{D.2}$$

Its x-component is ($m = 1, 2$):

$$S_{m,x} = -\frac{c}{8\pi}\mathrm{Re}\left(E_{m,z}H^{*}_{m,y}\right) \ . \tag{D.3}$$

From Maxwell's equations, the electric and magnetic field components of SPPs satisfy,

$$H_{m,y}(\omega,q) = -(-1)^{m+1} i\frac{\omega\varepsilon_m}{c\kappa_m}E_{m,x} \ . \tag{D.4}$$

Using this relation together with Eq. (2.3), we are able to write the energy flux density in terms of the x-component of the electric field:

$$S_{m,x} = \frac{q\omega\varepsilon_m}{8\pi\kappa_m^2}|E_{m,x}|^2 \ . \tag{D.5}$$

The $E_{m,x}$ component is determined by Eq. (3.8). Hence, the energy flux density, per unit length along y, is:

$$J = \int_{-\infty}^{+\infty} dz S_x = q\frac{\omega}{16\pi}\sum_{m=1,2}\frac{\varepsilon_m}{\kappa_m^3}|E_{m,x}(\omega,q)|^2 \ . \tag{D.6}$$

Appendix E

Differential reflectance in the presence of hot electrons

As a result of the evolution of the out-of-equilibrium carriers' population, the non-equilibrium optical conductivity, σ_{neq}, is assumed to vary slowly with time, so that it may be described as a function of both time and frequency,

$$\sigma_{\text{neq}}(\omega, t) = \frac{4\sigma_0}{\pi}\hbar\left(\gamma - i\omega\right)\int_0^{+\infty} d\varepsilon \frac{1 - f^{(e)}(\varepsilon, t) - f^{(h)}(\varepsilon, t)}{\left[\hbar\gamma + i\left(2\varepsilon - \hbar\omega\right)\right]\left[\hbar\gamma - i\left(2\varepsilon + \hbar\omega\right)\right]} \ . \tag{E.1}$$

Here, γ is the interband scattering rate, $f^{(e)}(\varepsilon, t)$ and $f^{(h)}(\varepsilon, t)$ are the electron and hole distributions with contributions from thermalized and non-thermalized carriers.

In general, the current density can be written as

$$j_x(t) = \int_{-\infty}^{\infty} dt' \sigma\left(t, t'\right) E_x\left(t'\right) \ , \tag{E.2}$$

where $E_x\left(t'\right)$ is the x-component of the probe's electric field at $z = 0$ and

$$\begin{aligned}\sigma\left(t, t'\right) &= \int_{-\infty}^{\infty} \frac{d\omega}{2\pi}\sigma_{\text{neq}}\left(\omega, t'\right)\exp\left\{-i\omega\left(t - t'\right)\right\} \\ &= \frac{4\sigma_0}{\pi}\int_{-\infty}^{\infty}\frac{d\omega}{2\pi}\hbar\left(\gamma_{\text{inter}} - i\omega\right)\int_0^{\infty} d\varepsilon \frac{1 - f^{(e)}(\varepsilon, t') - f^{(h)}(\varepsilon, t')}{\left(\hbar\gamma - i\left(2\varepsilon + \hbar\omega\right)\right)\left(\hbar\gamma + i\left(2\varepsilon - \hbar\omega\right)\right)}\exp\left\{-i\omega\left(t - t'\right)\right\} \ .\end{aligned} \tag{E.3}$$

The integral over ω in Eq. (E.3) can be solved by analytic continuation and using the residue theorem. The poles are located at

$$\omega = \pm 2\varepsilon/\hbar - i\gamma \ , \tag{E.4}$$

i.e, both of them lie within the lower half-plan. For $t < t'$ the integral vanishes, which traduces the causality principle, and the contour must be closed in the lower half plane. Employing the residue

theorem, Eq. (E.3) simplifies to:

$$\sigma\left(t,t'\right)=\frac{4\sigma_0}{\pi\hbar}\Theta\left(t-t'\right)e^{-\gamma(t-t')}\int_0^\infty d\varepsilon\left(1-f^{(e)}(\varepsilon,t')-f^{(h)}(\varepsilon,t')\right)\cos\left\{\frac{2\varepsilon}{\hbar}\left(t-t'\right)\right\}\ , \tag{E.5}$$

where the Heaviside function $\Theta\left(t-t'\right)$ expresses the causality principle.

It is worth noting that the electric field in Eq. (E.2) corresponds to the transmitted field at $z=0$. With this in mind, let us proceed to define the fields. The electric fields at $z=0$ can be written as follows:

$$E_x^{(i)}\left(\mathbf{r},t\right)=A_i\left(t\right)\cos\alpha e^{i(\sin\alpha k_a x-\cos\alpha k_a z-\omega_a t)}\ , \tag{E.6}$$

$$E_x^{(r)}\left(\mathbf{r},t\right)=A_r\left(t\right)\cos\alpha e^{i(\sin\alpha k_a x+\cos\alpha k_a z-\omega_a t)}\ , \tag{E.7}$$

$$E_x^{(t)}\left(\mathbf{r},t\right)=A_t\left(t\right)\cos\theta e^{i(n\sin\theta k_a x-n\cos\theta k_a z-\omega_a t)}\ , \tag{E.8}$$

where $k_a=\omega_a/c$ and ω_a is the wavevector and frequency of the probe beam, α and θ are the incident and transmitted angles of the probe, n is the index of refraction of the substrate and A_i, A_r and A_t are the incident, reflected and transmitted amplitudes of the fields. This amplitudes will be defined as Gaussian functions:

$$A_{i(r,t)}\left(t\right)=a_{i(r,t)}\exp\left(-\frac{t^2}{\tau_a^2}\right)\ , \tag{E.9}$$

where τ_a is the duration time of the probe beam.

Applying Maxwell's equations enables us to compute the corresponding magnetic fields. This results in the following expressions:

$$H_y^{(i)}\left(\mathbf{r},t\right)=\frac{\omega_a}{k_a c\cos\alpha}E_x^{(i)}\left(\mathbf{r},t\right)\ , \tag{E.10}$$

$$H_y^{(r)}\left(\mathbf{r},t\right)=-\frac{\omega_a}{k_a c\cos\alpha}E_x^{(r)}\left(\mathbf{r},t\right)\ , \tag{E.11}$$

$$H_y^{(t)}\left(\mathbf{r},t\right)=\frac{n\omega_a}{k_a c\cos\theta}E_x^{(t)}\left(\mathbf{r},t\right)\ . \tag{E.12}$$

The reflection and transmission coefficients are determined using the following boundary conditions:

$$E_x^{(i)}+E_x^{(r)}=E_x^{(t)}\ , \tag{E.13}$$

$$H_y^{(i)}+H_y^{(r)}=H_y^{(t)}+\frac{4\pi}{c}j_x(x,t)\ , \tag{E.14}$$

or in terms of the field amplitudes,

$$A_i\cos\alpha+A_r\cos\alpha=A_t\cos\theta\ , \tag{E.15}$$

$$A_i-A_r=nA_t+\frac{4\pi}{c}j_x(x,t)e^{-i(\sin\alpha k_a x-\omega_a t)}\ . \tag{E.16}$$

In the situation without pumping, the current is written simply as:

$$j_x(x,t) = \sigma_{\rm eq}\left(\omega_a\right) E_x^{(t)}(x,t) \ , \tag{E.17}$$

where $\sigma_{\rm eq}(\omega_a)$ is the equilibrium optical conductivity. At the frequency ω_a, $\sigma_{\rm eq}(\omega_a) \approx \sigma_0$. As a consequence, Eq. (E.16) yields:

$$A_i - A_r = nA_t + \frac{4\pi}{c}\sigma_0 A_t \cos\theta \ . \tag{E.18}$$

Using (E.15) and (E.18), the familiar expression for the linear transmission coefficient is obtained,

$$A_r = \frac{\cos\theta - n\cos\alpha + \dfrac{4\pi}{c}\sigma_0\cos\theta\cos\alpha}{\cos\theta + n\cos\alpha + \dfrac{4\pi}{c}\sigma_0\cos\theta\cos\alpha} A_i = t_a^{(0)} A_i \ . \tag{E.19}$$

In the case involving pumping, $j_x(x,t)$ is determined by Eq. (E.2) and the conductivity is given in Eq. (E.5). Therefore, multiplying Eq. (E.16) by $\cos\alpha$ and summing it with Eq. (E.15) yields:

$$\begin{aligned} 2A_i\cos\alpha &= \left(\cos\theta + n\cos\alpha\right) A_t + \frac{4\pi}{c} j_x(x,t)\cos\alpha e^{-i(\sin\alpha k_a x - \omega_a t)} \\ &= \left(\cos\theta + n\cos\alpha\right) A_t \\ &+ \frac{16\sigma_0}{c\hbar}\cos\alpha\cos\theta \\ &\int_{-\infty}^{\infty} dt' \int_0^{\infty} d\varepsilon \Theta\left(t-t'\right) e^{(i\omega_a - \gamma)(t-t')} \left(1 - f^{(e)}(\varepsilon,t') - f^{(h)}(\varepsilon,t')\right) \cos\left\{\frac{2\varepsilon}{\hbar}\left(t-t'\right)\right\} A_t\left(t'\right) \ . \end{aligned} \tag{E.20}$$

Applying a Fourier-transform in the variable t, Eq. (E.20) becomes:

$$\begin{aligned} 2\mathcal{A}_i\cos\alpha &= \left(n\cos\alpha + \cos\theta\right)\mathcal{A}_t \\ &+ \frac{16\sigma_0}{c\hbar}\cos\alpha\cos\theta \\ &\int_{-\infty}^{\infty} dt' \int_{t'}^{\infty} dt \int_0^{\infty} d\varepsilon e^{(i\omega_a - \gamma)(t-t')} e^{i\omega t} \left(1 - f^{(e)}(\varepsilon,t') - f^{(h)}(\varepsilon,t')\right) \cos\left\{\frac{2\varepsilon}{\hbar}\left(t-t'\right)\right\} A_t\left(t'\right) \ , \end{aligned} \tag{E.21}$$

where:

$$\mathcal{A}_{i(r,t)}(\omega) = \int dt e^{i\omega t} A_{i(r,t)}(t) \ . \tag{E.22}$$

The integral over the variable t in (E.21) yields:

$$\int_{t'}^{\infty} dt e^{(i\omega_a - \gamma)(t-t')} e^{i\omega t} \cos\left\{\frac{2\varepsilon}{\hbar}\left(t-t'\right)\right\} = \frac{i e^{it'\omega}\left(i\gamma + \omega + \omega_a\right)}{\left(i\gamma + \omega + \omega_a - 2\varepsilon/\hbar\right)\left(i\gamma + \omega + \omega_a + 2\varepsilon/\hbar\right)} \tag{E.23}$$

and consequently,

$$2\mathcal{A}_i \cos\alpha = (n\cos\alpha + \cos\theta)\,\mathcal{A}_t + \frac{16\sigma_0}{c\hbar}\cos\alpha\cos\theta \int_{-\infty}^{\infty} dt' \int_0^{\infty} d\varepsilon \left(1 - f^{(e)}(\varepsilon, t') - f^{(h)}(\varepsilon, t')\right) A_t\left(t'\right) \frac{i\left(i\gamma + \omega + \omega_a\right) e^{it'\omega}}{\left(i\gamma + \omega + \omega_a - 2\varepsilon/\hbar\right)\left(i\gamma + \omega + \omega_a + 2\varepsilon/\hbar\right)} \,, \tag{E.24}$$

or in terms of the non-equilibrium conductivity (E.1):

$$2\mathcal{A}_i \cos\alpha = (n\cos\alpha + \cos\theta)\,\mathcal{A}_t + \frac{4\pi}{c}\cos\alpha\cos\theta \int_{-\infty}^{\infty} dt' \sigma_{\text{neq}}(\omega + \omega_a, t') A_t\left(t'\right) e^{it'\omega} \,. \tag{E.25}$$

The last term of the equation represents a convolution of both pulses, since the non-equilibrium conductivity is a consequence of the pump beam. If there is a delay δ_t between pump and probe, the conductivity is simply changed to,

$$\sigma_{\text{neq}}\left(\omega, t'\right) \to \sigma_{\text{neq}}\left(\omega, t' + \delta_t\right) \,. \tag{E.26}$$

Eq. (E.25) can solved by iteration in $\Delta\sigma\left(\omega + \omega_a, t' + \delta_t\right) = \sigma_{\text{neq}}\left(\omega + \omega_a, t' + \delta_t\right) - \sigma_0$,

$$2\mathcal{A}_i \cos\alpha = \left(n\cos\alpha + \cos\theta + \frac{4\pi}{c}\sigma_0\cos\alpha\cos\theta\right)\mathcal{A}_t + \frac{4\pi}{c}\cos\alpha\cos\theta \int_{-\infty}^{\infty} dt' \Delta\sigma\left(\omega + \omega_a, t' + \delta_t\right) A_t\left(t'\right) e^{i\omega t'} \,. \tag{E.27}$$

The reflected and transmitted field amplitudes are expanded:

$$\mathcal{A}_{(r,t)} = \mathcal{A}^{(0)}_{(r,t)} + \mathcal{A}^{(1)}_{(r,t)} + ... \tag{E.28}$$

where $\mathcal{A}^{(j)}_{(r,t)}$ denotes the j-th iteration. The zeroth iteration consists in neglecting the second term in the RHS of (E.27) and yields Eq. (E.19) as expected. The first order of the transmitted amplitude is:

$$\mathcal{A}^{(1)}_t = -\frac{4\pi}{c} \frac{\cos\alpha\cos\theta t^{(0)}}{n\cos\alpha + \cos\theta + \frac{4\pi}{c}\sigma_0\cos\alpha\cos\theta} \int_{-\infty}^{\infty} dt' \Delta\sigma\left(\omega + \omega_a, t' + \delta_t\right) A_i\left(t'\right) e^{it'\omega} \,. \tag{E.29}$$

Using Eq. (E.15), the reflected field amplitude is determined to be:

$$\mathcal{A}_r = \frac{\cos\theta}{\cos\alpha}\mathcal{A}_t - \mathcal{A}_i \ . \tag{E.30}$$

Therefore, the expression for the iteration of zeroth-order is

$$\mathcal{A}_r^{(0)} = -\left(\frac{n\cos\alpha - \cos\theta + \frac{4\pi}{c}\cos\alpha\cos\theta\sigma_0}{n\cos\alpha + \cos\theta + \frac{4\pi}{c}\cos\alpha\cos\theta\sigma_0}\right)\mathcal{A}_i = -\hat{r}_a^{(0)}\mathcal{A}_i \tag{E.31}$$

and for the first-order,

$$\mathcal{A}_r^{(1)} = -\frac{4\pi}{c}\frac{\cos^2\theta t^{(0)}}{n\cos\alpha + \cos\theta + \frac{4\pi}{c}\sigma_0\cos\alpha\cos\theta}\int_{-\infty}^{\infty} dt'\Delta\sigma\left(\omega+\omega_a, t'+\delta_t\right)A_i\left(t'\right)e^{it'\omega} \ . \tag{E.32}$$

The reflectivity of the whole structure, under pumping, is defined to be

$$R_a(\delta_t) = \frac{\int_{-\infty}^{\infty} d\omega\left|\mathcal{A}_r(\omega)\right|^2}{\int_{-\infty}^{\infty} d\omega\left|\mathcal{A}_i(\omega)\right|^2} \ . \tag{E.33}$$

Substituting the expansion for $\mathcal{A}_r$, up to first-order in $\Delta\sigma$, in $R_a(\delta_t)$ yields:

$$R_a(\delta_t) \approx R_a^{(0)} + \frac{\cos^2\theta}{\cos\alpha}\frac{\left(\hat{t}^{(0)}\right)^2\hat{r}_a^{(0)}}{2\pi\Phi_a}\frac{4\pi}{c}\mathrm{Re}\int_{-\infty}^{\infty} d\omega\int_{-\infty}^{\infty} dt'\Delta\sigma\left(\omega+\omega_a, t'+\delta_t\right)\mathcal{A}_i(\omega)A_i\left(t'\right)e^{it'\omega} \ , \tag{E.34}$$

where

$$\Phi_a = \int dt\left|A_i(t)\right|^2 = \int_{-\infty}^{\infty}\frac{d\omega}{2\pi}\left|\mathcal{A}_i(\omega)\right|^2 = a_i^2\sqrt{\frac{\pi}{2}}\tau_a \tag{E.35}$$

and $R_a^{(0)} = \left|\hat{r}_a^{(0)}\right|^2$. Thus the differential reflectivity is:

$$\frac{\Delta R_a}{R_a} = \frac{R_a - R_a^{(0)}}{R_a^{(0)}} = \frac{\cos^2\theta}{\cos\alpha}\frac{\left(\hat{t}^{(0)}\right)^2}{2\pi\Phi_a\hat{r}_a^{(0)}}\frac{4\pi}{c}\mathrm{Re}\int_{-\infty}^{\infty} d\omega\int_{-\infty}^{\infty} dt'\Delta\sigma\left(\omega+\omega_a, t'+\delta_t\right)\mathcal{A}_i(\omega)A_i\left(t'\right)e^{it'\omega} \ . \tag{E.36}$$

$\mathcal{A}_i(\omega)$ is a Gaussian function centered at $\omega = 0$. Since the pulse spectral width is much smaller than ω_a, we make the approximation,

$$\Delta\sigma\left(\omega+\omega_a, t'+\delta_t\right) \approx \Delta\sigma\left(\omega_a, t'+\delta_t\right) \ . \tag{E.37}$$

Then, Eq. (E.36) simplifies to:

$$\frac{\Delta R_a}{R_a} \approx \frac{\cos^2\theta}{\cos\alpha}\frac{\left(\hat{t}_a^{(0)}\right)^2}{\Phi_a\hat{r}_a^{(0)}}\frac{4\pi}{c}\int_{-\infty}^{\infty} dt'\mathrm{Re}\Delta\sigma\left(\omega_a, t'+\delta_t\right)\left|A_i\left(t'\right)\right|^2 \ . \tag{E.38}$$

$\Delta R_a/R_a$ only depends on the real of $\sigma_{\text{neq}}\left(\omega_a, t' + \delta_t\right)$. In the limit $\gamma_{\text{inter}} \to 0$, using Sokhotski–Plemelj theorem, the real part of the conductivity is:

$$\text{Re}\sigma_{\text{neq}}\left(\omega_a, t' + \delta_t\right) = \sigma_0 \left(1 - f^{(e)}\left(\frac{\hbar\omega_a}{2}, t' + \delta_t\right) - f^{(h)}\left(\frac{\hbar\omega_a}{2}, t' + \delta_t\right)\right) \tag{E.39}$$

and consequently,

$$\frac{\Delta R_a}{R_a} = -\frac{\cos^2\theta}{\cos\alpha}\frac{\left(\hat{t}_a^{(0)}\right)^2}{\Phi_a \hat{r}_a^{(0)}}\frac{4\pi}{c}\sigma_0 \int_{-\infty}^{\infty} dt' \left|A_i\left(t'\right)\right|^2 \left\{f^{(e)}\left(\frac{\hbar\omega_a}{2}, t' + \delta_t\right) + f^{(h)}\left(\frac{\hbar\omega_a}{2}, t' + \delta_t\right)\right\} . \tag{E.40}$$

Appendix F

Numerical implementation of the hot electron model

The equations describing the model presented in Sec. 4.2 cannot be solved analytically. The most accurate and easy way to solve the differential equations is using the forth order Runge-Kutta method. If implemented without care, the calculation can take some time, so it is useful to provide some details of the implemented algorithm.

Since the pump is a 100-fs pulse, the initial time is chosen as $t_0 = 0.4$ ps. The initial conditions were: Fermi energy $E_F = F_e = F_h = 300$ meV and temperature $T_0 = 300$ K. To solve the differential equations, a step $h_1 = 0.02$ fs was used to solve the nonlinear Eqs. (4.36), (4.48) and (4.52) at each $h_2 \approx 0.3$ fs. The algorithm used was:

1. Apply Runge-kutta 4th order scheme with step h_1 to solve Eqs. (4.31) and (4.34) from time t_i to $t_f = t_i + h_2$;

2. At time $t_f = t_i + h_2$, calculate the integral (4.44):

$$\tilde{\varepsilon}(t_f) = I_0 + \frac{\hbar\omega_b}{2}\frac{e^{-t_f/\tau_\varepsilon}}{\tau_{ee}}\int_{t_i}^{t_f} dt' e^{t'/\tau_\varepsilon} n_{\mathrm{nt}}(t') \tag{F.1}$$

   and solve Eqs. (4.36), (4.48) and (4.52). I_0 is the value of the integral at the initial moment, which is zero in the beginning;

3. Update the values of time, t_i to t_f, and corresponding initial conditions of the integral:

$$I_0 \to \tilde{\varepsilon}(t_f) \tag{F.2}$$

   as well as the quasi-Fermi levels and temperature to $F_e(t_f)$, $F_h(t_f)$ and $T(t_f)$. Also update the initial non-thermalized and thermalized carrier concentrations;

This procedure is repeated until t_f equals the final time of the measurement chosen to be 2 ps.

Appendix G

Quantization of the SPP electromagnetic field

In this section, using the classical expression for the energy, the electromagnetic field, in a dispersive lossless dielectric medium, is quantized following Ref. [58].

For electric and magnetic fields with a harmonic time dependence:

$$\mathbf{E}(\mathbf{r},t) = \mathbf{E}_\omega(\mathbf{r})e^{-i\omega t} + \text{c.c} \ , \tag{G.1}$$

$$\mathbf{B}(\mathbf{r},t) = \mathbf{B}_\omega(\mathbf{r})e^{-i\omega t} + \text{c.c} \ , \tag{G.2}$$

the time-averaged classical electromagnetic energy in the presence of a dispersive, lossless dielectric is given by:

$$U_{\text{EM}}(\omega) = \frac{1}{4\pi}\int d^3r \left(\mathbf{E}^*_\omega(\mathbf{r})\frac{\partial}{\partial\omega}\left[\omega\varepsilon_r(\mathbf{r},\omega)\right]\mathbf{E}_\omega(\mathbf{r}) + |\mathbf{B}_\omega|^2\right) \ , \tag{G.3}$$

where $\varepsilon_r(\mathbf{r},\omega)$ is the relative dielectric function. The idea is to take the above equation as the quantum mechanical energy of a EM field eigenmode with frequency ω. We work in the Weyl gauge, in which the scalar potential is set to zero:

$$\phi = 0 \ , \tag{G.4}$$

such that the electric and magnetic fields are obtained only from the vector potential $\mathbf{A}$:

$$\mathbf{E}(\mathbf{r},t) = -\frac{1}{c}\frac{\partial\mathbf{A}(\mathbf{r},t)}{\partial t} \quad , \quad \mathbf{B}(\mathbf{r},t) = \nabla\times\mathbf{A}(\mathbf{r},t) \ . \tag{G.5}$$

In our case of interest, graphene is between two dielectrics, ε_1 and ε_2, that are homogeneous. Thus, $\mathbf{A}(\mathbf{r},t)$ is expanded by making explicit the momentum in the xy-plane and since plasmons follow a

dispersion relation $\omega_{\mathbf{q}} = \omega(\mathbf{q})$, the expansion is written as:

$$\mathbf{A}(\mathbf{r},t) = \frac{1}{\sqrt{\mathcal{S}}} \sum_{\mathbf{q}} \alpha_{\mathbf{q}} e^{-i\omega_{\mathbf{q}} t} e^{i\mathbf{q}\cdot\mathbf{r}} \mathbf{A}_{\mathbf{q}}(z) + \text{c.c} \ , \tag{G.6}$$

so that $\mathbf{q}$ not only is the plasmon momentum but also represents a mode $\omega_{\mathbf{q}}$. The coefficients $\alpha_{\mathbf{q}}$ are dimensionless. The mode functions $\mathbf{A}_{\mathbf{q}}$ have units $[\mathbf{A}] \cdot [\text{distance}]$ and S has units of area.

From Maxwell's Eqs. (A.3) and (A.4), we obtain the wave equation for $\mathbf{E}$:

$$\nabla \times \nabla \times \mathbf{E}_{\mathbf{q}}(\mathbf{r}) = \frac{\omega^2}{c^2} \varepsilon_r(\mathbf{r}, \omega_{\mathbf{q}}) \mathbf{E}_{\mathbf{q}}(\mathbf{r}) \ . \tag{G.7}$$

Using expansion (G.6) in the wave equation, the eigenvalue equation for $\mathbf{A}_{\mathbf{q}}(z)$ is obtained:

$$D_{\mathbf{q}} \times D_{\mathbf{q}} \times \mathbf{A}_{\mathbf{q}}(z) = \frac{\omega_{\mathbf{q}}^2}{c^2} \varepsilon_r(\mathbf{r}, \omega_{\mathbf{q}}) \mathbf{A}_{\mathbf{q}}(z) \ , \tag{G.8}$$

where the operator $D_{\mathbf{q}}$ defined as:

$$D_{\mathbf{q}} = i\mathbf{q} + \mathbf{e}_z \partial_z \ . \tag{G.9}$$

Equation (G.8) is just Ampere's law in the dielectric medium for the mode-function $\mathbf{A}_{\mathbf{q}}(z)$. Next, we assume that the total time-averaged energy for the vector potential is given by:

$$U_{\text{EM}} = \sum_{\mathbf{q}} U_{\text{EM}}(\omega_{\mathbf{q}}) |\alpha_{\mathbf{q}}|^2 \ . \tag{G.10}$$

The quantization of the theory is done by transforming the amplitudes $\alpha_{\mathbf{q}}$ into quantum mechanical operators:

$$\alpha_{\mathbf{q}} \to \sqrt{\frac{2\pi c}{L_{\mathbf{q}} \omega_{\mathbf{q}}}} \hat{a}_{\mathbf{q}} \quad , \quad \alpha_{\mathbf{q}}^* \to \sqrt{\frac{2\pi c}{L_{\mathbf{q}} \omega_{\mathbf{q}}}} \hat{a}_{\mathbf{q}}^\dagger \ , \tag{G.11}$$

with commutation relations:

$$\left[\hat{a}_{\mathbf{q}}, \hat{a}_{\mathbf{p}}^\dagger\right] = \delta_{\mathbf{q},\mathbf{p}} \ . \tag{G.12}$$

$L_{\mathbf{q}}$ is the called the mode-length. This term is determined by demanding that the quantum mechanical Hamiltonian obtained from Eq. (G.10):

$$\hat{H} = \sum_{\mathbf{q}} \frac{2\pi c}{2 L_{\mathbf{q}} \omega_{\mathbf{q}}} U_{\text{EM}}(\omega_{\mathbf{q}}) \left(\hat{a}_{\mathbf{q}}^\dagger \hat{a}_{\mathbf{q}} + \hat{a}_{\mathbf{q}} \hat{a}_{\mathbf{q}}^\dagger \right) \tag{G.13}$$

coincides with the Hamiltonian for a collection of harmonic oscillators:

$$\hat{H} = \frac{1}{2} \sum_{\mathbf{q}} \hbar \omega_{\mathbf{q}} \left(\hat{a}_{\mathbf{q}}^\dagger \hat{a}_{\mathbf{q}} + \hat{a}_{\mathbf{q}} \hat{a}_{\mathbf{q}}^\dagger \right) \ . \tag{G.14}$$

Thus $L_{\mathbf{q}}$ is:

$$L_{\mathbf{q}} = \frac{2\pi c}{\hbar\omega_{\mathbf{q}}^2} U_{\mathrm{EM}}(\omega_{\mathbf{q}}) \ . \tag{G.15}$$

Using expansion (G.6) in Eq. (G.3), the EM energy of mode $\mathbf{q}$ is found to be:

$$U_{\mathrm{EM}}(\omega_{\mathbf{q}}) = \frac{1}{4\pi\mathcal{S}} \int d^3r \left(\frac{\omega_{\mathbf{q}}^2}{c^2} \mathbf{A}_{\mathbf{q}}^*(\mathbf{r}) \frac{\partial}{\partial\omega_{\mathbf{q}}} \left[\omega_{\mathbf{q}}\varepsilon_r(\mathbf{r},\omega_{\mathbf{q}})\right] \mathbf{A}_{\mathbf{q}}(\mathbf{r}) + |\nabla \times \mathbf{A}_{\mathbf{q}}(\mathbf{r})|^2 \right) \ .$$

Using,

$$|\nabla \times \mathbf{A}_{\mathbf{q}}(\mathbf{r})|^2 = \nabla \times \cdot \left(\mathbf{A}_{\mathbf{q}}(\mathbf{r}) \times \nabla \times \mathbf{A}_{\mathbf{q}}(\mathbf{r})\right) + \mathbf{A}_{\mathbf{q}}^*(\mathbf{r}) \cdot \left(\nabla \times \nabla \times \mathbf{A}_{\mathbf{q}}(\mathbf{r})\right) \tag{G.16}$$

as well as $\mathbf{A}_{\mathbf{q}}(\mathbf{r}) = e^{i\mathbf{q}\cdot\mathbf{x}}\mathbf{A}_{\mathbf{q}}(z)$, together with the dispersion Eq. (G.8), a simplified expression for EM energy is obtained:

$$U_{\mathrm{EM}}(\omega_{\mathbf{q}}) = \frac{1}{2\pi\mathcal{S}} \frac{\omega_{\mathbf{q}}^2}{c^2} \int d^3r \mathbf{A}_{\mathbf{q}}^*(z) \left(\varepsilon_r(\mathbf{r},\omega_{\mathbf{q}}) + \frac{\omega_{\mathbf{q}}}{2} \frac{\partial\varepsilon_r(\mathbf{r},\omega_{\mathbf{q}})}{\partial\omega_{\mathbf{q}}} \right) \mathbf{A}_{\mathbf{q}}(z) \ . \tag{G.17}$$

By definition:

$$\int d^2x = \mathcal{S} \ , \tag{G.18}$$

so the final expression for $U_{\mathrm{EM}}(\omega_{\mathbf{q}})$ is:

$$U_{\mathrm{EM}}(\omega_{\mathbf{q}}) = \frac{\omega_{\mathbf{q}}^2}{2\pi c^2} \int dz \mathbf{A}_{\mathbf{q}}^*(z) \left(\varepsilon_r(z,\omega_{\mathbf{q}}) + \frac{\omega_{\mathbf{q}}}{2} \frac{\partial\varepsilon_r(\mathbf{r},\omega_{\mathbf{q}})}{\partial\omega_{\mathbf{q}}} \right) \mathbf{A}_{\mathbf{q}}(z) \ . \tag{G.19}$$

Hence, the mode length (G.15) is:

$$L_{\mathbf{q}} = \frac{1}{\hbar c} \int dz \mathbf{A}_{\mathbf{q}}^*(z) \left(\varepsilon_r(z,\omega_{\mathbf{q}}) + \frac{\omega_{\mathbf{q}}}{2} \frac{\partial\varepsilon_r(\mathbf{r},\omega_{\mathbf{q}})}{\partial\omega_{\mathbf{q}}} \right) \mathbf{A}_{\mathbf{q}}(z) \ . \tag{G.20}$$

Equation (G.20) remains valid for any linear optical medium (including effects of dispersion, non-locality, inhomogeneity and anisotropy if ε_r is generalized to tensor) as long as losses are neglected.

Finally, the quantized vector potential and electric field are:

$$\hat{\mathbf{A}}(\mathbf{r},t) = \sum_{\mathbf{q}} \sqrt{\frac{2\pi c}{L_{\mathbf{q}}\omega_{\mathbf{q}}\mathcal{S}}} \hat{a}_{\mathbf{q}} e^{-i\omega_{\mathbf{q}}t} e^{i\mathbf{q}\cdot\mathbf{r}} \mathbf{A}_{\mathbf{q}}(z) + \mathrm{c.c} \ , \tag{G.21}$$

$$\hat{\mathbf{E}}(\mathbf{r},t) = i \sum_{\mathbf{q}} \sqrt{\frac{2\pi\omega_{\mathbf{q}}}{L_{\mathbf{q}}c\mathcal{S}}} \hat{a}_{\mathbf{q}} e^{-i\omega_{\mathbf{q}}t} e^{i\mathbf{q}\cdot\mathbf{r}} \mathbf{A}_{\mathbf{q}}(z) + \mathrm{c.c} \ . \tag{G.22}$$

We now can determine the full expressions for $\mathbf{A}_{\mathbf{q}}(z)$ and $L_{\mathbf{q}}$ using Eq. (G.8) and (G.20) respectively. In our case, the dielectric function is:

$$\varepsilon_r(z,\omega_{\mathbf{q}}) = \Theta(z)\,\varepsilon_1 + \Theta(-z)\,\varepsilon_2 + \frac{4\pi i}{\omega_{\mathbf{q}}} \sigma(\mathbf{q},\omega_{\mathbf{q}}) \delta(z) \ , \tag{G.23}$$

where $\sigma(\mathbf{q},\omega_\mathbf{q})$ is graphene's conductivity function which we model using the Drude formula:

$$\sigma(\mathbf{q},\omega_\mathbf{q}) = i\frac{4\sigma_0}{\pi}\frac{E_F}{\hbar\omega_\mathbf{q}} \ . \tag{G.24}$$

In order to determine the plasmon mode, we look for p-polarized solutions of the electric field in the form of evanescent waves. For $z \neq 0$ we have from Gauss's law (A.1):

$$D_\mathbf{q} \cdot \mathbf{E}_\mathbf{q}(z) = 0 \ . \tag{G.25}$$

The mode-function must then take the form:

$$\mathbf{A}_\mathbf{q}(z) = \sqrt{\hbar c}\begin{cases} \mathbf{u}^{(+)}_{1,\mathbf{q}} e^{-\kappa_{1,\mathbf{q}} z} & z > 0 \\ \mathbf{u}^{(-)}_{2,\mathbf{q}} e^{\kappa_{2,\mathbf{q}} z} & z < 0 \end{cases} \ , \tag{G.26}$$

where:

$$\kappa_{n,\mathbf{q}} = \sqrt{q^2 - \frac{\omega_\mathbf{q}^2}{c^2}\varepsilon_n} \quad , \quad \mathbf{u}^{(\pm)}_{n,\mathbf{q}} = i\frac{\mathbf{q}}{q} \pm \frac{q}{\kappa_{n,\mathbf{q}}}\mathbf{e}_z \ . \tag{G.27}$$

Using Eqs. (G.23) and (G.26), Eq. (G.20) yields:

$$L_\mathbf{q} = \varepsilon_1 \left|\mathbf{u}^{(+)}_{1,\mathbf{q}}\right|^2 \frac{1}{2\kappa_{1,\mathbf{q}}} + \varepsilon_2 \left|\mathbf{u}^{(-)}_{2,\mathbf{q}}\right|^2 \frac{1}{2\kappa_{2,\mathbf{q}}} + \frac{2\pi i}{\omega_\mathbf{q}} \left|\mathbf{u}^{(+)}_{1,\mathbf{q}}\right|^2 \frac{\partial}{\partial\omega_\mathbf{q}} \left(\omega_\mathbf{q}\sigma(\mathbf{q},\omega_\mathbf{q})\right) \ . \tag{G.28}$$

Since the conductivity is given by Eq. (G.24), the mode length assumes the form:

$$L_\mathbf{q} = \varepsilon_1 \frac{\kappa_{1,\mathbf{q}}^2 + q^2}{2\kappa_{1,\mathbf{q}}^3} + \varepsilon_2 \frac{\kappa_{2,\mathbf{q}}^2 + q^2}{2\kappa_{2,\mathbf{q}}^3} \ . \tag{G.29}$$

G.1 Quantization of the optical field

The quantization of the incident, reflected and transmitted fields follows the same procedure as above. However, in these cases, the dielectric function is:

$$\varepsilon_r(z,\omega_\mathbf{q}) = \eta_i^2 \ , \tag{G.30}$$

where η_i is the refractive index of medium i, and the eigenmodes of the wave equation are:

$$\mathbf{A}_\mathbf{q}(\mathbf{r}) = \sqrt{\hbar c} e^{i\mathbf{k}\cdot\mathbf{r}}\mathbf{e}_\mathbf{k} \ , \tag{G.31}$$

where $\mathbf{e}_\mathbf{k}$ is the polarization vector. For a photon propagating in 3D space, the length mode $L_\mathbf{k}$, given in Eq. (G.20), is ill defined,

$$L_\mathbf{k} = \eta_i^2 \int dz = \eta_i^2 R \ . \tag{G.32}$$

Here R is interpreted as the distance between sample and position of the laser. If we have a beam of cross section $\mathcal{S}$, then:

$$V = \mathcal{S} \cdot R \tag{G.33}$$

is the volume occupied by a photon.

The quantized vector potential and electric field are:

$$\hat{\mathbf{A}}(\mathbf{r}, t) = \sum_{\mathbf{k}} \sqrt{\frac{2\pi\hbar c^2}{\eta_i^2 V \omega_{\mathbf{k}}}} \hat{b}_{\mathbf{k}} e^{i(\mathbf{k}\cdot\mathbf{r} - \omega_{\mathbf{k}} t)} \mathbf{e}_{\mathbf{k}} + \text{c.c} \ , \tag{G.34}$$

$$\hat{\mathbf{E}}(\mathbf{r}, t) = i \sum_{\mathbf{k}} \sqrt{\frac{2\pi\hbar\omega_{\mathbf{k}}}{\eta_i^2 V}} \hat{b}_{\mathbf{k}} e^{i(\mathbf{k}\cdot\mathbf{r} - \omega_{\mathbf{k}} t)} \mathbf{e}_{\mathbf{k}} + \text{c.c} \ . \tag{G.35}$$

Here $\hat{b}_{\mathbf{k}}$ ($\hat{b}^{\dagger}_{\mathbf{k}}$) is the destruction (creation) operator of photons of the optical field. The normalization factor:

$$\left(\frac{2\pi\hbar c^2}{\eta_i^2 V \omega_{\mathbf{k}}} \right)^{1/2} \tag{G.36}$$

corresponds to one photon in the volume V.

Finally, the magnetic field is:

$$\hat{\mathbf{H}}\,(\mathbf{r}, t) = i\eta_i \sum_{\mathbf{k}} \sqrt{\frac{2\pi\hbar\omega_{\mathbf{k}}}{\eta_i^2 V}} \hat{b}_{\mathbf{k}} e^{i(\mathbf{k}\cdot\mathbf{r} - \omega_{\mathbf{k}} t)} \hat{\mathbf{k}} \times \mathbf{e}_{\mathbf{k}} + \text{c.c} \ , \tag{G.37}$$

where $\hat{\mathbf{k}} = \mathbf{k}/k$ and $k = \eta\omega_{\mathbf{k}}/c$.

Appendix H

Description of the experiment with BBO

H.1 BBO description

BBO is a negative-birefringence uniaxial crystal [12, 59] with dielectric tensor in the crystal's frame:

$$\varepsilon = \begin{bmatrix} n_0^2 & 0 & 0 \\ 0 & n_0^2 & 0 \\ 0 & 0 & n_e^2 \end{bmatrix} \quad , \quad n_o > n_e \ , \tag{H.1}$$

where n_o is called the ordinary refractive index and n_e, the extraordinary refractive index ($n_e < n_o$). The z-axis is the crystal's optical axis. Because BBO's dielectric tensor has different eigenvalues, the EM wave propagates with different speed in different directions [50, 60]. Thus, it is convenient to determine the eigenmodes of the crystal. From Eqs. (A.3) and (A.4) in momentum-frequency space:

$$\mathbf{k} \times \mathbf{E}(\mathbf{r}, \omega) = \frac{\omega}{c} \mathbf{H}(\mathbf{r}, \omega) \quad , \quad \mathbf{k} \times \mathbf{H}(\mathbf{r}, \omega) = -\frac{\omega}{c} \mathbf{D}(\mathbf{r}, \omega) \ , \tag{H.2}$$

we find the wave equation for a plane wave:

$$\mathbf{k} \times (\eta \mathbf{k} \times \mathbf{H}) = -\frac{\omega^2}{c^2} \mathbf{H} \ , \tag{H.3}$$

where η is the inverse matrix of the dielectric tensor ε. The above equation is a eigenvalue problem:

$$\mathcal{L}\mathbf{H} = -\frac{\omega^2}{c^2} \mathbf{H} \ , \tag{H.4}$$

with $\mathcal{L} = \mathbf{k} \times (\eta \mathbf{k} \times)$ a hermitian operator. For:

$$\mathbf{k} = k(\cos\phi \sin\theta, \sin\phi \sin\theta, \cos\theta) \ , \tag{H.5}$$

the eigenmodes are easily found to be[1]:

$$\hat{\mathbf{h}}_o = (-\cos\phi\cos\theta, -\sin\phi\cos\theta, \sin\theta)\,, \quad k_o = \frac{\omega}{c} n_0\ , \tag{H.6}$$

$$\hat{\mathbf{h}}_e = (-\sin\phi, \cos\phi, 0)\,, \quad k_e = \frac{n_0 n_e}{\sqrt{n_0^2\sin^2\theta + n_e^2\cos^2\theta}} \frac{\omega}{c} = n(\theta)\frac{\omega}{c}\ . \tag{H.7}$$

The first mode is called ordinary (with ordinary polarization) and the second one extraordinary (with extraordinary polarization). Using Maxwell's equation, the respective eigenvectors for $\mathbf{D}$ are:

$$\hat{\mathbf{d}}_o = -\frac{\mathbf{k}_o}{k_o} \times \hat{\mathbf{h}}_o = (-\sin\phi, \cos\phi, 0) \tag{H.8}$$

and

$$\hat{\mathbf{d}}_e = -\frac{\mathbf{k}_e}{k_e} \times \hat{\mathbf{h}}_e = (\cos\theta\cos\phi, \cos\theta\sin\phi, -\sin\theta)\ . \tag{H.9}$$

Notice that from Maxwell's equations it follows that both $\mathbf{H}$ and $\mathbf{D}$ are always perpendicular to the wavevector. This is not true for the electric field $\mathbf{E}$ since the dielectric tensor is not isotropic.

It is also important to describe the experiment is the non-linear (NL) response of BBO. Since BBO has a trigonal structure with point group symmetry $3m$ [12, 59], its second order susceptibility tensor, $\chi^{(2)}_{ijk}$, contains the following non-vanishing elements:

$$\begin{aligned} xzx &= yzy\ , \\ xxz &= yyz\ , \\ zxx &= zyy\ , \\ zzz\ , & \\ yyy &= -yxx = -xxy = -xyx\ . \end{aligned}$$

We ignore losses and use Kleinman's symmetry to write the second order susceptibility tensor in contracted notation [12]:

$$\begin{aligned} d_{15} &= d_{24} = d_{31}\ , \\ d_{31} &= d_{32}\ , \\ d_{33}\ , & \\ d_{22} &= -d_{21} = -d_{16}\ , \end{aligned}$$

[1]The hat indicates that the vectors are normalized.

with the nonlinear susceptibility tensor written as:

$$d^{(2)} = \begin{bmatrix} 0 & 0 & 0 & 0 & d_{31} & -d_{22} \\ -d_{22} & d_{22} & 0 & d_{31} & 0 & 0 \\ d_{31} & d_{31} & d_{33} & 0 & 0 & 0 \end{bmatrix} . \tag{H.10}$$

H.2 Crystal and lab frames

It is convenient to distinguish between the crystal and the lab frames since in the lab frame we know the polarization and direction of the incident pulses and in the crystal frame it is easier to describe the NL SF-process because we know $d^{(2)}$.

To distinguish between lab and crystal coordinates, we write the coordinates in the lab frame with a prime. According to the crystal's data sheet, the BBO's optical axis is in the $y'z'$-plane and makes a angles $\theta = \theta_0 + \Psi$ with the y'-axis (see Fig. 6.4). However, in the crystal's frame, the optical axis is coincident with the z-axis. Thus, the transformation $O_R(\theta)$ that takes us from the lab frame to the crystal frame is:

$$\mathbf{e}_z = O_R(\theta)\, \mathbf{e}_z^{'} , \tag{H.11}$$

where:

$$O_R(\theta) = \begin{bmatrix} 1 & 0 & 0 \\ 0 & \sin\theta & -\cos\theta \\ 0 & \cos\theta & \sin\theta \end{bmatrix} . \tag{H.12}$$

The incident wavevectors are:

$$\mathbf{k}_a^{I'} = \frac{\omega}{c}(-\sin\alpha, \cos\alpha, 0) \quad , \quad \mathbf{k}_b^{I'} = \frac{\omega}{c}(\sin\alpha, \cos\alpha, 0) \tag{H.13}$$

and the respective fields outside of the crystal are:

$$\mathbf{D}_a^{I'} = D_a^I(-\cos\alpha, -\sin\alpha, 0)\, e^{i\mathbf{k}_a^{I'}\cdot\mathbf{r}} e^{-i\omega t} \quad , \quad \mathbf{D}_b^{I'} = D_b^I(-\cos\alpha, \sin\alpha, 0)\, e^{i\mathbf{k}_b^{I'}\cdot\mathbf{r}} e^{-i\omega t} . \tag{H.14}$$

In the crystal frame, they read:

$$\mathbf{k}_a^I = \frac{\omega}{c}(-\sin\alpha, \cos\alpha\sin\theta, \cos\alpha\cos\theta) \quad , \quad \mathbf{k}_b^I = \frac{\omega}{c}(\sin\alpha, \cos\alpha\sin\theta, \cos\alpha\cos\theta) \tag{H.15}$$

and

$$\mathbf{D}_a^I = D_a^I(-\cos\alpha, -\sin\alpha\sin\theta, -\cos\theta\sin\alpha)\, e^{i\mathbf{k}_a^I\cdot\mathbf{r}} e^{-i\omega t} , \tag{H.16}$$

$$\mathbf{D}_b^I = D_b^I(-\cos\alpha, \sin\alpha\sin\theta, \cos\theta\sin\alpha)\, e^{i\mathbf{k}_b^I\cdot\mathbf{r}} e^{-i\omega t} . \tag{H.17}$$

When enter the crystal, the ordinary and extraordinary components of the field will refract differently [50]. Thus, it is better to write fields a and b in terms of ordinary and extraordinary

components. For the wavevector $\mathbf{k}_b^I$, using Eq. (H.4), the eigenmodes are are found to be:

$$\mathbf{k}_b^o = \frac{\omega}{c} n_o \left(\sin\alpha_o, \cos\alpha_o \sin\theta, \cos\alpha_o \cos\theta\right) \tag{H.18}$$

and:

$$\mathbf{k}_b^e = \frac{\omega}{c} n_e(\theta, \alpha_e) \left(\sin\alpha_e, \cos\alpha_e \sin\theta, \cos\alpha_e \cos\theta\right) \ , \tag{H.19}$$

with:

$$\frac{1}{n_e^2(\theta, \alpha_e)} = \frac{\cos^2\alpha_e \cos^2\theta}{n_o^2} + \frac{\cos^2\alpha_e \sin^2\theta}{n_e^2} + \frac{\sin^2\alpha_e}{n_e^2} \ . \tag{H.20}$$

The respective eigen-polarizations are:

$$\hat{\mathbf{d}}_o = \frac{1}{\sqrt{\cos^2\alpha_o \sin^2\theta + \sin^2\alpha_o}} \left(-\cos\alpha_o \sin\theta, \sin\alpha_o, 0\right) \ , \tag{H.21}$$

$$\hat{\mathbf{d}}_e = \frac{1}{2} \frac{1}{\sqrt{\sin^2\alpha_e \cos^2\theta + \sin^2\theta}} \left(\sin\left(2\alpha_e\right)\cos\theta, \cos^2\alpha_e \sin\left(2\theta\right), -2\sin^2\alpha_e - 2\cos^2\alpha_e \sin^2\theta\right) \ . \tag{H.22}$$

For beam a, the results are the same but with $-\alpha_e$ and $-\alpha_o$. Thus, the fields a and b inside the crystal are:

$$\begin{aligned} \mathbf{D}_a = &- \frac{\sin\theta \ t_o D_a^I}{\sqrt{\cos^2\alpha_o \sin^2\theta + \sin^2\alpha_o}} e^{i\mathbf{k}_b^o \cdot \mathbf{r}} e^{-i\omega t} \hat{\mathbf{d}}_o(-\alpha_o) \\ &+ \frac{\cos\theta \sin\alpha \ t_e D_a^I}{\sqrt{\cos^2\theta \sin^2\alpha + \sin^2\theta}} e^{i\mathbf{k}_a^e \cdot \mathbf{r}} e^{-i\omega t} \hat{\mathbf{d}}_e(-\alpha_e) \ , \end{aligned} \tag{H.23}$$

$$\begin{aligned} \mathbf{D}_b = &- \frac{\sin\theta \ t_o D_b^I}{\sqrt{\cos^2\alpha_o \sin^2\theta + \sin^2\alpha_o}} e^{i\mathbf{k}_b^o \cdot \mathbf{r}} e^{-i\omega t} \hat{\mathbf{d}}_o(\alpha_o) \\ &- \frac{\cos\theta \sin\alpha \ t_e D_b^I}{\sqrt{\cos^2\theta \sin^2\alpha + \sin^2\theta}} e^{i\mathbf{k}_b^e \cdot \mathbf{r}} e^{-i\omega t} \hat{\mathbf{d}}_e(\alpha_e) \ , \end{aligned} \tag{H.24}$$

where t_o and t_e are the transmission coefficients for ordinary and extraordinary polarizations, respectively. The respective electric fields are given by $\mathbf{E} = \eta \mathbf{D}$:

$$\begin{aligned} \mathbf{E}_a = &- \frac{\sin\theta \ t_o E_a^I e^{i\mathbf{k}_b^o \cdot \mathbf{r}} e^{-i\omega t}}{n_o^2 \sqrt{\cos^2\alpha_o \sin^2\theta + \sin^2\alpha_o}} \hat{\mathbf{d}}_o(-\alpha_o) \\ &+ \frac{\cos\theta \sin\alpha \ t_e E_a^I e^{i\mathbf{k}_a^e \cdot \mathbf{r}} e^{-i\omega t}}{n_e^2(\theta, \alpha_e) \sqrt{\cos^2\theta \sin^2\alpha + \sin^2\theta}} \hat{\mathbf{d}}_e(-\alpha_e) + \frac{\cos\theta \sin\alpha \ t_e E_a^I e^{i\mathbf{k}_a^e \cdot \mathbf{r}} e^{-i\omega t}}{\bar{n}_e^2(\theta, \alpha_e) \sqrt{\cos^2\theta \sin^2\alpha + \sin^2\theta}} \hat{\mathbf{k}}_a \ , \end{aligned} \tag{H.25}$$

$$\mathbf{E}_b = -\frac{\sin\theta\ t_o E_b^I e^{i\mathbf{k}_b^o\cdot\mathbf{r}} e^{-i\omega t}}{n_o^2\sqrt{\cos^2\alpha_o\sin^2\theta+\sin^2\alpha_o}}\hat{\mathbf{d}}_o(\alpha_o) \tag{H.26}$$
$$-\frac{\cos\theta\sin\alpha\ t_e E_b^I e^{i\mathbf{k}_b^e\cdot\mathbf{r}} e^{-i\omega t}}{n_e^2(\theta,\alpha_e)\sqrt{\cos^2\theta\sin^2\alpha+\sin^2\theta}}\hat{\mathbf{d}}_e(\alpha_e) - \frac{\cos\theta\sin\alpha\ t_e E_b^I e^{i\mathbf{k}_b^e\cdot\mathbf{r}} e^{-i\omega t}}{\bar{n}_e^2(\theta,\alpha_e)\sqrt{\cos^2\theta\sin^2\alpha+\sin^2\theta}}\hat{\mathbf{k}}_b\ ,$$

where

$$\frac{1}{\bar{n}_e^2(\theta,\alpha_e)} = \frac{\left(n_e^2-n_o^2\right)\cos\alpha\cos\theta\sqrt{\cos^2\theta\sin^2\alpha+\sin^2\theta}}{n_e^2 n_o^2}\ . \tag{H.27}$$

The angles α_o and α_e, as well as the transmission coefficients, are determined by the boundary conditions.

H.3 Sum frequency generation

We start the calculation of the sum frequency process with the non-linear wave equation [12]:

$$\nabla\times\nabla\times\mathbf{E}_s - \frac{\omega_s^2}{c^2}\varepsilon(\omega_s)\mathbf{E}_s = \frac{4\pi\omega_s^2}{c^2}\mathbf{P}_{\rm NL}\ , \tag{H.28}$$

with $\mathbf{E}_s$ denoting the field at sum frequency $\omega_s = \omega_a + \omega_b$ and

$$\mathbf{P}_{\rm NL} = \chi^{(2)} : \mathbf{E}_a\mathbf{E}_b\ . \tag{H.29}$$

In practice, Eq. (H.28) is very difficult to solve. Nonetheless, we can make it easier if we approximate the fields by plane waves and remember that sum frequency generation is only appreciable when there is momentum conservation, that is, when $\Delta\mathbf{k} = \mathbf{k}_a + \mathbf{k}_b - \mathbf{k}_s$ is equal to zero. This is only true for the situation when ordinary components of fields a and b interact to produce a sum frequency field with extraordinary polarization:

$$o + o \rightarrow e\ . \tag{H.30}$$

Thus, only the ordinary components of fields a and b are of relevance when writing $\mathbf{P}_{\rm NL}$ in Eq. (H.29).

Taking into account only the ordinary polarizations, $\mathbf{P}_{\rm NL}$ is written:

$$\mathbf{P}_{\rm NL} = 2\begin{bmatrix} 0 & 0 & 0 & 0 & d_{31} & -d_{22} \\ -d_{22} & d_{22} & 0 & d_{31} & 0 & 0 \\ d_{31} & d_{31} & d_{33} & 0 & 0 & 0 \end{bmatrix}\begin{bmatrix} E_{ax}E_{bx} \\ E_{ay}E_{by} \\ 0 \\ 0 \\ 0 \\ E_{ax}E_{by}+E_{ay}E_{bx} \end{bmatrix} = 2\begin{bmatrix} -d_{22}\left(E_{ax}E_{by}+E_{ay}E_{bx}\right) \\ d_{22}\left(E_{ay}E_{by}-E_{ax}E_{bx}\right) \\ d_{31}\left(E_{ax}E_{bx}+E_{ay}E_{by}\right) \end{bmatrix}\ . \tag{H.31}$$

The z-component of the fields is not considered because the ordinary eigenmode only has x and

y-components. Explicitly, $\mathbf{P}_{\mathrm{NL}}$ is:

$$\begin{aligned}\mathbf{P}_{\mathrm{NL}} &= 2\begin{bmatrix} 0 \\ -d_{22}\dfrac{\sin^2\theta}{n_o^2\left(\sin^2\theta\cos^2\alpha+\sin^2\alpha\right)} \\ d_{31}\dfrac{\sin^4\theta-\sin^2\theta\tan^2\alpha}{n_o^4\cos^2\alpha\left(\sin^2\theta+\tan^2\alpha\right)^2}\end{bmatrix}\frac{t_o^2}{n_o^4}E_a^I E_b^I e^{i(\mathbf{k}_a^o+\mathbf{k}_b^o)\cdot\mathbf{r}} \\ &= 4\mathbf{p}_s\frac{t_o^2}{n_o^4}E_a^I E_b^I e^{i(\mathbf{k}_a^o+\mathbf{k}_b^o)\cdot\mathbf{r}}\ . \end{aligned} \tag{H.32}$$

From the experiment, the SF field appears at $\alpha_s = 0$, so its eigenmode is:

$$\hat{\mathbf{d}}_e(\alpha_s=0) = (0, \cos\theta, -\sin\theta)\ , \tag{H.33}$$

the polarization is:

$$\mathbf{P}_{\mathrm{NL}} = 4d_{\mathrm{eff}}\frac{t_o^2}{n_o^4}E_a^I E_b^I e^{i(\mathbf{k}_a^o+\mathbf{k}_b^o)\cdot\mathbf{r}}\hat{\mathbf{d}}_e(\alpha_s=0) + 4d_k\frac{t_o^2}{n_o^4}E_a^I E_b^I e^{i(\mathbf{k}_a^o+\mathbf{k}_b^o)\cdot\mathbf{r}}\hat{\mathbf{k}}_s\ , \tag{H.34}$$

where

$$\hat{\mathbf{k}}_s = \hat{\mathbf{k}}_a + \hat{\mathbf{k}}_b = (0, \sin\theta, \cos\theta) \tag{H.35}$$

is the direction of propagation of the SF signal and

$$d_{\mathrm{eff}} = \mathbf{p}_s\cdot\hat{\mathbf{d}}_e(\alpha_s=0) \quad , \quad d_k = \mathbf{p}_s\cdot\hat{\mathbf{k}}_s\ . \tag{H.36}$$

Finally, we can write the non-linear wave Eq. (H.28) as:

$$\begin{aligned}\nabla\times\nabla\times\mathbf{E}_s - \frac{\omega_s^2}{c^2}\varepsilon(\omega_s)\mathbf{E}_s = {}& \frac{16\pi\omega_s^2}{c^2}d_{\mathrm{eff}}\frac{t_o^2}{n_o^4}E_a^I E_b^I e^{i(\mathbf{k}_a^o+\mathbf{k}_b^o)\cdot\mathbf{r}}\hat{\mathbf{d}}_e(\alpha_s=0) \\ & + \frac{16\pi\omega_s^2}{c^2}d_k\frac{t_o^2}{n_o^4}E_a^I E_b^I e^{i(\mathbf{k}_a^o+\mathbf{k}_b^o)\cdot\mathbf{r}}\hat{\mathbf{k}}_s\ . \end{aligned} \tag{H.37}$$

This is still complicated to solve. However, we invoke the fact that the polarization cannot radiate an electromagnetic wave along its direction of propagation. In fact, from Gauss law:

$$\hat{\mathbf{k}}_s\cdot\mathbf{D}_s = 0 \equiv \hat{\mathbf{k}}_s\cdot\varepsilon(\omega)\mathbf{E}_s = 4\pi\hat{\mathbf{k}}_s\cdot\mathbf{P}_{\mathrm{NL}}\ , \tag{H.38}$$

so the condition for the $\hat{\mathbf{k}}_s$ component of the polarization is automatically satisfied. Thus, the radiated field only has an extraordinary component and the wave equation reduces to a scalar one:

$$\frac{d^2E_s}{d\xi^2} + \frac{\omega^2}{c^2}n_e^2(\theta,\alpha_s=0,\omega_s)E_s = -\frac{16\pi\omega_s^2}{c^2}d_{\mathrm{eff}}\frac{t_o^2}{n_o^4}E_a^I E_b^I e^{i(\mathbf{k}_a^o+\mathbf{k}_b^o)\cdot\mathbf{r}}\ , \tag{H.39}$$

with ξ denoting the variable along $\hat{\mathbf{k}}_s$. We now write the SF-field as

$$E_s = A_s(\xi)e^{ik_s\cdot\xi} \ , \tag{H.40}$$

with A_j being a slowly varying amplitude. Also, since the depletion of beams a and b is small, we approximate E_a^I and E_b^I as constants in Eq. (H.37). This then gives:

$$\frac{d^2A_s}{d\xi^2} + 2ik_s\frac{dA_s}{d\xi} + \left(\frac{\omega_s^2}{c^2}n_e^2(\theta,\alpha_s=0,\omega_s) - k_s^2\right)A_s(\xi) = -\frac{16\pi\omega_s^2}{c^2}d_{\text{eff}}\frac{t_o^2}{n_o^4}E_a^I E_b^I e^{i\Delta k\xi} \ , \tag{H.41}$$

with (for $\omega_a = \omega_b$):

$$\Delta k = \Delta\mathbf{k}\cdot\hat{\mathbf{k}}_s = 2\frac{\omega}{c}n_o(\omega)\cos\alpha_o - 2\frac{\omega}{c}n_e(\theta,\alpha_s=0,2\omega) \ . \tag{H.42}$$

Since, the crystal is mounted on a rotating stage, we can control θ and tune it so that $\Delta k = 0$. Hence from now on, we assume the condition of perfect phase match, $\Delta k = 0$. Using the slowly varying amplitude approximation, Eq. (H.41) becomes:

$$\frac{dA_s}{d\xi} \approx i\frac{8\pi\omega_s^2}{k_s c^2}d_{\text{eff}}\frac{t_o^2}{n_o^4}E_a^I E_b^I \ , \tag{H.43}$$

which has solution:

$$A_s = i\frac{8\pi\omega_s^2}{k_s c^2}\mathcal{D}d_{\text{eff}}\frac{t_o^2}{n_o^4}E_a^I E_b^I \ , \tag{H.44}$$

where $\mathcal{D}$ is an effective interaction distance. This allows us to conclude that the SF-field is of the form:

$$A_s \propto E_a^I E_b^I \ . \tag{H.45}$$

Since we have pulses with finite bandwidth,

$$A_s(\omega) = i\beta\int d\omega' E_b^I(\omega-\omega')E_a^I(\omega') \ , \tag{H.46}$$

where β the constant of proportionality,

$$\beta = i\frac{8\pi\omega_s^2}{k_s c^2}\mathcal{D}d_{\text{eff}}\frac{t_o^2}{n_o^4} \ , \tag{H.47}$$

that can be determined by fitting to the experimental results. From the Manley–Rowe relations (assuming no losses) [12], the intensity variation of beam a is:

$$\Delta I_a(t) = -\frac{1}{2}I_s(t) \ . \tag{H.48}$$

Here $I_s \propto |A_s(t)|^2$ is the intensity of the SF-field. Therefore, the power depletion is:

$$\Delta P_a(t) \approx -\frac{1}{2} P_s(t) \propto P_a^I P_b^I \ . \tag{H.49}$$

Appendix I

Lock-in amplifier

Lock-in amplifiers are used to detect and measure very small AC signals, all the way down to a few nanovolts [61, 62]. Accurate measurements may be made even when a small signal is obscured by noise sources many thousands of times larger. This device uses a technique known as phase-sensitive detection to extract signals in a defined frequency band around a specific reference frequency. Signals at frequencies outside the frequency band are rejected and do not affect the measurement.

In the experiment, the process under study is excited at a fixed reference frequency ν_r and the lock-in detects the response from the experiment at that frequency. In our case, the pump beam (beam b) is modulated by an optical chopper, that fixes ν_r. The lock-in then uses a phase-locked-loop (PLL) to generate the reference signal. The PLL locks the internal reference oscillator to the external reference, $\omega_r = 2\pi\nu_r$, resulting in a reference sine wave at ω_r with a fixed phase shift θ_{ref}. Since the PLL actively tracks the external reference, changes in ω_r do not affect the measurement.

To understand how the lock-in works, let us, for the sake of simplicity, consider the following example. Imagine that the optical chopper modulates the beam as a sine wave[1]. Then, the signal is of the form $V_{\text{sig}} \sin(\omega_r t + \theta_{\text{sig}})$, where V_{sig} is the signal amplitude. The lock-in amplifier generates its own sine wave, $V_{\text{L}} \sin(\omega_L t + \theta_{\text{ref}})$, and then multiplies it by the signal using a phase sensitive detector (PSD). The output of the PSD is the product of two sine waves:

$$\begin{aligned} V_{\text{psd}} &= V_{\text{L}} V_{\text{sig}} \sin(\omega_r t + \theta_{\text{sig}}) \sin(\omega_L t + \theta_{\text{ref}}) \\ &= \frac{V_{\text{L}} V_{\text{sig}}}{2} \cos\left[(\omega_r - \omega_L)\, t + \theta_{\text{sig}} - \theta_{\text{ref}}\right] \\ &- \frac{V_{\text{L}} V_{\text{sig}}}{2} \cos\left[(\omega_r + \omega_L)\, t + \theta_{\text{sig}} + \theta_{\text{ref}}\right] \ , \end{aligned}$$

one at the difference frequency $\omega_r - \omega_L$ and the other at the sum frequency $\omega_r + \omega_L$. If the PSD output is passed through an ideal low pass filter, the AC signals are removed. Then, in general, there is nothing left. However, if ω_r equals ω_L, the difference frequency component will be a DC

[1] In reality, the chopper modulates the beam as a square wave. This is not a problem, since the lock-in's reference can be locked to the square wave's first harmonic.

signal. In this case, the filtered PSD output will be:

$$V_{\text{psd}} = \frac{V_{\text{L}} V_{\text{sig}}}{2} \cos\left(\theta_{\text{sig}} - \theta_{\text{ref}}\right) \ . \tag{I.1}$$

This is a very nice signal because it is a DC signal proportional to the signal amplitude. This is possible because the PPL locks ω_L equal to ω_r. It also ensures that the phase between the signals does not change with time, otherwise $\cos\left(\theta_{\text{sig}} - \theta_{\text{ref}}\right)$ would change and V_{psd} would not be a DC signal.

The phase dependency $\theta = \theta_{\text{sig}} - \theta_{\text{ref}}$ can be eliminated by adding a second PSD. If the second PSD multiplies the signal with the reference oscillator shifted by 90°, its low pass filtered output will be:

$$V_{\text{psd2}} = \frac{V_{\text{L}} V_{\text{sig}}}{2} \sin\theta \ . \tag{I.2}$$

The first output is usually called x-component while the second, the y-component:

$$x = V_{\text{sig}} \cos\theta \qquad y = V_{\text{sig}} \sin\theta \tag{I.3}$$

and they represent the signal as a vector relative to the lock in reference oscillator. By computing the magnitude R of the signal vector, the phase dependency is removed:

$$R = \sqrt{x^2 + y^2} = V_{\text{sig}} \ , \tag{I.4}$$

where R measures the signal amplitude and does not depend upon the phase between the signal and lock in reference.

In practice, things are a bit more complicated. Since ideal filters don't exist, some noise will always be present at the output of the PSD. Real filters[2] have a bandwidth of frequencies that are allowed to pass. Frequencies outside this bandwidth are heavily attenuated. Mathematically, filters are well described in the frequency domain. The relationship between the incoming signal $V_{\text{in}}(\omega)$ and the filtered signal $V_{\text{out}}(\omega)$, in the frequency domain, is given by:

$$V_{\text{out}}(\omega) = H(\omega) V_{\text{in}}(\omega) \ , \tag{I.5}$$

where $H(\omega)$ is called the transfer function of the filter. For low-pass filters, $H(\omega)$ is well approximated by:

$$H(\omega) = \frac{1}{1 + i\omega\tau} \ , \tag{I.6}$$

where $\tau = RC$ is the filter time constant and R and C are the resistance and capacitance of the RC circuit, that is, the low-pass filter. The cut-off frequency f_c is defined as the frequency at which the signal power is reduced by -3 dB or one half. The attenuation grows ten times every tenfold frequency increase above $f_c = f_{-3\text{dB}}$. This equals 20 dB/decade corresponding to an amplitude

[2] In the case of the Lock-in, these filters are low-pass filters.

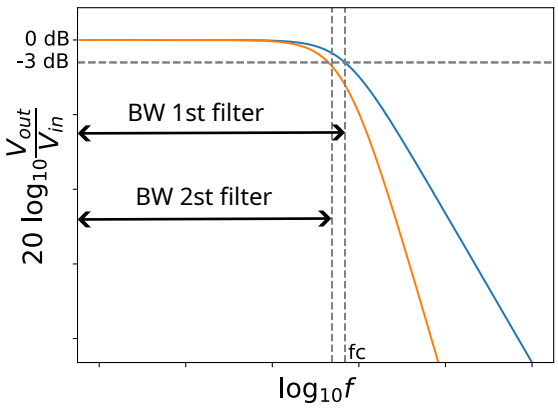

Figure I.1: Attenuation $20\log_{10} V_{\text{out}}/V_{\text{int}}$ of frequencies for a low pass filter. First order (blue line) and second order (orange line) low pass filters. Increasing the order of the filter decreases the bandwidth (BW) and improves the roll-off.

reduction by a factor of 2 every doubling of the frequency. For the filter described by $H(\omega)$, the cut-off frequency is:

$$f_c = \frac{1}{2\pi\tau} \ . \tag{I.7}$$

Compared to the idealized filter, the first-order filter has a fairly poor roll-off behavior. To increase the roll-off steepness it is common to cascade several of these filters. For every filter added the filter order is increased by 1. Since the output of one filter becomes the input to the following one, we can simply multiply their transfer functions. The transfer function of an n-th order filter is:

$$H_n(\omega) = \left(\frac{1}{1+i\omega\tau}\right)^n \ . \tag{I.8}$$

In Fig. I.1 the behavior of a first and second order filters is shown.

We now have a complete picture of the principles behind lock-in amplifier. After mixing the input signal with the reference signal, the input signal spectrum is shifted by the demodulation frequency ω_r. Low-pass filtering further transforms the spectrum through a multiplication by the filter transfer function $H_n(\omega)$. The demodulated signal contains all frequency components around the reference frequency, weighted by the filter response:

$$V_{\text{out}}(\omega) = H_n(\omega) V_{\text{in}}(\omega - \omega_r) \ . \tag{I.9}$$

This equation clearly shows that demodulation behaves like a bandpass filter in that it picks out the frequency spectrum centered at ν_r and extending on each side by $f_{-3\text{dB}}$.

The choice of the time constant (or cut-off frequency) and filter's roll-off is usually a trade-off between the quality of the results and the time that takes to do the experiment. The bigger the filter's time constant and order, the longer it takes for the lock-in's output to settle. Although, a

bigger time constant and filter order means more stable results, this is not a synonym of better results, since the experimental conditions change over time. In our case, the laser power fluctuates over the day and if the experiment takes too long, this fluctuations will start to appear in the final results. Therefore, the order and time constant are chosen to give the most stable outputs in the lowest time possible. The best combination is found by trial. A time constant of 1 second and a 60 dB/decade are enough to get good results, and this was the combination used to measure the pump depletion.

I.1 The dB unit

The dB is a logarithmic way of describing a ratio. The ratio may be power, sound pressure, voltage or intensity or several other things. In electrical circuits, dissipated power is typically proportional to the square of voltage or current when the impedance is constant. Taking voltage as an example, this leads to the equation for power gain level L_G:

$$L_G = 20 \log_{10} \left(\frac{V_{\text{out}}}{V_{\text{in}}} \right) \text{ dB} , \tag{I.10}$$

where V_{out} is the root-mean-square (rms) output voltage and V_{int} is the rms input voltage.

Appendix J

TOPAS-C

TOPAS-C is an optical parametric amplifier (OPA) [63]. This device exploits the second-order nonlinearity of nonlinear crystals such as BBO to transfer energy from a fixed frequency pump pulse to a variable frequency signal pulse, whose frequency is easily tuned.

The principle of an OPA is shown in Fig. J.1: in a nonlinear crystal, energy is transferred from a high frequency and high intensity pump beam, at frequency ω_3, to a lower frequency and lower intensity signal beam, at frequency ω_1, which is amplified. Additionally, a third beam, called the idler beam, at frequency ω_2, is created to fulfill energy conservation. In principle, the signal frequency to be amplified can vary from 0 to pump frequency ω_3, and correspondingly the idler can vary from ω_3 to 0. This mechanism is similar to DF generation, except for the strength of the interacting fields: DF generation arises when the fields at ω_3 and ω_1 have comparable intensities, while OPA occurs when the field at ω_1 is much weaker. The OPA process is efficient when, in addition to energy conservation, the phase-matching condition:

$$\Delta\mathbf{k} = \mathbf{k}_1 + \mathbf{k}_2 - \mathbf{k}_3 = 0 \tag{J.1}$$

is satisfied, where $\mathbf{k}_i$ is the wave vector of the i-th beam.

The TOPAS-C provides an optical amplifier with continuously variable frequency (determined by the phase-matching condition) and represents an easy way of changing the output frequency of an otherwise fixed femtosecond laser system. In our case, the pump is the output from the amplifier at $\lambda_3 = 800$ nm and the output from TOPAS-C is to be changed between 800 nm and 729 nm in

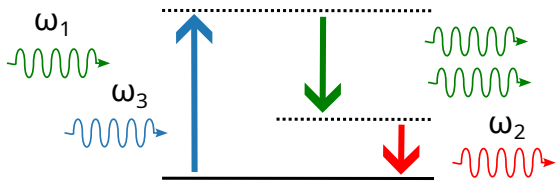

Figure J.1: Optical parametric amplification: the pump at frequency ω_3 excites the system that relaxes via stimulated emission of photons at frequency ω_1, thus amplifying the signal.

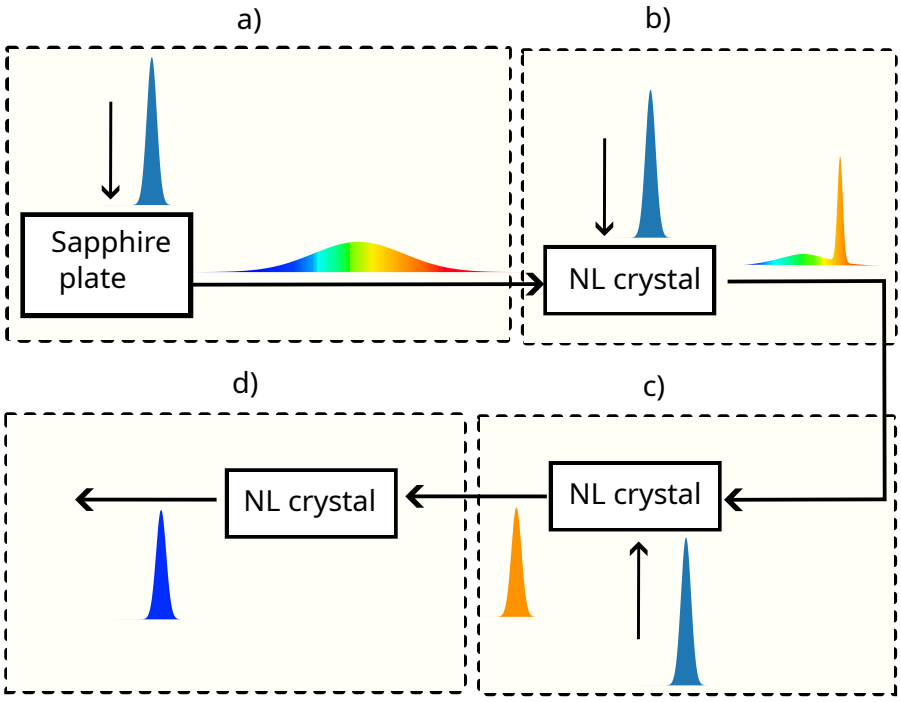

Figure J.2: TOPAS-C schematics. Each box represents a stage. The pump at $\lambda_3 = 800$ nm, here represented by the blue pulse, is used to generate the WLC and the signal pulse, ω_1 (orange pulse), as well as for signal amplification. **a)** WLC generation. The WLC is used as seed for the signal pulse. **b)** First stage amplification: in this stage a particular frequency bandwidth, around ω_1, of the WLC is amplified. The idler pulse is also created in this stage (not represented in the image). **c)** Second stage of amplification: the signal at frequency ω_1 is further amplified. **d)** The signal is used for second-harmonic generation. The final output frequency is $2\omega_1$.

order to properly DF scan the SPP dispersion and find a resonance.

The TOPAS-C operation is divided into four stages:

1. a seed pulse generation stage which will be the signal for optical parametric amplification (Fig. J.2 **a)**). In TOPAS-C the seed is a white light continuum (WLC) pulse that is generated by focusing a small fraction of the input pump in a sapphire plate. The WLC spectra usually contain an intense residual peak at the driving pulse wavelength (which contains most of the energy) and extends down to 450 nm in the visible and up to 1600 nm in the IR. Usually the bluer and redder frequencies have a spectral energy density which is 3 and 4 orders or magnitude lower than that of the driving pulse. The WLC displays excellent shot-to-shot stability and diffraction-limited spatial beam quality;

2. first parametric amplification stage (Fig. J.2 **b)**). In this stage the wavelength $\lambda_1 \in [1600, 1458]$ nm of the WLC is amplified, thus creating the signal beam. The amplified wavelength is controlled by the time delay between WLC and pump as well as by the NL crystal angle, that ensures phase match;

3. second parametric amplification stage with amplification of the signal (Fig. J.2 **c)**).

4. nonlinear generation of output signal (Fig. J.2 **d)**). In some cases, the frequency signal is not the one desired; in our case we are interested in the second harmonic of the signal. At the end of the TOPAS-C setup a set of nonlinear crystals are used to double the signal frequency to the desired range $\lambda_b \in [800, 729]$ nm.

In total, TOPAS-C has five controllable parameters to change the output frequency: the time delay between WLC and first pump and the NL crsytal angle, in the first stage; the NL crystal angle in the second stage and time delay between signal and pump; NL crystal angle for second harmonic of the signal. These parameters need to be calibrated for TOPAS-C to be used properly. There is another parameter related to the probe that must also be calibrated. Whenever we change the output frequency of TOPAS-C, the time delay between pump and probe changes. Thus, to make the pulses arrive at the same time, the probe delay line must also change accordingly. This means that the probe delay line must be calibrated relative to the TOPAS-C scan in frequency.

Appendix K

Boxcar averager

The duty-cycle of both TOPAS-C and amplifier, in Fig. 6.3, is 1 KHz. The electronic signal contains relevant information only in a fraction of each period; outside of that short interval only noise exists. The boxcar averager is a device that achieves a high signal-to-noise ratio (SNR) in a minimal amount of measurement time because it captures the signal from a well-defined temporal window in each period, meaning that all signal components outside that window are rejected [55, 56].

In a typical periodic pulsed signal, the information is contained in a short pulse of duration τ_p, with a significant waiting time between individual pulses. The signal is characterized by its duty cycle $d = \tau_p\Omega$, where Ω is the repetition rate of the pulses. If the duty cycle is low, measuring continuously in time results in a low SNR, as the time intervals between individual pulses contribute to the captured noise but not to the signal. With a boxcar averager it is possible to acquire the signal only during the pulse duration, ignoring the time intervals between pulses. This corresponds to a multiplication of the input signal with a boxcar function, which is a rectangular pulse train. By matching the period of the boxcar function $1/\Omega$, the box car window width T_{box} and its position t_0 with respect to the signal pulses, the noise between signal pulses can be discarded. The signal, $s(t)$, is then integrated over the duration of T_{box}:

$$s_{\text{box}} = \int_{-T_{\text{box}}/2}^{T_{\text{box}}/2} s(t)dt \ . \tag{K.1}$$

Finally, the integrated signal s_{box} is averaged over N periods.

The width of the boxcar window T_{box} and its position t_0, are important parameters when optimizing the SNR. For example, consider the electronic signal from the photodetector. This signal comes from the charge and discharge of the photodetector and is well described by the function[1]:

$$s(t) = s_0 e^{-t/\tau_{\text{RC}}} \left\{ 1 + \text{Erf}\left(\frac{t}{\tau_{\text{R}}} - \frac{\tau_{\text{R}}}{2\tau_{\text{RC}}} \right) \right\} \ , \tag{K.2}$$

where τ_{R} is the photodiode's rise time and the $\tau_{\text{RC}} = RC$ is the system's RC time. The captured

[1] See Appendix (K.1) for derivation.

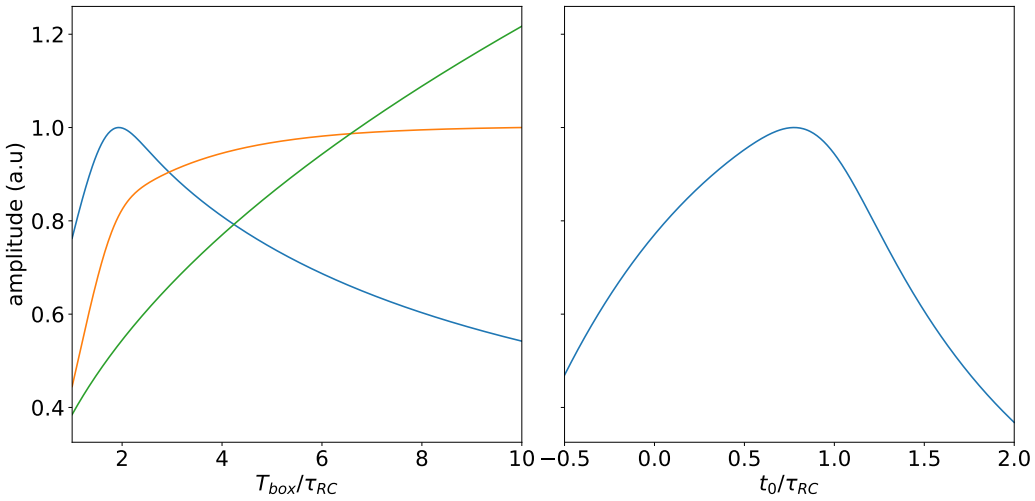

Figure K.1: **(Right)** s_{box} (orange), n_{box} (green) and SNR (blue) as functions of the boxcar window T_{box}. Here the position with respect to the signal pulses is $t_0 \approx 0.84\ \tau_{\mathrm{RC}}$. **(Left)** SNR as a function of the position with respect to the signal pulses, t_0. The window width for integration is $T_{\mathrm{box}} \approx 1.92\ \tau_{\mathrm{RC}}$. In both plots $\tau_{\mathrm{R}} = 3\ \mu$s and $\tau_{\mathrm{RC}} = 4\tau_{\mathrm{R}}$. SNR is maximized for $t_0 \approx 0.84\ \tau_{\mathrm{RC}}$ and $T_{\mathrm{box}} \approx 1.92\ \tau_{\mathrm{RC}}$.

signal increases with the boxcar window width until it approaches an amplitude of 1 when the full pulse is captured by the boxcar window. Nonetheless, the captured noise also increases with T_{box}. In the case of white noise, the captured noise n_{box} increases proportionally to the square root of the boxcar window width:

$$n_{\mathrm{box}} \propto \sqrt{T_{\mathrm{box}}}\ , \tag{K.3}$$

so choosing a big window T_{box} to fully capture the signal may not be the best option to maximize the signal to noise ratio:

$$\mathrm{SNR} = s_{\mathrm{box}}/n_{\mathrm{box}}\ . \tag{K.4}$$

Figure K.1 shows how s_{box}, n_{box} and SNR behave as functions of T_{box} and t_0. Depending on T_{box} and t_0, the SNR can be maximized.

Usually, the integration is averaged over multiple periods N. Assuming a white noise floor and an ideal boxcar window, the captured signal $\bar{s}$ increases linearly with N:

$$\bar{s} = \sum_{i=1}^{N} s_{\mathrm{box}} = N s_{\mathrm{box}}\ , \tag{K.5}$$

whereas the noise contribution $\bar{n}$ increases as the square root of the sum of the squares of the captured noise:

$$\bar{n} = \sqrt{\sum_{i=1}^{N} n_{\mathrm{box}}^2} = \sqrt{N} n_{\mathrm{box}}\ . \tag{K.6}$$

Therefore, for N boxcar periods, assuming that the signal s_{box} and the noise n_{box} are the same in

each period, the final SNR is given by:

$$\mathrm{SNR} = \frac{\bar{s}}{\bar{n}} = \frac{s_{\mathrm{box}}}{n_{\mathrm{box}}}\sqrt{N} \ . \tag{K.7}$$

K.1 Signal from a photodetector

In this appendix we derive a phenomenological expression for the photodetector electronic signal due to a ultrashort light pulse. The voltage signal is determined by the differential equation:

$$\frac{ds}{dt} + \frac{s}{\tau_{\mathrm{RC}}} = \frac{V_{\mathrm{in}}}{\tau_{\mathrm{RC}}} \ , \tag{K.8}$$

s is the electronic signal, τ_{RC} is the photodetector's RC time and V_{in} is the driving voltage pulse caused by the ultrashort light pulse. Since the light pulse is much shorter than the circuits time response, the relevant time is not the light pulse width, but the rise time of the photodiode τ_{R}. We write V_{in} as:

$$V_{in}(t) = V_i e^{-t^2/\tau_{\mathrm{R}}^2} \ . \tag{K.9}$$

Equation (K.8) is solved using the Green's function method. The full solution is the sum of the homogeneous solution V_h and a particular solution V_p:

$$s(t) = V_{\mathrm{h}}(t) + V_p(t) \ . \tag{K.10}$$

The homogeneous solution is simply:

$$V_h(t) = V_0 e^{-t/\tau_{\mathrm{RC}}} \ . \tag{K.11}$$

The particular solution is determined by:

$$V_p(t) = \int_{-\infty}^{+\infty} dt' G(t-t') V_{\mathrm{in}}(t') \ . \tag{K.12}$$

For Eq. (K.8), Green's function is:

$$G(t) = \begin{cases} 0 & t < 0 \\ e^{-t/\tau_{\mathrm{RC}}} & t > 0 \end{cases} \ , \tag{K.13}$$

so the integral in (K.12) yields:

$$V_p(t) = \frac{1}{2} e^{-t/\tau_{\mathrm{RC}}} V_{\mathrm{in}} \sqrt{\pi} \tau_{\mathrm{R}} \left\{ 1 + \mathrm{Erf}\left(\frac{t}{\tau_{\mathrm{R}}} - \frac{\tau_{\mathrm{R}}}{2\tau_{\mathrm{RC}}} \right) \right\} \ . \tag{K.14}$$

Using the results (K.11) and (K.14), the full solution to (K.8) is:

$$s(t) = e^{-t/\tau_{\mathrm{RC}}} \left(V_0 + \frac{1}{2} V_{\mathrm{in}} \sqrt{\pi} \tau_{\mathrm{R}} \left\{ 1 + \mathrm{Erf} \left(\frac{t}{\tau_{\mathrm{R}}} - \frac{\tau_{\mathrm{R}}}{2\tau_{\mathrm{RC}}} \right) \right\} \right) \ . \tag{K.15}$$

At $t = 0$ and for the cases of interest ($\tau_{\mathrm{R}} < \tau_{\mathrm{RC}}$):

$$s(t = 0) = s_0 \approx V_0 + \frac{1}{2} V_{\mathrm{in}} \sqrt{\pi} \tau_{\mathrm{R}} \ . \tag{K.16}$$

I set:

$$\frac{1}{2} V_{\mathrm{in}} \sqrt{\pi} \tau_{\mathrm{R}} = s_0 \ , \tag{K.17}$$

so that the final expression assumes the simplified form:

$$s(t) = s_0 e^{-t/\tau_{\mathrm{RC}}} \left\{ 1 + \mathrm{Erf} \left(\frac{t}{\tau_{\mathrm{R}}} - \frac{\tau_{\mathrm{R}}}{2\tau_{\mathrm{RC}}} \right) \right\} \ . \tag{K.18}$$

Bibliography

[1] T. J. Constant, S. M. Hornett, D. E. Chang, and E. Hendry. All-optical generation of surface plasmons in graphene. *Nature Photonics*, 12:124 – 127, 2016. doi: 10.1038/nphys3545.

[2] Baicheng Yao, Yuan Liu, Shu-Wei Huang, Chanyeol Choi, Zhenda Xie, Jaime Flor Flores, Yu Wu, Mingbin Yu, Dim-Lee Kwong, Yu Huang, Yunjiang Rao, Xiangfeng Duan, and Chee Wei Wong. Broadband gate-tunable terahertz plasmons in graphene heterostructures. *Nature Photonics*, 12(1):22–28, Jan 2018. ISSN 1749-4893. doi: 10.1038/s41566-017-0054-7. URL `https://doi.org/10.1038/s41566-017-0054-7`.

[3] P. R. Wallace. The band theory of graphite. *Phys. Rev.*, 71:622–634, May 1947. doi: 10.1103/PhysRev.71.622. URL `https://link.aps.org/doi/10.1103/PhysRev.71.622`.

[4] K. S. Novoselov, A. K. Geim, S. V. Morozov, D. Jiang, Y. Zhang, S. V. Dubonos, I. V. Grigorieva, and A. A. Firsov. Electric field effect in atomically thin carbon films. *Science*, 306(5696): 666–669, 2004. doi: 10.1126/science.1102896. URL `https://www.science.org/doi/abs/10.1126/science.1102896`.

[5] A. H. Castro Neto, F. Guinea, N. M. R. Peres, K. S. Novoselov, and A. K. Geim. The electronic properties of graphene. *Rev. Mod. Phys.*, 81:109–162, Jan 2009. doi: 10.1103/RevModPhys.81.109. URL `https://link.aps.org/doi/10.1103/RevModPhys.81.109`.

[6] YU. V. BLUDOV, AIRES FERREIRA, N. M. R. PERES, and M. I. VASILEVSKIY. A primer on surface plasmon-polaritons in graphene. *International Journal of Modern Physics B*, 27(10): 1341001, 2013. doi: 10.1142/S0217979213410014.

[7] P. A. D. Goncalves and N. M. R. Peres. *An introduction to graphene plasmonics*. World Scientific Publishing, 2016.

[8] Taiichi Otsuji, Vyacheslav Popov, and Victor Ryzhii. Active graphene plasmonics for terahertz device applications. *Journal of Physics D: Applied Physics*, 47(9):094006, feb 2014. doi: 10.1088/0022-3727/47/9/094006. URL `https://dx.doi.org/10.1088/0022-3727/47/9/094006`.

[9] Rui Dias, Jose C. Viana Gomes, and Mikhail I. Vasilevskiy. Analysis of all-optical generation of graphene surface plasmons by a frequency-difference process. *Applied Sciences*, 12(23), 2022.

ISSN 2076-3417. doi: 10.3390/app122312376. URL https://www.mdpi.com/2076-3417/12/23/12376.

[10] Rui Dias, Diogo Cunha, and Mikhail Vasilevskiy. Generation of hot surface plasmons in graphene by a powerful optical beam. In *2023 23rd International Conference on Transparent Optical Networks (ICTON)*, pages 1–4, 2023. doi: 10.1109/ICTON59386.2023.10207270.

[11] Xianghan Yao, Mikhail Tokman, and Alexey Belyanin. Efficient nonlinear generation of thz plasmons in graphene and topological insulators. *Phys. Rev. Lett.*, 112:055501, Feb 2014. doi: 10.1103/PhysRevLett.112.055501. URL https://link.aps.org/doi/10.1103/PhysRevLett.112.055501.

[12] R. W. Boyd. *Nonlinear Optics*. Academic Press, Boston, 2008.

[13] T. J. Constant, S. M. Hornett, D. E. Chang, and E. Hendry. Intensity dependences of the nonlinear optical excitation of plasmons in graphene. *Phil. Trans. R. Soc. A*, 375:20160066, 2017. doi: 10.1098/rsta.2016.0066.

[14] S. A. Jensen, Z. Mics, I. Ivanov, H. S. Varol, D. Turchinovich, F. H. L. Koppens, M. Bonn, and K. J. Tielrooij. Competing ultrafast energy relaxation pathways in photoexcited graphene. *Nano Letters*, 14(10):5839–5845, Oct 2014. ISSN 1530-6984. doi: 10.1021/nl502740g. URL https://doi.org/10.1021/nl502740g.

[15] Isaac John Luxmoore, Choon How Gan, Peter Qiang Liu, Federico Valmorra, Penglei Li, Jérôme Faist, and Geoffrey R. Nash. Strong coupling in the far-infrared between graphene plasmons and the surface optical phonons of silicon dioxide. *ACS Photonics*, 1(11):1151–1155, Nov 2014. doi: 10.1021/ph500233s. URL https://doi.org/10.1021/ph500233s.

[16] C. J. Tollerton, J. Bohn, T. J. Constant, S. A. R. Horsley, D. E. Chang, E. Hendry, and D. Z. Li. Origins of all-optical generation of plasmons in graphene. *Scientific Reports*, 9:3267, 2019. doi: 10.1038/s41598-019-39961-1.

[17] Yongrui Wang, Mikhail Tokman, and Alexey Belyanin. Second-order nonlinear optical response of graphene. *Phys. Rev. B*, 94:195442, Nov 2016. doi: 10.1103/PhysRevB.94.195442. URL https://link.aps.org/doi/10.1103/PhysRevB.94.195442.

[18] S. A. Mikhailov. Non-linear electromagnetic response of graphene. *Europhysics Letters*, 79 (2):27002, jun 2007. doi: 10.1209/0295-5075/79/27002. URL https://dx.doi.org/10.1209/0295-5075/79/27002.

[19] Kung-Hsuan Lin, Shao-Wei Weng, Po-Wei Lyu, Tsong-Ru Tsai, and Wei-Bin Su. Observation of optical second harmonic generation from suspended single-layer and bi-layer graphene. *Applied Physics Letters*, 105(15), 10 2014. ISSN 0003-6951. doi: 10.1063/1.4898065. URL https://doi.org/10.1063/1.4898065. 151605.

[20] Eugene I. Blount. Formalisms of band theory. *Journal of Physics C: Solid State Physics*, 13: 305–373, 1962.

[21] G. B. Ventura, D. J. Passos, J. M. B. Lopes dos Santos, J. M. Viana Parente Lopes, and N. M. R. Peres. Gauge covariances and nonlinear optical responses. *Phys. Rev. B*, 96:035431, Jul 2017. doi: 10.1103/PhysRevB.96.035431. URL `https://link.aps.org/doi/10.1103/PhysRevB.96.035431`.

[22] D. J. Passos, G. B. Ventura, J. M. Viana Parente Lopes, J. M. B. Lopes dos Santos, and N. M. R. Peres. Nonlinear optical responses of crystalline systems: Results from a velocity gauge analysis. *Phys. Rev. B*, 97:235446, Jun 2018. doi: 10.1103/PhysRevB.97.235446. URL `https://link.aps.org/doi/10.1103/PhysRevB.97.235446`.

[23] N. Bloembergen and P. S. Pershan. Light waves at the boundary of nonlinear media. *Phys. Rev.*, 128:606–622, Oct 1962. doi: 10.1103/PhysRev.128.606. URL `https://link.aps.org/doi/10.1103/PhysRev.128.606`.

[24] Ronald Ulbricht, Euan Hendry, Jie Shan, Tony F. Heinz, and Mischa Bonn. Carrier dynamics in semiconductors studied with time-resolved terahertz spectroscopy. *Rev. Mod. Phys.*, 83: 543–586, Jun 2011. doi: 10.1103/RevModPhys.83.543. URL `https://link.aps.org/doi/10.1103/RevModPhys.83.543`.

[25] Z. Fei, A. S. Rodin, G. O. Andreev, W. Bao, A. S. McLeod, M. Wagner, L. M. Zhang, Z. Zhao, G. Dominguez, M. Thiemens, M. M. Fogler, A. H. Castro-Neto, C. N. Lau, F. Keilmann, and D. N. Basov. Gate-tuning of graphene plasmons revealed by infrared nano-imaging. *Nature*, 487:82, 2012. doi: 10.1038/nature11253.

[26] Jianing Chen, Michela Badioli, Pablo Alonso-Gonzalez, Suko Thongrattanasiri, Florian Huth, Johann Osmond, Marko Spasenovic, Alba Centeno, Amaia Pesquera, Philippe Godignon, Amaia Zurutuza, Nicolas Camara, Javier Garcia de Abajo, Rainer Hillenbrand, and Frank Koppens. Optical nano-imaging of gate-tunable graphene plasmons. *Nature*, 487:77, 2012. doi: 10.1038/nature11254.

[27] Hassan A. Hafez, Sergey Kovalev, Jan-Christoph Deinert, Zoltán Mics, Bertram Green, Nilesh Awari, Min Chen, Semyon Germanskiy, Ulf Lehnert, Jochen Teichert, Zhe Wang, Klaas-Jan Tielrooij, Zhaoyang Liu, Zongping Chen, Akimitsu Narita, Klaus Müllen, Mischa Bonn, Michael Gensch, and Dmitry Turchinovich. Extremely efficient terahertz high-harmonic generation in graphene by hot dirac fermions. *Nature*, 561(7724):507–511, Sep 2018. ISSN 1476-4687. doi: 10.1038/s41586-018-0508-1. URL `https://doi.org/10.1038/s41586-018-0508-1`.

[28] F. Rana. Graphene terahertz plasmon oscillators. *IEEE Transactions on Nanotechnology*, 7(1): 91–99, jan 2008. doi: 10.1109/tnano.2007.910334. URL `https://doi.org/10.1109%2Ftnano.2007.910334`.

[29] A. Freddie Page, Fouad Ballout, Ortwin Hess, and Joachim M. Hamm. Nonequilibrium plasmons with gain in graphene. *Phys. Rev. B*, 91:075404, Feb 2015. doi: 10.1103/PhysRevB.91.075404. URL https://link.aps.org/doi/10.1103/PhysRevB.91.075404.

[30] S. A. Mikhailov. Theory of the strongly nonlinear electrodynamic response of graphene: A hot electron model. *Phys. Rev. B*, 100:115416, Sep 2019. doi: 10.1103/PhysRevB.100.115416. URL https://link.aps.org/doi/10.1103/PhysRevB.100.115416.

[31] P. J. Hale, S. M. Hornett, J. Moger, D. W. Horsell, and E. Hendry. Hot phonon decay in supported and suspended exfoliated graphene. *Phys. Rev. B*, 83:121404, Mar 2011. doi: 10.1103/PhysRevB.83.121404. URL https://link.aps.org/doi/10.1103/PhysRevB.83.121404.

[32] Jahan M. Dawlaty, Shriram Shivaraman, Mvs Chandrashekhar, Farhan Rana, and Michael G. Spencer. Measurement of ultrafast carrier dynamics in epitaxial graphene. *Applied Physics Letters*, 92(4), 01 2008. ISSN 0003-6951. doi: 10.1063/1.2837539. URL https://doi.org/10.1063/1.2837539. 042116.

[33] Isabella Gierz, Jesse C. Petersen, Matteo Mitrano, Cephise Cacho, I. C. Edmond Turcu, Emma Springate, Alexander Stöhr, Axel Köhler, Ulrich Starke, and Andrea Cavalleri. Snapshots of non-equilibrium dirac carrier distributions in graphene. *Nature Materials*, 12(12):1119–1124, Dec 2013. ISSN 1476-4660. doi: 10.1038/nmat3757. URL https://doi.org/10.1038/nmat3757.

[34] J. M. Hamm, A. F. Page, J. Bravo-Abad, F. J. Garcia-Vidal, and O. Hess. Nonequilibrium plasmon emission drives ultrafast carrier relaxation dynamics in photoexcited graphene. *Phys. Rev. B*, 93:041408, Jan 2016. doi: 10.1103/PhysRevB.93.041408. URL https://link.aps.org/doi/10.1103/PhysRevB.93.041408.

[35] Laura Kim, Seyoon Kim, Pankaj K. Jha, Victor W. Brar, and Harry A. Atwater. Mid-infrared radiative emission from bright hot plasmons in graphene. *Nature Materials*, 20(6):805–811, Jun 2021. ISSN 1476-4660. doi: 10.1038/s41563-021-00935-2. URL https://doi.org/10.1038/s41563-021-00935-2.

[36] A. Freddie Page, Joachim M. Hamm, and Ortwin Hess. Polarization and plasmons in hot photoexcited graphene. *Phys. Rev. B*, 97:045428, Jan 2018. doi: 10.1103/PhysRevB.97.045428. URL https://link.aps.org/doi/10.1103/PhysRevB.97.045428.

[37] Mathieu Massicotte, Giancarlo Soavi, Alessandro Principi, and Klaas-Jan Tielrooij. Hot carriers in graphene, fundamentals and applications. *Nanoscale*, 13:8376–8411, 2021. doi: 10.1039/D0NR09166A. URL http://dx.doi.org/10.1039/D0NR09166A.

[38] D. Brida, A. Tomadin, C. Manzoni, Y. J. Kim, A. Lombardo, S. Milana, R. R. Nair, K. S. Novoselov, A. C. Ferrari, G. Cerullo, and M. Polini. Ultrafast collinear scattering and carrier

multiplication in graphene. *Nat. Commun.*, 4(1):1987, Jun 2013. ISSN 2041-1723. doi: 10.1038/ncomms2987. URL https://doi.org/10.1038/ncomms2987.

[39] Andrea Tomadin, Sam M. Hornett, Hai I. Wang, Evgeny M. Alexeev, Andrea Candini, Camilla Coletti, Dmitry Turchinovich, Mathias KlÃ€ui, Mischa Bonn, Frank H. L. Koppens, Euan Hendry, Marco Polini, and Klaas-Jan Tielrooij. The ultrafast dynamics and conductivity of photoexcited graphene at different fermi energies. *Science Advances*, 4(5):eaar5313, 2018. doi: 10.1126/sciadv.aar5313. URL https://www.science.org/doi/abs/10.1126/sciadv.aar5313.

[40] Farhan Rana, Jared H. Strait, Haining Wang, and Christina Manolatou. Ultrafast carrier recombination and generation rates for plasmon emission and absorption in graphene. *Phys. Rev. B*, 84:045437, Jul 2011. doi: 10.1103/PhysRevB.84.045437. URL https://link.aps.org/doi/10.1103/PhysRevB.84.045437.

[41] Selcuk Akturk, Xun Gu, Pablo Gabolde, and Rick Trebino. The general theory of first-order spatio-temporal distortions of gaussian pulses and beams. *Opt. Express*, 13(21):8642–8661, Oct 2005. doi: 10.1364/OPEX.13.008642. URL http://www.opticsexpress.org/abstract.cfm?URI=oe-13-21-8642.

[42] G. X. Ni, L. Wang, M. D. Goldflam, M. Wagner, Z. Fei, A. S. McLeod, M. K. Liu, F. Keilmann, B. Özyilmaz, A. H. Castro Neto, J. Hone, M. M. Fogler, and D. N. Basov. Ultrafast optical switching of infrared plasmon polaritons in high-mobility graphene. *Nature Photonics*, 10(4):244–247, Apr 2016. ISSN 1749-4893. doi: 10.1038/nphoton.2016.45. URL https://doi.org/10.1038/nphoton.2016.45.

[43] Aaron Bostwick, Taisuke Ohta, Thomas Seyller, Karsten Horn, and Eli Rotenberg. Quasiparticle dynamics in graphene. *Nature Physics*, 3(1):36–40, Jan 2007. ISSN 1745-2481. doi: 10.1038/nphys477. URL https://doi.org/10.1038/nphys477.

[44] Aaron Bostwick, Florian Speck, Thomas Seyller, Karsten Horn, Marco Polini, Reza Asgari, Allan H. MacDonald, and Eli Rotenberg. Observation of plasmarons in quasi-freestanding doped graphene. *Science*, 328(5981):999–1002, 2010. doi: 10.1126/science.1186489. URL https://www.science.org/doi/abs/10.1126/science.1186489.

[45] Frank H. L. Koppens and Klaas-Jan Tielrooij. Hot plasmons make graphene shine. *Nature Materials*, 20(6):721–722, Jun 2021. ISSN 1476-4660. doi: 10.1038/s41563-021-00952-1. URL https://doi.org/10.1038/s41563-021-00952-1.

[46] Hayes W and Rodney Loudon. *Scattering of Light by Crystals*. Dover Publications, 2004.

[47] Radi A. Jishi. *Feynman Diagram Techniques in Condensed Matter Physics*. Cambridge University Press, 2013. doi: 10.1017/CBO9781139177771.

[48] W. Thomas Pollard, Soo-Y. Lee, and Richard A. Mathies. Wave packet theory of dynamic absorption spectra in femtosecond pump-probe experiments. *The Journal of Chemical Physics*, 92(7):4012–4029, 04 1990. ISSN 0021-9606. doi: 10.1063/1.457815. URL https://doi.org/10.1063/1.457815.

[49] Zhigang Sun, Zhongqi Jin, J. Lu, Dong H. Zhang, and Soo-Y. Lee. Wave packet theory of dynamic stimulated Raman spectra in femtosecond pump-probe spectroscopy. *The Journal of Chemical Physics*, 126(17):174104, 05 2007. ISSN 0021-9606. doi: 10.1063/1.2715593. URL https://doi.org/10.1063/1.2715593.

[50] Malvin Carl Teich Bahaa E. A. Saleh. *Fundamentals of Photonics*. John Wiley I& Sons, Inc., 1991. doi: 10.1002/0471213748.

[51] Selcuk Akturk, Xun Gu, Mark Kimmel, and Rick Trebino. Extremely simple single-prism ultrashort-pulse compressor. *Opt. Express*, 14(21):10101–10108, Oct 2006. doi: 10.1364/OE.14.010101. URL https://opg.optica.org/oe/abstract.cfm?URI=oe-14-21-10101.

[52] Ming Lai, Shui T. Lai, and Casimir Swinger. Single-grating laser pulse stretcher and compressor. *Appl. Opt.*, 33(30):6985–6987, Oct 1994. doi: 10.1364/AO.33.006985. URL https://opg.optica.org/ao/abstract.cfm?URI=ao-33-30-6985.

[53] Eksma Optics. https://eksmaoptics.com/nonlinear-and-laser-crystals/nonlinear-crystals/beta-barium-borate-bbo-crystals/.

[54] Thorlabs. https://www.thorlabs.com/thorProduct.cfm?partNumber=DET10A/M.

[55] Stanford Research Systems. https://www.thinksrs.com/downloads/pdfs/manuals/Boxcarm.pdf.

[56] Zurich Instruments. https://www.zhinst.com/europe/en/resources/principles-of-boxcar-averaging, .

[57] Newport. https://www.newport.com/p/2007.

[58] Beatriz A. Ferreira, B. Amorim, A. J. Chaves, and N. M. R. Peres. Quantization of graphene plasmons. *Phys. Rev. A*, 101:033817, Mar 2020. doi: 10.1103/PhysRevA.101.033817. URL https://link.aps.org/doi/10.1103/PhysRevA.101.033817.

[59] David N. Nikogosyan. *Nonlinear Optical Crystals: A Complete Survey*. Springer New York, NY, 2006. doi: 10.1007/b138685.

[60] Arthur McGurn. *Nanophotonics*. Springer Cham, 2018. doi: 10.1007/978-3-319-77072-7.

[61] Zurich Instruments. https://www.zhinst.com/europe/en/resources/principles-of-lock-in-detection, .

[62] Zurich Instruments. `https://www.thinksrs.com/downloads/pdfs/manuals/SR830m.pdf`, .

[63] C Manzoni and G Cerullo. Design criteria for ultrafast optical parametric amplifiers. *Journal of Optics*, 18(10):103501, aug 2016. doi: 10.1088/2040-8978/18/10/103501. URL `https://dx.doi.org/10.1088/2040-8978/18/10/103501`.